HEATING OF TURBULENT SOLAR AND LABORATORY PLASMAS

Gordon W. Inverarity

A Thesis Submitted for the Degree of PhD
at the
University of St Andrews

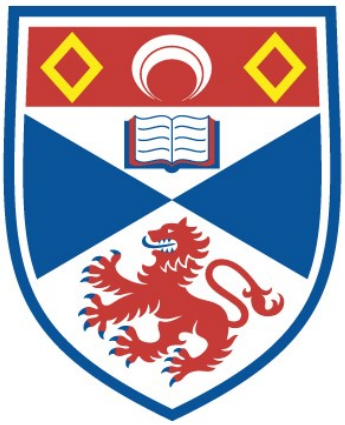

1995

Heating of Turbulent Solar and Laboratory Plasmas

Gordon W. Inverarity

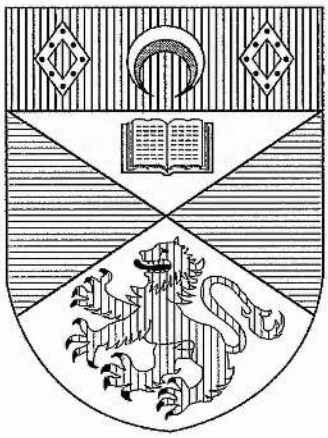

Thesis submitted for the degree of Doctor of Philosophy
of the University of St. Andrews.

ProQuest LLC.
789 East Eisenhower Parkway
P.O. Box 1346
Ann Arbor, MI 48106 – 1346

Declaration

1. I, Gordon Walker Inverarity, hereby certify that this thesis has been composed by myself, that it is a record of my own work, and that it has not been accepted in partial or complete fulfilment of any other degree or professional qualification.

   Signed .. ..Date ..3.5.95.....

2. I was admitted to the Faculty of Science of the University of St. Andrews under Ordinance General No. 12 in October 1991 and as a candidate for the degree of Ph.D. in October 1992.

   Signed ....Date ..3.5.95.....

3. I hereby certify that the candidate has fulfilled the conditions of the Resolution and Regulations appropriate to the Degree of Ph.D.

   Signature of Supervisor ....Date ..3.5.95.....

4. In submitting this thesis to the University of St. Andrews I understand that I am giving permission for it to be made available for use in accordance with the regulations of the University Library for the time being in force, subject to any copyright vested in the work not being affected thereby. I also understand that the title and abstract will be published, and that a copy of the work may be made and supplied to any bona fide library or research worker.

Abstract

The model of Heyvaerts and Priest (1992) for steady-state heating of the turbulent medium within a sheared solar coronal arcade structure is here developed. The energy input into the corona is calculated at the large scales of the model. At the smaller scales the effects of coronal turbulence are modelled in the form of an enhanced turbulent viscosity and magnetic diffusivity, which are related to the injected power density in the steady state. Matching the expressions for the injected and dissipated power enables the calculation of a heating power consistent with both boundary motions and turbulent effects with a minimum of arbitrary parameters — the price to be paid is that the inertial range spectrum must be prescribed and imposed at all scales.

While it is capable of reproducing the observed levels of coronal heating (300 Wm^{-2} (3×10^5 erg $\mathrm{cm}^{-2}\mathrm{s}^{-1}$) for the quiet Sun, 800 Wm^{-2} (8×10^5 erg $\mathrm{cm}^{-2}\mathrm{s}^{-1}$) for a coronal hole and 10^4 Wm^{-2} (10^7 erg $\mathrm{cm}^{-2}\mathrm{s}^{-1}$) for an active region (Withbroe and Noyes, 1977)), there are some mathematical and physical difficulties present. These are eliminated as far as is possible and it is found that the final results for heating levels differ little from the original model although there is a much greater consistency between the imposed and predicted energy power spectra.

The modified approach is applied to the problems of photospheric motions twisting a coronal flux tube and of rapid motions injecting Alfvén waves into an arcade. In the former case comparable levels of heating are obtained. For a driven and damped standing wave, however, desired levels of heating are only obtained when a global resonance occurs.

Attempts are also made to find similar steady-state equilibria possessing flow for fusion experiments in order to apply the above procedure to investigate turbulence in laboratory plasmas. This has been hampered by the difficulty in finding simple appropriate equilibria with many scales present.

The heavens declare the glory of God;
And the firmament shows His handiwork.
Day unto day utters speech.
And night unto night reveals knowledge.
There is no speech nor language
Where their voice is not heard.
Their line has gone out through all the earth,
And their words to the end of the world.

In them He has set a tabernacle for the sun,
Which is like a bridegroom coming out of his chamber,
And rejoices like a strong man to run its race.
Its rising is from one end of heaven,
And its circuit to the other end;
And there is nothing hidden from its heat.

Psalm 19 vv. 1–6 (New King James Version)

Per aspera ad astra
(Through difficulties to the stars)

Contents

Publications

The contents of Chaps. 3–6 of this thesis have been published in conference proceedings (Càrgese Workshop on Magnetic Turbulence and Transport — Inverarity and Priest (1993a); Pichl Workshop on Plasma Physics — Inverarity and Priest (1993b, 1994)) in which constant scale-independent turbulent viscosity and magnetic diffusivity were used. Chapters 4 & 5 have been published in "Astronomy and Astrophysics" (Inverarity et al., 1995; Inverarity and Priest, 1995a) and Chap. 6 has been accepted for publication in the same journal (Inverarity and Priest, 1995b), scale-dependent turbulent viscosity and magnetic diffusivity being used therein. In addition to the Càrgese and 1994 Pichl meetings, oral presentations have been given at the U.K. National Astronomy meeting in Edinburgh, 1994 and the U.K. MHD meeting in Cambridge, 1994.

Acknowledgements

Most aspects of this thesis reflect the abilities and experience of many individuals. I would like to thank those who immediately spring to mind, but inevitably there will be influences who remain unacknowledged. First of all thanks are due to my supervisors, Prof. Eric Priest of St. Andrews University, who has provided many valuable contacts and opportunities throughout the term of this Ph.D in addition to his solar expertise, and Dr. Chris Gimblett of Culham laboratory, who has guided my fusion work. The critical abilities and expertise of other members of the Solar Group have also been both a valuable resource and encouragement in resolving problems in my work and keeping me going. In understanding the problems of turbulence I am indebted to Drs. Marco Velli, Sean Oughton and Prof. Jean Heyvaerts for explaining many less than obvious aspects of the field, and also Dr. Daniel Gómez who motivated a critical examination of the consistency of this work. Those who have proof-read different parts of this thesis are also thanked: Eric Priest, Chris Gimblett, Sean Oughton, Mark Child, Duncan MacKay and Cheryl Mundie. My stays in Abingdon were made very enjoyable by members of All Saints Church and, in particular, the Dicksons who were happy to provide accommodation for the majority of my time there. Finally, I wish to express my gratitude to Prof. Jean Heyvaerts without whose assistance and insight I would not have completed this thesis and to those who kept me going throughout the period of my research, notably my parents, Zara Johnston, Richard Moseley, Clare Parnell and Derryck Reid.

This work has been supported by a Cooperative Award in Science and Engineering funded by the U.K. Science and Engineering Research Council (latterly the Particle Physics and Astronomy Research Council) and A.E.A. Technology.

Chapter 1

Turbulence

1.1 Introduction

The word "turbulence" has three meanings, broadly speaking; one is associated with unpredictable events, another with commotion amongst a crowd, and a third with a physical phenomenon displayed, for example, in the weather. Thus, a politician's thoughts might turn to the break-up of the Soviet Union, a historian's to the French revolution, while to the modern traveller atmospheric turbulence is all too familiar. This variation is reflected in the semantics of the Latin word "turba", which literally means a tumult or uproar and which later acquired the association with crowds. Similarly "turbulentus", the derived adjective, introduces the association with weather through the translation "stormy" or "boisterous" (Cassell's Latin-English Dictionary). In all three cases the notion of unpredictability is central, but it is the latter sense which will be pursued in this thesis, particularly with regard to magnetofluids.

A walk along the East Sands of St. Andrews on a calm day provides an opportunity to experience turbulence in an everyday context. Looking out to sea, waves can be observed slowly travelling towards the land. As a wave approaches the shallower water near the beach a crest develops at a small region of the wavefront and grows in time. The leading part of the crest moves ahead of the main body of the wave and succumbs to the effects of gravity, accompanied by a familiar crashing sound. A much thinner layer of frothing water is projected forward at higher speed and gradually slows down, the effervescence being maintained throughout. Eventually the bubbling dies away and a smooth, thin layer of water, sandwiched between its precursor and successor, reaches the observer's feet from where it retreats beneath advancing layers. Encapsulated within this scene we have transition to turbulence, turbulence conveyed by a mean flow, freely-decaying turbulence, turbulent viscosity, and laminar flow.

What properties of turbulence can be identified in the foregoing description? Unpredictability is the first. For a wave far from the shore a parcel of fluid can be followed first as it is disturbed

and then in its subsequent motion. Experimentally a neutrally buoyant marker could be placed in the sea, then its motions followed and compared with wave solutions of the Navier-Stokes fluid equations[1], with broad agreement being apparent. However, in the breaking wave the motion of an individual parcel of fluid is unpredictable: simulations will exhibit similar global behaviour but the detailed behaviour of an individual fluid element will not reproduce the results of an experiment. Indeed, repeating the experiment with a marker starting under similar conditions will lead to a different path being traced out, and so we should certainly not expect to be able to predict theoretically the detailed motion of turbulent flow.

A second property is that of mixing. If a cloud of dye is injected into a fluid there will be some spreading of the cloud with time due to molecular motions within the fluid. In the sea, a passing wave will enhance diffusion but to a considerably lesser extent than will a breaking wave, in which the volume containing dye increases substantially in a short time. An instance of this aspect of turbulence being applied in recognisable circumstances will be familiar to many, namely the predilection of James Bond, in the guise of Sean Connery, for dry martinis which have been "shaken, not stirred!"; here the churning drives the turbulence which in turn mixes the gin and vermouth. More seriously, enhanced mixing can be exploited in the clearing of oil spillages, when detergent sprayed on the oil slick requires the assistance of rough weather to mix with the oil and break up the slick. This was particularly apparent in the grounding of the Braer off the Shetland coast in January 1992 following which there was little environmental damage even though the stormy weather prevented the application of detergent by aircraft: the violence of the wind and waves alone acted to disperse the oil. This was in direct contrast to the Alaskan oil spill from the Exxon Valdez in March 1989 where calm weather prevailed and considerable damage resulted.

Despite having beneficial uses, turbulence is more usually regarded as a hindrance to humanity's efforts to harness nature. Two instances of this are increased resistance to motion through a turbulent fluid (drag), and the reduction of lift generated by an aircraft wing as it encounters atmospheric turbulence. Later on in this thesis the problem of turbulence in magnetically confined plasma in laboratory fusion experiments will be examined in more detail; it will suffice for now to say that the turbulence there makes it hard to keep the plasma of several million degrees isolated from the metal containing vessel, with the results that the plasma cools, becoming less capable of maintaining thermal fusion reactions, and the vessel becomes damaged by the encounter.

With the exception of this fusion context, all of these processes can be described by the Navier-Stokes equations of fluid motion, which, along with the longevity of the equations, bears witness to their comprehensive description of fluid behaviour. Yet although the equations have been identified, exact solutions remain elusive apart from in a few special cases. Extracting information from the equations, therefore, forms the basis of most fluid mechanics research, both analytical and computational. The former is hampered by the difficulty and scarcity of methods for solving nonlin-

[1] An introduction to the equations and their solutions may be found in Batchelor (1967) and Landau and Lifschitz (1987).

ear differential equations, while limitations in computer memory still preclude numerical solutions of turbulent flow at appropriate Reynolds numbers, despite substantial improvements.

1.2 Fluid Turbulence

Turbulence in fluids has been studied more extensively than that in magnetofluids, which is in its infancy in terms of the methods employed and confidence in results obtained.[2] The presence of magnetic field adds the complications of a preferred direction which cannot be removed by a coordinate transformation, and of additional equations and nonlinear terms. For completeness the methodology for analysing fluid turbulence is now reviewed in some detail. The generalisation to MHD flows will be tackled in Sect. 1.3 using the same methods, but presented in considerably less detail.

1.2.1 Development of Turbulent Flow

To proceed mathematically we start with the Navier-Stokes equation, appropriate for incompressible fluid flow in the absence of gravity:

$$\frac{\partial \boldsymbol{u}}{\partial t} + (\boldsymbol{u} \cdot \nabla)\boldsymbol{u} = -\frac{1}{\rho}\nabla p + \nu \nabla^2 \boldsymbol{u}, \tag{1.1}$$

$$\nabla \cdot \boldsymbol{u} = 0, \tag{1.2}$$

where $\boldsymbol{u}$ is the velocity, t is time, ρ is the mass density, p is the hydrostatic pressure and ν is the kinematic viscosity. It can be seen that this forms a system of four equations in the four unknowns u_1, u_2, u_3 and p. McComb (1990, Sect. 2.1) proceeds to eliminate the pressure from Eq. (1.1) by taking the divergence and solves the resulting Poisson equation

$$\nabla^2 p = -\rho \nabla \cdot ((\boldsymbol{u} \cdot \nabla)\boldsymbol{u}), \tag{1.3}$$

using Green's functions and von Neumann boundary conditions. The final expression for p is then substituted back into Eq. (1.1) to give three equations in the three velocity components. This procedure is mathematically tedious and does not lend anything to the physical understanding of the problem. However, it provides the basis for a more formal treatment of the process by which the Navier-Stokes equation and its moments can be expressed in Fourier space, taking account of the fact that for turbulence the velocity is a random variable and not a continuous function. When it becomes necessary to eliminate the pressure term in Sect. 1.2.5 a simpler approach will be followed, given by Lesieur (1990), amongst others.

Any turbulent flow can be considered as consisting of a background flow, $\overline{\boldsymbol{u}}$, onto which the turbulent fluctuations, $\boldsymbol{u}'$, are superposed: $\boldsymbol{u} = \overline{\boldsymbol{u}} + \boldsymbol{u}'$. Noting that the average of the fluctuations

[2] This is simply due to the comparative ease of fluid experiments, which can be performed at room temperatures using simpler equipment than is the case for either hot plasma or flowing metal suffused with an external magnetic field.

and the average of any product of mean and fluctuating parts is zero, Eq. (1.1) and Eq. (1.2) become, upon averaging and expressing in tensor form[3],

$$\frac{\partial \overline{u}_i}{\partial t} + \overline{u}_j \frac{\partial \overline{u}_i}{\partial x_j} + \frac{\partial}{\partial x_j}\overline{u_i' u_j'} = -\frac{1}{\rho}\frac{\partial \overline{p}}{\partial x_i} + \nu \frac{\partial^2 \overline{u}_i}{\partial x_j \partial x_j}, \tag{1.4}$$

$$\frac{\partial \overline{u}_i}{\partial x_i} = 0, \tag{1.5}$$

where Eq. (1.7) has been invoked in obtaining Eq. (1.4) and the Einstein summation convention is used here and hereafter. Subtraction from the original equations gives the corresponding equations for the fluctuating parts:

$$\frac{\partial u_i'}{\partial t} + u_j' \frac{\partial \overline{u}_i}{\partial x_j} + \overline{u}_j \frac{\partial u_i'}{\partial x_j} + \frac{\partial}{\partial x_j}\left(u_i' u_j' - \overline{u_i' u_j'}\right) = -\frac{1}{\rho}\frac{\partial p'}{\partial x_i} + \nu \frac{\partial^2 u_i'}{\partial x_j \partial x_j}, \tag{1.6}$$

$$\frac{\partial u_i'}{\partial x_i} = 0. \tag{1.7}$$

An energy equation for small scales can be formed by multiplying Eq. (1.6) by u_i', averaging such that $\overline{\overline{f} f'} = 0$ and re-arranging to obtain

$$\frac{\partial}{\partial t}\overline{u_i' u_i'} + \overline{u}_j \frac{\partial}{\partial x_j}\overline{u_i' u_i'} = -\frac{\partial}{\partial x_j}\left\{\overline{u_i' u_i' u_j'} + \frac{2}{\rho}\overline{u_j' p'} - \nu \frac{\partial}{\partial x_j}\overline{u_i' u_i'}\right\} - 2\overline{u_i' u_j'}\frac{\partial \overline{u}_i}{\partial x_j} - 2\nu \overline{\frac{\partial u_i'}{\partial x_j}\frac{\partial u_i'}{\partial x_j}}. \tag{1.8}$$

A similar equation may be obtained for the large-scale energy evolution from Eq. (1.4):

$$\frac{\partial}{\partial t}\overline{u}_i \overline{u}_i + \overline{u}_j \frac{\partial}{\partial x_j}\overline{u}_i \overline{u}_i = -\frac{\partial}{\partial x_j}\left\{\frac{2}{\rho}\overline{u}_j \overline{p} - \nu \frac{\partial}{\partial x_j}\overline{u}_i \overline{u}_i\right\} - 2\overline{u}_i \frac{\partial}{\partial x_j}\overline{u_i' u_j'} - 2\nu \frac{\partial \overline{u}_i}{\partial x_j}\frac{\partial \overline{u}_i}{\partial x_j}. \tag{1.9}$$

The left sides of Eqs. (1.8) and (1.9) give the time-evolution of the energy at small and large scales, respectively. The first term on the right of each is a divergence term which vanishes after integrating over the volume, invoking the divergence theorem to convert each to a surface integral and using the boundary condition that the velocity vanishes on any surface or at infinity. It can also be seen that after adding the two equations the second terms of the right sides of each combine into a divergence term which similarly vanishes, showing that these terms do not convert kinetic energy into any other form of energy but only act to transfer it between large and small scales. The remaining terms show that viscous effects convert the energy present at both large and small scales into heat.

From an experimental point of view it is Eqs. (1.4) and (1.5) which are most useful as they consist in the main of the mean values of the variables of interest, which are the parts most easily measured; the only exception is the quadratic quantity $\overline{u_i' u_j'}$, which is called the Reynolds stress tensor. Mathematically, if $\overline{u}_i$ is regarded as a mean flow and u_i' as a perturbation then, from a purely linear perspective in which terms quadratic in perturbation quantities are ignored, Eq.

[3] Jeffreys (1931) and Temple (1960) describe the usage and manipulation of Cartesian tensors.

(1.4) involves only mean quantities indicating that the mean flow is unaffected by the perturbation, while Eq. (1.6) gives the evolution of the perturbation. However, an examination of Eqs. (1.8) and (1.9) shows that there is interaction between the mean and perturbation flow energies through the nonlinear terms, with either the perturbation receiving energy from the mean flow or vice versa. Thus an unstable perturbation cannot grow without limit as there is only a finite source of energy available (Stuart, 1958).

1.2.2 Eddy viscosity

The Reynolds stress tensor has an important rôle to play in attempts to model turbulence in terms of the large-scale average flow. The viscous dissipation term of Eq. (1.1) arises from the divergence of a viscous stress tensor

$$s_{ij} = \rho\nu\left(\frac{\partial u_i}{\partial x_j} + \frac{\partial u_j}{\partial x_i}\right), \tag{1.10}$$

which leads to the diffusion term in the incompressible case when

$$\frac{\partial s_{ij}}{\partial x_j} = \rho\,\nu\nabla^2\boldsymbol{u}. \tag{1.11}$$

As it has been observed that the effect of the Reynolds stress tensor is to reduce the average flow's energy by transferring it to the perturbed flow (Sect. 1.2.1) it is tempting to write the divergence of the Reynolds stress tensor as a diffusion term with an "effective" or "turbulent" viscosity:

$$-\frac{\partial\overline{u_i'u_j'}}{\partial x_j} = \nu_{\text{turb}}\frac{\partial^2\overline{u}_i}{\partial x_j\partial x_j}. \tag{1.12}$$

It cannot be emphasised enough that the concept of turbulent viscosity arises purely from this analogy and not from any physical or analytical considerations. There is absolutely no reason why the effect of small-scale perturbations on large-scale flow should act as a diffusion process, a fact stressed by McComb (1990, p20) who also notes that there are cases where the eddy viscosity may be zero or infinite for certain flows. Furthermore, Tennekes and Lumley (1972, p3) make the point that turbulence is a property of the *flow* while viscosity is a property of the *fluid* itself, thus again emphasising the differing natures of molecular and turbulent viscosities .

1.2.3 Averages

The unpredictability of the motion of a particle in a turbulent flow has already been mentioned, but this does not mean that it is impossible to say anything about such flows; while the close-up details are obscured it is possible to step back and say something about global properties. For example, the total energy associated with the Niagara Falls exhibits no significant change over periods of hours and a waterspout or hurricane can be visually identified although its exact position may be hard to predict. These two examples show the persistence of energy and vorticity in fluid

flows. In MHD flows, additional quantities of interest are the magnetic helicity, which measures the overall twist and linkage of the magnetic field-lines, and the correlation between the magnetic and velocity fields. Many others could be listed, but these few serve to illustrate directions amenable to investigation.

In calculating global quantities it is natural to use averages. For a given system an experiment can, in principle, be repeated over and over and an average be taken over all the runs — this is termed an ensemble average and is calculated as

$$\langle f(x,t)\rangle = \lim_{N\to\infty} \frac{1}{N}\sum_{n=1}^{N} f_n(x,t), \tag{1.13}$$

where $f_n(x,t)$ is the measurement taken from the nth experimental run. The use of an arithmetic mean permits the following properties, which have been taken for granted in the mean flow/perturbation decomposition, to be formally proved:

$$\langle\langle f\rangle\rangle = \langle f\rangle, \tag{1.14}$$

$$\left\langle \frac{\partial f}{\partial t} \right\rangle = \frac{\partial}{\partial t}\langle f\rangle, \tag{1.15}$$

$$\left\langle \frac{\partial f}{\partial x} \right\rangle = \frac{\partial}{\partial x}\langle f\rangle, \tag{1.16}$$

$$\langle Af\rangle = A\langle f\rangle, \tag{1.17}$$

$$\langle\langle f\rangle g\rangle = \langle f\rangle\langle g\rangle, \tag{1.18}$$

$$\langle f+g\rangle = \langle f\rangle + \langle g\rangle, \tag{1.19}$$

where A is a constant. This procedure, however, is impractical in situations which exist outside laboratory control, such as the Sun. The ergodic hypothesis then provides an alternative means of averaging by supposing that the quantity of interest should not change much when averaged in a small sub-volume of the turbulent flow or a sub-interval of time: if the system is assumed to be ergodic the space- or time-averages will be equivalent to the ensemble average.

1.2.4 Correlation Tensors

Turning to the experimental aspects of turbulence research, the question must be asked of how the energy or other global property of a turbulent flow is to be measured. It turns out that most global quantities can be expressed in terms of the correlation between local quantities measured at two or more points in space and/or time. Different measurements can be collected into a correlation tensor[4] measuring the correlation between different vector components:

$$R_{\alpha\beta}(\boldsymbol{x},\boldsymbol{r}) = \langle u_\alpha(\boldsymbol{x})u_\beta(\boldsymbol{x}+\boldsymbol{r})\rangle, \tag{1.20}$$

where the angled brackets denote an ensemble average. If the components u_α and u_β are in phase their product will always be positive definite or negative definite so that the correlation $R_{\alpha\beta}$ is a

[4] Greek subscripts are used from now on due to the preponderance of i's, j's and k's in MHD.

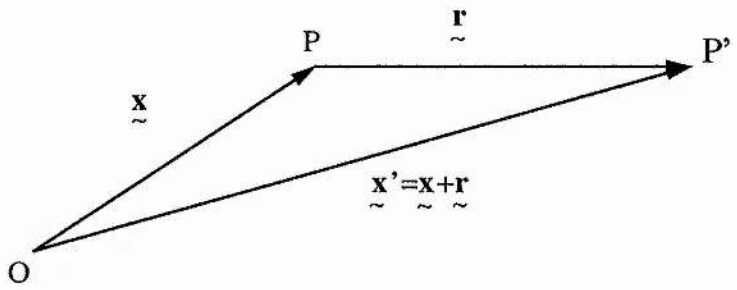

Figure 1.1: Configuration used in forming a two-point spatial correlation.

non-zero quantity; on the other hand, if the two components are independent random variables their product is as likely to be positive as it is negative with the product being zero on average. Thus, the correlation tensor gives a measure of the relation between the velocity components at given points and times. Time correlations can also be included in the definition, Eq. (1.20), but, as this thesis is concerned with statistically stationary turbulence in which there is little change over time-scales of interest, the velocity components comprising the tensor will be measured simultaneously, with time being considered as an implicit parameter in the tensor.

So far a correlation tensor sheds no light on turbulence apart from providing a framework for interpreting experimental results. However, the introduction of the assumption of spatial homogeneity into any model of turbulence requires correlation tensors to have a particular structure which can be written in terms of the global quantities already mentioned, like energy and helicity. This can be seen by starting from some necessary consequences of homogeneity. First, the correlation should not depend on the absolute position of the two points at which the velocity components are being measured, only on their separation. Thus,

$$\langle u_\alpha(\boldsymbol{x}) u_\beta(\boldsymbol{x}+\boldsymbol{r})\rangle = R_{\alpha\beta}(\boldsymbol{r}), \tag{1.21}$$

which must follow anyway if a spatial average is used rather than an ensemble average; when turbulence is homogeneous it is likely that ergodicity will hold so that this is entirely consistent with earlier comments in Sect. 1.2.3. Another consequence of homogeneity is that it should not matter where the origin is taken; that is, the correlation should be identical when measured from $\boldsymbol{x}$ or $\boldsymbol{x}+\boldsymbol{r}$, leading to the requirement that

$$R_{\alpha\beta}(\boldsymbol{r}) = R_{\beta\alpha}(-\boldsymbol{r}), \tag{1.22}$$

which is obtained by putting first $\boldsymbol{x} = \boldsymbol{y}$ into Eq. (1.21) then $\boldsymbol{x} = \boldsymbol{y} - \boldsymbol{r}$.

From Fig. 1.1 it can be seen that the velocity at P is independent of $\boldsymbol{x}' = \boldsymbol{x} + \boldsymbol{r}$ while the velocity at P' is independent of $\boldsymbol{x}$. Also invoking Eq. (1.2) then gives the result

$$\frac{\partial R_{\alpha\beta}}{\partial x'_\beta} = \frac{\partial R_{\alpha\beta}}{\partial x_\alpha} = 0, \tag{1.23}$$

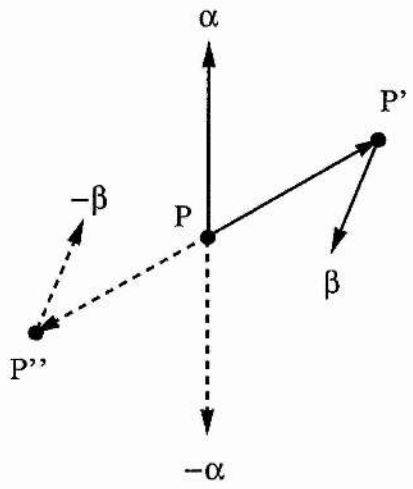

Figure 1.2: Reflection of point P' and associated vectors about P (adapted from Fig. 2 of Robertson (1940)).

assuming that the ensemble average has been taken (Curle and Davies (1968, p263) — this result is not confined to homogeneous turbulence). Finally, $\partial/\partial x'_\beta = -\partial/\partial x_\alpha = \partial/\partial r_\alpha$ so that

$$\frac{\partial R_{\alpha\beta}}{\partial r_\alpha} = \frac{\partial R_{\alpha\beta}}{\partial r_\beta} = 0, \tag{1.24}$$

the latter result coming from applying Eq. (1.25) to the former then swapping indices. Other properties may be derived (Stanišić, 1988, p131) but these serve to illustrate the restrictions and simplifications imposed on the correlation tensor under incompressible, homogeneous and isotropic turbulence.

A further assumption often made is that the turbulence is isotropic (i.e. does not depend on the orientation of the coordinate axes). It will be seen in Sect. 1.3.6 that this is not as appropriate for the MHD situation, but for fluids it has been argued that if eddies are small compared to spatial inhomogeneities the flow will appear locally isotropic (Batchelor, 1953). Thus, as well as being invariant to spatial translation the correlation should not depend on the orientation of the coordinate axes, so that

$$R_{\alpha\beta}(\boldsymbol{r}) = R_{\beta\alpha}(\boldsymbol{r}), \tag{1.25}$$

which can be shown by taking the αth velocity component at a point P, and the βth at P' (Fig. 1.2). If the whole figure is reflected in the point P then translated to P'', the correlation between $u_\alpha(\boldsymbol{0})$ at P and $u_\beta(\boldsymbol{r})$ at P', the vectors being measured with respect to P, should equal the correlation between $-u_\beta(\boldsymbol{0})$ at P'' and $-u_\alpha(\boldsymbol{r})$ at P, the vectors now being measured with respect to P''.

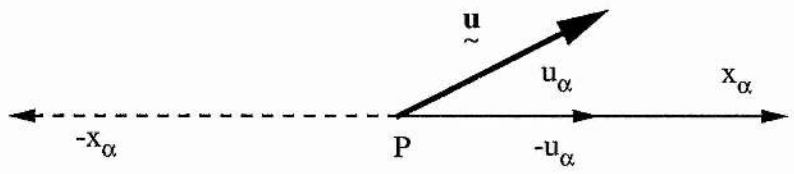

Figure 1.3: Mean field with respect to original axes and new axes obtained by rotating system by π around axis at P directed out of page (adapted from Lesieur (1990, p105)).

An important property relating to the mean-field decomposition is that the mean velocity must be zero in an isotropic system. In Fig. 1.3 the αth mean velocity component with respect to the first axis system (bold) must equal the αth component with respect to the system obtained by rotating the α-axis at origin $\boldsymbol{x}$ by π about the axis out of the page at $\boldsymbol{x}$ (dashed). Thus,

$$\langle u_\alpha(\boldsymbol{x})\rangle = -\langle u_\alpha(\boldsymbol{x})\rangle = 0. \tag{1.26}$$

Now we come to the principal advantage of homogeneity; Robertson (1940) started from the fact that the scalar quadratic form, $R(\boldsymbol{r};\boldsymbol{a},\boldsymbol{b}) = R_{\alpha\beta}(\boldsymbol{r})a_\alpha b_\beta$, must be invariant under any rotation or translation of the rigid system formed by $\boldsymbol{r}$, $\boldsymbol{a}$ and $\boldsymbol{b}$. Using the fact that the geometric invariants of this system are the angles between the vectors (measured by the scalar products $r^2, a^2, b^2, r_\alpha a_\alpha, r_\alpha b_\alpha$ and $a_\alpha b_\alpha$) and the volume of the parallelepiped, $\boldsymbol{r}\cdot(\boldsymbol{a}\times\boldsymbol{b}) = \varepsilon_{\alpha\beta\gamma}r_\alpha a_\beta b_\gamma$, the quadratic form was constructed as

$$R(\boldsymbol{r};\boldsymbol{a},\boldsymbol{b}) = A(r)[r_\alpha a_\alpha][r_\beta b_\beta] + B(r)a_\alpha b_\alpha + C(r)\varepsilon_{\alpha\beta\gamma}r_\alpha a_\beta b_\gamma, \tag{1.27}$$

since $R(\boldsymbol{r};\boldsymbol{a},\boldsymbol{b})$ is linear in both $\boldsymbol{a}$ and $\boldsymbol{b}$. Hence the correlation tensor may be written as

$$R_{\alpha\beta}(\boldsymbol{r}) = A(r)r_\alpha r_\beta + B(r)\delta_{\alpha\beta} + C(r)\varepsilon_{\alpha\beta\gamma}r_\gamma. \tag{1.28}$$

For an isotropic system, however, Eq. (1.25) requires that $C(r) = 0$, so that finally

$$R_{\alpha\beta}(\boldsymbol{r}) = A(r)r_\alpha r_\beta + B(r)\delta_{\alpha\beta}. \tag{1.29}$$

Although homogeneous turbulence is often criticised for bearing little relation to the real world, compressibility and boundaries in particular being excluded, the advantage bestowed in giving structure to the correlation tensor is a significant one when developing any theory of turbulence, and not to be surrendered lightly.

1.2.5 Fourier Space

In order to express the correlation structure in terms of global quantities it is helpful to work in Fourier space — the abode of most analytical theories of turbulence prior to the 1960s —

by taking the Fourier transform of all quantities and equations associated with the turbulent flow. Throughout this thesis the following definition of the Fourier transform and its inverse will be used:

$$\hat{\boldsymbol{f}}(\boldsymbol{k}) = \frac{1}{(2\pi)^N} \int_{-\infty}^{\infty} \mathrm{e}^{-i\,\boldsymbol{k}\cdot\boldsymbol{x}} \boldsymbol{f}(\boldsymbol{x})\,\mathrm{d}\boldsymbol{x}, \tag{1.30}$$

$$\boldsymbol{f}(\boldsymbol{x}) = \int_{-\infty}^{\infty} \mathrm{e}^{i\,\boldsymbol{k}\cdot\boldsymbol{x}} \hat{\boldsymbol{f}}(\boldsymbol{k})\,\mathrm{d}\boldsymbol{k}. \tag{1.31}$$

where N denotes the dimensionality of the problem with the infinite range of integration being applied to each dimension. Furthermore, for problems which can be regarded as periodic we have, in three dimensions,

$$\hat{\boldsymbol{f}}_{\alpha\beta\gamma} = \frac{1}{L_\alpha L_\beta L_\gamma} \int_{-L_\alpha}^{L_\alpha} \int_{-L_\beta}^{L_\beta} \int_{-L_\gamma}^{L_\gamma} \mathrm{e}^{-i\,\boldsymbol{k}\cdot\boldsymbol{x}} \boldsymbol{f}(\boldsymbol{x})\,\mathrm{d}\boldsymbol{x}, \tag{1.32}$$

$$\boldsymbol{f}(\boldsymbol{x}) = \mathrm{Re}\left\{ \sum_{\alpha,\beta,\gamma=0}^{\infty} \mathrm{e}^{i\,\boldsymbol{k}\cdot\boldsymbol{x}} \hat{\boldsymbol{f}}_{\alpha\beta\gamma} \right\}, \tag{1.33}$$

where $\boldsymbol{k} = (2\alpha\pi/L_\alpha, 2\beta\pi/L_\beta, 2\gamma\pi/L_\gamma)$, L_α being the periodicity in the α direction and similarly for β and γ. For most physical problems N will be 2 or 3, as will the number of coordinates encapsulated in the vectors $\boldsymbol{x}$ and $\boldsymbol{k}$. The integrals in Eqs. (1.32) and (1.33) can be evaluated provided $\boldsymbol{f}(\boldsymbol{x})$ is periodic, but for Eqs. (1.30) and (1.31) the integrals are only guaranteed to converge if $\boldsymbol{f}$ is absolutely integrable or Lebesgue square-integrable, i.e. $\int |\boldsymbol{f}(\boldsymbol{x})|\mathrm{d}\boldsymbol{x}$ or $\int f^2(\boldsymbol{x})\mathrm{d}\boldsymbol{x}$ is bounded. The periodicity condition can be justified and imposed for homogeneous turbulence, but the latter is harder to justify for a random $\boldsymbol{f}(\boldsymbol{x})$. Batchelor (1953, Sect. 2.5) sidesteps this issue by using Fourier-Stieltjes integrals rather than Fourier integrals, but a more popular approach is to use the method of generalised functions, also known as distributions (Lighthill, 1958), to justify the usage of Fourier integrals, which are used from now on.

The following vector functions may now be transformed as follows:

$$\frac{\partial f}{\partial x} \rightarrow i\,k_x \hat{f}, \tag{1.34}$$

$$\nabla f \rightarrow i\,\boldsymbol{k}\hat{\boldsymbol{f}}, \tag{1.35}$$

$$\nabla \cdot \boldsymbol{f} \rightarrow i\,\boldsymbol{k} \cdot \hat{\boldsymbol{f}}, \tag{1.36}$$

$$\nabla \times \boldsymbol{f} \rightarrow i\,\boldsymbol{k} \times \hat{\boldsymbol{f}}, \tag{1.37}$$

$$\nabla^2 f \rightarrow -k^2 \hat{\boldsymbol{f}}, \tag{1.38}$$

$$\boldsymbol{f} \cdot \boldsymbol{g} \rightarrow \begin{cases} \sum_{\mu,\nu,\zeta=0}^{\infty} \hat{\boldsymbol{f}}_{\alpha-\mu,\beta-\nu,\gamma-\zeta} \cdot \hat{\boldsymbol{g}}_{\mu\nu\zeta}, \\ \int \hat{\boldsymbol{f}}(\boldsymbol{k}-\boldsymbol{k}_1) \cdot \hat{\boldsymbol{g}}(\boldsymbol{k}_1)\mathrm{d}\boldsymbol{k}_1. \end{cases} \tag{1.39}$$

The latter relation is termed the convolution of $\boldsymbol{f}$ and $\boldsymbol{g}$, taking the summation form for periodic problems and the integral form for infinitely domained problems.

It is now possible to express Eqs. (1.1) and (1.2) in Fourier space by using the above properties (the following equations are based on Orszag (1970) and Lesieur (1990, Chpts. IV & V),

which differ slightly in notation and presentation):

$$\left(\frac{\partial}{\partial t}+\nu k^2\right)\hat{u}_\alpha(\boldsymbol{k},t) = -\frac{i}{2}P_{\alpha\beta\gamma}(\boldsymbol{k})\int \hat{u}_\beta(\boldsymbol{p},t)\hat{u}_\gamma(\boldsymbol{k}-\boldsymbol{p},t)\mathrm{d}\boldsymbol{p}, \tag{1.40}$$

$$k_\alpha\hat{u}_\alpha(\boldsymbol{k},t) = 0, \tag{1.41}$$

where

$$P_{\alpha\beta}(\boldsymbol{k}) = \delta_{\alpha\beta}-\frac{k_\alpha k_\beta}{k^2}, \tag{1.42}$$

$$P_{\alpha\beta\gamma}(\boldsymbol{k}) = k_\beta P_{\alpha\gamma}(\boldsymbol{k})+k_\gamma P_{\alpha\beta}(\boldsymbol{k}), \tag{1.43}$$

$P_{\alpha\beta}$ being the tensor which projects a vector onto the plane perpendicular to $\boldsymbol{k}$. Lesieur (1990, pp. 93–94) explains the derivation in more detail. As for the velocity, the correlation tensors can be Fourier-transformed:

$$S_{\alpha\beta}(\boldsymbol{k}) = \left(\frac{1}{2\pi}\right)^3\int \mathrm{e}^{-i\boldsymbol{k}\cdot\boldsymbol{r}}R_{\alpha\beta}(\boldsymbol{r})\mathrm{d}\boldsymbol{r}. \tag{1.44}$$

Furthermore (Lesieur, 1990, p109),

$$\langle\hat{u}_\alpha(\boldsymbol{p})\hat{u}_\beta(\boldsymbol{k})\rangle = \left(\frac{1}{2\pi}\right)^3\delta(\boldsymbol{k}+\boldsymbol{p})\int \mathrm{e}^{-i\boldsymbol{k}\cdot\boldsymbol{r}}R_{\alpha\beta}(\boldsymbol{r})\mathrm{d}\boldsymbol{r}, \tag{1.45}$$

so that

$$\langle\hat{u}_\alpha(\boldsymbol{p})\hat{u}_\beta(\boldsymbol{k})\rangle = S_{\alpha\beta}(\boldsymbol{k})\delta(\boldsymbol{k}+\boldsymbol{p}). \tag{1.46}$$

Using Eqs. (1.40) and (1.46) it is possible to derive the equation for the time evolution of the second-order cumulant $S_{\alpha\beta}(\boldsymbol{k})$:

$$\left(\frac{\partial}{\partial t}+2\nu k^2\right)S_{\alpha\beta}(\boldsymbol{k}) = -\frac{i}{2}P_{\alpha\rho\sigma}(\boldsymbol{k})\int T_{\beta\rho\sigma}(-\boldsymbol{k},\boldsymbol{p})\mathrm{d}\boldsymbol{p}-\frac{i}{2}P_{\beta\rho\sigma}(-\boldsymbol{k})\int T_{\alpha\rho\sigma}(\boldsymbol{k},\boldsymbol{p})\mathrm{d}\boldsymbol{p}. \tag{1.47}$$

Note that this equation is not closed since it involves $T_{\alpha\beta\gamma}(\boldsymbol{k},\boldsymbol{p})$, which is the Fourier transform of the third-order, three-point correlation:

$$T_{\alpha\beta\gamma}(\boldsymbol{k},\boldsymbol{p}) = \left(\frac{1}{2\pi}\right)^6\int\langle u_\alpha(\boldsymbol{x}+\boldsymbol{y})u_\beta(\boldsymbol{x}+\boldsymbol{z})v_\gamma(\boldsymbol{x})\rangle\mathrm{e}^{-i\boldsymbol{k}\cdot\boldsymbol{y}-i\boldsymbol{p}\cdot\boldsymbol{z}}\mathrm{d}\boldsymbol{y}\mathrm{d}\boldsymbol{z}, \tag{1.48}$$

and where

$$\langle u_\alpha(\boldsymbol{k})u_\beta(\boldsymbol{p})u_\gamma(\boldsymbol{q})\rangle = T_{\alpha\beta\gamma}(\boldsymbol{k},\boldsymbol{p})\delta(\boldsymbol{k}+\boldsymbol{p}+\boldsymbol{q}). \tag{1.49}$$

Similarly, the time evolution of T is given by

$$\begin{aligned}\left(\frac{\partial}{\partial t}+\nu(k^2+p^2+|\boldsymbol{k}+\boldsymbol{p}|^2)\right)T_{\alpha\beta\gamma}(\boldsymbol{k},\boldsymbol{p}) = \\ -\frac{i}{2}P_{\alpha\rho\sigma}(\boldsymbol{k})\int U_{\beta\gamma\rho\sigma}(\boldsymbol{p},-\boldsymbol{k}-\boldsymbol{p},\boldsymbol{q})\mathrm{d}\boldsymbol{q}-\frac{i}{2}P_{\alpha\rho\sigma}(\boldsymbol{p})\int U_{\beta\gamma\rho\sigma}(-\boldsymbol{k}-\boldsymbol{p},\boldsymbol{k},\boldsymbol{q})\mathrm{d}\boldsymbol{q} \\ -\frac{i}{2}P_{\alpha\rho\sigma}(-\boldsymbol{k}-\boldsymbol{p})\int U_{\beta\gamma\rho\sigma}(\boldsymbol{k},\boldsymbol{p},\boldsymbol{q})\mathrm{d}\boldsymbol{q}-iP_{\alpha\rho\sigma}(\boldsymbol{k})S_{\beta\rho}(\boldsymbol{p})S_{\gamma\sigma}(-\boldsymbol{k}-\boldsymbol{p}) \\ -iP_{\alpha\rho\sigma}(\boldsymbol{p})S_{\beta\rho}(-\boldsymbol{k}-\boldsymbol{p})S_{\gamma\sigma}(\boldsymbol{k})-iP_{\alpha\rho\sigma}(-\boldsymbol{k}-\boldsymbol{p})S_{\beta\rho}(\boldsymbol{k})S_{\gamma\sigma}(\boldsymbol{p}),\end{aligned} \tag{1.50}$$

where

$$U_{\alpha\beta\gamma\mu}(\boldsymbol{k},\boldsymbol{p},\boldsymbol{q}) = \left(\frac{1}{2\pi}\right)^9 \int [\langle u_\alpha(\boldsymbol{x}+\boldsymbol{y})u_\beta(\boldsymbol{x}+\boldsymbol{z})u_\gamma(\boldsymbol{x}+\boldsymbol{w})u_\mu(\boldsymbol{x})\rangle - R_{\alpha\beta}(\boldsymbol{y}-\boldsymbol{z})R_{\gamma\mu}(\boldsymbol{w}) - R_{\alpha\gamma}(\boldsymbol{y}-\boldsymbol{w})R_{\beta\mu}(\boldsymbol{z}) - R_{\alpha\mu}(\boldsymbol{y})R_{\beta\gamma}(\boldsymbol{z}-\boldsymbol{w})] \mathrm{e}^{-i\boldsymbol{k}\cdot\boldsymbol{y}-i\boldsymbol{p}\cdot\boldsymbol{z}-i\boldsymbol{q}\cdot\boldsymbol{w}}\mathrm{d}\boldsymbol{y}\mathrm{d}\boldsymbol{z}\mathrm{d}\boldsymbol{w}, \quad (1.51)$$

and

$$\langle u_\alpha(\boldsymbol{k})u_\beta(\boldsymbol{p})u_\gamma(\boldsymbol{q})u_\mu(\boldsymbol{m})\rangle = S_{\alpha\beta}(\boldsymbol{k})S_{\gamma\mu}(\boldsymbol{q})\delta(\boldsymbol{k}+\boldsymbol{p})\delta(\boldsymbol{q}+\boldsymbol{m}) + S_{\alpha\gamma}(\boldsymbol{k})S_{\beta\mu}(\boldsymbol{p})\delta(\boldsymbol{k}+\boldsymbol{q})\delta(\boldsymbol{p}+\boldsymbol{m}) + S_{\alpha\mu}(\boldsymbol{k})S_{\beta\gamma}(\boldsymbol{p})\delta(\boldsymbol{k}+\boldsymbol{m})\delta(\boldsymbol{p}+\boldsymbol{q}) + U_{\alpha\beta\gamma\mu}(\boldsymbol{k},\boldsymbol{p},\boldsymbol{q})\delta(\boldsymbol{k}+\boldsymbol{p}+\boldsymbol{q}+\boldsymbol{m}). \quad (1.52)$$

It should be emphasised that $U_{\alpha\beta\gamma\mu}$ is a *cumulant* which is related to the *moment* given by the left side of Eq. (1.52). As can be seen, the two are directly related: the choice of which to use in formulating the turbulence equations is a matter of preference. Leslie (1973) uses moments, for example, but in a schematic form rather than giving the full equations, as does Biskamp (1993). Orszag (1970, 1977) uses cumulants, on the other hand, and gives the first few equations of the hierarchy in full. In the author's opinion Orszag (1977) provides the most complete map of the path followed in this introduction, the following equations being taken from this work, while Orszag and Kruskal (1968) provide precise definitions of cumulants and their relations to moments and prove convergence of the integrals in the above cumulant time-evolution equations[5].

The pattern of the time-evolution of the nth-order cumulant depending on the $(n+1)$th cumulant continues at all orders giving rise to the problem of closure: in order to determine the behaviour of u_α an infinite set of equations with an infinite number of unknowns must be solved. As this is not feasible, given the size and increasingly complicated nature of each equation, some approximation is required to reduce this system to a solvable, closed, finite system of equations.

1.2.6 Quasi-normal closure

One of the early attempts at closure considered the approach of setting the nth-order cumulant to zero, the so-called cumulant discard approximation. At its simplest level the third-order cumulant can be neglected (neglecting the second is tantamount to neglecting all the energy!). Equation (1.47) then has solution

$$S_{\alpha\beta}(\boldsymbol{k},t) = S_{\alpha\beta}(\boldsymbol{k},0)\mathrm{e}^{-2\nu k^2 t}, \quad (1.53)$$

so that the energy at each scale simply decays with time. In this case all nonlinear effects, which are intrinsic to turbulence, have been neglected. This being unreasonable, Eq. (1.50) is next included

[5]This work also shows that second- and third-order cumulants are identical to the corresponding moments when the sum of the wavevector set is zero; in the case of the third-order moment this is simply a result of the fact that if $\boldsymbol{u}(\boldsymbol{x},t)$ is a solution of the Navier-Stokes equations then so is $\boldsymbol{u}'(\boldsymbol{x},t) = \boldsymbol{u}(\boldsymbol{x}-\boldsymbol{U}t,t)+\boldsymbol{U}$, known as Galilean invariance. It is then possible to transform to a frame where $\langle u_\alpha\rangle = 0$ whereby the decomposed triple correlation contains this zero factor, leading to the identification with the moment correlation.

in the system and the fourth-order cumulant is neglected instead. As well as being a mathematical truncation of the system this approximation is credible from a physical perspective since one of the many central limit theorems of statistics can be invoked; roughly speaking, a large sum of independent identically distributed random variables tends to a multivariate Gaussian distribution with zero mean. For the case of four random variables

$$\langle X_i X_j X_k X_l \rangle = \langle X_i X_j \rangle \langle X_k X_l \rangle + \langle X_i X_k \rangle \langle X_j X_l \rangle + \langle X_i X_l \rangle \langle X_j X_k \rangle, \tag{1.54}$$

after averaging the joint probability density functions for fourth- and second-order multivariates (here the X's are random variables and the subscripts are simply labels). Using this property in Eq. (1.51) leads to the result that the fourth-order cumulant is identically zero for a Gaussian distribution; but the zero-mean property means that the third-order cumulant should similarly be identically zero in this case, thus returning to the preceding cumulant-discard approximation. Thankfully, though, even if the initial flow is set up to be purely Gaussian it cannot remain so, as can be seen by putting $T \equiv 0$ in Eq. (1.50): the initial time derivative of T is then non-zero. This is why discarding the fourth-order cumulant (Millionshtchikov, 1941; Proudman and Reid, 1954) is known as the quasi-normal approximation.

To make further progress in numerically solving the quasi-normal system a further reduction in complexity of the equations can be achieved by examining the form of the correlation tensors under the assumption of isotropy. In general the second-order cumulant can be written as (Sect. 1.2.4)

$$S_{\alpha\beta}(\boldsymbol{k}) = A(k) k_\alpha k_\beta + B(k) \delta_{\alpha\beta}. \tag{1.55}$$

Invoking incompressibility, Eq. (1.24), the transform of the correlation tensor contracts according to

$$k_\alpha S_{\alpha\beta}(\boldsymbol{k}) = k_\beta S_{\alpha\beta}(\boldsymbol{k}) = 0, \tag{1.56}$$

whence $A(k) = -B(k)/k^2$ and

$$S_{\alpha\beta}(\boldsymbol{k}) = B(k) P_{\alpha\beta}(\boldsymbol{k}), \tag{1.57}$$

where $P_{\alpha\beta}$ is given by Eq. (1.42). The function $B(k)$ may be related to the kinetic energy spectrum as follows. Starting from

$$E_v = \frac{1}{2} R_{\alpha\alpha}(\boldsymbol{0}) = \frac{1}{2} \int_{-\infty}^{\infty} S_{\alpha\alpha}(\boldsymbol{k}) \mathrm{d}\boldsymbol{k}, \tag{1.58}$$

where E_v is the kinetic energy, the integral on the right may be expressed in spherical polar coordinates (k, θ, ϕ) so that $\mathrm{d}\boldsymbol{k} = k^2 \sin\theta \, \mathrm{d}k \, \mathrm{d}\theta \, \mathrm{d}\phi$ and integration performed directly over the θ and ϕ coordinates (since $S_{\alpha\alpha}$ does not depend on θ or ϕ because of isotropy (N.B. $P_{\alpha\alpha}(\boldsymbol{k}) = 2$)) to give

$$E_v = 4\pi \int_0^{\infty} k^2 B(k) \mathrm{d}k. \tag{1.59}$$

Writing the kinetic energy in terms of its spectrum,

$$E_v = \int_0^{\infty} E(k) \mathrm{d}k, \tag{1.60}$$

enables the function $B(k)$ to be written as

$$B(k) = \frac{E(k)}{4\pi k^2}, \tag{1.61}$$

so that the second-order cumulant can finally be given in terms of the kinetic energy spectrum as

$$S_{\alpha\beta}(\boldsymbol{k}) = \frac{E(k)}{4\pi k^2} P_{\alpha\beta}(\boldsymbol{k}), \tag{1.62}$$

which justifies the statement in Sect. 1.2.4 that the correlation tensors can be expressed in terms of the energy. The third-order cumulant may similarly be reduced under the assumption of isotropy (Proudman and Reid, 1954) but this more complicated expression is not presented here.

The quasi-normal equations are completed with the additional assumption that at $t = 0$ the turbulence is exactly Gaussian, so that $T_{\alpha\beta\gamma}(\boldsymbol{k}, \boldsymbol{p}, 0) = 0$. Equation (1.50) then has solution

$$\begin{aligned} T_{\alpha\beta\gamma}(\boldsymbol{k}, \boldsymbol{p}, t) &= -i \int_0^t \mathrm{e}^{-\nu(k^2+p^2+q^2)(t-s)} \left[P_{\alpha\rho\sigma}(\boldsymbol{k}) S_{\beta\rho}(\boldsymbol{p}, s) S_{\gamma\sigma}(\boldsymbol{q}, s) + P_{\beta\rho\sigma}(\boldsymbol{p}) S_{\alpha\rho}(\boldsymbol{k}, s) S_{\gamma\sigma}(\boldsymbol{q}, s) \right. \\ &\quad \left. + P_{\gamma\rho\sigma}(\boldsymbol{q}) S_{\alpha\rho}(\boldsymbol{k}, s) S_{\beta\sigma}(\boldsymbol{p}, s) \right] \mathrm{d}s, \end{aligned} \tag{1.63}$$

which is then substituted into Eq. (1.47), and Eq. (1.62) is invoked to yield (after some manipulation!) the quasi-normal system (Orszag, 1977):

$$\begin{aligned} \left(\frac{\partial}{\partial t} + 2\nu k^2 \right) E(k,t) &= \int \mathrm{d}\boldsymbol{p} \int_0^t \mathrm{d}s\, \mathrm{e}^{-\nu(k^2+p^2+q^2)(t-s)} \frac{k^2}{4\pi p^2 q^2} \left\{ 2k^2 a(k,p,q) E(p,s) E(q,s) \right. \\ &\quad \left. - E(k,s) \left[p^2 b(k,p,q) E(q,s) + q^2 b(k,q,p) E(p,s) \right] \right\}, \end{aligned} \tag{1.64}$$

$$4k^2 a(k,p,q) = P_{\alpha\beta\gamma}(\boldsymbol{k}) P_{\beta\delta}(\boldsymbol{p}) P_{\gamma\rho}(\boldsymbol{q}) P_{\alpha\delta\rho}(\boldsymbol{k}), \tag{1.65}$$

$$2k^2 b(k,p,q) = -P_{\alpha\beta\gamma}(\boldsymbol{k}) P_{\gamma\alpha\delta}(\boldsymbol{p}) P_{\beta\delta}(\boldsymbol{q}), \tag{1.66}$$

$$\boldsymbol{q} = -\boldsymbol{k} - \boldsymbol{p}, \tag{1.67}$$

The quasi-normal approximation was in use for some years until Ogura (1963) showed numerically that the quasi-normal system can admit solutions with a negative kinetic energy spectrum as time advances.

1.2.7 Eddy-damped quasi-normal Markovian (EDQNM) approximation

Eddy damping

Orszag (1970) gives three aspects of turbulence which the quasi-normal approximation fails to represent adequately, namely that it does not relax to equilibrium as expected but instead when perturbed tends repeatedly to overshoot the attempt to return and leads to oscillatory behaviour; associated with this is the fact that the characteristic decay time is longer than expected and, as just mentioned, it is possible to obtain negative values for the kinetic energy spectrum. A partial solution is to introduce an artificial damping term in the exponential term of Eq. (1.64), for example,

to model the effects of the neglected fourth-order cumulant. So far consensus between the various authors cited has been found, but now differences appear in the precise form of the modified damping. Orszag (1977, p313) uses

$$\exp\left\{-\int_s^t [\eta(k,r)+\eta(p,r)+\eta(q,r)]\mathrm{d}r\right\}, \tag{1.68}$$

with η an eddy viscosity defined in Eq. (1.70) while Lesieur (1990, p168) chooses

$$\exp\left\{-[\mu_{kpq}+\nu(k^2+p^2+q^2)](t-s)\right\}. \tag{1.69}$$

In either case although the relaxation to equilibrium is improved, the eddy-damped quasi-normal equations are still capable of achieving a negative kinetic energy spectrum.

Markovian approximation

A Markov chain is a discrete sequence of random variables which have the property that the state of the nth random variable depends only on its predecessor. This is sometimes extended in continuous systems to modify a variable which strictly depends on all past times (a memory or history property) to depend only on the present time. For the eddy-damped quasi-normal approximation this Markovian approximation changes the variables in the damping time integral (other than those in the exponential which depend on intermediate times s) to depending on the present time t only, by setting $s = t$. Thus, the relaxation time is just an integral over the exponential term. Again differences appear; the Orszag form is (Orszag, 1977, p319)

$$\eta(k,t) = \nu k^2 + b\sqrt{k^3 E(k,t)}, \tag{1.70}$$

where b is a dimensionless constant. However, hereafter the spectral equations are given in the form used by Lesieur.

EDQNM equations

With the inclusion of eddy-damping and Markovianisation Lesieur's equations are

$$\left(\frac{\partial}{\partial t}+2\nu k^2\right)E(k,t) = \int_\Delta \mathrm{d}p\,\mathrm{d}q\,\theta_{kpq}(t)\frac{k}{pq}b(k,p,q)E(q,t)[k^2E(p,t)-p^2E(k,t)], \tag{1.71}$$

$$b(k,p,q) = \frac{1}{2}k^2 P_{\alpha\beta\gamma}(\boldsymbol{k})P_{\beta\delta\alpha}(\boldsymbol{p})P_{\gamma\delta}(\boldsymbol{q}), \tag{1.72}$$

$$= \frac{p}{k}(xy+z^3),$$

$$\theta_{kpq}(t) = \int_0^t \exp -[\mu_{kpq}+\nu(k^2+p^2+q^2)](t-\tau)\mathrm{d}\tau, \tag{1.73}$$

where Δ indicates that $\boldsymbol{k}+\boldsymbol{p}+\boldsymbol{q}=0$ and x, y and z are the cosines of the interior angles of the triangle opposite sides $\boldsymbol{k}, \boldsymbol{p}$ and $\boldsymbol{q}$, respectively.

An alternative choice of damping term is that of Leith (1971) who chose

$$\theta_{kpq}(t) = \frac{1 - \exp\left[-\mu_{kpq}^{\mathrm{RS}} t\right]}{\mu_{kpq}^{\mathrm{RS}}}, \tag{1.74}$$

with another change in notation having been made to correspond to that of Rose and Sulem (1978) who incorporate the viscous terms in μ_{kpq}: $\mu_{kpq}^{\mathrm{RS}} = \mu_{kpq} + \nu(k^2 + p^2 + q^2)$. Under the assumption that the wavenumber "damping" rates are approximately independent, the triple damping rate may be split into components due to each wavevector according to

$$\mu_{kpq}(t) = \mu_k(t) + \mu_p(t) + \mu_q(t), \tag{1.75}$$

$$\mu_k(t) = \nu k^2 + \lambda_d \left[\int_0^k p^2 E(p,t)\mathrm{d}p\right]^{1/2}, \tag{1.76}$$

where λ_d is a free parameter, so that the total decay rate is the sum of the individual rates. These final forms of $\theta_{kpq}(t)$, $\mu_{kpq}(t)$ and $\mu_k(t)$ most closely reflect those of Pouquet et al. (1976) which will be referred to extensively in this thesis. However, again for completeness another form listed in Rose and Sulem (1978) is

$$\theta_{kpq} = \frac{1}{\mu_{kpq}}, \tag{1.77}$$

$$\mu_{kpq} = \mu_k + \mu_p + \mu_q, \tag{1.78}$$

$$\mu_k = \nu k^2 + \lambda\sqrt{k^3 E(k)}, \tag{1.79}$$

λ again being a free parameter. The form of eddy-damped quasi-normal Markovian approximation given by Eqs. (1.71)–(1.72) and (1.74)–(1.76) can be shown to guarantee that the kinetic energy spectrum is positive definite (Orszag, 1977), a property known as realisability.

1.2.8 Invariants

For most differential equations there will be certain quantities which are constant and which may be used to assist in solving or determining the properties of solutions of the equations (Stephani, 1989). Although the equations presented so far have been couched in the language of infinite Fourier space, when it comes to performing calculations with computers there must be some truncation in wavenumber space. We are thus interested in the invariants of the original system which also remain invariant in the truncated system[6]. Furthermore, it is the inviscid case which is usually considered since viscosity destroys the invariant nature of many physical quantities of interest. These remaining "rugged invariants" are presented in Table 1.1, but it should be noted that the very word "invariant" is a misnomer in the context of turbulence, which only occurs in fluids possessing a small viscosity. No systematic study of invariants has been performed to the author's knowledge; in general, physical insight suggests a candidate quantity whose invariance can then be checked. Thus, this set cannot be

[6] A well-known case which does not survive is the circulation $\oint \boldsymbol{u} \cdot \mathrm{d}\boldsymbol{l}$.

Two-dimensional Navier-Stokes		Three-dimensional Navier-Stokes	
Kinetic energy	$E_v = \frac{1}{2}\int v^2 \mathrm{d}S$	Kinetic energy	$E_v = \frac{1}{2}\int v^2 \mathrm{d}V$
Enstrophy	$\Omega = \frac{1}{2}\int \omega^2 \mathrm{d}S$	Kinetic helicity	$H_v = \frac{1}{2}\int \boldsymbol{v}\cdot\boldsymbol{\omega}\mathrm{d}V$

Table 1.1: Rugged invariants in two and three-dimensional Navier-Stokes turbulence.

regarded as necessarily being complete, although it is believed that this is the case — see Kraichnan (1973), Montgomery (1977), Kraichnan and Montgomery (1980, pp. 551–553) and Lesieur (1990, pp. 131–132, 266–267) for further details.

1.2.9 Kolmogorov spectrum

The origins of turbulence may differ widely in a variety of situations but at the scales on which molecular viscosity acts little of the differences remain — all that is left is a seething body of small eddies. This property was further extended by Kolmogorov (1941) and Oboukhov (1941) who postulated a range in wavenumber space in which the kinetic energy spectrum does not depend on either the energy injection or the dissipation, i.e. $k_{\min} \ll k \ll k_{\mathrm{diss}}$ and, in particular, the kinetic energy spectrum is independent of the viscosity. Despite being independent of the detail of the energy injection process, in a stationary state three distinct quantities must all be equal: the rate of flow through wavenumber space, rate of dissipation and rate of injection of energy per unit mass, $\varepsilon = -\mathrm{d}E_v/\mathrm{d}t$. The energy per unit mass spectrum (dimension L^3T^{-2}) should then depend only on the quantities ε (dimension L^2T^{-3}) and k (dimension L^{-1}). Dimensional analysis then gives

$$E(k) = C_K \varepsilon^{2/3} k^{-5/3}, \tag{1.80}$$

in which C_K is a constant called the Kolmogorov constant. Other derivations of this result have been given, one of the best being that of Orszag and Kruskal (1968) who work from the spectral cumulant equations. See also Batchelor (1953, pp. 121–122) and Lesieur (1990, pp. 137–141). For future reference the approach of Oboukhov (Lesieur, 1990, pp. 139–140) was to express the rate of transfer of energy per unit mass in terms of a characteristic relaxation time, $\tau(k)$. Dimensional analysis then gives

$$\varepsilon = A^2 \tau(k) E^2(k) k^4, \tag{1.81}$$

where A is a dimensionless constant. For the fluid situation under consideration the relaxation time is taken to be $\tau(k) = (k u_k)^{-1}$, where the characteristic eddy speed is given by $u_k = \sqrt{kE(k)}$. Rearranging Eq. (1.81) with these assumptions again gives the Kolmogorov spectrum with $C_K = A^{-4/3}$.

Modifications have also been made to make the theory more appropriate near dissipation scales but this will not be pursued here.

1.2.10 Cascades

The effect of turbulence (which may be regarded as the net effect of many instabilities) in transferring energy between large and small scales was hinted at in Eqs. (1.8) and (1.9). For example, it is known from two-dimensional[7] numerical experiments that there is a tendency for the energy to undergo an inverse cascade, with a transfer from small to large scales while the enstrophy forward-cascades (André and Lesieur, 1977; Basdevant et al., 1978; Tatsumi and Yanase, 1981). There are means of determining the direction of cascade for a particular rugged invariant without recourse to numerics. Fjortoft's theorem is illustrated by Lesieur (1990, pp. 267–268) for the inviscid two-dimensional Navier-Stokes equation truncated to having only three wavevectors, $\boldsymbol{k}_1, \boldsymbol{k}_2$ and $\boldsymbol{k}_3$. Taking $\boldsymbol{k}_2 = 2\boldsymbol{k}_1$ and $\boldsymbol{k}_3 = 3\boldsymbol{k}_1$ for simplicity, conservation of energy and enstrophy requires that the changes in energy, δE, obey the following relations[8]:

$$\delta E_1 + \delta E_2 + \delta E_3 = 0, \tag{1.82}$$

$$k_1^2 \delta E_1 + k_2^2 \delta E_2 + k_3^2 \delta E_3 = 0, \tag{1.83}$$

the latter relation arising because the enstrophy spectrum is just $k^2 E(k)$. This system admits the solution

$$\delta E_1 = -\frac{5}{8}\delta E_2, \tag{1.84}$$

$$\delta E_3 = -\frac{3}{8}\delta E_2, \tag{1.85}$$

$$k_1^2 \delta E_1 = -\frac{5}{32} k_2^2 \delta E_2, \tag{1.86}$$

$$k_3^2 \delta E_3 = -\frac{27}{32} k_2^2 \delta E_2, \tag{1.87}$$

from which it can be seen that if there is a source at scale k_2 ($\delta E_2 < 0$) more energy will transfer to scale k_1 than to scale k_3; similarly more enstrophy goes to k_3 than to k_1.

The second method for predicting cascade directions assumes the system to be in statistical equilibrium and constructs the Gibbs distribution for the system invariants (Kraichnan, 1973; Orszag, 1977, Sect. 5.2). Both this and Fjortoft's theorem, then, depend critically on the invariants of the system. Since direct numerical simulations broadly agree with the conclusions obtained from both simplified approaches we have some evidence for believing the rugged invariants of Table 1.1 to constitute a complete set; mathematical proof, as always, would be reassuring. Further information can be obtained in Kraichnan (1967) and Batchelor (1969).

[7] In two dimensions it is the enstrophy which forward-cascades and so the enstrophy transfer rate, ε_Ω, with dimension T^{-3}, is used instead of ε, giving rise to the inertial range kinetic energy spectrum $E(k) = C\varepsilon_\Omega^{2/3} k^{-3}$. For wavenumbers below the injection wavenumber the Kolmogorov spectrum applies (Kraichnan, 1967; Kraichnan, 1971; Biskamp, 1993, p198).

[8] $\delta E_2 < 0$ indicates the presence of a source at scale k_2, energy being transferred from k_2 to k_1 and k_3

1.3 MHD turbulence

So far only the fluid case has been dealt with in order to provide background to the methods used in describing turbulence both qualitatively and quantitatively. However, as this thesis is concerned with the effects of turbulence in magnetofluids, it is now appropriate to turn to the equations of visco-resistive, incompressible magnetohydrodynamics presented in dimensionless form (see Sect. 3.2 for details of the particular non-dimensionalisation used in this thesis):

$$\frac{\partial \boldsymbol{v}}{\partial \tau} + (\boldsymbol{v} \cdot \nabla)\boldsymbol{v} = -\nabla p + \boldsymbol{j} \times \boldsymbol{b} + \nu \nabla^2 \boldsymbol{v}, \tag{1.88}$$

$$\frac{\partial \boldsymbol{b}}{\partial \tau} = \nabla \times (\boldsymbol{v} \times \boldsymbol{b}) + \eta \nabla^2 \boldsymbol{b}, \tag{1.89}$$

$$\boldsymbol{j} = \nabla \times \boldsymbol{b}, \tag{1.90}$$

$$\eta \boldsymbol{j} = \mathrm{e} + \boldsymbol{v} \times \boldsymbol{b}, \tag{1.91}$$

$$\nabla \cdot \boldsymbol{b} = 0, \tag{1.92}$$

$$\nabla \cdot \boldsymbol{v} = 0, \tag{1.93}$$

where $\boldsymbol{v}$ is the velocity, $\boldsymbol{b}$ the magnetic flux density (from now on referred to as the magnetic field following MHD convention), $\boldsymbol{j}$ the current density, $\boldsymbol{e}$ the electric field, τ the time, p the hydrostatic pressure, ν the kinematic viscosity, and η the magnetic diffusivity. Given the ground to be covered in introducing the subject of turbulence, no justification will be given here for these equations or the quantities involved therein. Instead the reader is referred to Shercliff (1965), Cowling (1976), Roberts (1967) and Priest (1982).

1.3.1 Development of turbulent flow

It is now possible to form the equations for the transfer of kinetic and magnetic energy between large and small scales comparable to Eqs. (1.8) and (1.9). Writing $v_i = \overline{v}_i + v_i'$ and $b_i = \overline{b}_i + b_i'$ we have, after averaging and subtracting the resulting equations from the originals:

$$\frac{\partial \overline{v}_i}{\partial t} + \overline{v}_j \frac{\partial \overline{v}_i}{\partial x_j} = -\overline{v'_j \frac{\partial v'_i}{\partial x_j}} - \frac{\partial}{\partial x_i}\left(\overline{p} + \frac{1}{2}\overline{b}_j\overline{b}_j + \frac{1}{2}\overline{b'_j b'_j}\right) + \overline{b}_j \frac{\partial \overline{b}_i}{\partial x_j} + \overline{b'_j \frac{\partial b'_i}{\partial x_j}} + \nu \frac{\partial^2 \overline{v}_i}{\partial x_j \partial x_j}, \tag{1.94}$$

$$\frac{\partial v'_i}{\partial t} + \overline{v}_j \frac{\partial v'_i}{\partial x_j} = -v'_j \frac{\partial \overline{v}_i}{\partial x_j} - v'_j \frac{\partial v'_i}{\partial x_j} + \overline{v'_j \frac{\partial v'_i}{\partial x_j}} - \frac{\partial}{\partial x_i}\left(p' + \frac{1}{2}b'_j b'_j - \frac{1}{2}\overline{b'_j b'_j} + \overline{b}_j b'_j\right) + \overline{b}_j \frac{\partial b'_i}{\partial x_j} + b'_j \frac{\partial \overline{b}_i}{\partial x_j} + b'_j \frac{\partial b'_i}{\partial x_j} - \overline{b'_j \frac{\partial b'_i}{\partial x_j}} + \nu \frac{\partial^2 v'_i}{\partial x_j \partial x_j}, \tag{1.95}$$

$$\frac{\partial \overline{b}_i}{\partial t} + \overline{v}_j \frac{\partial \overline{b}_i}{\partial x_j} = -\overline{v'_j \frac{\partial b'_i}{\partial x_j}} + \overline{b}_j \frac{\partial \overline{v}_i}{\partial x_j} + \overline{b'_j \frac{\partial v'_i}{\partial x_j}} + \eta \frac{\partial^2 \overline{b}_i}{\partial x_j \partial x_j}, \tag{1.96}$$

$$\frac{\partial b'_i}{\partial t} + \overline{v}_j \frac{\partial b'_i}{\partial x_j} = -v'_j \frac{\partial \overline{b}_i}{\partial x_j} - v'_j \frac{\partial b'_i}{\partial x_j} + \overline{v'_j \frac{\partial b'_i}{\partial x_j}} + \overline{b}_j \frac{\partial v'_i}{\partial x_j} + b'_j \frac{\partial \overline{v}_i}{\partial x_j} + b'_j \frac{\partial v'_i}{\partial x_j} - \overline{b'_j \frac{\partial v'_i}{\partial x_j}} + \eta \frac{\partial^2 b'_i}{\partial x_j \partial x_j}, \tag{1.97}$$

$$\frac{\partial \overline{v}_i}{\partial x_i} = 0, \tag{1.98}$$

$$\frac{\partial v'_i}{\partial x_i} = 0, \tag{1.99}$$

$$\frac{\partial \overline{b}_i}{\partial x_i} = 0, \tag{1.100}$$

$$\frac{\partial b_i}{\partial x_i} = 0. \tag{1.101}$$

These lead to the energy equations,

$$\frac{\mathrm{d}}{\mathrm{d}t}\frac{1}{2}\overline{v'_i v'_i} = -\frac{\partial}{\partial x_j}\left(\overline{v'_i v'_i v'_j} + \overline{v'_j p'} + \frac{1}{2}\overline{v'_j b'_i b'_i} + \overline{v'_j b'_i}\,\overline{b}_j + \nu\varepsilon_{ijk}\overline{\omega'_j v'_k}\right) \overbrace{-\overline{v'_i v'_j}\frac{\partial \overline{v}_i}{\partial x_j}}^{(1)} \overbrace{+\overline{b}_j \overline{v'_i \frac{\partial b'_i}{\partial x_j}}}^{(2)} \overbrace{+\overline{v'_i b'_j}\frac{\partial \overline{b}_i}{\partial x_j}}^{(3)} \overbrace{+\overline{v'_i b'_j \frac{\partial b'_i}{\partial x_j}}}^{(4)} - \nu\,\overline{\omega'_i \omega'_i}, \tag{1.102}$$

$$\frac{\mathrm{d}}{\mathrm{d}t}\frac{1}{2}\overline{b'_i b'_i} = -\frac{\partial}{\partial x_j}\left(\frac{1}{2}\overline{v'_j b'_i b'_i} + \varepsilon_{jik}\overline{J'_i b'_k}\right) \overbrace{-\overline{b'_i v'_j}\frac{\partial \overline{b}_i}{\partial x_j}}^{(5)} \overbrace{+\overline{b}_j \overline{b'_i \frac{\partial v'_i}{\partial x_j}}}^{(2)} \overbrace{+\overline{b'_i b'_j}\frac{\partial \overline{v}_i}{\partial x_j}}^{(6)} \overbrace{+\overline{b'_i b'_j \frac{\partial v'_i}{\partial x_j}}}^{(4)} - \eta\,\overline{J'_i J'_i}, \tag{1.103}$$

$$\frac{\mathrm{d}}{\mathrm{d}t}\frac{1}{2}\overline{v}_i\overline{v}_i = -\frac{\partial}{\partial x_j}\left(\overline{v}_j\overline{p} + \frac{1}{2}\overline{v}_j\overline{b}_i\overline{b}_i + \frac{1}{2}\overline{v}_j\overline{b'_i b'_i} + \varepsilon_{jik}\overline{\omega}_i\overline{v}_k\right) \overbrace{-\overline{v}_i\overline{v'_j \frac{\partial v'_i}{\partial x_j}}}^{(1)} \overbrace{+\overline{v}_i\overline{b}_j\frac{\partial \overline{b}_i}{\partial x_j}}^{(7)} \overbrace{+\overline{v}_i\overline{b'_j \frac{\partial b'_i}{\partial x_j}}}^{(6)} - \nu\,\overline{\omega}_i\overline{\omega}_i, \tag{1.104}$$

$$\frac{\mathrm{d}}{\mathrm{d}t}\frac{1}{2}\overline{b}_i\overline{b}_i = -\frac{\partial}{\partial x_j}\varepsilon_{jik}\overline{J}_i\overline{b}_k - \overbrace{\overline{b}_i\overline{v_j'\frac{\partial b_i'}{\partial x_j}}}^{(5)} + \overbrace{\overline{b}_i\overline{b}_j\frac{\partial \overline{v}_i}{\partial x_j}}^{(7)} + \overbrace{\overline{b}_i\overline{b_j'\frac{\partial v_i'}{\partial x_j}}}^{(3)} - \eta\,\overline{J}_i\overline{J}_i. \tag{1.105}$$

The vorticity is defined as $\omega_i = \varepsilon_{ijk}\partial v_k/\partial x_j$ while the current density, J_i, has been expressed in capitals, despite being dimensionless, to avoid confusion with the tensor index j. The identity

$$A_i\frac{\partial^2 A_i}{\partial x_j\partial x_j} = -\frac{\partial}{\partial x_i}\varepsilon_{ijk}\left(\varepsilon_{jlm}\frac{\partial A_m}{\partial x_l}\right)A_k - \varepsilon_{ijk}\varepsilon_{ilm}\frac{\partial A_k}{\partial x_j}\frac{\partial A_m}{\partial x_l}, \tag{1.106}$$

was also used in the derivation of these energy equations (alternatively written as $\boldsymbol{A}\cdot\nabla^2\boldsymbol{A} = -\nabla\cdot[(\nabla\times\boldsymbol{A})\times\boldsymbol{A}] - |\nabla\times\boldsymbol{A}|^2$).

The right sides of Eqs. (1.102)–(1.105) consist of three types of term. The first is a divergence which, when integrated over the volume, gives a surface integral after the divergence theorem has been applied. This gives information about how the kinetic and magnetic energies within the volume are affected by the behaviour at the boundary. It is now assumed that the processes occuring are regular in character, occurring only at the large scales which give rise to the mean flows after averaging. With this assumption the small-scale terms v_i', b_i' and p' are zero at the boundary, so that the surface contributions in Eqs. (1.102) and (1.103) vanish completely, while the contribution in Eq. (1.104) is just the work done by the gas and magnetic pressures, and also viscous stresses; correspondingly, in Eq. (1.105) it is the Poynting flux which determines the introduction of magnetic energy at the boundary.

The second type of term is the final one in each of the four energy equations and describes the conversion of kinetic and magnetic energy by viscous and resistive effects, respectively, into the internal energy of the magnetofluid, manifested as an increased temperature — these effects occur at all scales.

The remaining terms, marked by the braces and numbered, describe the nonlinear effects on each type of energy and the interaction between large and small scales. It can be seen that taken together these terms conserve kinetic and magnetic energy because each of the similarly numbered terms combines into a divergence upon addition (taking into account Eqs. (1.98)–(1.101)). This gives a surface integral which makes no net contribution to the energy balance because it involves small-scale terms already assumed to be zero at the surface boundary or at infinity. However, the presence of these terms in the individual energy equations indicates a complex interchange of energy, with the possibility of each form being converted into either or both of the other two at large *and* small scales, unlike the earlier fluid case where the energy exchange was only a two-way process between large and small-scale kinetic energy. It can now be seen that adopting the concepts of turbulent viscosity and magnetic diffusivity to approximate these nonlinear effects as diffusion terms in the large-scale equations is even further removed from a physical basis than in the fluid case. For the record, the required approximations in Eqs. (1.94) and (1.96) are that

$$\overline{b_j'\frac{\partial b_i'}{\partial x_j}} - \overline{v_j'\frac{\partial v_i'}{\partial x_i}} - \frac{\partial}{\partial x_i}\frac{1}{2}\overline{b_j'b_j'} = \nu_{\mathrm{turb}}\frac{\partial^2\overline{u}_i}{\partial x_j\partial x_j}, \tag{1.107}$$

Quantity	Definition	Spectral Integral
Kinetic energy	$E_v = \frac{1}{2}\int v^2 \,\mathrm{d}V$	$= \int E_k^V \,\mathrm{d}k,$
Magnetic energy	$E_m = \frac{1}{2}\int b^2 \,\mathrm{d}V$	$= \int E_k^M \,\mathrm{d}k,$
Kinetic helicity	$H_v = \frac{1}{2}\int \boldsymbol{v}\cdot\boldsymbol{\omega} \,\mathrm{d}V$	$= \int H_k^V \,\mathrm{d}k,$
Magnetic helicity	$H_m = \frac{1}{2}\int \boldsymbol{a}\cdot\boldsymbol{b} \,\mathrm{d}V$	$= \int H_k^M \,\mathrm{d}k,$
Cross helicity	$H_c = \frac{1}{2}\int \boldsymbol{v}\cdot\boldsymbol{b} \,\mathrm{d}V$	$= \int H_k^C \,\mathrm{d}k,$

Table 1.2: Energies and helicities with their spectral definitions.

$$\overline{b_j' \frac{\partial v_i'}{\partial x_j}} - \overline{v_j' \frac{\partial b_i'}{\partial x_i}} = \eta_{\mathrm{turb}} \frac{\partial^2 \bar{b}_i}{\partial x_j \partial x_j}. \tag{1.108}$$

Moffatt (1978), however, has justified the use of turbulent magnetic diffusivity as a diffusion term with a kinematic argument. This argument is only applicable in instances where the effect of the plasma flow outweighs the effect of the magnetic field, such as in the solar interior, and requires the inclusion of an alpha effect term, $\nabla \times (\alpha \boldsymbol{b})$, whenever the driving flow is helical in nature. In the solar corona and laboratory plasmas the former assumption is clearly invalid, while for a shear-flow driven magnetic arcade the flow must possess helicity, and so an induction equation involving turbulent magnetic diffusivity as a diffusion term must also include an alpha effect term for consistency (the kinematic approach having been accepted for the sake of argument). This still leaves the problem of justifying the use of turbulent viscosity and magnetic diffusivity as diffusion terms in the coronal context.

1.3.2 Eddy-damped quasi-normal Markovian approximation

Following the procedures described in Sect. 1.2 Pouquet et al. (1976) derived the EDQNM approximation for the homogeneous, isotropic, helical, three-dimensional MHD situation. The various energies and helicities and their corresponding spectral definitions are given in Table 1.2 (Frisch et al., 1975). In particular the eddy-damping rate was chosen to be

$$\mu_k = C_S \left[\int_0^k q^2 (E_q^{\mathrm{V}} + E_q^{\mathrm{M}}) \mathrm{d}q\right]^{1/2} + C_A k \left[2\int_0^k E_q^{\mathrm{M}} \mathrm{d}q\right]^{1/2} + (\nu + \eta)k^2, \tag{1.109}$$

where[9] $C_S = 0.26$ in order to ensure that the coefficient of the Kolmogorov spectrum, obtained by numerically solving the EDQNM equations in the absence of magnetic field, is 1.4; $C_A = 1/\sqrt{3}$ is obtained analytically by assuming a Gaussian large-scale magnetic field. Note that in this work there

[9] C_S was given as 0.36 in Pouquet et al. (1976) but was corrected in Léorat et al. (1981).

is no large-scale background field, which would be incompatible with the assumption of isotropy (cf. Eq. (1.26) in this thesis), so an energy integral has been used in the second term instead of the background field which appears in Kraichnan (1965) (Sect. 1.3.4). Respectively, the three terms of the eddy-damping rate account for the effects of nonlinear scrambling, the Alfvén effect (Sect. 1.3.5), and molecular viscosity and magnetic diffusivity. Again

$$\mu_{kpq} = \mu_k + \mu_p + \mu_q, \tag{1.110}$$

and the triad-relaxation time is taken to be

$$\theta_{kpq}(t) = \frac{1 - \exp\left(-\mu_{kpq} t\right)}{\mu_{kpq}}. \tag{1.111}$$

The spectral equations are then

$$\left(\frac{\partial}{\partial t} + 2\nu k^2\right) E_k^V = F_k^V + \int_\Delta \mathrm{d}p\,\mathrm{d}q\theta_{kpq}(T_{VV}^V + T_{\tilde{V}\tilde{V}}^V + T_{VM}^V + T_{MM}^V + T_{\tilde{M}\tilde{M}}^V), \tag{1.112}$$

$$\left(\frac{\partial}{\partial t} + 2\eta k^2\right) E_k^M = F_k^M + \int_\Delta \mathrm{d}p\,\mathrm{d}q\theta_{kpq}(T_{VM}^M + T_{\tilde{V}\tilde{M}}^M + T_{MM}^M + T_{\tilde{M}\tilde{M}}^M), \tag{1.113}$$

$$\left(\frac{\partial}{\partial t} + 2\nu k^2\right) H_k^V = \tilde{F}_k^V + \int_\Delta \mathrm{d}p\,\mathrm{d}q\theta_{kpq}(T_{V\tilde{V}}^{\tilde{V}} + T_{\tilde{V}M}^{\tilde{V}} + T_{M\tilde{M}}^{\tilde{V}}), \tag{1.114}$$

$$\left(\frac{\partial}{\partial t} + 2\eta k^2\right) H_k^M = \tilde{F}_k^M + \int_\Delta \mathrm{d}p\,\mathrm{d}q\theta_{kpq}(T_{V\tilde{M}}^{\tilde{M}} + T_{\tilde{V}M}^{\tilde{M}} + T_{M\tilde{M}}^{\tilde{M}}), \tag{1.115}$$

where the F_k terms denote uniformly distributed random forcing and

$$T_{VV}^V = \frac{k}{pq} b_{kpq}(k^2 E_p^V E_q^V - p^2 E_q^V E_k^V), \tag{1.116}$$

$$T_{\tilde{V}\tilde{V}}^V = -\frac{1}{pq^2} c_{kpq}(k^2 H_p^V H_q^V - p^2 H_q^V H_k^V), \tag{1.117}$$

$$T_{VM}^V = \frac{kp}{q} c_{kpq} E_q^M E_k^V, \tag{1.118}$$

$$T_{MM}^V = \frac{k^3}{pq} c_{kpq} E_p^M E_q^M, \tag{1.119}$$

$$T_{\tilde{M}\tilde{M}}^V = -\frac{k^3 q}{2p} h_{kpq} H_p^M H_q^M, \tag{1.120}$$

$$T_{VM}^M = \frac{k^5}{p^3 q} c_{kpq} E_p^V E_q^M + \frac{k}{pq} h_{kpq}(k^2 E_p^M E_q^V - p^2 E_q^V E_k^M), \tag{1.121}$$

$$T_{\tilde{V}\tilde{M}}^M = \frac{kq}{p} h_{kpq}\left(\frac{k^2}{p^2} H_p^V H_q^M - \frac{p^2}{q^2} H_q^V H_k^M\right), \tag{1.122}$$

$$T_{MM}^M = -\frac{k^3}{pq} c_{kpq} E_q^M E_k^M, \tag{1.123}$$

$$T_{\tilde{M}\tilde{M}}^M = kp^2 e_{kpq} H_q^M H_k^M, \tag{1.124}$$

$$T_{V\tilde{V}}^{\tilde{V}} = \frac{k}{pq} b_{kpq}(k^2 H_p^V E_q^V - p^2 E_q^V H_k^V) - \frac{k^2 p}{q^2} c_{kpq}(E_p^V H_q^V - H_q^V E_k^V), \tag{1.125}$$

$$T_{\tilde{V}M}^{\tilde{V}} = -\frac{kp}{q} c_{kpq} E_q^M H_k^V, \tag{1.126}$$

$$T^{\tilde{V}}_{M\tilde{M}} = \frac{k^4}{q} f_{kpq} H^M_p E^M_q, \tag{1.127}$$

$$T^{\tilde{M}}_{V\tilde{M}} = \frac{k}{pq} h_{kpq} (k^2 H^M_p E^V_q - p^2 E^V_q H^M_k), \tag{1.128}$$

$$T^{\tilde{M}}_{\tilde{V}M} = \frac{k}{pq} h_{kpq} \left(\frac{k^2}{p^2} H^V_p E^M_q - \frac{p^2}{k^2} H^V_q E^M_k \right), \tag{1.129}$$

$$T^{\tilde{M}}_{M\tilde{M}} = \frac{p^2}{k} e_{kpq} H^M_q E^M_k - \frac{kp}{q} j_{kpq} E^M_q H^M_k, \tag{1.130}$$

$$b_{kpq} = \frac{p}{k}(xy + z^3), \tag{1.131}$$

$$c_{kpq} = \frac{pz}{k}(1 - y^2), \tag{1.132}$$

$$e_{kpq} = x(1 - z^2), \tag{1.133}$$

$$f_{kpq} = z - xy - 2zy^2, \tag{1.134}$$

$$h_{kpq} = 1 - y^2, \tag{1.135}$$

$$j_{kpq} = \frac{pz}{k}(1 - x^2), \tag{1.136}$$

x, y and z are the usual cosines of the triangle formed by vectors $\boldsymbol{k}$, $\boldsymbol{p}$ and $\boldsymbol{q}$, and $\triangle$ indicates that the three wavevectors satisfy the triangle relation $\boldsymbol{k} + \boldsymbol{p} + \boldsymbol{q} = \boldsymbol{0}$. Quantities with a tilde involve helicities.

Pouquet et al. (1976) concentrated on nonlocal effects whereby the wavenumbers in the triad are of markedly different magnitudes. A small parameter, a, was defined such that the ratio of the smallest to middle wavenumber in the triad is less than a. Equations (1.112)–(1.115) were then expanded in a to give

$$\left(\frac{\partial E^V_k}{\partial t}\right)_{\text{Nloc}} = -k\Gamma_k (E^V_k - E^M_k) - \tilde{\Gamma}_k k^2 H^M_k - 2\left(\frac{2}{5}\nu^V_k + \nu^M_k + \nu^R_k\right) k^2 E^V_k + O(a^2), \tag{1.137}$$

$$\left(\frac{\partial E^M_k}{\partial t}\right)_{\text{Nloc}} = k\Gamma_k (E^V_k - E^M_k) + \tilde{\Gamma}_k H^V_k + \alpha^R_k k^2 H^M_k - 2\nu^V_k k^2 E^M_k + O(a^2), \tag{1.138}$$

$$\left(\frac{\partial H^V_k}{\partial t}\right)_{\text{Nloc}} = -k\Gamma_k (H^V_k - k^2 H^M_k) - \tilde{\Gamma}_k k^2 E^M_k - 2\left(\frac{2}{5}\nu^V_k + \nu^M_k + \nu^R_k\right) k^2 H^V_k + O(a^2), \tag{1.139}$$

$$\left(\frac{\partial H^M_k}{\partial t}\right)_{\text{Nloc}} = \frac{\Gamma_k}{k}(H^V_k - k^2 H^M_k) + \tilde{\Gamma}_k E^V_k + \alpha^R_k E^M_k - 2\nu^V_k k^2 H^M_k + O(a^2), \tag{1.140}$$

where

$$\alpha^R_k = \alpha^V_k - \alpha^M_k, \tag{1.141}$$

$$\alpha^V_k = -\frac{4}{3}\int_{k/a}^{\infty} \theta_{kqq} H^V_q \, \mathrm{d}q, \tag{1.142}$$

$$\alpha^M_k = -\frac{4}{3}\int_{k/a}^{\infty} \theta_{kqq} q^2 H^M_q \, \mathrm{d}q, \tag{1.143}$$

$$\nu^V_k = \frac{2}{3}\int_{k/a}^{\infty} \theta_{kqq} E^V_q \, \mathrm{d}q, \tag{1.144}$$

Two-dimensional MHD		Three-dimensional MHD	
Total energy	$E_t = \frac{1}{2}\int (v^2 + b^2)\,\mathrm{d}S$	Total energy	$E_t = \frac{1}{2}\int (v^2 + b^2)\,\mathrm{d}V$
Cross helicity	$H_c = \frac{1}{2}\int \boldsymbol{v}\cdot\boldsymbol{b}\,\mathrm{d}S$	Cross helicity	$H_c = \frac{1}{2}\int \boldsymbol{v}\cdot\boldsymbol{b}\,\mathrm{d}V$
Mean-square potential	$A = \frac{1}{2}\int a^2\,\mathrm{d}S$	Magnetic helicity	$H_m = \frac{1}{2}\int \boldsymbol{a}\cdot\boldsymbol{b}\,\mathrm{d}V$

Table 1.3: Rugged invariants in two- and three-dimensional MHD turbulence. The vector potential, $\mathbf{a}$, is related to the magnetic field by $\mathbf{b} = \nabla \times \mathbf{a}$.

$$\nu_k^M = \frac{2}{3}\int_{k/a}^{\infty} \theta_{kqq} E_q^M \mathrm{d}q, \tag{1.145}$$

$$\nu_k^R = \frac{2}{15}\int_{k/a}^{\infty} \theta_{kqq}^2 q \frac{\partial \mu_q}{\partial q}(E_q^V - E_q^M)\mathrm{d}q, \tag{1.146}$$

$$\Gamma_k = \frac{4}{3}k\int_0^{ak} \theta_{kkq} E_q^M \mathrm{d}q, \tag{1.147}$$

$$\tilde{\Gamma}_k = \frac{4}{3}\int_0^{ak} \theta_{kkq} q^2 H_q^M \mathrm{d}q. \tag{1.148}$$

The interchange between kinetic and magnetic energies exhibited in Eqs. (1.102)–(1.105) now extends to the kinetic and magnetic helicities. Furthermore, a dynamo effect is present in the form of the Γ coefficients.

1.3.3 Invariants

Table 1.3 gives the known rugged invariants for two- and three-dimensional MHD (Biskamp, 1993, pp. 179–180). The boundary conditions under which ideal invariance holds are as follows (Matthaeus and Goldstein, 1982). For the total energy either $\hat{\boldsymbol{n}}\cdot\boldsymbol{b} = 0$ (perfectly conducting boundary) and $\hat{\boldsymbol{n}}\cdot\boldsymbol{v} = 0$ (free-slip boundary), $\boldsymbol{v} = \boldsymbol{0}$ on the boundary (no-slip boundary), or the velocity, magnetic field, and pressure are spatially periodic, where $\hat{\boldsymbol{n}}$ is the normal to the boundary, to ensure invariance. For the cross helicity, either $\hat{\boldsymbol{n}}\cdot\boldsymbol{v} = \hat{\boldsymbol{n}}\cdot\boldsymbol{b} = 0$, or $\boldsymbol{v}\cdot\boldsymbol{b}$ and $v^2/2 + p$ are spatially periodic and $\boldsymbol{b} = \boldsymbol{0}$ on the boundary. Finally, invariance of the magnetic helicity requires $\hat{\boldsymbol{n}}\cdot\boldsymbol{v} = \hat{\boldsymbol{n}}\cdot\boldsymbol{b} = 0$, or $-\nabla\phi = \boldsymbol{0}$ on the boundary and either $\boldsymbol{v} = \boldsymbol{0}$ or $\boldsymbol{b} = \boldsymbol{0}$ on the boundary, where ϕ is the electrostatic potential given by $\boldsymbol{e} = -\nabla\phi - \partial\boldsymbol{a}/\partial\tau$ and $\boldsymbol{a}$ is the vector potential, or $\boldsymbol{a}, \phi, \boldsymbol{v}$ and $\boldsymbol{b}$ are spatially periodic. In three-dimensional MHD with a constant background field, however, the magnetic helicity is no longer an ideal invariant; rather, a "total magnetic helicity" $\hat{H}_m = H_m + 2\boldsymbol{b}_0\cdot\boldsymbol{a}_0$, where $\nabla\times\boldsymbol{a} = \boldsymbol{0}$, is conserved in periodic geometry (Matthaeus and Goldstein, 1982; Stribling et al., 1994).

1.3.4 Kraichnan spectrum

Iroshnikov (1964) and Kraichnan (1965) analysed the inertial range for MHD by noting that, in addition to the effects of instabilities relaxing eddies, the propagation and interaction of Alfvén waves through a magnetofluid would also cause eddy relaxation. Following the approach of Oboukhov (Sect. 1.2.9) the characteristic relaxation time is now taken to be $\tau(k) = (kc_{a0})^{-1}$, where c_{a0} is the Alfvén speed based on the background field, whence re-arrangement of Eq. (1.81) leads to the Kraichnan spectrum

$$E(k) = A^{-1}\sqrt{\varepsilon c_{a0}}k^{-3/2}. \tag{1.149}$$

A further consequence of the interacting wave approach is that in the inertial range there is approximate equipartition of kinetic and magnetic energy so that both spectra are equal to the above expression. This is shown by expressing the momentum and induction equations with uniform and fluctuating components, $\boldsymbol{b}_0$ and $\boldsymbol{b}_1$, respectively, in terms of Elsässer variables, $\boldsymbol{z}^{\pm} = \boldsymbol{v} \pm \boldsymbol{b}_1$:

$$\left(\frac{\partial}{\partial t} + \boldsymbol{z}^{\mp}\cdot\nabla\right)\boldsymbol{z}^{\pm} \mp (\boldsymbol{b}_0\cdot\nabla)\boldsymbol{z}^{\pm} = -\nabla\left(p + \frac{b_1^2}{2}\right) + \nu_+\nabla^2\boldsymbol{z}^{\pm} + \nu_-\nabla^2\boldsymbol{z}^{\mp}, \tag{1.150}$$

where $\nu_{\pm} = (\nu \pm \eta)/2$. For Alfvén waves propagating in an infinite medium we have $\boldsymbol{v} = \pm\boldsymbol{b}$, whence either $\boldsymbol{z}^+ = \boldsymbol{0}$ or $\boldsymbol{z}^- = \boldsymbol{0}$, so that the correlation $\langle \boldsymbol{z}^+\cdot\boldsymbol{z}^-\rangle$ is zero. In a turbulent medium, however, where the waves are less well defined it can only be expected that as the two "waves" separate they gradually become decorrelated until at infinity $\langle \boldsymbol{z}^+\cdot\boldsymbol{z}^-\rangle = \langle v^2\rangle - \langle b^2\rangle = 0$, giving asymptotic equipartition of kinetic and magnetic energy. In fact, equipartition is a result of the implicit assumption of there being no globally averaged correlation between velocity and magnetic field (Politano et al., 1989). Numerical simulations reveal that the magnetic energy spectrum always exceeds the kinetic energy spectrum in such cases (Fyfe and Montgomery, 1976; Fyfe et al., 1977b; Biskamp and Welter, 1989).

Finally, Matthaeus and Zhou (1989) have repeated the above procedure with a hybrid time-scale, $\tau_3(k)$, based on both the eddy-relaxation time of Sect. 1.2.9, $\tau_{\rm nl}(k)$, and the Alfvénic time-scale of this section, $\tau_A(k)$, as

$$\frac{1}{\tau_3(k)} = \frac{1}{\tau_{\rm nl}(k)} + \frac{1}{\tau_A(k)}. \tag{1.151}$$

Assuming a steady state of isotropic turbulence with no cross helicity, and equipartition of kinetic and magnetic energy leads to the spectrum

$$E(k) = Z^2(Z_0)A^{-4/3}\varepsilon^{2/3}k^{-5/3}, \tag{1.152}$$

where

$$Z = \frac{1}{2}\left(\sqrt{y} + \sqrt{-y + 2\sqrt{y^2 + 4Z_0}}\right), \tag{1.153}$$

$$Z_0 = \left(\frac{A^2kB_0^3}{\varepsilon}\right)^{1/3}, \tag{1.154}$$

$$y = \left(\frac{1}{2}+\sqrt{\frac{1}{4}+\left(\frac{4}{3}Z_0\right)^3}\right)^{1/3} + \left(\frac{1}{2}-\sqrt{\frac{1}{4}+\left(\frac{4}{3}Z_0\right)^3}\right)^{1/3}, \quad (1.155)$$

and B_0 has been expressed in units of the Alfvén speed. If $B_0 \to 0$, then $Z_0 \to 0, y \to 1, Z \to 1$ and the Kolmogorov spectrum of Sect. 1.2.9 is obtained. For large B_0, on the other hand, $Z_0 \to \infty$ whence $y \to 0, Z \to Z_0^{1/4}$ and $E(k) \to A^{-1}\sqrt{B_0\epsilon}k^{-3/2}$. Thus, in the low-field limit a Kolmogorov spectrum is obtained while for high fields the Kraichnan spectrum results.

1.3.5 Cascades, selective decay and dynamic alignment

Determining cascade directions in MHD is much harder than for fluids due to the presence of additional rugged invariants. It is still possible to apply Fjortoft's theorem if one of these is zero (most commonly the cross helicity) with the conclusion that the total energy forward-cascades in both two and three dimensions; in 2D it is the mean-square potential which inverse-cascades, while in 3D it is the magnetic helicity. The approach of using Gibbs distributions is also applicable, inasmuch as the system can be said to be in statistical equilibrium (Frisch et al., 1975; Fyfe and Montgomery, 1976; Fyfe et al., 1977a; Montgomery et al., 1978; Stribling and Matthaeus, 1990, 1991; Biskamp, 1993). However, this leaves unanswered the question of what happens when velocity and magnetic fields are correlated, so that the cross helicity is non-zero, or what happens in decaying turbulence, when a steady state cannot be achieved.

For a decaying system there is no forcing; examination of the equations for the rate of change of the various quantities,

$$\frac{\mathrm{d}E_t}{\mathrm{d}t} = -\eta\int j^2\mathrm{d}V - \nu\int\omega^2\,\mathrm{d}V, \quad (1.156)$$

$$\frac{\mathrm{d}H_c}{\mathrm{d}t} = -\frac{\eta+\nu}{2}\int\boldsymbol{\omega}\cdot\boldsymbol{j}\,\mathrm{d}V, \quad (1.157)$$

$$\frac{\mathrm{d}H_m}{\mathrm{d}t} = -\eta\int\boldsymbol{j}\cdot\boldsymbol{b}\,\mathrm{d}V, \quad (1.158)$$

$$\frac{\mathrm{d}A}{\mathrm{d}t} = -\eta\int b^2\,\mathrm{d}S, \quad (1.159)$$

shows that the integrands of Eqs. (1.156) and (1.159) are always negative while those of Eqs. (1.157) and (1.158) can be positive or negative. Biskamp (1993, pp. 186–187) uses order of magnitude arguments to compare the decay rates but Ting et al. (1986) argue that there is no absolute guarantee that any one rate should exceed another. Various situations have been identified from the evidence of numerical simulations, however. If the cross helicity is zero then the total energy appears to decay more quickly than the magnetic helicity in 3D and the mean-square potential in 2D — these latter quantities can be taken to be approximately constant in their respective situations and a variational principle be applied to minimise the energy given the constancy of the appropriate quantity. This, then, is the situation termed "selective decay" (Fyfe and Montgomery, 1976; Matthaeus and Montgomery, 1980; Ting et al., 1986; Biskamp and Welter, 1989; Stribling and Matthaeus,

1991). For non-zero cross helicity, the case of the total energy decaying with respect to the cross helicity is termed "dynamic alignment"[10], so-called because a state of minimal energy is achieved ($|E| = 2|H_c| = 2A$), which corresponds to $\boldsymbol{v} = \pm\boldsymbol{b}$ — an Alfvénic state with equipartition of kinetic and magnetic energy[11] (Pouquet and Patterson, 1978; Grappin et al., 1982; Pouquet et al., 1986; Ting et al., 1986; Stribling and Matthaeus, 1991). Most of these simulations have been performed with one of the rugged invariants set to zero, usually the cross helicity for the selective decay situation, and the magnetic helicity or mean-square potential for dynamic alignment. Amongst this miasma of numerical results three seminal papers are those of Ting et al. (1986) for 2D decaying MHD turbulence and Stribling and Matthaeus (1990, 1991) for 3D decaying MHD turbulence, which consider the effects of having all three rugged invariants present simultaneously. Ting et al. (1986) identified four classes of behaviour in 2D. If $H_c \simeq 0$ and $E_v \leq E_m$ then a situation of minimum energy consistent with an approximately constant mean-square potential is reached, analagous to the Taylor state of fusion experiments (Sect. 7.8). The case $E_v \gg E_m$ gives Navier-Stokes-like behaviour in which the magnetic field lines behave as passive scalars carried by the flow. Starting with large H_c leads to dynamic alignment as might have been expected from previous experiments, but this time it is still achieved even in the presence of non-zero A. Finally, a fourth type of erratic behaviour is found when $H_c \simeq 0$ but E_m and E_v are significant, with the final state being highly dependent on the specific initial conditions used. In 3D, Stribling and Matthaeus (1991) also found four types of behaviour. Starting with $H_c = 0$ and $H_m \neq 0$ leads to selective decay while $H_m = 0$ and $H_c \neq 0$ leads to dynamic alignment, as might be expected. Having both H_c and H_m non-zero, however, leads to a situation in which both selective decay and dynamic alignment occur simultaneously, while having both helicities initially zero leads to neither process operating — rather a pure direct cascade of total energy instead occurs. These results are further supported by the equilibrium statistical mechanical arguments of Stribling and Matthaeus (1990).

The driven situation differs from the decaying in that energy and helicity are being continuously supplied to the system — selective decay, the principle on which all the decay results are based, no longer applies. Rather than use variational principles to explain numerical results, the approach of equilibrium statistical mechanics is used to indicate cascade directions. While for unforced turbulence the magnetic helicity, say, can accumulate at large scales relative to the energy it is nevertheless decaying. In the driven situation, however, a steady state can be achieved as a result of the re-supplying of dissipated energy and helicity. Again the qualitative behaviour depends on the velocity/magnetic field correlation — if $H_c = 0$ an inverse cascade of mean-square potential or magnetic helicity proceeds alongside a direct cascade of total energy (Frisch et al., 1975; Pouquet et al., 1976; Fyfe et al., 1977a; Fyfe et al., 1977b; Pouquet, 1978). The inverse cascade inevitably carries some associated magnetic energy: this is most easily seen in 2D where $\boldsymbol{b} = \nabla \times (a(x,y)\hat{z})$

[10] This has also arisen as a result of "selective decay" but has been given a different name due to its association with Alfvén wave propagation.

[11] These effects are just those of the "Alfvén effect" (Kraichnan, 1965; Pouquet et al., 1976; Fyfe et al., 1977b; Moffatt, 1978).

leads to the relation $b^2 = |\nabla a|^2$, so that the magnetic energy spectrum, E_k^M, is related to the mean-square potential spectrum A_k by $E_k^M = k^2 A_k$. For $H_c \neq 0$, the dynamic alignment situation arises with $\boldsymbol{v}$ and $\boldsymbol{b}$ highly correlated (Ghosh et al., 1988), but now with power spectra quite different from Kraichnan's. Biskamp (1993, p206) summarises the results of Grappin et al. (1983) who wrote the fluctuation spectra as

$$E^{\pm} = \int E_k^{\pm} \mathrm{d}k = \frac{1}{2} |\boldsymbol{z}^{\pm}|^2 \mathrm{d}V. \tag{1.160}$$

The spectra derived are

$$E_k^{\pm} \simeq \nu c_{a0} \left(\frac{k}{k_{\mathrm{diss}}} \right)^{-m_{\pm}}, \tag{1.161}$$

where $m_+ + m_- = 3, \varepsilon_+/\varepsilon_- \simeq m_+/m_-$, the energy injection rates are given by $\varepsilon_{\pm} = 2\nu \int_{k_{\mathrm{inj}}}^{k^{\pm}} k^2 E_k^{\pm} \mathrm{d}k$ and the values of $m_{\pm}$ depend on the level of correlation in the system. The Kraichnan spectrum can be recovered for uncorrelated forcing since $\boldsymbol{v} \cdot \boldsymbol{b} = (|\boldsymbol{z}^+|^2 - |\boldsymbol{z}^-|^2)/4$, whence $E_k^+ = E_k^-, \varepsilon^+ = \varepsilon^-$ and $m_+ = m_- = 3/2$. Ghosh et al. (1988) also observed the growth of correlation to the maximal state where $H_c = \pm 2E_t$ and noted that in this case the nonlinear terms of the MHD equations are zero, so that turbulent processes become suppressed.

In conclusion, there are roughly four categories of behaviour for MHD turbulent cascades. For a decaying system with no cross helicity selective decay occurs, with a direct cascade of total energy being accompanied by a mild inverse cascade of either mean-square potential in 2D or magnetic helicity in 3D; for a decaying system with appreciable cross helicity an Alfvénic state is approached; for a driven system with no cross helicity a direct cascade of total energy is again accompanied by an inverse cascade of the appropriate quantity, this time leading to a sizeable dynamo effect; and finally, for a driven system with appreciable cross helicity the cross helicity maximises and power laws other than Kraichnan's are obtained.

1.3.6 Large-scale background magnetic field

It has already been noted that in the presence of a uniform background magnetic field the magnetic helicity is no longer a rugged invariant; rather, a total magnetic helicity, $\hat{H}_m = H_m + 2\boldsymbol{b}_0 \cdot \boldsymbol{a}_0$ where $\nabla \times \boldsymbol{a}_0 = \boldsymbol{0} \neq \boldsymbol{b}_0$, is now conserved for periodic boundary conditions (Stribling et al., 1994). Intuitively it is expected that the presence of a large magnetic field will impose a preferred direction on plasma motions and it has been found to be so from direct numerical simulations in 2D (Shebalin et al., 1983) and 3D (Oughton et al., 1994). Montgomery and Turner (1981) used a perturbation approach to show analytically that for a sufficiently strong field the magnetofluid behaviour decomposes into that of 2D MHD in planes perpendicular to the background magnetic field along with Alfvén waves propagating along the background field. Montgomery and Turner (1982) then showed that it may be possible to have simultaneous inverse cascades of both mean-square potential and magnetic helicity, though their results should perhaps be modified in the light

of Stribling et al. (1994) for magnetic helicity and Hossain et al. (1985), who state that mean-square potential is no longer a rugged invariant.

Hossain et al. (1985) numerically showed that for 2D MHD threaded with a uniform background magnetic field the excitation of the inverse cascade of magnetic energy proceeds at a lower rate than would be the case without the background field, a conclusion supported by Cattaneo and Vainshtein (1991) in 2D. Oughton et al. (1994) found a similar suppression of turbulence in 3D.

Some work has also been done in deriving the equations of reduced MHD, in which the plasma motions and field perturbations are confined to be two-dimensional, while Alfvén waves may propagate along a strong background field (Strauss, 1976; Montgomery, 1982; Zank and Matthaeus, 1992).

1.4 Summary

The problem of fluid turbulence suffers from the fact that direct numerical simulations are unable to achieve sufficient resolution for many realistic applications due to the colossal demands on computer memory[12] (Rogallo and Moin, 1984). A compromise often used is to truncate the full system of cumulant equations in spectral space and apply various approximations to simplify further the solution process. However, the system of cumulant equations truncated in wavenumber space is known not to be equivalent to the original Navier-Stokes equations as many inviscid invariants of the latter are no longer conserved. On the positive side the energy and enstrophy transfer results appear to agree with limited numerical simulations and laboratory experiments.

Examinations of MHD turbulence are compounded by the fact that more variables are present so that it is even harder to produce realistic numerical solutions, and even the simplified EDQNM approximation requires much tedious manipulation of equations. Furthermore, the behaviour obtainable is more complex due to the interchange of energy, both between different scales and between the kinetic and magnetic forms. Present MHD turbulence models are far from accurately modelling astrophysical plasmas since they are based on incompressible fluid techniques, homogeneity assumptions (which require artificial random forcing throughout the volume rather than the expected transmission of energy through boundaries) and the often-used isotropy condition which breaks down in the presence of strong background fields. Ultimately turbulence theories should break away from the constraints of the Fourier representation, but in the meantime a promising approach is based on the equations of reduced MHD (Sect. 1.3.6) in Fourier space, which can incorporate the effects of anisotropy due to a strong background field while retaining isotropy in the plane perpendicular to the background field and can also allow eddy relaxation by Alfvén waves propagating along the background field. At present no MHD turbulence model seems to be capable of exhibiting all of these essential properties for astrophysical turbulent situations.

[12]The number of grid-points required scales as $Re^{9/4}$: solar coronal turbulence is expected for Reynolds numbers of order 10^{10}–10^{12}.

Chapter 2

The Sun

2.1 Introduction

Faced with the question, "What do you do for a living?" the solar researcher probably has an easier time explaining his or her profession than many other scientists. After all, the Sun is a body which can be experienced with the unaided senses and whose effects are apparent to everyone. More than that, we depend on the Sun for our very existence; the base of our food chain is the chemical energy which is photosynthesised from sunlight by plants; the heat of the Sun provides the temperatures under which the biochemistry of organic life can operate; moisture evaporates from the sea to form clouds under the influence of that same heat, and is later deposited as the rain which facilitates the growth of plant life. The absence of sunlight is known to have a detrimental effect on people to the extent of receiving the clinical designation Seasonal Affective Disorder, evidence for which is particularly apparent in Scandinavian towns north of the Arctic Circle where depression is more prevalent during the winter than in similar areas which receive diurnal sunlight.

These examples consider the effects of the Sun on the Earth under current circumstances, but it is worth considering how the Earth may be affected on a much longer time-scale. As our solar system orbits the galaxy it is expected that it will at some stage pass through the clouds of interstellar dust known to be present. In such a cloud the amount of heat and light reaching the Earth would be reduced with important consequences for life; in particular an Ice Age could be triggered, a taste of which was experienced during the Maunder minimum of 1645–1715 when solar activity fell to an unusually low level and when skating on the Thames became a common sight (Withbroe and Kalkofen, 1993). Conversely global warming might be due to an increase in the energy output of the Sun, as well as due to industrial pollution.

Just as with the natural world, many aspects of modern technology depend on various effects of the Sun. A familiar example is that of solar power — the direct conversion of sunlight to electrical power in the photo-voltaic cell. Less well known is the use of ground transmitters to direct

electromagnetic waves at the ionosphere which acts as a reflector to particular wavelengths, allowing local broadcasting of television and radio signals. However, there are also ways in which the Sun interferes with technology. The advent of electricity provided a standard of living which is taken for granted by those who enjoy it and is coveted by the developing world. Generation has become centralised in large power stations which feed electricity to outlying substations by a network of power cables, sometimes stretching for thousands of kilometres. Canada's distribution was severely disrupted in 1989 due to a coronal mass ejection (C.M.E.), associated with a solar flare (Gosling, 1992, 1993), which had ejected plasma towards the Earth. The Earth's magnetic field deformed when the plasma reached its vicinity. Combined with the long conducting power cables this provided the perfect recipe for the generation of electric current and caused a surge to flow along the cables, which then damaged power transmission equipment and caused electricity blackouts on the eastern coasts of Canada and the United States. Power companies now have an interest in solar information bulletins provided by various observatories and can take preventive action following the observation of a significant solar outburst but prior to the arrival of the plasma at the Earth. The deformation of the Earth's magnetic field by approaching solar plasma also leads to disturbances in the ionosphere with poor reflection of ground-based transmissions leading to damped and distorted signals often called "poor reception". Even the communications satellite, which provides a more reliable means of global communication, can be damaged by solar plasma or find its orbit decaying due to increased friction with the heated plasma. Ironically this was evidenced in the case of the Solar Maximum Mission satellite which dropped to an orbit three miles lower as a result of the 1989 C.M.E.

Thus it can be seen that the Sun is a key influence in our daily lives. In a world where the occupants have the power to alter the climate and where the interactions of nature with technology introduce new perils it is obviously an advantage to gather information, and hopefully gain understanding, about the Sun. The two following sections summarise present-day knowledge about the Sun in general and the outer atmosphere, with which this thesis is concerned, in particular.

2.2 Solar Atmosphere

The Sun is usually classified into different regions characterised by their dominant physical processes which, in the case of the solar atmosphere, are identified from the absorption and emission lines of the electromagnetic spectrum. Such lines are due to the various ionisation states of atoms absorbing or emitting photons of light and have been measured in the laboratory; comparison with the solar spectrum then reveals the properties of the solar atmosphere. In particular, the plasma temperature can be obtained from the intensity of each line, and also from the very presence of particular lines since certain ionisation states only appear once the internal energy of each atom (measured by the temperature) becomes large enough for large-scale ionisation to occur. Furthermore, magnetic fields have been demonstrated to alter the spectral lines of certain atoms by splitting

them[1], this phenomenon being known as the Zeeman effect, so that the magnetic field in the solar atmosphere can be measured. Finally the Doppler shift of the spectral lines of moving objects to higher or lower ends of the spectrum gives an indication of the line-of-sight motion of the solar atmosphere.

The most readily apparent region in the solar atmosphere is the photosphere, so-called from its Greek root "light", which emits predominantly in visible light and obscures all other regions to the unaided eye. It is characterised by a temperature of around 6000 K and a density of 10^{23} m^{-3} (10^{17} cm^{-3}). The photosphere may thus be regarded as the "surface" of the Sun from the point of view of the visible spectrum. Structures which are visible at the photosphere are sunspots, which can be seen with the unaided eye on a projected image of the solar disk, and the variously-sized granules. Sunspots are a result of the solar magnetic field emerging from the dense interior; the field acts to suppress the convective rolls which carry heated plasma from the solar interior to the surface, so that there is a diminished supply of heat in comparison with regions lacking the intense fields of the sunspot (several thousand gauss), with the result that the sunspot region is cooler, and hence darker, than its surroundings (Kippenhahn, 1994, Chaps. 6,7). The phenomenon of granulation (Roudier and Muller, 1986), whereby the photosphere appears to be composed of tiles of width 1400 km (granules) when viewed in white light, also involves convection. These tiles comprise packets of rising and sinking plasma which typically last for 10–15 minutes and have vertical velocities of order 1 km s^{-1}. Supergranules, on the other hand, result from the larger convective rolls occurring deeper within the Sun, and are predominantly horizontal flows of size 30,000 km, speed 0.5 km s^{-1} and duration of about a day. Unlike the smaller granules, which can be seen because of the temperature differences between granules, supergranules cannot be seen in white light because neighbouring supergranules are close in temperature — instead it is through the Doppler-shifted wavelengths of the moving material that these large cells are seen. In between these two extremes exist cells at all scales, the medium-sized of which are termed meso-granules of size, approximate speed and duration 5000–10000 km, 60 ms^{-1} and 2 hours, respectively.

Travelling outward, the density continues to decrease with the temperature following suit until the latter reaches around 4000 K, the temperature minimum. Beyond this point is the chromosphere[2], named from the Greek word for "colour" because during an eclipse photospheric light is observed to scatter from this region. A notable feature of this scattering is that prior to the eclipse the solar spectrum is that of an absorption spectrum, in which dark lines indicate that elements in the solar atmosphere are absorbing the light emitted from lower down in the Sun, but as the eclipse proceeds the spectrum dims until at totality, when the moon covers the Sun, there is a reversal to the situation of bright emission lines against a dark spectrum, when the coronal plasma is being seen (Kippenhahn, 1994, p64). Surprisingly, the temperature starts to rise slowly through the

[1] Magnesium is particularly susceptible, hence its name.

[2] Proctor (1899, p301) no doubt with a classical education somewhat superior to that of today's scientists, abhorred this term preferring the more accurate "chromatosphere" instead. Despite this, chromosphere seems to have become ensconced in the solar vernacular.

chromosphere against the density's continuing decline, until in the transition region a rapid increase takes place with the temperature reaching up to 3–6 $\times 10^6$ K in the corona (Hara et al., 1992)).

We come now to the other part of the solar atmosphere visible to the unaided eye, and then only at times of eclipse. Providentially, our moon on occasion has an apparent diameter slightly greater than that of the Sun so that on the occasions when the two are aligned as seen from a particular location on Earth, the photospheric floodlight is obscured, thus enabling the corona[3], named from the Latin for crown, to be seen. Perhaps halo would be a better description for this richly structured glow, the visible extent of which is comparable to the Sun's surface area — it is a region of surprisingly high temperature, of the order of millions of kelvins, and densities typically of order 10^{15} m^{-3} at the coronal base and 10^7 m^{-3} at the Earth's orbit so that a hypothetical hand placed in coronal material would feel little pain due to the low thermal energy content (it would feel plenty from the radiation output near the Sun, however!). Vaiana and Rosner (1978) provide a readable, although dated, description of the corona from both observational and theoretical approaches while an extensive account of the solar atmosphere may be found in Priest (1982, Chap. 1).

2.3 Solar Interior

Unlike the surface and atmosphere of the Sun, the interior regions are hidden from view. Identification of the conditions therein depends on the application of knowledge about physical processes, derived from laboratory experiments, to create models which match the conditions at the solar surface; such models can then be extrapolated to predict the conditions within the Sun.

Considering the Sun to be a vast accumulation of matter, Newton's law of gravitation indicates that just as a submersible experiences greater pressure as it moves deeper in the ocean so the pressure within the Sun will increase under the weight of overlying material as the centre is approached. Eddington (1920) first theorised that under such great pressures the core of the Sun would provide suitable conditions for the fusion of the hydrogen known from spectroscopic analysis to be present in the Sun[4]; the liberation of vast amounts of nuclear energy then enhances the internal energy of the core and atoms gain sufficient energy to become almost entirely ionised. Photons, which mostly interact with atoms by giving up their energy to raise an electron to a higher energy level[5], cannot then interact with these atoms, but instead radiate out from the core with little impedance. The region in which this mechanism predominates is designated the radiation zone. Further from the core the Sun is expected to be cooler so that atoms will not be so strongly ionised; photons can now be absorbed and re-emitted by the ions, leading to the plasma becoming increasingly opaque to the photons being released in the core. Increasingly, the plasma absorbs the

[3]Note that the absence of the suffix "sphere" suggests the lack of the spherical symmetry which is apparent in the layers so far discussed.

[4]Prior to this Helmholtz had supposed that the Sun was powered by the energy released during its gravitational collapse; Kelvin concluded from this model that the Sun would then be twenty million years old.

[5]Direct interaction with the nucleus is also possible, but far less probable.

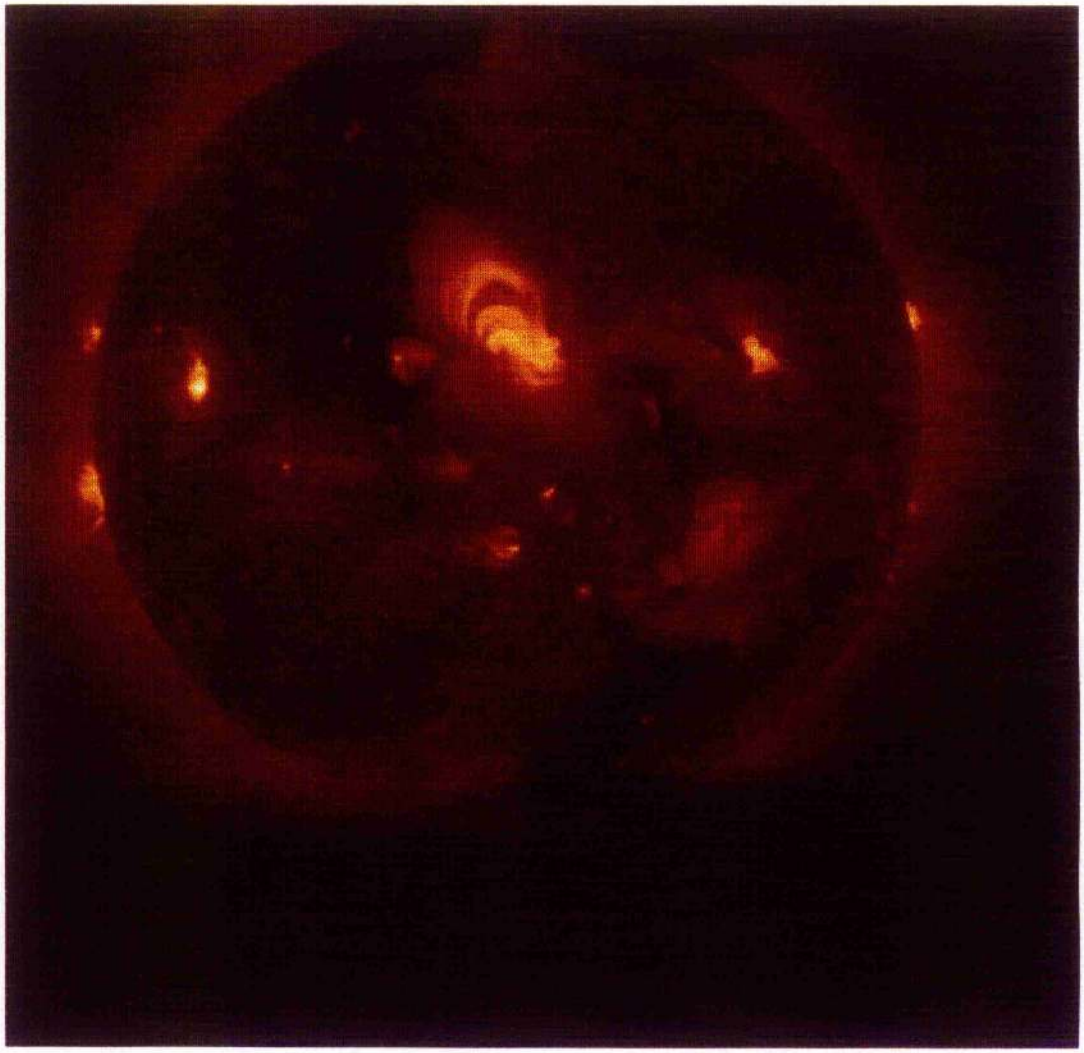

Figure 2.1: Yohkoh Soft X-ray Telescope image of the corona from the Yohkoh mission of ISAS, Japan. The X-ray telescope was constructed by the Lockheed Palo Alto Research Laboratory, the National Astronomical Observatory of Japan, and the University of Tokyo with the support of NASA and ISAS. This particular image was taken at 03:00 UT on 14/11/94. The colour scale has been adjusted to minimise contrast.

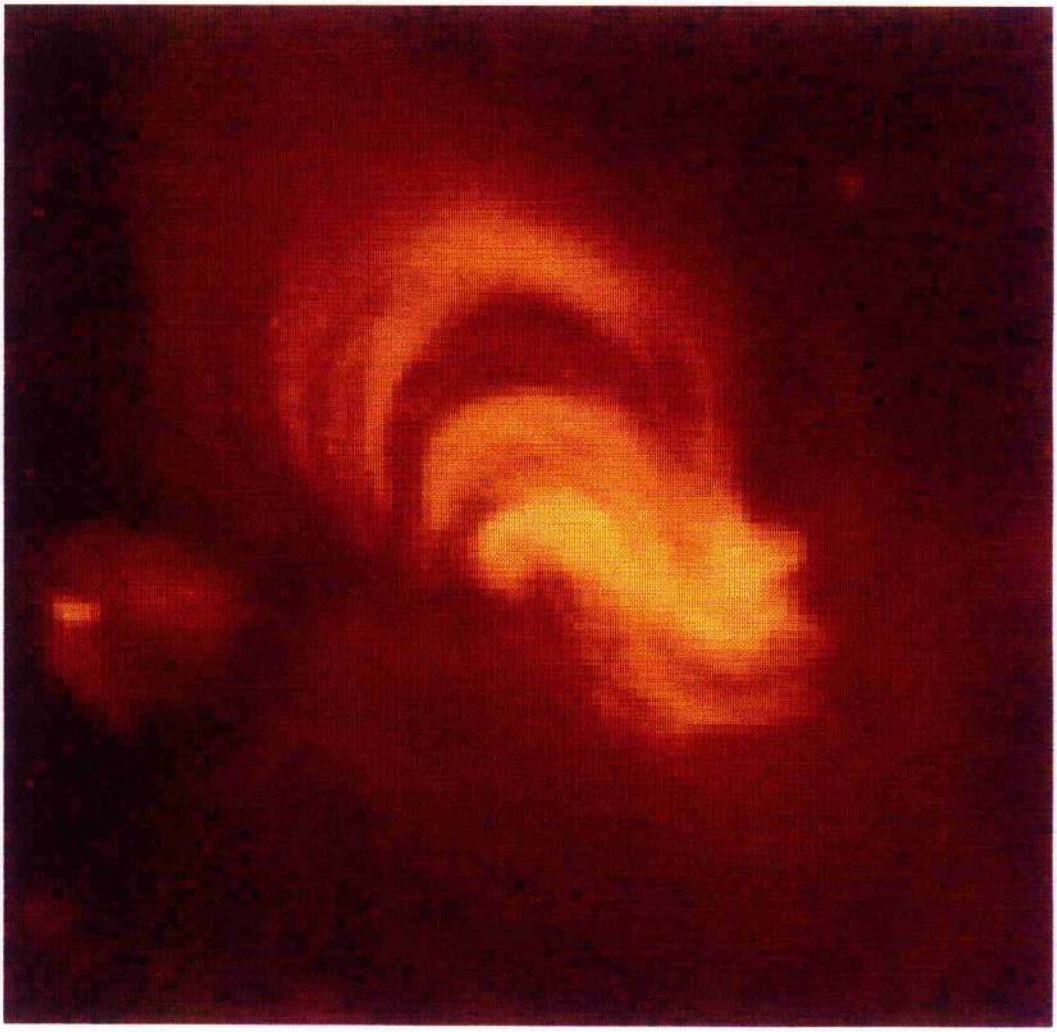

Figure 2.2: Magnification of the main active region of Fig. 2.1.

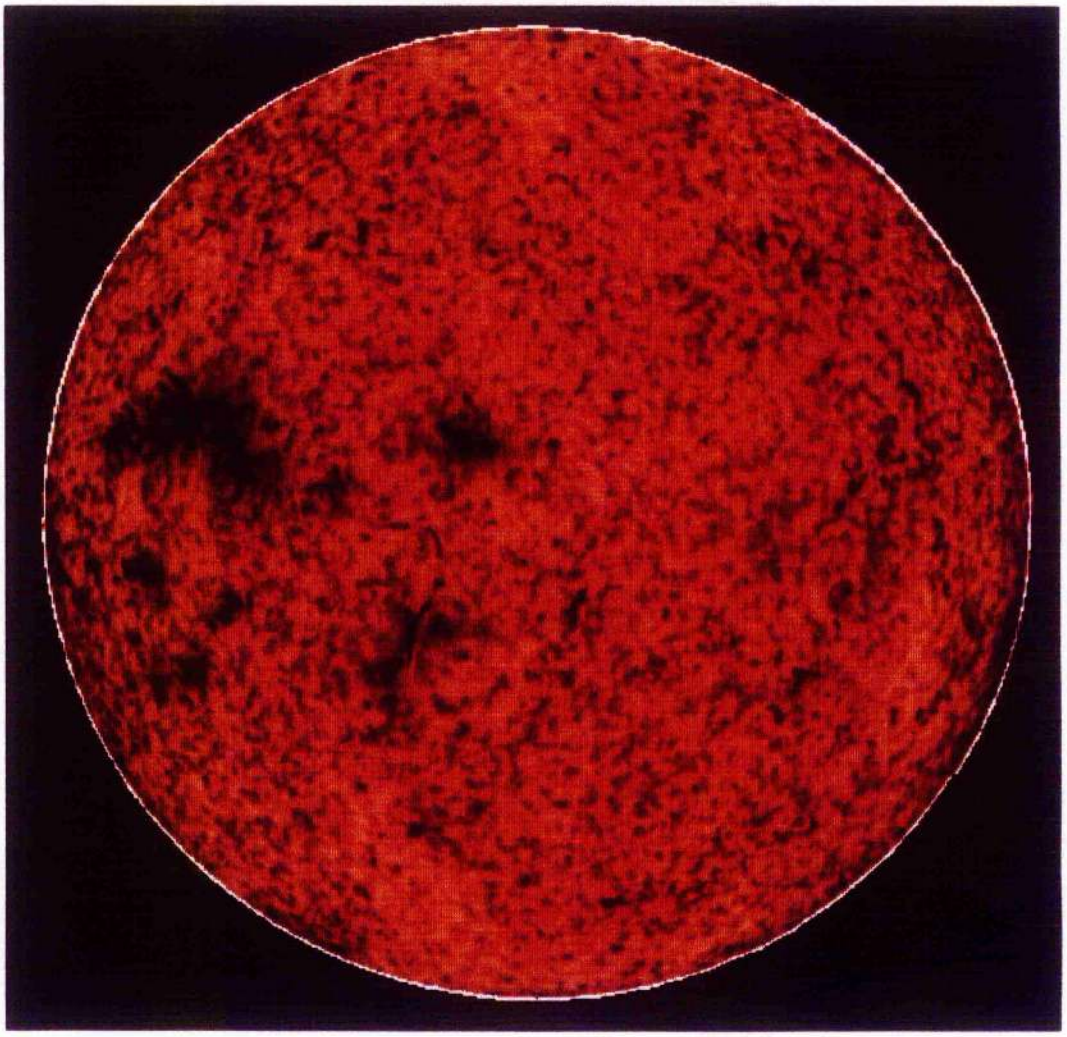

Figure 2.3: He 10830 Å image taken at the U.S. National Solar Observatory at Kitt Peak, Arizona at 18:06 UT on 10/11/94.

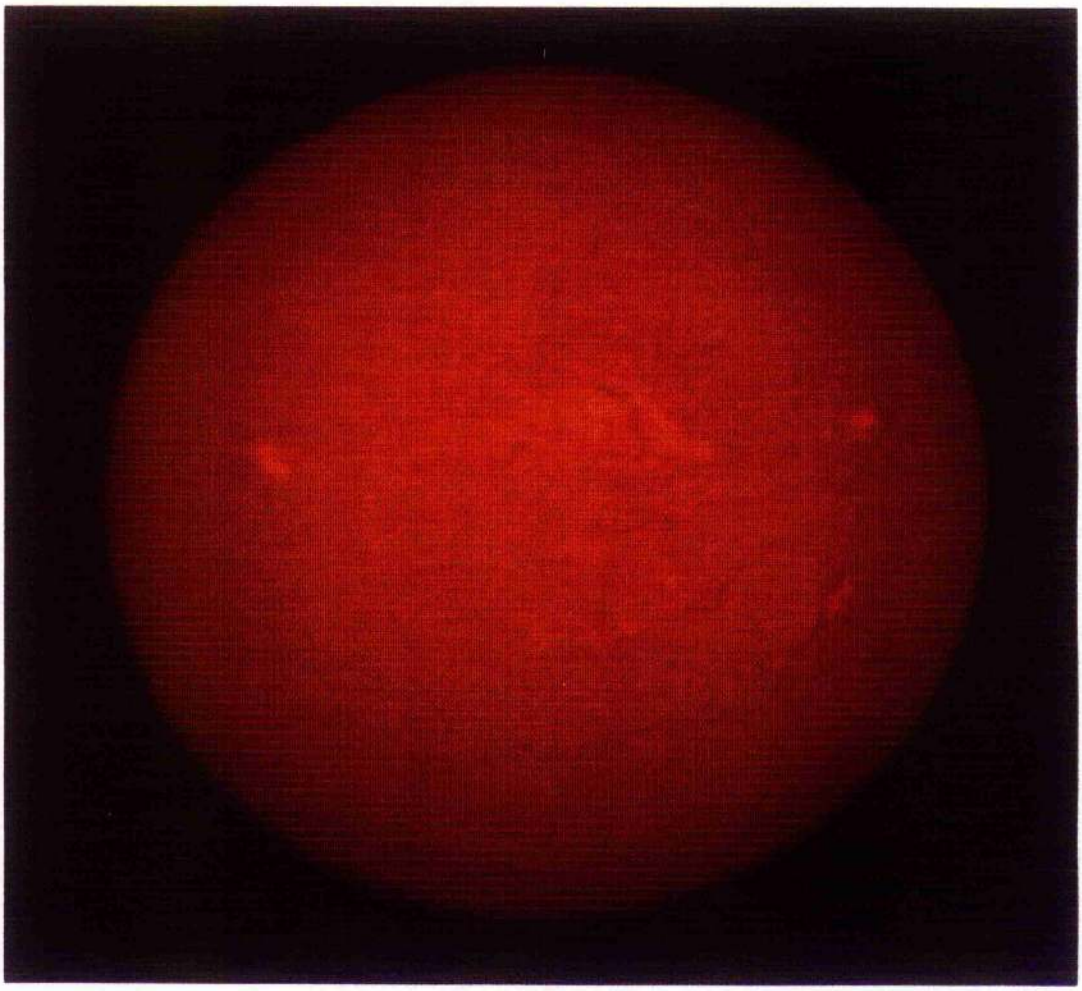

Figure 2.4: Hydrogen-α image taken at Holloman Air Force Base, New Mexico at 20:24 UT on 14/11/94.

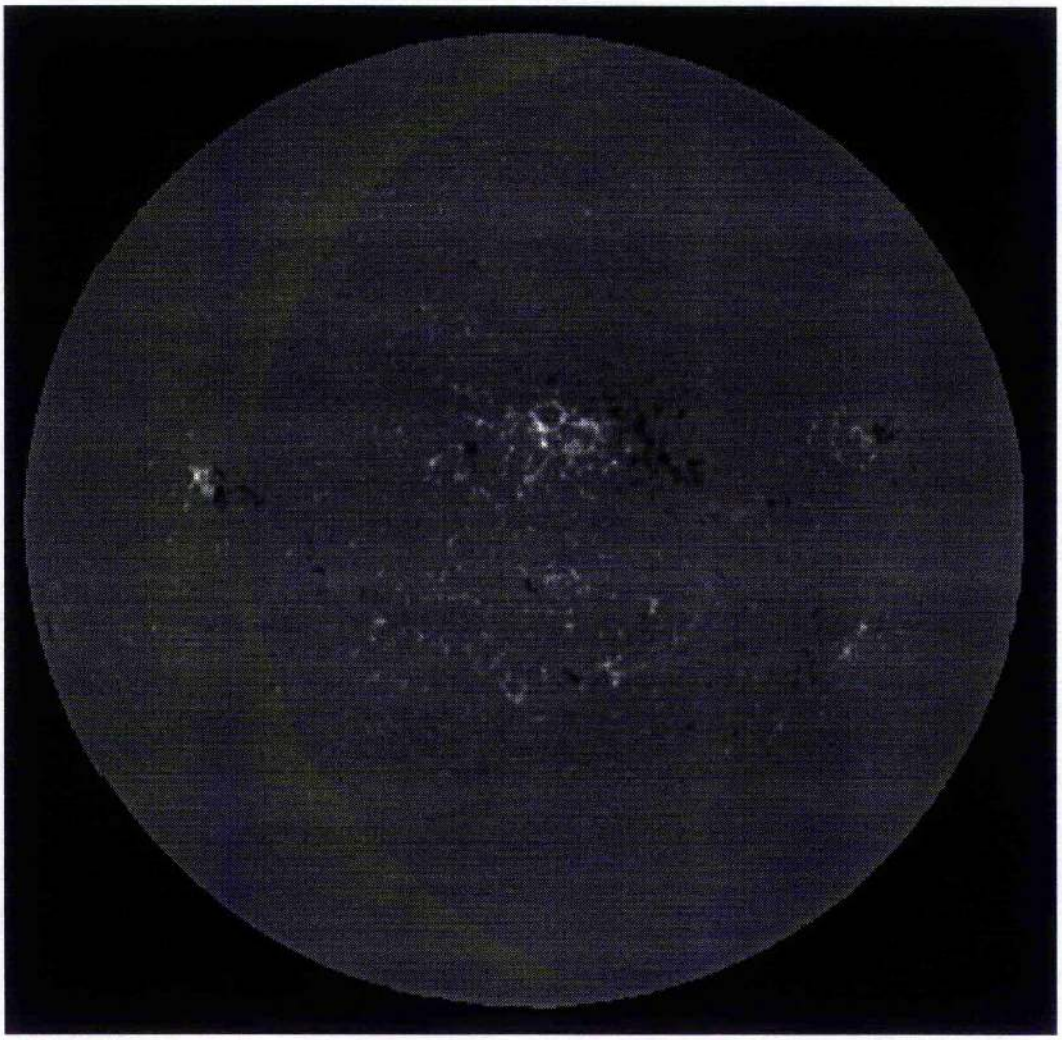

Figure 2.5: Magnetogram image taken at Kitt Peak at 17:58 UT on 14/11/94.

energy radiated from the core and, being hotter than the regions of the Sun still further out, it must rely on other mechanisms for transferring the energy outward. Neglecting gravity, conduction would seem the obvious candidate but with its inclusion buoyancy effects become important — an element of plasma expands upon heating so that its density is lower than that of its surroundings, whereupon it rises to the "surface" of the Sun, cools, contracts and starts to descend; meanwhile other plasma has flowed in to fill the void, thus creating convective motions which are akin to those in a pot of broth being heated on a stove (Priest, 1982, pp. 15–17).

Models employing the above principles can be constructed to permit quantitative predictions to be made. The simplest polytropic laws, where the pressure varies as some power of the density, neglect the varying state of ionisation, whereas the MHD equation of state, the acronym indicating the authors Mihalas, Hummer and Däppen (Mihalas et al., 1988), considers these variations in detail. A standard solar model may be created by calibrating the initial helium abundance and the efficiency of convection at mixing the plasma in the model to obtain the measured luminosity (3.8×10^{26} W) and radius of the Sun (6.96×10^{8} m). Here "standard" refers to the calibration, rather than to a particular universally accepted model (Bahcall and Cribier, 1990; Ulrich and Cox, 1991). Roxburgh (1985) gives the following conditions for a standard model:

1. The Sun is spherically symmetric and in hydrostatic equilibrium.
2. Energy is transported by radiative transport, except in regions which are convectively unstable.
3. The energy of the Sun is produced by nuclear reactions converting hydrogen to helium.
4. The Sun is in thermal equilibrium, except for small changes in entropy due to a slow change in pressure, density and temperature during evolution.
5. The chemical evolution is due to the nuclear reactions from the proton-proton chain and the carbon-nitrogen cycle.
6. Matter is unmixed, except in regions that are convectively unstable.
7. The Sun was initially homogeneous and has evolved without mass loss to have the present luminosity, $L_{\odot}$, and radius, $R_{\odot}$.

Most of the information we have about the solar interior results from measurements of the neutrino flux emerging from the Sun and from helioseismology.

The neutrino is a fundamental particle whose presence may be regarded as a characteristic signature of nuclear interactions. The electron neutrino (there are two other types, namely the muon neutrino and tauon neutrino) is involved in the reactions of the proton-proton cycle of low atomic number particles present in the Sun. The key characteristic of the neutrino is its ability to travel through matter with very little interaction, so that neutrinos flow from the Sun's core and through the Earth with little hindrance. Currently several experiments are recording the neutrino

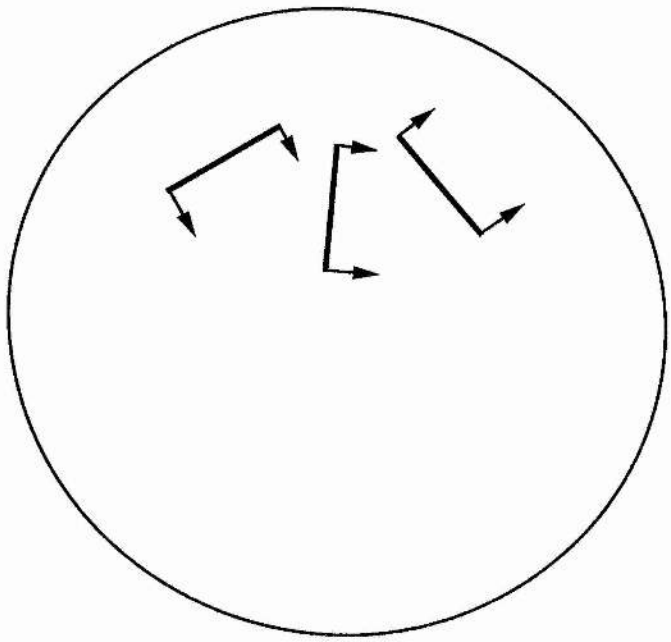

Figure 2.6: Refraction of a sound wave within the Sun as a result of the increasing temperature, and hence sound speed, as the centre is approached.

flux. One is a tank of industrial cleaning fluid, basically chlorine 37, embedded in a disused mine in South Dakota; the neutrinos occasionally interact with the chlorine to produce argon, which is then detected. The Kamiokande experiment, on the other hand, observes Cerenkov radiation (a blue flash produced when a particle travels faster than the speed of light in the surrounding medium) in pure water. Both of these experiments detect the neutrinos from the boron reactions which have energy 10 MeV, believed to be less prevalent than the neutrinos arising from the proton-proton reaction: unfortunately the latter also have lower energy (0.1 MeV) and so are much harder to track down. As it is, less than one neutrino is detected per day, on average, out of the billions believed to pass through the apparatus every second, but the very fact that neutrinos are found at levels of the order of magnitude of those predicted by nuclear physics indicates that fusion reactions are occurring in the Sun, confirming Eddington's hypothesis. This field of research is far from being concluded, however, as the observed rate of detection is only about one-half to one-third of that expected from atomic theory. Details of these experiments and results may be found in Davis et al. (1990), Nakahata and the Kamiokande II Collaboration (1990) and Davis and Cox (1991).

An important discovery in 1960 (Leighton et al., 1962) was that the surface of the Sun is "ringing"; that is, spectroscopy revealed red and blue-shifted wavelengths across the entire solar surface indicating that standing waves are present (see, for example, Duvall et al. (1988) for a modern set of data). Further studies (Mein, 1966; Frazier, 1968) showed these waves to be evanescent in the solar atmosphere and that the wave power is contained in particular modes (Deubner, 1975),

consistent with the hypothesis of sound waves being trapped within the Sun (Ulrich, 1970; Leibacher and Stein, 1971) and interfering with each other at appropriate frequencies to produce standing waves. The present understanding is that of waves whose restoring forces are those of gas pressure in the case of the so-called p-mode, and gravity in the gravity wave (g-mode) . The p-mode is easier to illustrate (Fig. 2.6): for a large pressure wavefront propagating within the Sun it is expected that each end will be at different depths within the Sun, with consequently different temperatures. Since the speed of sound increases with temperature, the end of the wavefront nearer the centre will travel faster than that nearer the surface, resulting in a pivoting motion known as refraction. Eventually the wave is turned to propagate back toward the surface where the rapid drop in density provides an upper reflective boundary; for appropriate wavenumbers the standing wave can be detected as the rising and falling of surface anti-nodes. A particular mode is characterised by the number of nodal lines crossing the equator, m, the total number of nodal lines, l (i.e. m lines of longitude and $l-m$ of latitude), while n characterises the number of radial modes. For a perfectly symmetrical, non-rotating star the number of nodes intersecting any great circle[6] would be the same, making the use of both l and m unnecessary as just one would suffice. However, this is precisely where the advantages of helioseismology arise — the observed differences, of the order of nano-seconds for milli-second frequencies (Libbrecht and Woodard, 1990), between the values of the frequency corresponding to each combination of l, m and n, and some m-independent frequency (usually averaged over all values of m or evaluated at m=0) provides data with which to examine the effects of p-mode oscillations and so test models of the solar interior. The use of other averaging techniques enables different effects to be probed — the g-mode deep within the radiation zone of the Sun, for example.

The principal triumph of helioseismology has been in determining the rotation of the solar interior. It has been known that the solar surface rotates at different rates depending on latitude, the equator undergoing a complete revolution in about 25 days while the poles take around 34 days[7]. However, investigations into other aspects of the interior have been less clear-cut in the agreement between data and theory, the frequency splitting due to an internal magnetic field being a case in point[8].

Having given a summary of the means by which data is acquired and models of the solar interior are constructed, and with the caveat that the conclusions drawn are of a less reliable nature than those for the solar atmosphere, some quantitative results can now be given: the core is believed to have a temperature of around 10^7 K and a density of 10^5 kg m^{-3} (100 g cm^{-3}).

[6] A great circle is one which divides a sphere into two equal halves.

[7] The unseen internal rotation is a key factor in solar dynamo modelling.

[8] Some analysis has suggested the existence of a mega-gauss field at the base of the convection zone (Dziembowski and Goode, 1990).

2.4 Coronal Heating

The high temperature of the corona, its sparsity and rich structure were described in Sect. 2.2. Another property of the corona which further motivates the study of coronal heating is its dynamic nature; far from being everywhere a static plasma cloud confined to lie within a few solar radii of the Sun, the corona accommodates an outward flow of plasma reaching to the periphery of the solar system and beyond, the densest and hence most visible region of which is closest to the Sun. This expansion was first theorised by Parker (1958), who noted that the outward pressure of an unmagnetised plasma would not be sufficiently opposed by gravitational forces to permit a static equilibrium, and has since been confirmed by satellites which measure the properties of this solar wind[9] in situ. With the wind carrying both thermal and magnetic energy, and further depletion arising as a result of X-ray emission (Parker, 1987b) and the drain of cool coronal material down to the photosphere along magnetic arcades, not to mention the obvious electromagnetic emissions, the inevitable question arises of what maintains the corona's high temperature. Withbroe and Noyes (1977) have collected estimates for the energy requirements of various coronal features in the form of a power density. They give the loss rate of the quiet, largely non-magnetic areas of the Sun as 300 $\mathrm{Wm^{-2}}$ (3×10^5 erg $\mathrm{cm^{-2}s^{-1}}$), that of a coronal hole as 800 $\mathrm{Wm^{-2}}$ (8×10^5 erg $\mathrm{cm^{-2}s^{-1}}$) and an active region as 10^4 $\mathrm{Wm^{-2}}$ (10^7 erg $\mathrm{cm^{-2}s^{-1}}$). These figures may be compared with the entire energy emission (luminosity) averaged over the whole solar surface of 6×10^7 $\mathrm{Wm^{-2}}$ (6×10^{10} erg $\mathrm{cm^{-2}s^{-1}}$).

Initial theoretical investigations focused on the ability of sound waves to dissipate their energy while travelling through the corona. It is well known that a nonlinear wave has differing speeds of propagation for crests and troughs, with the result that crests can catch up with troughs and steepen into shock waves which propagate with speeds in excess of the plasma sound speed. An immediate consequence of this is that the surrounding medium has insufficient time to adapt to the sudden change in pressure associated with the wave. Shock waves have been considered in the context of coronal heating because the large plasma velocity gradients, which arise in the presence of shocks, are particularly prone to viscous damping when compared with sub-sonic waves. During the late seventies studies of the chromosphere and transition region using ultra-violet spectrometers on the OSO-8 satellite addressed the question of whether sound waves actually propagate from the photosphere into the corona. The findings of the various authors broadly agree that these waves are present within the chromosphere and transition region, but that the maximum power density carried by the waves is at most 10 $\mathrm{Wm^{-2}}$ (10^4 erg $\mathrm{cm^{-2}s^{-1}}$) (Athay and White, 1978, 1979a, 1979b; Bruner, 1978; White and Athay, 1979a, 1979b). However, this energy does not necessarily serve to heat the corona, as shown in a further paper by Bruner (1981) who found that sound waves appear to propagate both inwardly and outwardly through the chromosphere and transition region

[9] General reviews of the theory of the solar wind may be found in Holzer (1979) and Marsch (1994), and some data obtained by Voyager in Matthaeus and Goldstein (1982, Table 1).

in roughly equal proportions, further reducing the estimated maximum power transmitted to the corona to 0.3 Wm^{-2} (300 erg $cm^{-2}s^{-1}$).

While ultra-violet observations were deprecating sound waves as the primary mechanism of coronal heating, X-ray observations were focusing attention on the rôle of the solar magnetic field. As with ultra-violet observations, satellites or rockets must be used to observe at X-ray wavelengths, which are filtered out by the Earth's atmosphere and ionosphere before reaching the surface. The early seventies saw the launch of the American Skylab, whose mission specification included a programme of solar observation, providing better continuity of observation than that obtained with the shorter flights of rocket-based telescopes and a greater adaptability than unmanned satellites. When compared with magnetogram data, which measures the photospheric magnetic field, the X-ray data identified a visual correlation between the high temperature (3–6 $\times 10^6$ K) active regions of the corona and the sites of emerging magnetic flux (Vaiana et al., 1973); subsequently Golub et al. (1980) published a quantitative correlation between the two data sets once techniques and models for interpreting the X-ray data were better established[10]. This vindicated an earlier paper by Tucker (1973) who had considered the possibility of steady-state heating by the dissipation of magnetic energy and concluded that either very small scales must be present or an anomalous resistivity be involved. Rosner, Golub, Coppi and Vaiana (1978) came to the same conclusion and also found that the available magnetic energy exceeds that required to supply the coronal radiation losses. So within the space of a decade the paradigm of acoustic wave heating of the corona was superseded by a belief in heating which is magnetic in nature; but by what mechanism?

Theorists have proposed models for the various aspects of the photospheric/coronal interaction. For instance, the frozen flux theorem, also known as Alfvén's theorem, shows that in a perfectly conducting plasma the magnetic field lines will move with the plasma, and vice-versa (Priest, 1982, pp. 99–101). Magnetic field lines emerge through the photosphere in intense flux tubes, which appear as sunspots, and then spread throughout the corona. The "frozen-in" field lines are then carried by the convective motions of the photosphere, doing work on the magnetic field and transferring energy to the corona in the process (Van Hoven, 1993). For motions faster than the propagation speed of a transverse perturbation along a magnetic field line, known as an Alfvén wave, this energy injection is in the form of such waves, while for slower motions the magnetic field has time to adapt to the motions at its photospheric footpoints with the result that currents are driven from the photosphere into the corona as the structure evolves quasi-statically through a sequence of equilibria (Longcope and Sudan, 1992). The availability of energy for heating the corona having been demonstrated does not in itself guarantee that the energy will be converted into internal energy within the corona. For example, Alfvén waves may travel far from the Sun before there is any appreciable damping, with similar problems being apparent for the large currents flowing through the highly conducting corona. In general, the existence of large gradients acting over small scales is required in order that classical

[10]More recently the advent of the Normal Incidence X-ray Telescope (NIXT) (Golub et al., 1990) and Yohkoh (Ogawara et al., 1992) have provided even better data which are now being analysed (Golub et al., 1994).

viscous and resistive effects become non-negligible.

In the case of wave heating in the MHD context there are a limited number of wave-modes available; the Alfvén wave, which may propagate in both an incompressible and a compressible medium, and the fast and slow magneto-acoustic waves. The slow magneto-acoustic wave is essentially a sound wave which propagates in the direction of the magnetic field, while the fast wave is able to propagate in all directions, notably perpendicular to the magnetic field. The similarity of the slow wave to the sound wave suggests that it too will carry insufficient energy to heat the corona, while the fast wave was considered by Hollweg (1978) who argued that it is totally internally reflected at the transition between chromosphere and corona; Schwarz and Leroy (1982) also analysed the fast mode numerically and found little energy transmitted to the corona. Turning attention to the Alfvén wave then, two mechanisms have been suggested which generate gradients in the presence of inhomogeneities in the plasma: namely resonant absorption and phase mixing. Just as the interface between the sea and air has waves travelling along it, but with little propagation occurring in either the air above or water beneath, so the interface between regions of differing plasma density and magnetic field strength supports MHD waves. Magnetic field lines in the form of loops (Priest, 1978; Rosner, Tucker and Vaiana, 1978; Antiochos, 1994) passing through regions of varying density and field strength will experience a changing Alfvén speed. The footpoints of these field lines, meanwhile, are anchored in the highly conducting, dense photosphere and are subject to its motions, the more rapid of which launch Alfvén waves along the coronal loops. There will exist regions where the Alfvén frequency of the loop (comparable to the natural frequency of a guitar string) will match the excitation frequency at the photosphere and within which the Alfvén wave will resonate with the photospheric driver, producing a layer containing oscillations of considerably larger amplitude than those of the surrounding medium. Gradients will form which, it is hoped, will lead to viscous and resistive heating of the plasma within the resonance layer. This then is the principle of resonant absorption, but a specific surface wave and means of dissipation must be explicitly chosen in order to construct a coronal heating model. Ionson (1978) used ideal (inviscid and perfectly conducting) equations, with the consequence that MHD waves in this model cannot be dissipated by collisional processes. Kinetic theory, however, is not so constrained and allows a wave to give up its energy by accelerating plasma particles of appropriate velocity, a process called Landau damping; Ionson's model thus employs kinetic Alfvén waves for the surface waves, the surface itself being a sheath surrounding a flux tube. Remaining within the continuum framework Hollweg and Yang (1988) used the Braginskii (1965) viscosity tensor for a collisional plasma to calculate the damping of an MHD wave. The simpler case of resonant absorption in an incompressible plasma can also be modelled, as this time the Alfvén frequency and the position of the resonance layer depend only on the magnetic gradients, but no more will be said here about this less mathematically involved situation. See also Wentzel (1979), Goossens (1991) and Hollweg (1983, 1984a, 1984b, 1987).

Phase mixing is also concerned with the varying Alfvén speed within an inhomogeneous plasma but can be applied to open field lines, characteristically found in coronal holes. In this

case neighbouring Alfvén waves which are launched in phase will rapidly become out of phase as they travel through regions of differing density and magnetic field strength. This leads to gradients between the waves and the possibility of dissipation. Further details may be found in Heyvaerts and Priest (1983) and Cally (1991).

For slower motions of the field-line footpoints at the photosphere the field has sufficient time to adjust along a substantial portion of its length so that, instead of waves being excited, the changing magnetic field generates electric currents which flow through the conducting corona (Sakurai and Levine, 1981). It is argued that since the magnetic forces dominate pressure forces in the corona any magnetic structure, excepting prominences, must exist in a force-free state (that is the current density is parallel to the magnetic field, leading to there being no magnetic force) for there to be any possibility of equilibrium. Eventually resistive effects lead to the dissipation of such currents and the heating of the plasma, with regions of high current density experiencing greatest heating (Rosner, Golub, Coppi and Vaiana, 1978; Sturrock and Uchida, 1981): this again illustrates the necessity of gradients, for in MHD the current density is proportional to the curl of the magnetic field. In the simplest scenario two oppositely directed field lines are driven to approach one another by the motion of the surrounding plasma; the closer they approach, the larger the magnetic gradient and hence the stronger the current driven perpendicularly to both flow and field lines. Sooner or later resistivity prevents any further increase in current density as the gradients diffuse and the field lines cancel each other resulting in heating, a process called annihilation. In practice field lines are curved so that in any such encounter only a small portion of each field line will be involved in the interaction, with strong currents flowing in a very localised region, while the surroundings are less affected. Annihilation may be expected within this diffusion region, but there remains the question of what happens to the rest of the field lines. Apparently broken in the middle, they reconnect on each side of the diffusion region and are carried away by the tension forces along with the outflowing plasma into which they are frozen. Rather than the magnetic field simply cancelling, as in the annihilation situation, a change in the magnetic topology has also occurred, leading to a state of lower magnetic energy and heating of the plasma within the small diffusion region. The detailed dynamics within the diffusion region lie within the realm of kinetic theory; nevertheless, theories accounting for local heating of plasma, acceleration of plasma from reconnection events in the Earth's magnetospheric tail and solar flare theories have been based on the MHD description with a measure of credibility and success in achieving observed levels of localised coronal heating. Comprehensive reviews of the rôle of current sheets in coronal heating are given by Priest (1981, 1985, 1991), while articles on annihilation may be found in Clark (1964) and Phan and Sonnerup (1990), and on reconnection in Hones (1984), particularly Axford (1984) and Priest (1984). See also Parker (1993) for a discussion of the time-scales involved, but note that an alternative conclusion is that classical resistive effects can cause sufficient dissipation if a turbulent cascading process occurs, a scenario neglected by Parker.

The reconnection mechanism is regarded as a prime candidate in explaining solar flares.

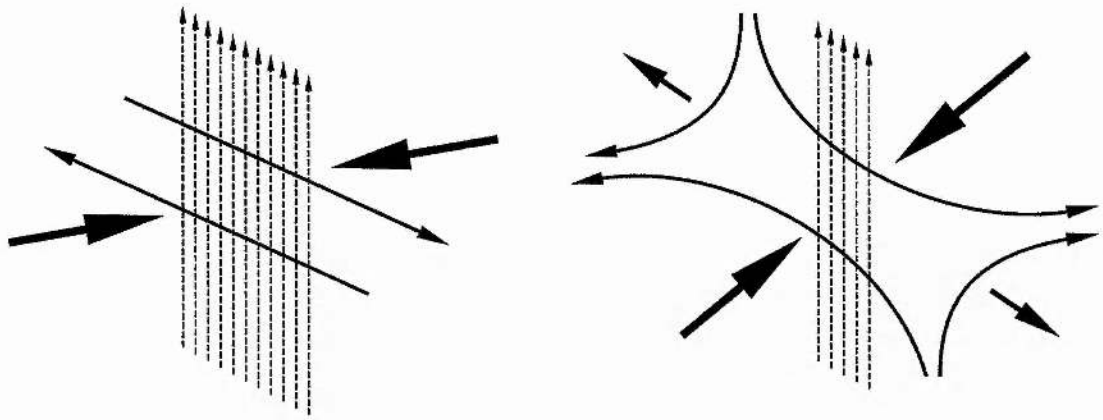

Figure 2.7: The photospheric flow (large arrows) drives oppositely directed field lines together, resulting in their mutual annihilation (left) or reconnection (right). In each case a large vertical current is generated.

It has already been said that one effect of moving the footpoints of equilibrium field structures is to store magnetic energy in the coronal field: several authors have also suggested that this motion leads to discontinuities in the field structure in the form of current sheets by causing flux sources to approach one another or by shearing arcade structures (Parker, 1972; Taylor, 1986; Parker, 1987a; van Ballegooijen, 1988; Vekstein et al., 1991; Vekstein and Priest, 1992). van Ballegooijen (1985), however, counters the argument of Parker (1972) by showing that invariance in the field along the loop is not required for equilibrium and that discontinuities in the field have their origin in a discontinuous photospheric driving flow. In any case, if current sheets form along the separatrices which demarcate the topologically distinct regions of the field (Low and Wolfson, 1988) or in any other way, all that is then required is an instability, perhaps the tearing mode, to trigger large-scale reconnection along the current sheets, leading to energy release. The largest flares release about 10^{25} J (10^{32} erg), but those of strengths 10^{20} J (10^{27} erg) and 10^{17} J (10^{24} erg) are frequently observed and are termed microflares and nanoflares respectively, the prefix indicating their energy content in relation to the largest flares. Lin et al. (1984) observed microflares in two active regions lasting up to several tens of seconds and occurring every six minutes on average, while Parker (1988) has suggested that nanoflares occurring with sufficient frequency would release sufficient energy to account for the coronal heating requirements. The detailed mechanisms of how current sheets are created and reconnect form an active area of solar research; one possibility is that flux emerging through the solar photosphere may impinge on existing arcades and lead to current sheets and reconnection (Heyvaerts et al., 1977); another is that an arcade may overlie a prominence which then erupts (Priest et al., 1989) and drags the arcade upwards and inwards, forming a current sheet in which reconnection occurs when the gradients become sufficiently large (Priest, 1992b). Further details of flares may be found in Priest (1981), particularly pp. 1–46 and 139–215, and

references therein. On the observational side, Cargill (1994) describes the possible interpretations of the spectral observations used in identifying flares, while Sturrock et al. (1984) describe the constituent phases of a solar flare.

In order to calculate how much energy is released in a dynamic reconnection model it is necessary to know the energy content of the relaxed state. Application of the calculus of variations shows that a potential field (zero current density) is the state with minimum magnetic energy. However, there may be further constraints which make the potential state unattainable; for example, the twist and connectedness of a flux tube is measured by the magnetic helicity, which is known to decay at a much slower rate than the magnetic energy and so may be taken to be an invariant of the structure (Matthaeus and Montgomery, 1980; Berger, 1984). The calculus of variations then indicates that the force-free state, already mentioned in the context of slow photospheric motions, is the state of minimum energy (Chandrasekhar and Woltjer, 1958; Woltjer, 1958). This principle of relaxation of a stressed magnetic structure to a force-free state has been applied by Heyvaerts and Priest (1984), Browning and Priest (1986), Vekstein (1987a) and Dixon et al. (1989) to the corona.

Thus far all the models described have been concerned with MHD flows which are well-prescribed and which lead to the build-up of large gradients in plasma velocity and/or magnetic field. However, it is well-known from hydrodynamic experiments that the very existence of large gradients leads to the flow becoming irregular as instabilities are triggered and turbulence develops (Lesieur, 1990, Chap. III) — indeed, observations show that power laws of emission against wavenumber, indicative of turbulent cascades, are a ubiquitous characteristic of the Sun (Martens and Gómez, 1992; Gómez et al., 1993a, 1993b), although the resolution of the instruments is insufficient to provide solid confirmation. The presence of cascades would have important implications for coronal heating models because, as has been described in Chap. 1, turbulent flows tend to break up large-scale structures into successively smaller eddies until eventually viscosity and resistivity become significant in dissipating the kinetic and magnetic energy, respectively. Hollweg (1984b) has suggested that this is triggered by the Kelvin-Helmholtz instability once the build-up of gradients can no longer be subdued by classical dissipation, while van Ballegooijen (1985, 1986) and Mikić et al. (1989) find that the random motions of the photospheric footpoints of coronal fields lead to the creation of fine scales in the magnetic field structure and strong electric currents. In a sense a turbulent flow is sucking energy from large scales to scales small enough for even minute differences in fields to lead to large gradients, as opposed to the large differences acting over larger scales required for non-turbulent models. In fact the amount of heating appears to be independent of the molecular viscosity and resistivity, changes in the value of which simply mean that the cascade proceeds to whatever scales are required to dissipate the cascading energy. Further evidence for solar turbulence comes from line-spectra which exhibit broadening of lines which cannot be attributed to thermal effects alone; unresolved motions are responsible, perhaps in the form of Alfvén waves or turbulent motions. Saba and Strong (1991) measure such broadenings as being over 60 km s^{-1} in excess of thermal line-broadening in a quiescent active region. This thesis addresses the effects of turbulence

Reference	Mechanism	Scaling
Sturrock and Uchida (1981)	Stochastic Magnetic Pumping	$B_c B_p L^{-2}$
Heyvaerts and Priest (1984)	Reconnection	B_p^2
van Ballegooijen (1986)	Cascade	$B_c^2 L^{-2}$
Parker (1988)	Nanoflares	$B_p^2 L^{-1}$
Hollweg (1990)	Turbulent cascade	L^{-1}

Table 2.1: Table 1 of Walijeski et al. (1992) giving scaling laws for the various coronal heating mechanisms. B_p is the photospheric magnetic field, B_c is the coronal magnetic field and L is the loop length.

on simple wave and current dissipation theories of coronal heating and concludes that its presence provides an explanation for how waves and currents may deposit their energy as heat in the corona.

The following articles and books provide a more extensive background to the whole subject of coronal heating: Kuperus et al. (1981), Priest (1982), Vekstein (1987a, 1987b), Gómez (1990), Hollweg (1990), Browning (1991), Priest and Hood (1991), Ulmschneider et al. (1991), Priest (1992a, 1993) and Zirker (1993). Finally, an interesting comparison of some of the above-mentioned models with soft X-ray data has been made by Walijeski et al. (1992) for the scaling laws in their Table 1 (Table 2.1 here); they found that none of these scaling laws adequately fit the data.

Chapter 3

Heyvaerts and Priest (1992)

3.1 Preliminaries

The title of this paper is "A self-consistent turbulent model for solar coronal heating" and it has substantial bearing on the content of this thesis, meriting the detailed narrative of this chapter. When discussing the physical assumptions and mathematical procedures some points will be explained in this chapter, while for other points requiring more detailed analysis or which have been modified in the course of this work the reader is referred to the appropriate section of the thesis. Before proceeding, however, the typographical errors of a mathematical nature appearing in Heyvaerts and Priest (1992) are enunciated in Table 3.1 to avoid confusion.

3.2 Behaviour at large scales

At observable scales the corona exhibits loop structures believed to consist of plasma confined by magnetic field. As already described in Chap. 2, the anchoring of such field-lines into moving, dense, photospheric plasma provides a means for stresses to be built up in the magnetic field, driving currents into the corona in the process. For motions much slower than the Alfvén speed, the arcade slowly evolves through a sequence of equilibria, driven by the photospheric flow, in which energy is continually supplied to the corona (Heyvaerts and Priest, 1984; Browning and Priest, 1986). It is further assumed that these motions maintain the bulk of the solar coronal medium in a state of fully-developed MHD turbulence, either by field-tangling (Parker, 1983a, 1983b; van Ballegooijen, 1986) or else by developing instabilities in the stressed coronal medium (Chiuderi and Van Hoven, 1979; Galeev et al., 1981; Chiueh and Zweibel, 1987; Strauss and Otani, 1988; Bodo et al., 1991). An arcade of loops is modelled in local Cartesian coordinates (Figs. 3.1 and 3.2) defined in the region $-h < x < h$, $-\infty < y < \infty$ and $-l < z < l$ where the uniform background field is $B_0\hat{z}$.

Equation	Correction
(14)	$t = \dfrac{l}{c_{a0}}\tau$
	$\boldsymbol{r} = l\boldsymbol{a}$
	$\boldsymbol{J} = \dfrac{B_0}{\mu_0 l}\boldsymbol{j}$
(30)	$\boldsymbol{e}_{\rm tphot} = -V(x)\hat{\boldsymbol{x}}$
(32)	$\boldsymbol{e}_{\rm tcor} = -\left(\eta\dfrac{\partial b}{\partial z} + V(x)\right)\hat{\boldsymbol{x}}$
(79)	$t(\lambda) = \dfrac{\lambda}{\overline{v}}\left(\dfrac{2\pi}{\lambda k_{\rm min}}\right)^{1/3}$
(80)	$t_A = \dfrac{l}{c_{a0}}$
(85)	$1 = \dfrac{q}{\pi}\displaystyle\int_{K_m}^{K_M} {\rm d}K\, x\, \Lambda(K) \times \dfrac{((x^2+2K^2)/\sqrt{x^2+4K^2})\sinh\sqrt{x^2+4K^2} + x\sinh x}{\cosh\sqrt{x^2+4K^2} - \cosh x}$
(91c)	$K_m^2 < x < K_M$

Table 3.1: Typographical errors in Heyvaerts and Priest (1992).

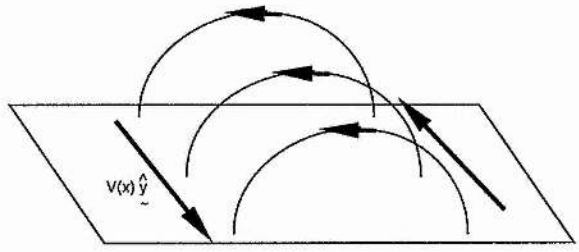

Figure 3.1: Sheared arcade configuration.

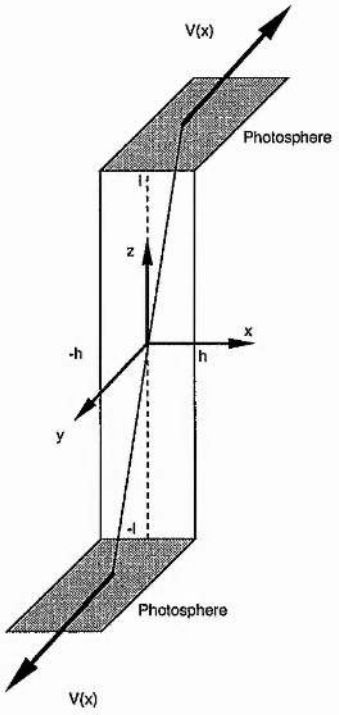

Figure 3.2: Sheared slab model of the arcade. The vertical dotted line and sloping solid line denote a magnetic field line prior to and during shearing, respectively.

The equations of incompressible MHD are used,

$$\rho\left(\frac{\partial \boldsymbol{u}}{\partial t}+(\boldsymbol{u}\cdot\nabla)\boldsymbol{u}\right) = -\nabla P+\boldsymbol{J}\times\boldsymbol{B}+\eta_v\,\nabla^2\boldsymbol{u}, \tag{3.1}$$

$$\frac{\partial \boldsymbol{B}}{\partial t} = \nabla\times(\boldsymbol{u}\times\boldsymbol{B})+\eta_m\,\nabla^2\boldsymbol{B}, \tag{3.2}$$

$$\boldsymbol{J} = \frac{1}{\mu_0}\nabla\times\boldsymbol{B}, \tag{3.3}$$

$$\boldsymbol{J} = \Sigma(\boldsymbol{E}+\boldsymbol{u}\times\boldsymbol{B}), \tag{3.4}$$

$$\nabla\cdot\boldsymbol{B} = 0, \tag{3.5}$$

$$\nabla\cdot\boldsymbol{u} = 0, \tag{3.6}$$

consisting of fourteen scalar equations in the fourteen variables $(\rho, P, \boldsymbol{u}, \boldsymbol{B}, \boldsymbol{J}, \boldsymbol{E})$, three parameters (η_v, η_m, Σ) and one fundamental constant (μ_0), where ρ is the mass density, P is the hydrostatic gas pressure, $\boldsymbol{u}$ is the velocity, $\boldsymbol{B}$ is the magnetic field, $\boldsymbol{J}$ is the current density, $\boldsymbol{E}$ is the electric field, η_v is the shear viscosity, η_m is the magnetic diffusivity, Σ is the conductivity and μ_0 is the permeability of free space. The arcade is now defined by $-q < x < q$, $-\infty < y < \infty$ and $-1 < z < 1$, where $q = h/l$ is the inverse aspect ratio of a loop and the notation used for the dimensionless arcade coordinates, $\boldsymbol{a} = \boldsymbol{r}/l$, is just that of the previous dimensional coordinates $\boldsymbol{r} = (x, y, z)$. Similarly the dimensionless Laplacian $\nabla' = \nabla l$ is just written as ∇. Other dimensionless units are now introduced, defined by

$$t = \frac{l}{c_{a0}}\,\tau, \tag{3.7}$$

$$P = \frac{B_0^2}{\mu_0}\,\beta, \tag{3.8}$$

$$\boldsymbol{u} = c_{a0}\,\boldsymbol{v}, \tag{3.9}$$

$$\boldsymbol{B} = B_0\,\boldsymbol{b}, \tag{3.10}$$

$$\boldsymbol{J} = \frac{B_0}{\mu_0\, l}\,\boldsymbol{j}, \tag{3.11}$$

$$\boldsymbol{E} = c_{a0}\,B_0\,\boldsymbol{e}. \tag{3.12}$$

The dimensionless viscosity and magnetic diffusivity are defined as

$$\nu = \frac{\eta_v}{\rho\, l\, c_{a0}}, \tag{3.13}$$

$$\eta = \frac{\eta_m}{l\, c_{a0}}, \tag{3.14}$$

where $c_{a0} = B_0/\sqrt{\mu_0\,\rho}$ is a representative Alfvén speed in the corona. The MHD equations become

$$\frac{\partial \boldsymbol{v}}{\partial \tau}+(\boldsymbol{v}\cdot\nabla)\boldsymbol{v} = -\nabla\beta+\boldsymbol{j}\times\boldsymbol{b}+\nu\,\nabla^2\boldsymbol{v}, \tag{3.15}$$

$$\frac{\partial \boldsymbol{b}}{\partial \tau} = \nabla\times(\boldsymbol{v}\times\boldsymbol{b})+\eta\,\nabla^2\boldsymbol{b}, \tag{3.16}$$

$$\boldsymbol{j} = \nabla\times\boldsymbol{b}, \tag{3.17}$$

$$\boldsymbol{j} = \frac{1}{\eta}(\boldsymbol{e} + \boldsymbol{v} \times \boldsymbol{b}), \tag{3.18}$$

$$\nabla \cdot \boldsymbol{b} = 0, \tag{3.19}$$

$$\nabla \cdot \boldsymbol{v} = 0. \tag{3.20}$$

Taking the uniform background magnetic field, time-independent case of the Heyvaerts and Priest (1983) phase-mixing paper, particular forms for the velocity and magnetic field are chosen in which a flow along the y-direction produces a globally steady-state two-and-a-half dimensional field with all variables independent of y:

$$\boldsymbol{v} = v(x,z)\,\hat{\boldsymbol{y}}, \tag{3.21}$$

$$\boldsymbol{b} = \hat{\boldsymbol{z}} + b(x,z)\,\hat{\boldsymbol{y}}. \tag{3.22}$$

The y-components of Eqs. (3.15) and (3.16) then reduce to

$$\frac{\partial b}{\partial z} + \nu \nabla^2 v = 0, \tag{3.23}$$

$$\frac{\partial v}{\partial z} + \eta \nabla^2 b = 0, \tag{3.24}$$

while the x- and z-components of Eq. (3.15) give the pressure balance condition:

$$\nabla \left(\beta + \frac{b^2}{2} \right) = 0. \tag{3.25}$$

A simple sheared arcade can be modelled by taking $v(x,z)$ to be an odd function of z, thus ensuring that the photospheric flow is oppositely directed at each end of the arcade. For consistency Eqs. (3.23) and (3.24) then demand that $b(x,z)$ be an even function of z. These two assumptions now reduce the required number of boundary conditions to two which are obtained by considering the electric field at the photosphere/corona boundary and by imposing a shear flow at the photosphere.

The coronal electric field is calculated from Eqs. (3.17), (3.18), (3.21) and (3.22) and has a component tangential to the background field of

$$\boldsymbol{e}_\perp = -\left(\eta \frac{\partial b}{\partial z} + v \right) \hat{\boldsymbol{x}}. \tag{3.26}$$

The photosphere is taken to be an ideal region ($\eta = 0$) because it has a much larger density, and hence conductivity, than the corona (up to 10^7 times denser than an active region). Since the corona has been taken to have a uniform η so far there is a discontinuity in the magnetic diffusivity; the electromagnetic requirement that the tangential component of the electric field be continuous across the boundary then requires that

$$\frac{\partial b}{\partial z} = 0 \text{ at } z = \pm 1. \tag{3.27}$$

The second boundary condition is obtained by imposing the shear flow at the photosphere as

$$v(x,1) = V(x), \tag{3.28}$$

where the form of $V(x)$ is unspecified at this stage. However, it is assumed to be a stochastic function.

Within coronal loops there is generally some structure on scales smaller than the maximum size; assuming periodic extension along the width of the arcade then enables a Fourier expansion to be taken (Sect. 4.2):

$$v(x,z) = \sum_{n=1}^{\infty}\left[v_n^{(1)}(z)\cos\frac{n\pi x}{q} + v_n^{(2)}(z)\sin\frac{n\pi x}{q}\right], \tag{3.29}$$

$$b(x,z) = \sum_{n=1}^{\infty}\left[b_n^{(1)}(z)\cos\frac{n\pi x}{q} + b_n^{(2)}(z)\sin\frac{n\pi x}{q}\right], \tag{3.30}$$

the use of which simplifies Eqs. (3.23) and (3.24) to

$$\frac{\mathrm{d}b_n^{(i)}}{\mathrm{d}z} + \nu\left(\frac{\mathrm{d}^2 v_n^{(i)}}{\mathrm{d}z^2} - \frac{n^2\pi^2}{q^2}v_n^{(i)}\right) = 0, \tag{3.31}$$

$$\frac{\mathrm{d}v_n^{(i)}}{\mathrm{d}z} + \eta\left(\frac{\mathrm{d}^2 b_n^{(i)}}{\mathrm{d}z^2} - \frac{n^2\pi^2}{q^2}b_n^{(i)}\right) = 0, \tag{3.32}$$

where the superscript (i) takes values 1 and 2. The photospheric flow is similarly expanded as

$$V(x) = \sum_{n=1}^{\infty}\left[V_n^{(1)}\cos\frac{n\pi x}{q} + V_n^{(2)}\sin\frac{n\pi x}{q}\right], \tag{3.33}$$

while Eq. (3.27) becomes

$$\frac{\mathrm{d}b_n^{(i)}}{\mathrm{d}z} = 0 \text{ at } z = 1. \tag{3.34}$$

Seeking solutions of the form $\exp(\sigma z)$ gives the solution to the system Eqs. (3.31)–(3.34) as

$$v_n^{(i)}(z) = \frac{\lambda_n^2 V_n^{(i)}}{\sqrt{1+4\lambda_n^2}}\left(\frac{\sinh(\sigma_-\frac{z}{H})}{\sigma_-\sinh\frac{\sigma_-}{H}} + \frac{\sinh(\sigma_+\frac{z}{H})}{\sigma_+\sinh\frac{\sigma_+}{H}}\right), \tag{3.35}$$

$$b_n^{(i)}(z) = \frac{\nu}{H}\frac{\lambda_n^2 V_n^{(i)}}{\sqrt{1+4\lambda_n^2}}\left(\frac{\cosh(\sigma_-\frac{z}{H})}{\sigma_-\sinh\frac{\sigma_-}{H}} - \frac{\cosh(\sigma_+\frac{z}{H})}{\sigma_+\sinh\frac{\sigma_+}{H}}\right), \tag{3.36}$$

where

$$H = \sqrt{\eta\nu}, \tag{3.37}$$

$$\lambda_n = \sqrt{\eta\nu}\,\frac{n\pi}{q}, \tag{3.38}$$

$$\sigma_\pm = \frac{1}{2}(\sqrt{1+4\lambda_n^2} \pm 1). \tag{3.39}$$

Starting from Poynting's theorem,

$$\frac{\partial}{\partial t}\left(\frac{b^2}{2} + \frac{e^2}{2}\right) = -\nabla\cdot(\boldsymbol{e}\times\boldsymbol{b}) - \boldsymbol{v}\cdot(\boldsymbol{j}\times\boldsymbol{b}) - \eta j^2, \tag{3.40}$$

and Eq. (3.15) an energy equation can be created:

$$\frac{\partial}{\partial t}\left(\frac{v^2}{2}+\frac{b^2}{2}+\frac{e^2}{2}\right)=-\nabla\cdot\left[\left(\beta+\frac{v^2}{2}\right)\boldsymbol{v}+\nu\boldsymbol{\omega}\times\boldsymbol{v}-\boldsymbol{e}\times\boldsymbol{b}\right]-\eta j^2-\nu\omega^2, \tag{3.41}$$

where $\boldsymbol{\omega}=\nabla\times\boldsymbol{v}$ is the vorticity. In MHD the electric field strength is small in comparison with the magnetic field strength so Eq. (3.41) describes the time evolution for the sum of the kinetic and magnetic energy densities. The divergence term on the right side corresponds to a surface flux term when the equation is integrated over the volume and the divergence theorem applied. However, for the particular ansatz under consideration, Eqs. (3.21) and (3.22), the normal to the photospheric surface at $z=\pm 1$ is directed in the $\mp\hat{\boldsymbol{z}}$-direction, while the flow is purely in the $\hat{\boldsymbol{y}}$-direction so that $\boldsymbol{v}\cdot\mathrm{d}\boldsymbol{S}\equiv 0$, and similarly for the $\hat{\boldsymbol{x}}$-normal to the loop cavity. For the $\hat{\boldsymbol{y}}$-normal the flux into one side of the arcade is equal to the flux out of the opposite side. Overall there is no net contribution from the first divergence term. The second term is the viscous flux — from Eq. (3.21)

$$\boldsymbol{\omega}=-\frac{\partial v}{\partial z}\hat{\boldsymbol{x}}+\frac{\partial v}{\partial x}\hat{\boldsymbol{z}}, \tag{3.42}$$

so that $\boldsymbol{\omega}\times\boldsymbol{v}=-v\partial v/\partial x\,\hat{\boldsymbol{x}}-v\partial v/\partial z\,\hat{\boldsymbol{z}}$. Being periodic in x and independent of y there is no net flux through the faces with normals $\hat{\boldsymbol{x}}$ and $\hat{\boldsymbol{y}}$, but there is a contribution through each photospheric boundary of

$$\phi_{\mathrm{zvisc}}=-\nu v\frac{\partial v}{\partial z}. \tag{3.43}$$

Similarly the Poynting flux has a flux through each photospheric boundary of

$$\phi_{\mathrm{zPoynt}}=-vb. \tag{3.44}$$

Since it is the total energy injection which is important, a photospheric surface integral will have to be performed at some stage. The contribution from integrating in the y-direction just gives the y-independent flux contribution multiplied by the length over which the integration is performed, while for the x-direction the result can be expressed in terms of an average in the x-direction for ease of use later on, defined as

$$\langle f(x)\rangle=\frac{1}{2q}\int_{-q}^{q}f(x)\mathrm{d}x. \tag{3.45}$$

The x-averaged power density contribution from each photospheric boundary due to the viscous and Poynting fluxes is calculated using Eqs. (3.43)–(3.45) to be (Sect. 4.5)

$$|\langle\phi_{\mathrm{zvisc}}\rangle| = \sum_{n=1}^{\infty}\frac{V_n^2}{2\eta}\frac{2\lambda_n^2\frac{H}{\sqrt{1+4\lambda_n^2}}\sinh\frac{\sqrt{1+4\lambda_n^2}}{H}}{\cosh\frac{\sqrt{1+4\lambda_n^2}}{H}-\cosh\frac{1}{H}}, \tag{3.46}$$

$$|\langle\phi_{\mathrm{zPoynt}}\rangle| = \sum_{n=1}^{\infty}\frac{V_n^2}{2\eta}\frac{\frac{H}{\sqrt{1+4\lambda_n^2}}\sinh\frac{\sqrt{1+4\lambda_n^2}}{H}+H\sinh\frac{1}{H}}{\cosh\frac{\sqrt{1+4\lambda_n^2}}{H}-\cosh\frac{1}{H}}, \tag{3.47}$$

so that the total contribution from both boundaries is just $F = 2|\langle\phi_{\rm zvisc}\rangle| + 2|\langle\phi_{\rm zPoynt}\rangle|$, which gives

$$F = \sum_{n=1}^{\infty} \frac{V_n^2}{\eta} \frac{\frac{(1+2\lambda_n^2)}{\sqrt{1+4\lambda_n^2}} H \sinh \frac{\sqrt{1+4\lambda_n^2}}{H} + H \sinh \frac{1}{H}}{\cosh \frac{\sqrt{1+4\lambda_n^2}}{H} - \cosh \frac{1}{H}} . \tag{3.48}$$

Information about the turbulent photospheric velocity is contained in the square of the amplitudes of the Fourier velocity components at the end points, namely $V_n^2 = (V_n^{(1)})^2 + (V_n^{(2)})^2$, the form for which was determined by choosing a dimensional Kolmogorov spectrum since magnetic effects in the photosphere are less significant than in the corona (Sect. 4.3):

$$\overline{V}^2(k) = \frac{2}{3} k_{\rm min}^{2/3} \overline{v}^2 k^{-5/3}, \tag{3.49}$$

chosen so that

$$\int_{k_{\rm min}}^{\infty} \overline{V}^2(k) {\rm d}k = \overline{v}^2, \tag{3.50}$$

where $\overline{v}$ is the root-mean-square (r.m.s.) photospheric velocity and $k_{\rm min} = 2\pi/(2h) = \pi/h$ defines the wavenumber associated with the maximum shearing scale. Equations (3.33) and (3.45) give

$$\langle V^2(x)\rangle = \frac{1}{2} \sum_{n=1}^{\infty} V_n^2. \tag{3.51}$$

By definition $\overline{v}^2 = c_{a0}^2 \langle V^2(x)\rangle$ in physical space so that Eqs. (3.50) and (3.51) give

$$\int_{k_{\rm min}}^{\infty} \overline{V}^2(k) {\rm d}k = \frac{c_{a0}^2}{2} \sum_{n=1}^{\infty} V_n^2 = \overline{v}^2. \tag{3.52}$$

The integral is approximated by $\pi/h \sum_{n=1}^{\infty} \overline{V}^2(k)$ so that

$$\overline{V}^2(k) = \frac{c_{a0}^2}{2} \frac{h}{\pi} V_n^2, \tag{3.53}$$

whence

$$V_n^2 = \frac{4}{3} \left(\frac{\overline{v}}{c_{a0}} \right)^2 n^{-5/3}. \tag{3.54}$$

Finally, a cutoff is derived by considering only eddy motions on time-scales less than the time for an Alfvén wave to cross any loop of the arcade (Sect. 4.4). Defining the typical eddy speed at scale λ by

$$v^2(\lambda) = \int_{2\pi/\lambda}^{\infty} \overline{V}^2(k) {\rm d}k = \overline{v}^2 \left(\frac{\lambda k_{\rm min}}{2\pi} \right)^{2/3}, \tag{3.55}$$

and the typical time-scale of an eddy as $t(\lambda) = \lambda / v(\lambda)$, Heyvaerts and Priest obtain

$$t(\lambda) = \frac{\lambda}{\overline{v}} \left(\frac{2\pi}{\lambda k_{\rm min}} \right)^{1/3}. \tag{3.56}$$

The Alfvén transit time is in fact defined as being half the time to cross the loop, $t_A = l/c_{a0}$, so that $t(\lambda) > t_A$ leads to the wavenumber cutoff inequality

$$n < N_A = \left(\frac{2q c_{a0}}{\overline{v}} \right)^{3/2}, \tag{3.57}$$

assuming $k = n\pi/q$.

3.3 Behaviour at small scales

The turbulent dissipation part of the model is based on the work of Pouquet et al. (1976), who derive an asymptotic expansion of the EDQNM approximation for isotropic MHD turbulence including the effects of kinetic and magnetic helicity (Sect. 1.3.2). This work was adapted by Heyvaerts and Priest by assuming that there is no helicity injection during the shearing process. The equations for the kinetic and magnetic energies (Eqs. (1.112) and (1.113), here presented in dimensional form) are considerably simplified. The large-scale contribution is considered to be modelled deterministically and so has been neglected from these equations which now represent the non-local effects of the small scales of the turbulence up to first order in the expansion parameter, a:

$$\frac{\partial}{\partial t}(E_V(k)) = -2\left(\frac{2}{5}\nu_k^V + \nu_k^M + \nu_k^R\right) k^2 E_V(k), \tag{3.58}$$

$$\frac{\partial}{\partial t}(E_M(k)) = -2\nu_k^V k^2 E_M(k), \tag{3.59}$$

with the various ν_k's given in Eqs. (1.144) – (1.146). As is usual for isotropic turbulence models, evenly-distributed random forces are implicitly present to enable the existence of a steady state. If, further, the Alfvén effect (Sect. 1.3.5) is assumed to be dominant the resulting equipartition of kinetic and magnetic energy helicity ($E_k^V = E_k^M$ and $H_k^V = k^2 H_k^M$) permits further simplification so that $\nu_k^R = 0$ and $\nu_k^M = \nu_k^V$. The effective turbulent viscosity and magnetic diffusivity are inferred from Eqs. (3.58) and (3.59) to be

$$\eta_v = \frac{7}{5}\rho\nu_k^V \tag{3.60}$$

$$\eta_m = \nu_k^V. \tag{3.61}$$

The eddy-damping rate, Eq. (1.109), simplifies by assuming that in the presence of a background field the Alfvén effect proves the dominant eddy relaxation mechanism, so much so that the nonlinear scrambling and molecular dissipation effects can be neglected. Furthermore, the Alfvén waves generated now propagate along this background field rather than being random excitations throughout the magnetofluid so that now the Alfvén speed corresponding to the background field is the appropriate characteristic speed rather than the "energy" used in Eq. (1.109). Overall then (Sect. 4.6)

$$\mu_k = \frac{kc_{a0}}{\sqrt{3}}, \tag{3.62}$$

was used. Furthermore it was implicitly assumed that non-local effects such that $k \ll p$ were being investigated. Equation (3.62) then implies that $\mu_k \ll \mu_p$ and Eq. (1.110) gives

$$\mu_{kpq} \simeq 2\mu_p. \tag{3.63}$$

It is also assumed that after some time a steady state has developed; the limit $t \to \infty$ is implicitly taken in Eq. (1.111) so that

$$\theta_{kpq} = \frac{1}{\mu_{kpq}}. \tag{3.64}$$

Putting these approximations together in Eq. (1.144) gives

$$\nu_k^V = \frac{2}{3}\int_{k/a}^{\infty} \frac{\sqrt{3}}{2\,p\,c_{a0}} E(p)\mathrm{d}p, \tag{3.65}$$

where $E(p)$ is the kinetic energy spectrum.

In the corona magnetic effects dominate, so a Kraichnan spectrum (Kraichnan, 1965) is chosen to model the energy cascades resulting from the turbulence:

$$E(k) = C\sqrt{\varepsilon\, c_{a0}}\, k^{-3/2}, \tag{3.66}$$

where ε is the energy transfer per unit time and unit mass and C is a constant whose value is taken as 0.9 following Pouquet et al.'s numerical simulations. Equation (3.65) integrates to give

$$\eta_m = \nu_k^V = \frac{2\sqrt{3}}{9} C \sqrt{\frac{\varepsilon}{c_{a0}}} \left(\frac{k}{a}\right)^{-3/2}. \tag{3.67}$$

For numerical calculations a cutoff between large and small sub-grid scales is used, above which explicit calculations are made and below which the eddy viscosity formulation is used. Kraichnan (1976) does this by choosing the expansion parameter to be $a = k/k_{\mathrm{cut}}$, whence for $k \ll k_{\mathrm{cut}}$ the eddy viscosity is independent of k (verified numerically). This is fine for a numerical simulation, but for the simple model of Heyvaerts and Priest no consideration has been made of the instabilities leading to turbulence or of eddy motions which require additional velocity and magnetic field components. This problem was avoided by instead choosing $a = 1$ and placing the cutoff at the largest horizontal scale of the system, $k_{\mathrm{min}} = \pi/h$. Thus,

$$\eta_m = \frac{2\sqrt{3}}{9} C \sqrt{\frac{\varepsilon}{c_{a0}}} \left(\frac{h}{\pi}\right)^{3/2}. \tag{3.68}$$

This approach has the drawback, though, that the expansions of Pouquet et al. (1976), Eqs. (1.137) – (1.140), can only be valid at $k = k_{\mathrm{min}}$, if at all, since the neglected terms are of order unity!

A balance between energy injected at large scales and that cascading to small scales is invoked to determine the effective dissipation coefficients (so far given up to the energy transfer rate ε). The energy injected at large scales over a length L of the y-direction by the photospheric eddies is

$$Q_{\mathrm{inj}} = 2hL\frac{B_0^2}{\mu_0} c_{a0} F, \tag{3.69}$$

where F is the previously calculated dimensionless power density, Eq. (3.48), which then cascades to molecular length scales and is dissipated by the viscous and resistive effects:

$$Q_{\mathrm{diss}} = 2h2lL\rho\varepsilon. \tag{3.70}$$

In a statistically-steady state the injection and dissipation of kinetic and magnetic energy must balance, so equating Eqs. (3.69) and (3.70) gives

$$\varepsilon = \frac{c_{a0}^3}{2l} F. \tag{3.71}$$

Next, Eq. (3.71) is substituted into Eq. (3.67), which is then inverted to give ε in terms of ν_k^{v} and thence the turbulent viscosity, ν, by Eqs. (3.13) and (3.60), finally yielding

$$F = \frac{675}{98\,C^2}\left(\frac{\pi}{q}\right)^3 \nu^2. \tag{3.72}$$

A characteristic turbulent velocity, often measured from line spectra in terms of line-broadening due to unresolved motions, is calculated from the power density by integrating the Kraichnan spectrum

$$v_{\mathrm{turb}}^2 = \int_{k_{\mathrm{min}}}^{\infty} C\sqrt{\varepsilon c_{a0}}\, p^{-3/2}\mathrm{d}p, \tag{3.73}$$

which gives

$$v_{\mathrm{turb}}^2 = 2Cc_{a0}^2\sqrt{\frac{Fq}{2\pi}}, \tag{3.74}$$

when Eq. (3.71) is invoked.

3.4 Steady-state energy balance

In a steady state the rate of injection of energy will match the rate of transfer of energy from large to small scales and the rate of dissipation of energy due to classical molecular effects. With this equality the former two values may be used when trying to calculate the latter, which is the object of the exercise but also the hardest to model. After equating Eqs. (3.48) and (3.72), substituting Eq. (3.54), using the cutoff, Eq. (3.57), and writing

$$x = \frac{1}{H} = \sqrt{\frac{7}{5}}\frac{1}{\nu}, \tag{3.75}$$

$$\alpha_n = \frac{2n\pi}{q}, \tag{3.76}$$

$$\Lambda_n = \sqrt{\frac{5}{7}}\frac{98}{675}\left(\frac{q}{\pi}\right)^3 C^2 V_n^2, \tag{3.77}$$

this yields a transcendental equation for x, i.e. for the turbulent viscosity:

$$1 = \sum_{n=1}^{N_A} \Lambda_n x \frac{\frac{(x^2+\alpha_n^2/2)}{\sqrt{x^2+\alpha_n^2}}\sinh\sqrt{x^2+\alpha_n^2} + x\sinh x}{\cosh\sqrt{x^2+\alpha_n^2} - \cosh x}. \tag{3.78}$$

A solution to this was sought by approximating the sum as an integral (Sect. 3.5.2):

$$1 \simeq \frac{q}{\pi}\int_{\frac{x}{q}}^{\frac{\pi}{q}N_A} x\Lambda_0\, K^{-5/3}\psi(x,K)\,\mathrm{d}K\,, \tag{3.79}$$

where

$$\psi(x,K) = \frac{\frac{(x^2+2K^2)}{\sqrt{x^2+4K^2}}\sinh\sqrt{x^2+4K^2} + x\sinh x}{\cosh\sqrt{x^2+4K^2} - \cosh x} \tag{3.80}$$

and

$$\Lambda_0 = \sqrt{\frac{5}{7}}\frac{392}{2025}\left(\frac{\overline{v}}{c_{a0}}\right)^2\left(\frac{q}{\pi}\right)^{4/3} C^2. \tag{3.81}$$

The function $\psi(x,K)$ was then approximated in three domains

$$\psi(x,K) = \begin{cases} K & x \ll K, \\ x & K \ll x \ll K^2, \\ x^2/K^2 & x \gg K^2, \end{cases} \tag{3.82}$$

which led to the following system of algebraic equations (Sect. 3.5.2):

$$\frac{K_m}{3\Lambda_0} = \begin{cases} x(K_M^{1/3} - K_m^{1/3}) & x < K_m, \\ \frac{1}{2}x^2 K_m^{-2/3} - \frac{3}{2}x^{4/3} + xK_M^{1/3} & K_m < x < K_m^2, \\ \frac{1}{8}x^3 K_m^{-8/3} + \frac{3}{8}x^{5/3} - \frac{3}{2}x^{4/3} + xK_M^{1/3} & K_m^2 < x < K_M, \\ \frac{1}{8}x^3 K_m^{-8/3} + \frac{3}{8}x^{5/3} - \frac{1}{2}x^2 K_M^{-2/3} & K_M < x < K_M^2, \\ \frac{1}{8}x^3(K_m^{-8/3} - K_M^{-8/3}) & K_M^2 < x, \end{cases} \tag{3.83}$$

where $K_m = \pi/q$ and $K_M = N_A K_m$.

Heyvaerts and Priest showed that the solution lies in the region $K_m^2 < x < K_M^2$. For large x the following approximate solutions were formed:

$$x = 1.33 \times 10^5 C^{-2/3} Q^{-5/3} w^{-2/3} M^{2/3} D^{-1/3}, \tag{3.84}$$

$$\eta_v/\rho = 1.94 \times 10^{12} C^{2/3} Q^{5/3} w^{2/3} M^{1/3} D^{-1/6} \text{ cm}^2\text{s}^{-1}, \tag{3.85}$$

$$\langle F \rangle = 1.46 \times 10^6 C^{-2/3} Q^{1/3} w^{4/3} M^{5/3} D^{1/6} \text{ erg cm}^{-2}\text{s}^{-1}, \tag{3.86}$$

$$v_{\text{turb}} = 70\, C^{1/3} Q^{1/3} w^{1/3} M^{2/3} D^{-1/3} \text{ km s}^{-1}, \tag{3.87}$$

where $h = Q$ 1000 km, $v = w$ km s^{-1}, $B = M$ 100 G, $n = D \times 10^{10}$ cm^{-3} and an arcade half-length of 10^4 km is assumed.

3.5 Further analysis of Heyvaerts and Priest (1992)

3.5.1 Series convergence

The convergence of the large-scale flux, Eq. (3.48), can be examined by noting that

$$F = \sum_{n=1}^{\infty} \frac{V_n^2}{\eta x^2} \psi(x,k), \tag{3.88}$$

where ψ is given by Eq. (3.80), $x = 1/H$ and $k = n\pi/q$. Writing $F = \sum_{n=1}^{\infty} F_n$ and combining the fact that $\psi(x,k) \to k$ as $n \to \infty$ from Eq. (3.82) with Eq. (3.54) then shows that $F_n \propto n^{-2/3}$ whence F diverges if the Kolmogorov spectrum is used at all scales. Physically this means that either the form of the spectrum must change as viscosity becomes important since the assumptions used in deriving the spectrum break down, or that a cutoff should be applied in wavenumber space — Heyvaerts and Priest followed the latter approach, Eq. (3.57).

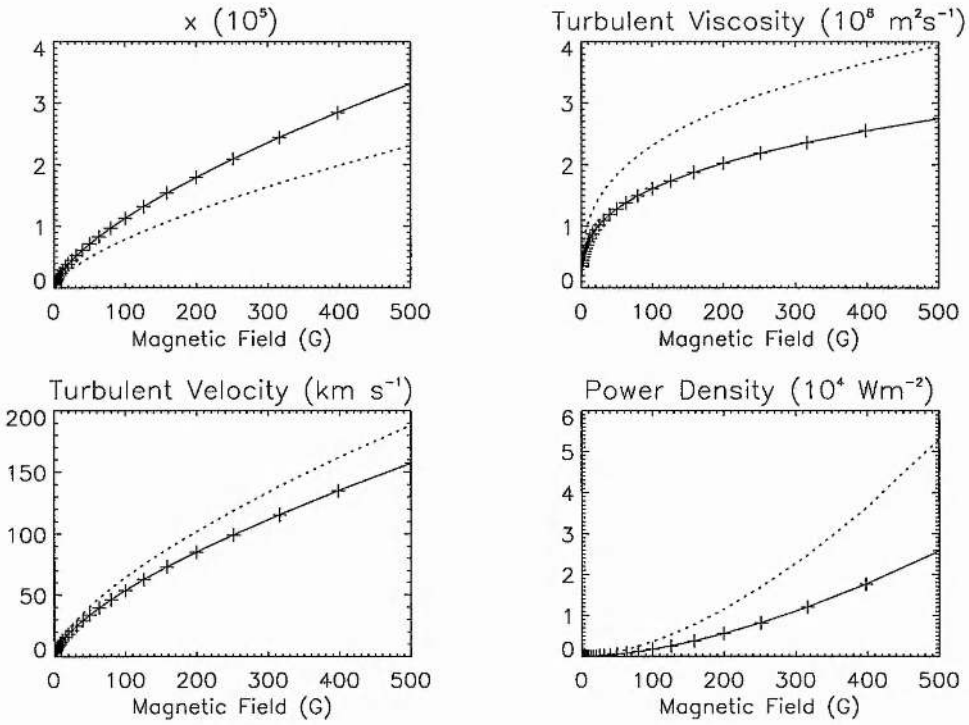

Figure 3.3: Comparison of the various methods. The graphs are for an inverse aspect ratio of q=0.1, density $= 2 \times 10^{16}$ m^{-3} (2×10^{10} cm^{-3}), r.m.s. photospheric velocity $= 1$ km s^{-1} and half-loop length $= 10^4$ km. The solid curve is the solution of the integral equation, Eq. (3.79), and the dotted line the summation form, Eq. (3.78), with the Heyvaerts and Priest spectrum, Eq. (3.54). The scaling laws, Eqs. (3.85)–(3.87), are given by the crosses.

3.5.2 Comparison of methods

Figure 3.3 compares the results obtained from the summation form, Eq. (3.78), the integration form, Eq. (3.79) and the scaling laws derived by Heyvaerts and Priest, Eqs. (3.85)–(3.87). The plotted turbulent velocity is a characteristic velocity; the value of the variance of the vector turbulent velocity $\langle v^2 \rangle$ is actually $2v_{\rm turb}^2$, with the variance of the line of sight component being $2/3v_{\rm turb}^2$, as in Heyvaerts and Priest (1992) ($v_{\rm turb}$ being the value plotted in the second graph of Fig. 3.3). All the plotted quantities depend on the parameters $q, \overline{v}, B_0$ and ρ — however, the latter three always appear in the combination $\overline{v}/(B_0/\sqrt{\mu\rho})$, which is a hybrid Alfvén Mach number comparing the r.m.s. photospheric velocity with the characteristic coronal Alfvén speed. The behaviour with density, ρ, or r.m.s. photospheric velocity may easily be obtained from Fig. 3.3; writing $M_A = \overline{v}\sqrt{\mu\rho}/B_0$ it is possible to express either ρ or $\overline{v}$ in terms of the other quantities, such as $\overline{v} = M_A B_0/\sqrt{\mu\rho}$. Fixing the Alfvén Mach number and density then allows $\overline{v}$ to be related to B_0 and the values on the x-axis can be read off the graph to give the corresponding r.m.s. photospheric velocity. Similarly, write $\rho = M_A^2 B_0^2/(\overline{v}^2\mu_0)$, then fix M_A and $\overline{v}$ to relate ρ to B_0. The turbulent magnetic diffusivity is obtained from the turbulent viscosity graph by multiplying by 5/7.

Examination of Fig. 3.3 shows that the results obtained by solving Eqs. (3.78) and (3.79) are different. The integral form is exact as the inverse aspect ratio, q, approaches infinity, which is not very appropriate for this model where the inverse aspect ratio is never greater than unity. For this reason it is the summation form of the steady-state energy balance which will be focused on in the rest of this thesis. However, it can be seen from Fig. 3.3 that the use of the integral form leads to simple approximations which match the numerical solution to Eq. (3.79) very closely and can be calculated extremely quickly. In fact, the errors between the scaling laws, Eqs. (3.84)–(3.87), and the numerical solution to Eq. (3.79) decrease as the magnetic field increases. For fields greater than 20G the error is less than 1%, while for a field of 1G the error approaches 10%. As coronal magnetic fields are usually no smaller than 1G the scaling laws thus provide an excellent approximation for the solutions to Eq. (3.79) and hence a good order of magnitude approximation for the turbulent variables plotted in Fig. 3.3.

3.5.3 Self-consistency of the model

The consistency of the solutions for the large-scale velocity and magnetic field perturbations, Eqs. (3.21) and (3.22), for the solutions of Heyvaerts and Priest, Eqs. (3.29), (3.30), (3.35) and (3.36), with the prescribed Kraichnan spectrum, Eq. (3.66), is now examined. Before making the comparison it should be noted that this Kraichnan spectrum is based on isotropic three-dimensional MHD, whereas $v_n^{(i)}$ and $b_n^{(i)}$ approximate a one-dimensional anisotropic situation. With that in mind and with the kinetic energy given by $1/2\langle v^2(x,z)\rangle = \sum_{n=1}^{\infty} v_n^2(z)/4$, the spectra $v_n^2/4$ and $b_n^2/4$, where $v_n^2(z) = (v_n^{(1)})^2 + (v_n^{(2)})^2$ and $b_n^2(z) = (b_n^{(1)})^2 + (b_n^{(2)})^2$ are plotted in Fig. 3.4 evaluated at the photosphere, $z = 1$, and the corona, $z = 0.5$, along with spectra which have been averaged in

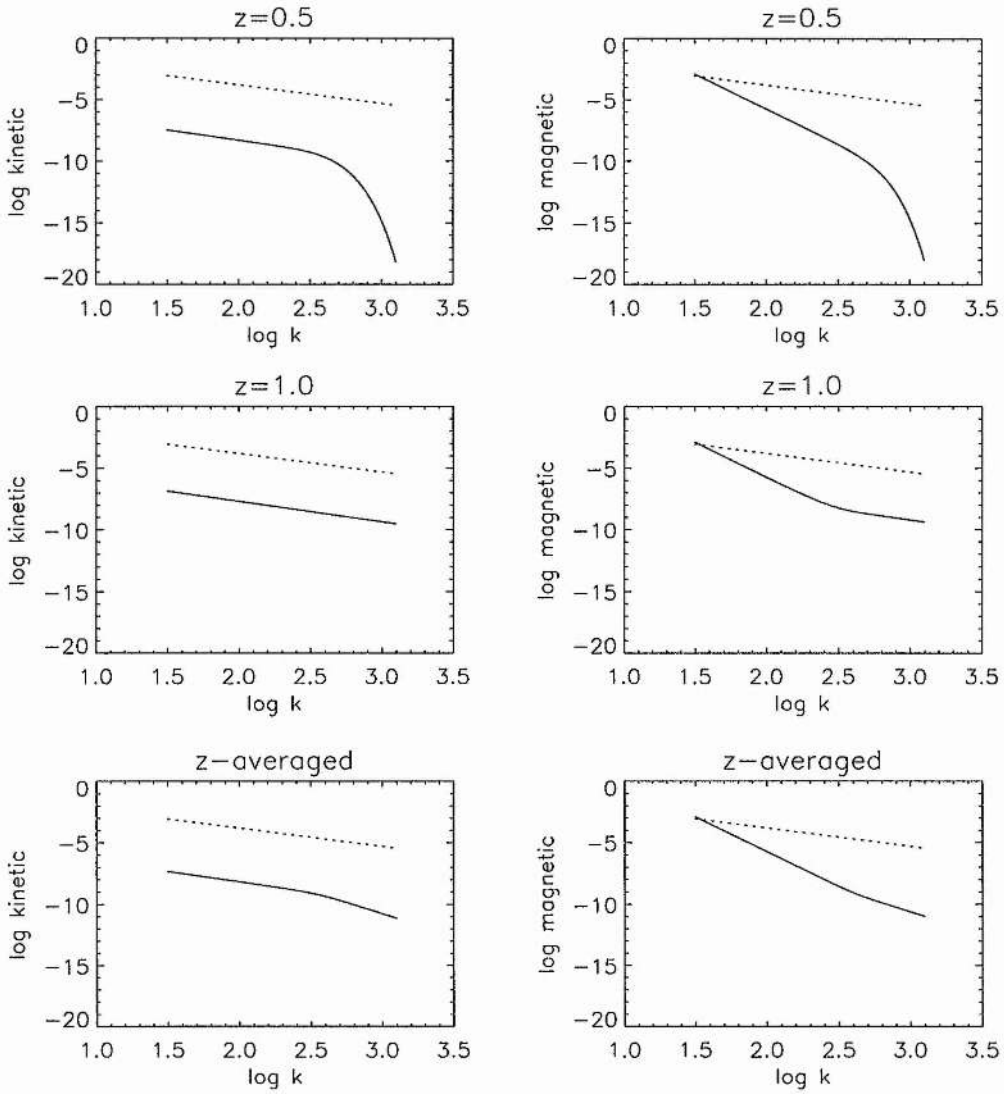

Figure 3.4: Comparison of $v_n^2(z)/4$ and $b_n^2(z)/4$ (solid lines) for the scale-independent turbulent viscosity and magnetic diffusivity of Heyvaerts and Priest evaluated in the corona, $z = 0.5$ (top row), at the photosphere, $z = 1.0$ (middle row) and averaged over z (bottom row) with the imposed Kraichnan spectrum, Eq. (3.89) (dotted lines), for large scales — the kinetic spectra appear on the left and the magnetic on the right. The kinetic energy spectrum at the photosphere is just the imposed $k^{-5/3}$ Kolmogorov spectrum, where $k = n\pi/q$ is the dimensionless wavenumber.

the z-direction. The Kraichnan spectrum has to be couched in appropriate dimensionless units in order to make a comparison with the spectra derived from the dimensionless v_n and b_n. Taking Eqs. (3.66), (3.71) and $k = n\pi/q$ then following the method used in deriving the Kolmogorov spectrum in Sect. 3.2 gives

$$E_n = C\sqrt{\frac{Fq}{2\pi}}n^{-3/2}. \tag{3.89}$$

Figure 3.4 indicates that there are significant differences between the imposed Kraichnan spectrum and the resulting kinetic and magnetic energy per unit mass spectra when an average is taken over the length of the loop. There is also variation in the calculated spectra between photosphere and corona.

Chapter 4

Sheared Arcade Modifications

4.1 Modifications to the model

The test of self-consistency between the imposed Kraichnan spectrum, Eq. (3.66), and the large-scale behaviour predicted by the model of Heyvaerts and Priest (1992) performed in Sec. 3.5.3 and plotted in Fig. 3.4 shows that there are order of magnitude differences between the two which do not even have the same power law exponents — the model clearly needs to be drastically improved. Certain aspects are now examined in greater detail and altered where appropriate prior to the test being repeated.

4.2 Fourier expansions

A change in notation is now made whereby the discrete Fourier transforms are expressed in complex variable notation rather than the sines and cosines used so far:

$$\mathcal{F}(f(x)) = \hat{f}_n = \frac{1}{2q}\int_{-q}^{q} f(x)\exp\left(\frac{-in\pi x}{q}\right)\mathrm{d}x, \tag{4.1}$$

with inverse

$$\mathcal{F}^{-1}(\hat{f}_n) = f(x) = \mathrm{Re}\sum_{n=0}^{\infty}\hat{f}_n\exp\left(\frac{in\pi x}{q}\right). \tag{4.2}$$

The average, Eq. (3.45), of Eq. (4.2) is given by

$$\langle f(x)\rangle = \hat{f}_0, \tag{4.3}$$

which, when combined with Eq. (1.39) leads to the expression for the average of the product of two functions depending on x being

$$\langle f(x)g(x)\rangle = \mathrm{Re}\sum_{n=0}^{\infty}\hat{f}_{-n}\hat{g}_n. \tag{4.4}$$

For real $f(x)$, $\hat{f}_{-n} = \hat{f}_n^*$, where * denotes the complex conjugate so that, in particular,

$$\langle V^2(x) \rangle = \sum_{n=0}^{\infty} |\hat{V}_n|^2. \tag{4.5}$$

Thus, $|\hat{V}_n|^2$ is equivalent to $V_n^2/2$.

4.3 Spectrum of photospheric motions

Up to Eq. (3.78) the solutions to the large-scale part of the model equations are exact. However, from this point approximations were introduced in order to make an explicit solution for the parameter X possible[1]. It has already been pointed out that the integral approximation, Eq. (3.79), is exact as the inverse aspect ratio, q, approaches infinity and that this is not very appropriate here since the inverse aspect ratio is never greater than unity, usually being taken to be about 0.1. However, the Kolmogorov spectrum is derived within the framework of the integral limit of an infinite box so it is then necessary to translate this into the finite box of the large scales under consideration. Starting from the Kolmogorov spectrum, Eq. (3.49), Heyvaerts and Priest obtained the approximation Eq. (3.54) via the exact relation of Eq. (3.52), where V_n is dimensionless but all other quantities are dimensional. However, replacing Eq. (3.49) back into the left side of Eq. (3.52) leads to the value $\frac{2}{3}\zeta(5/3)\,\overline{v}^2 \simeq 1.42\,\overline{v}^2$, where $\zeta(x) = \sum_{n=1}^{\infty} n^{-x}$ is the Riemann zeta function; this is significantly different from the value $\overline{v}^2$. An alternative spectrum is now calculated which does satisfy Eq. (3.52) by bounding the integral on the left with its upper and lower Riemann sums of rectangular strips of width π/h:

$$\frac{\pi}{h}\sum_{n=1}^{\infty} \overline{V}^2\left(\frac{(n+1)\pi}{h}\right) \leq \int_{k_{\min}}^{\infty} \overline{V}^2(k)\mathrm{d}k \leq \frac{\pi}{h}\sum_{n=1}^{\infty} \overline{V}^2\left(\frac{n\pi}{h}\right). \tag{4.6}$$

Replacing the central integral by its equivalent sum from Eq. (3.52) permits comparison between the discrete and continuous Fourier spectra and yields the following bounds for V_n^2 with the use of Eq. (3.49):

$$\frac{4}{3}\left(\frac{\overline{v}}{c_{a0}}\right)^2 (n+1)^{-5/3} \leq V_n^2 \leq \frac{4}{3}\left(\frac{\overline{v}}{c_{a0}}\right)^2 n^{-5/3}. \tag{4.7}$$

It can be seen that the form used by Heyvaerts and Priest was in fact the upper bound for the spectrum. Equation (3.49) is now modified to

$$V_n^2 = \frac{4}{3}\delta\left(\frac{\overline{v}}{c_{a0}}\right)^2 n^{-5/3}, \tag{4.8}$$

where $\delta = 3/(2\zeta(5/3)) \simeq 0.706$ is a constant, which satisfies Eq. (3.52) identically. The equivalent expression in complex notation is

$$|\hat{V}_n|^2 = \frac{2}{3}\delta\left(\frac{\overline{v}}{c_{a0}}\right)^2 n^{-5/3}, \tag{4.9}$$

which applies when $n \geq 1$ ($k \geq k_{\min}$).

[1] x is now written as X to avoid confusion with the Cartesian coordinate x.

4.4 Wave inequalities

Although the sum over the wavenumbers in the velocity and magnetic field has been taken to infinity, Heyvaerts and Priest introduced constraints which reduce the accessible wavenumbers to a finite range based on the characteristic time-scale for an eddy of scale λ and the Alfvén transit time for the loop: Eq. (3.57). However, for the wave case the inequalities are reversed leading to the requirement $n > N_A$ which, for large magnetic field strengths, can give a minimum mode number of several hundred thousand or more. This division of wavenumber space seems to be a consequence of the definition of the characteristic eddy velocity rather than of the division of time-scales according to whether motions are faster or slower than the Alfvén transit time (Heyvaerts, 1990). An alternative inequality can be derived which does not divide the wavenumber range by choosing the typical speed for an eddy of size λ to be $c_{a0}|\hat{V}_n|$, where $\hat{V}_n$ is the dimensionless discrete Fourier transform introduced in Eq. (4.1)[2]. The time-scale of this eddy is then $\lambda/v(\lambda)$, as before, giving

$$t(\lambda) = \frac{2h}{c_{a0} n |\hat{V}_n|}, \tag{4.10}$$

where the dimensional values $k = n\pi/h$ and $\lambda = 2\pi/k$ have been used. The condition that the eddy time-scale be greater than the Alfvén transit time[3], $2l/c_{a0}$, for shear motions then leads to the inequality

$$|\hat{V}_n| < \frac{q}{n}, \tag{4.11}$$

when $n \geq 1$. The ability to write the average of the product of two x-dependent variables in terms of the Fourier transforms is now used. For the case of $V^2(x)$ this equals the r.m.s. photospheric speed squared:

$$\overline{v}^2 = c_{a0}^2 \sum_{n=1}^{\infty} |\hat{V}_n|^2, \tag{4.12}$$

where $\hat{V}_0 = 0$ has been taken. Using Eq. (4.11) and the fact that $\sum_{n=1}^{\infty} n^{-2} = \pi^2/6$ leads to the necessary condition

$$q > \frac{\sqrt{6}}{\pi} \frac{\overline{v}}{c_{a0}}. \tag{4.13}$$

This parallels a simpler argument based on the global photospheric shearing time-scale, $2h/\overline{v}$. Comparison with the Alfvén transit time gives

$$q > \frac{\overline{v}}{c_{a0}}, \tag{4.14}$$

which agrees with Eq. (4.13) in order of magnitude. The fact that without a wavenumber cutoff the sum in Eq. (3.48) is taken to infinity does not create problems mathematically, as it will be seen to be convergent in Sect. 4.5 once the behaviour of ν and η have been determined from scale-dependent turbulence arguments. For typical coronal values of $q = 0.1$ and an r.m.s. photospheric velocity of

[2] This is equivalent to $k^{1/2}\overline{V}(k)$, up to a dimensionless constant, when continuous Fourier transforms are used.
[3] The Alfvén transit time is now defined for the whole-loop length.

1 km s^{-1} this necessary condition will be true when $c_{a0} > 7.8$ km s^{-1}, i.e. for a background field component greater than 0.5 G — this is easily satisfied for active-region loops. Altogether, then, the power density, Eq. (3.48) may be summed until it converges to the required accuracy without worrying about wavenumber cutoffs.

4.5 Scale-dependent turbulent viscosity and magnetic diffusivity

So far the model has employed a constant scale-independent turbulent viscosity and magnetic diffusivity to account for the effect of small scales on the observable large-scale features, a common approach for numerical large-eddy simulations which discriminate between large and small scales by defining a cutoff wavenumber, usually determined by the mesh size, and explicitly solving the equations for scales larger than the cutoff scale. Various expressions for the turbulent viscosity and magnetic diffusivity are obtained by approximating the equations for the small-scale turbulence. In the fluid context Kraichnan (1976) and Chollet and Lesieur (1981) have shown that the turbulent viscosity obtained from the direct interaction approximation (DIA) and the EDQNM, respectively, are independent of scale provided the scales being examined are far removed from the cutoff, but that close to the cutoff the turbulent viscosity does depend on the wavenumber[4]. Physically this is to be expected because the dissipation of an eddy depends on scales smaller than the eddy itself. Heyvaerts and Priest essentially examined the effects of all scales on the largest of the system by choosing the asymptotic expansion parameter in the model of Pouquet et al. (1976) to be unity, and then placing the cutoff at the minimum wavenumber. Given the results of Kraichnan and Chollet and Lesieur (indicating the unreliability of the scale-independent turbulent viscosity near the cutoff) and the fact that the approximation is not valid for wavenumbers greater than $k_{\min}$ (i.e. anywhere in the inertial range under consideration!), an improved description of scale-dependent effects on the turbulent viscosity and magnetic diffusivity is clearly necessary.

In order to proceed, the notion of scale should be defined more precisely. The turbulence theory of Pouquet et al. is expressed in Fourier transform space, the medium having been assumed to be infinite in extent or periodic. The rough scale of a structure is then the reciprocal of the modulus of its wavenumber. This cannot be translated directly into the arcade model because the x and z-dimensions are finite in extent. For the x-coordinate a discrete Fourier transform can be used instead since it is credible that the shearing photospheric velocity may be periodically extended to regions $|x| > q$ to satisfy the Dirichlet conditions of Fourier analysis. However, in the z-direction the physical conditions in the regions $|z| \leq 1$ and $|z| > 1$ are markedly different, with the former representing the sparse corona and the latter the dense solar interior. The equations for both media

[4]Domaradzki et al. (1987) and Chekhlov et al. (1994) compare large-eddy simulations employing eddy viscosities of the Kraichnan form with direct numerical simulations and find good agreement.

are different, with the corona being an effectively resistive medium whereas in the photosphere the frozen-in approximation is regarded as appropriate. It is not reasonable, therefore, to assume periodic extension of the z-profile of the velocity and magnetic fields since the boundary velocity field plays a crucial rôle in the process. The term "scale" is used to refer to the wavenumber resulting from a discrete Fourier transform in the x-direction only, defined in Eq. (4.1).

The introduction of scale-dependent turbulent viscosity and magnetic diffusivity means that the nonlinear terms in the momentum and induction equations can no longer be expressed as $\nu\nabla^2\boldsymbol{v}$ and $\eta\nabla^2\boldsymbol{b}$, respectively, where ν and η are turbulent. The dimensionless turbulent viscosity and magnetic diffusivity are approximated in Fourier space where the calculations will be made but the corresponding expressions in physical space are not calculated. Equations (3.15) and (3.16) are retained, but with general nonlinear force terms in place of the Laplacian terms used by Heyvaerts and Priest. Solutions in the form of Eqs. (3.21) and (3.22) are again sought and the assumption is made that, whatever the form of the nonlinear forces in physical space, they will again only have components in the y-direction. Thus,

$$\frac{\partial b}{\partial z} + f_{\text{v-nonlin}} = 0, \tag{4.15}$$

$$\frac{\partial v}{\partial z} + f_{\text{b-nonlin}} = 0. \tag{4.16}$$

Discrete Fourier transforms of these equations are taken in the x-direction and at this point the forms of the nonlinear terms are introduced in the guise of a scale-dependent turbulent viscosity and magnetic diffusivity:

$$\hat{f}_n^{\text{v-nonlin}} = \hat{\nu}_n \left(\frac{\mathrm{d}^2\hat{v}_n}{\mathrm{d}z^2} - \frac{n^2\pi^2}{q^2}\hat{v}_n \right), \tag{4.17}$$

$$\hat{f}_n^{\text{b-nonlin}} = \hat{\eta}_n \left(\frac{\mathrm{d}^2\hat{b}_n}{\mathrm{d}z^2} - \frac{n^2\pi^2}{q^2}\hat{b}_n \right), \tag{4.18}$$

which are akin to the transforms of $\nu\nabla^2 v$ and $\eta\nabla^2 b$, but now with scale-dependent turbulent viscosity and magnetic diffusivity[5]. For the sake of mathematical tractability the turbulent viscosity and magnetic diffusivity are assumed to be x-dependent only. The ordinary differential equations in z,

$$\frac{\mathrm{d}\hat{b}_0}{\mathrm{d}z} + \hat{\nu}_0 \frac{\mathrm{d}^2\hat{v}_0}{\mathrm{d}z^2} = 0, \tag{4.19}$$

$$\frac{\mathrm{d}\hat{v}_0}{\mathrm{d}z} + \hat{\eta}_0 \frac{\mathrm{d}^2\hat{b}_0}{\mathrm{d}z^2} = 0, \tag{4.20}$$

$$\frac{\mathrm{d}\hat{b}_n}{\mathrm{d}z} + \hat{\nu}_n \left(\frac{\mathrm{d}^2\hat{v}_n}{\mathrm{d}z^2} - \frac{n^2\pi^2}{q^2}\hat{v}_n \right) = 0, \tag{4.21}$$

$$\frac{\mathrm{d}\hat{v}_n}{\mathrm{d}z} + \hat{\eta}_n \left(\frac{\mathrm{d}^2\hat{b}_n}{\mathrm{d}z^2} - \frac{n^2\pi^2}{q^2}\hat{b}_n \right) = 0, \tag{4.22}$$

[5] The $-\hat{\nu}_n k^2 \hat{v}_n$ and $-\hat{\eta}_n k^2 \hat{b}_n$ components can be considered as having been adopted from Eqs. (1.112) and (1.113) and so are not completely ad hoc in nature — the $\hat{\nu}_n \mathrm{d}^2\hat{v}_n/\mathrm{d}z^2$ and $\hat{\eta}_n \mathrm{d}^2\hat{b}_n/\mathrm{d}z^2$ terms cannot be justified so easily, however, due to the inconsistency between the 3D transforms of Pouquet et al. (1976) and the 1D transforms used here.

subject to the boundary conditions,

$$\left.\frac{\mathrm{d}\hat{b}_n}{\mathrm{d}z}\right|_{z=1} = 0, \tag{4.23}$$

$$\hat{v}_n(1) = \hat{V}_n, \tag{4.24}$$

for all $n \geq 0$, are solved in a manner similar to that of Heyvaerts and Priest, apart from the introduction of $\hat{\nu}_n$, $\hat{\eta}_n$, $H_n = \sqrt{\hat{\eta}_n \hat{\nu}_n}$ and with a complex $\hat{V}_n$, until

$$\hat{v}_n(z) = \frac{\lambda_n^2 \hat{V}_n}{\sqrt{1+4\lambda_n^2}} \left(\frac{\sinh\left(\sigma_- \frac{z}{H_n}\right)}{\sigma_- \sinh \frac{\sigma_-}{H_n}} + \frac{\sinh\left(\sigma_+ \frac{z}{H_n}\right)}{\sigma_+ \sinh \frac{\sigma_+}{H_n}} \right), \tag{4.25}$$

$$\hat{b}_n(z) = \frac{\hat{\nu}_n}{H_n} \frac{\lambda_n^2 \hat{V}_n}{\sqrt{1+4\lambda_n^2}} \left(\frac{\cosh\left(\sigma_- \frac{z}{H_n}\right)}{\sigma_- \sinh \frac{\sigma_-}{H_n}} - \frac{\cosh\left(\sigma_+ \frac{z}{H_n}\right)}{\sigma_+ \sinh \frac{\sigma_+}{H_n}} \right), \tag{4.26}$$

where

$$\lambda_n = \sqrt{\hat{\eta}_n \hat{\nu}_n}\, \frac{n\pi}{q}, \tag{4.27}$$

$$V(x) = \sum_{n=0}^{\infty} \hat{V}_n \mathrm{e}^{in\pi x/q}, \tag{4.28}$$

$$\sigma_\pm = \frac{1}{2}(\sqrt{1+4\lambda_n^2} \pm 1). \tag{4.29}$$

The case $n = 0$, not explicitly given by Heyvaerts and Priest, has general solution

$$\hat{v}_0(z) = A \sinh\left(\frac{z}{\sqrt{\hat{\eta}_0 \hat{\nu}_0}}\right), \tag{4.30}$$

$$\hat{b}_0(z) = -A\sqrt{\frac{\hat{\nu}_0}{\hat{\eta}_0}} \cosh\left(\frac{z}{\sqrt{\hat{\eta}_0 \hat{\nu}_0}}\right) + B, \tag{4.31}$$

where A and B are arbitrary constants and the odd and even natures of $\hat{v}_0(z)$ and $\hat{b}_0(z)$ have been preserved. These solutions exhibit boundary layer behaviour depending on the inverse Hartmann number $\sqrt{\hat{\eta}_0 \hat{\nu}_0}$ (Montgomery, 1993). However, the problem under consideration is not a true boundary layer situation because the turbulent resistivity is discontinuous, taking a finite value in the corona ($|z| > 1$) and zero at the photosphere ($z = \pm 1$). The requirement that the tangential component of the electric field be zero at the boundary then introduces the artificial boundary condition, Eq. (4.23), which removes the hyperbolic behaviour and, together with Eq. (4.24), leads to the solution

$$\hat{v}_0(z) = \hat{V}_0 = 0, \tag{4.32}$$

$$\hat{b}_0 = \text{arbitrary constant}. \tag{4.33}$$

The z-component of the dimensionless Poynting flux ($\boldsymbol{e} \times \boldsymbol{b}$) can be easily calculated from the above results and Eqs. (3.21) and (3.22). When averaged in the x-direction this gives a form

equivalent to that of Heyvaerts and Priest with the turbulent viscosity and magnetic diffusivity now being scale-dependent. For computational purposes, however, this is now recast in terms of hyperbolic cotangents to avoid the overflow problems associated with taking the ratio of large numerator and denominator. Thus,

$$|\langle\phi_{z\text{-poynt}}\rangle| = \sum_{n=1}^{\infty} \frac{\hat{\nu}_n}{H_n} \frac{|\hat{V}_n|^2}{\sqrt{1+4\lambda_n^2}} \left(\sigma_+ \coth \frac{\sigma_-}{H_n} - \sigma_- \coth \frac{\sigma_+}{H_n} \right). \tag{4.34}$$

The viscous flux was calculated with the assumption of constant viscosity in the viscous stress tensor, however, and the earlier result cannot be adopted without further justification. The "viscous" forces in the momentum equation may still be expressed as the divergence of a viscous stress tensor, $\boldsymbol{f}_{\text{v-nonlin}} = \nabla \cdot \overline{\overline{\sigma}}$, and the viscous heating flux as $-\boldsymbol{v} \cdot \overline{\overline{\sigma}}$. Although expressions for $\overline{\overline{\sigma}}$ are unavailable in physical space they can be transformed to Fourier space where

$$\hat{f}_n^{\text{visc}} = \frac{in\pi}{q} \hat{\sigma}_n^{\text{yx}} + \frac{\mathrm{d}}{\mathrm{d}z} \hat{\sigma}_n^{\text{yz}}. \tag{4.35}$$

Comparing this with the form of the nonlinear force adopted earlier, Eq. (4.17), leads to a particular form for the stress tensor consistent with both these expressions:

$$\hat{\sigma}_n^{\text{yz}} = \hat{\nu}_n \frac{\mathrm{d}\hat{v}_n}{\mathrm{d}z}, \tag{4.36}$$

$$\hat{\sigma}_n^{\text{yx}} = \frac{in\pi}{q} \hat{\nu}_n \hat{v}_n. \tag{4.37}$$

The average flux injected over one boundary is then simply

$$\langle\phi_{z\text{-visc}}\rangle = \sum_{n=1}^{\infty} \hat{\nu}_n \hat{v}_n^* \frac{\mathrm{d}\hat{v}_n}{\mathrm{d}z}, \tag{4.38}$$

since $\mathrm{d}\hat{v}_0/\mathrm{d}z = 0$, which again leads to the form of the viscous flux calculated previously but now with scale-dependent turbulent viscosity and magnetic diffusivity. This is recast as

$$|\langle\phi_{z\text{-visc}}\rangle| = \sum_{n=1}^{\infty} \frac{\hat{\nu}_n}{H_n} \frac{|\hat{V}_n|^2}{\sqrt{1+4\lambda_n^2}} \left(\lambda_n^2 \coth \frac{\sigma_-}{H_n} + \lambda_n^2 \coth \frac{\sigma_+}{H_n} \right), \tag{4.39}$$

with $|\hat{V}_n|^2$ rather than V_n^2. Thus, the total flux injected through both boundaries is

$$F = 2 \sum_{n=1}^{\infty} \sqrt{\frac{\hat{\nu}_n}{\hat{\eta}_n}} \frac{|\hat{V}_n|^2}{\sqrt{1+4\lambda_n^2}} \left[\sigma_+^2 \coth \frac{\sigma_-}{H_n} + \sigma_-^2 \coth \frac{\sigma_+}{H_n} \right]. \tag{4.40}$$

The factor 2 appears here because of the form of the transform and inverse transform, Eqs. (4.1) and (4.2). Any average over x will be double that obtained with the cos and sin form of the Fourier expansion. In this case, however, the spectrum of photospheric motions is halved, Eq. (4.9), so that there is no net effect.

To an accuracy of 10^{-15}, $\coth x$ is indistinguishable from 1 whenever $x > 20$. In this case the flux above simplifies to

$$2 \sum_{n=1}^{\infty} \sqrt{\frac{\hat{\nu}_n}{\hat{\eta}_n}} \frac{|\hat{V}_n|^2}{\sqrt{1+4\lambda_n^2}} (1 + 2\lambda_n^2) \tag{4.41}$$

once the definitions of $\sigma_\pm$ have been taken into account. The condition for the transition between Eqs. (4.40) and (4.41) is that $\sigma_\pm/H_n > 20$ to ensure that both the coth terms have become unity. For the scale-independent turbulent viscosity and magnetic diffusivity of Heyvaerts and Priest this gives

$$n > \frac{q}{\pi}\sqrt{20(20 \mp X)}, \tag{4.42}$$

[6]where $X = 1/H$. Taking the positive sign then gives the critical number of terms as

$$N_c = \left[\frac{q}{\pi}\sqrt{20(20+X)}\right], \tag{4.43}$$

where the square brackets denote taking the integer part of the enclosed expression. The case of the scale-dependent turbulent viscosity and magnetic diffusivity currently under consideration is more complicated because the H_n term also depends on n. The corresponding condition is

$$n > \frac{q}{\pi}\sqrt{20(20 \mp Y n^{3/2})}, \tag{4.44}$$

with $Y = 1/H_1 = 1/\sqrt{\hat{\nu}_1\hat{\eta}_1}$. This can then be re-written as a quartic inequality in n, but rather than do that a simpler approximation can be made by noting that Y will be much larger than unity since the dimensionless turbulent viscosity and magnetic diffusivity evaluated at the largest scale of the system are inverse viscous and resistive Lundquist numbers which will be much less than unity; also $n \geq 1$ so that, on taking the positive sign for reasons already mentioned, the $20Yn^{3/2}$ term dominates, giving an approximate critical number of terms as

$$N_c = \left[400\left(\frac{q}{\pi}\right)^4 Y^2\right]. \tag{4.45}$$

Returning to Eq. (4.41) it will be seen from Eq. (4.53) that for large n, λ_n will be small and the term being summed is approximately $|\hat{V}_n|^2$ which is proportional to $n^{-5/3}$ when a Kolmogorov spectrum is used, Eq. (4.9). The infinite sum is then convergent, unlike the case of the constant turbulent viscosity and magnetic diffusivity, when the sum is proportional to $n^{-2/3}$ (Sect. 3.5.1).

With this cutoff the large-scale injected total flux may now be written as

$$\begin{aligned} F &= 2\sum_{n=1}^{N_c}\sqrt{\frac{\hat{\nu}_n}{\hat{\eta}_n}}\frac{|\hat{V}_n|^2}{\sqrt{1+4\lambda_n^2}}\left[\sigma_+^2\coth\frac{\sigma_-}{H_n}+\sigma_-^2\coth\frac{\sigma_+}{H_n}\right] \\ &\quad +2\sum_{n=N_c+1}^{\infty}\sqrt{\frac{\hat{\nu}_n}{\hat{\eta}_n}}\frac{|\hat{V}_n|^2}{\sqrt{1+4\lambda_n^2}}(1+2\lambda_n^2). \end{aligned} \tag{4.46}$$

The boundary between nonlinear effects and the adoption of terms akin to viscous and diffusive effects is very blurred in the foregoing justification of scale-dependent turbulent effects, which is not surprising given the ill-defined nature of turbulent viscosity and magnetic diffusivity in MHD. However, short of detailed numerical investigations there seems to be little else to try while still remaining within the framework of Heyvaerts and Priest (1992).

[6]If $X > 20$, $\coth(\sigma_+/H)$ is always indistinguishable from unity.

4.6 Local eddy-damping

In evaluating the expressions for the turbulent viscosity and magnetic diffusivity, Eqs. (3.60) and (3.61), an expression has to be used for the eddy damping rate. Rather than use the full expression used by Pouquet et al. which involves molecular dissipation, nonlinear scrambling and relaxation by Alfvén waves, Heyvaerts and Priest focused on the latter effect, Eq. (3.62), from which an expression can be derived for the triad-relaxation rate $\mu_{kpq} = \mu_k + \mu_p + \mu_q$. In deriving Eq. (3.67) the form μ_{kqq} was used to describe the effects of small scales q on the scale of interest k. Heyvaerts and Priest then approximated μ_{kqq} as $2\mu_q$ which would be the case if $k \ll q$ from Eq. (3.62). However, by choosing the value of the expansion parameter used by Pouquet et al. to be $a = 1$ they implicitly focused on local wavenumber interactions, in which case $k \approx q$ and the non-local triad-relaxation rate becomes $\mu_{kqq} \approx 3\mu_q$. Equation (3.67) then becomes

$$\eta_m = \nu_k^{\mathrm{v}} = \frac{4C}{9\sqrt{3}}\sqrt{\frac{\varepsilon}{c_{a0}}}k^{-3/2}. \tag{4.47}$$

A new form of the turbulent viscosity and magnetic diffusivity may be obtained directly from Eq. (4.47) by retaining the k-dependence. This is because a structure of size $2\pi/k$ can only react to smaller scale turbulent motions in a diffusive way, giving a magnetic diffusivity dependent on k. For $a = 1$, non-dimensionalising and using Eq. (3.71) gives

$$\eta(k) = \frac{4\,C}{9\sqrt{3}}\left(\frac{F}{2}\right)^{1/2} k^{-3/2}, \tag{4.48}$$

$$\nu(k) = \frac{7}{5}\eta(k). \tag{4.49}$$

These may be regarded as approximations to the discrete Fourier transforms $\hat{\eta}_n$ and $\hat{\nu}_n$ by letting $k = n\pi/q$. Thus,

$$\hat{\eta}_n = n^{-3/2}\,\hat{\eta}_1, \tag{4.50}$$

$$\hat{\nu}_n = n^{-3/2}\,\hat{\nu}_1, \tag{4.51}$$

which enables the parameters H_n and λ_n to be written as

$$H_n = n^{-3/2}H_1, \tag{4.52}$$

$$\lambda_n = \frac{\pi}{q}n^{-1/2}H_1, \tag{4.53}$$

where $H_1 = \sqrt{\hat{\eta}_1\hat{\nu}_1}$. In particular,

$$\hat{\nu}_1 = \frac{28C}{45\sqrt{3}}\left(\frac{F}{2}\right)^{1/2}\left(\frac{\pi}{q}\right)^{-3/2}, \tag{4.54}$$

which, when inverted, gives

$$F = \frac{6075}{392\,C^2}\left(\frac{\pi}{q}\right)^{3}\hat{\nu}_1^2, \tag{4.55}$$

while

$$\hat{\eta}_1 = \frac{5}{7}\hat{\nu}_1. \tag{4.56}$$

Equating with Eq. (4.46) and using Eq. (4.9) leads to a transcendental equation for Y:

$$1 = \frac{224C^2}{3645}\sqrt{\frac{7}{5}}\delta\left(\frac{\overline{v}}{c_{a0}}\right)^2\left(\frac{q}{\pi}\right)^3 Y^2\left\{\sum_{n=1}^{N_c}\frac{n^{-5/3}}{\sqrt{1+4\lambda_n^2}}\left[\sigma_+^2\coth\frac{\sigma_-}{H_n}+\sigma_-^2\coth\frac{\sigma_+}{H_n}\right]\right.$$
$$\left.+\sum_{n=N_c+1}^{\infty}\frac{n^{-5/3}}{\sqrt{1+4\lambda_n^2}}(1+2\lambda_n^2)\right\}, \tag{4.57}$$

where now

$$Y = \frac{1}{H_1} = \sqrt{\frac{7}{5}}\frac{1}{\hat{\nu}_1}, \tag{4.58}$$

$$\lambda_n = \frac{\pi}{qY\sqrt{n}}, \tag{4.59}$$

$$\sigma_\pm = \frac{1}{2}(\sqrt{1+4\lambda_n^2}\pm 1). \tag{4.60}$$

This is solved for the Hartmann number Y, with the scale-dependent transformed viscosity and magnetic diffusivity now being

$$\hat{\nu}_n = \sqrt{\frac{7}{5}}Y^{-1}n^{-3/2}, \tag{4.61}$$

$$\hat{\eta}_n = \sqrt{\frac{5}{7}}Y^{-1}n^{-3/2}, \tag{4.62}$$

and with the power density being obtained from Eq. (4.55).

4.7 Results and Comments

Figure 4.1 compares the results obtained from the Heyvaerts and Priest summation method, Eq. (3.78), using their Kolmogorov spectrum, Eq. (3.54), with the summation method based on the local eddy-damping rate, weighted Kolmogorov spectrum and scale-dependent turbulent viscosity and magnetic diffusivity, Eq. (4.57), and truncating the series when convergence is achieved to six significant figures (which occurs well before N_A, Eq. (3.57)). The curves of turbulent viscosity and power density (and hence turbulent velocity from Eq. (3.74)) reverse order due to the differing numerical coefficients of the power density in Eqs. (3.72) and (4.55). There is no significant difference between the original model of Heyvaerts and Priest (1992) and the results obtained with the modifications introduced in this chapter, which is probably due to the fact that the largest contribution to the injected flux at $k_{\min}$ is little changed by the modifications. It is only the behaviour at the small scales of the large-scale model (still within the inertial range range) which have changed quite significantly (Sect. 4.9).

Figure 4.2 presents the results from the modifications introduced in this chapter for varying magnetic field and inverse aspect ratio. Heating is greater for arcades with large inverse aspect

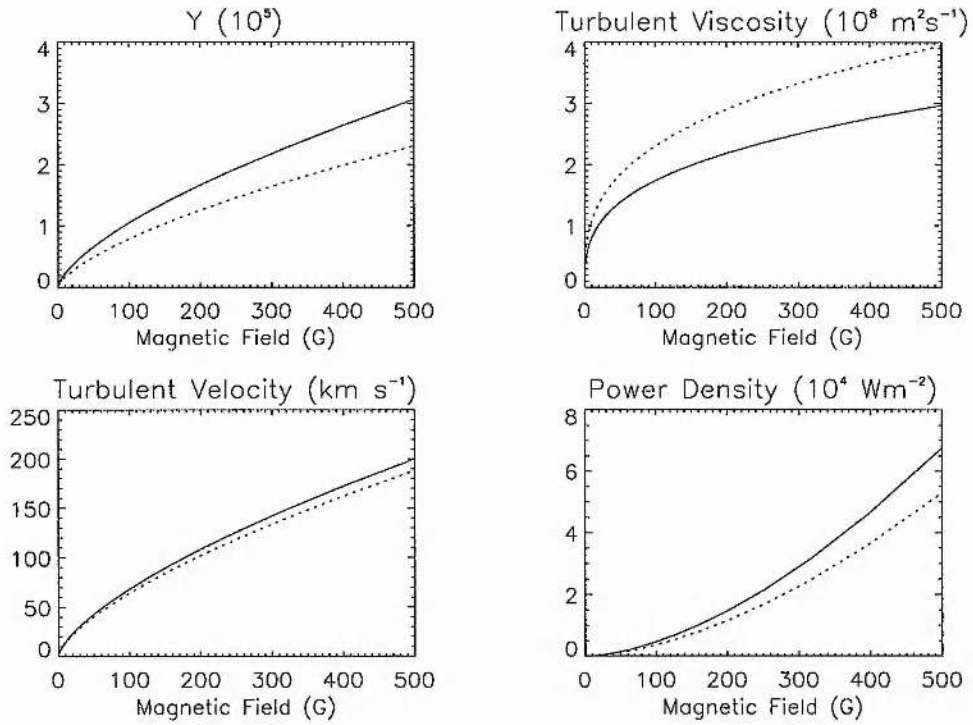

Figure 4.1: Comparison of the various models. The graphs have an inverse aspect ratio of q = 0.1, density = 2×10^{10} cm^{-3}, r.m.s. photospheric velocity = 1 km s^{-1} and half-loop length = 10^4 km. The solid curve shows the results obtained with the scale-dependent turbulent viscosity and magnetic diffusivity model with weighted spectrum and local eddy-damping rate, while the dashed line shows the results from the Heyvaerts and Priest summation form with the unweighted Kolmogorov spectrum. Y is a Hartmann number calculated at the largest scale.

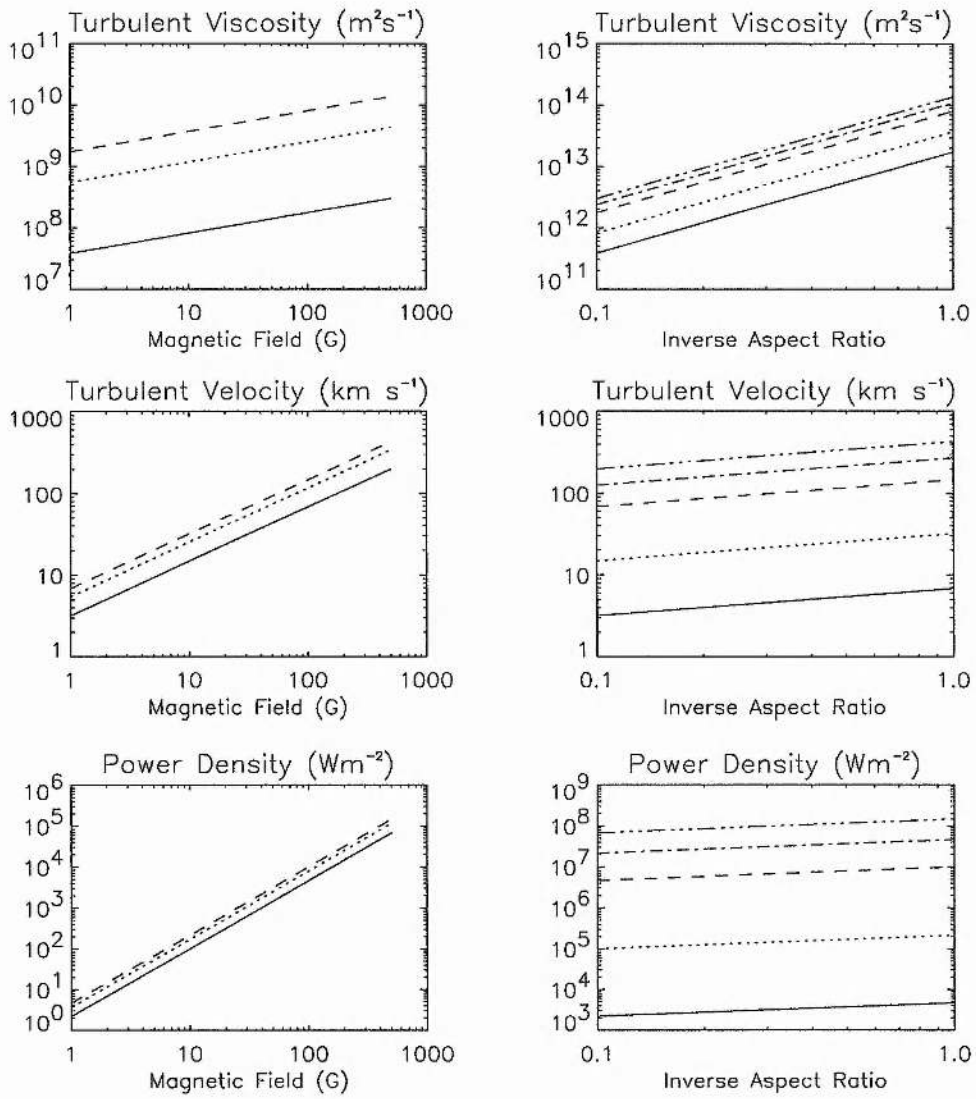

Figure 4.2: Variation of turbulent variables, using the weighted spectrum, scale-dependence and the local eddy-damping rate, with magnetic field in gauss on the left and with inverse aspect ratio on the right. On the left different curves represent arcades with inverse aspect ratios of 0.1 (solid), 0.5 (dotted) and 1.0 (dashed) while on the right the curves represent background magnetic fields, B_0, of 1G, 10G, 100G, 250G and 500G in ascending order. The turbulent viscosity has been evaluated at the maximum horizontal scale of the arcade; the turbulent viscosity at other scales may be obtained by multiplying by $(\pi/(hk))^{3/2}$, where k is the dimensional wavenumber of interest. The density, r.m.s. photospheric velocity and the half-loop length have the same values as in Fig. 4.1.

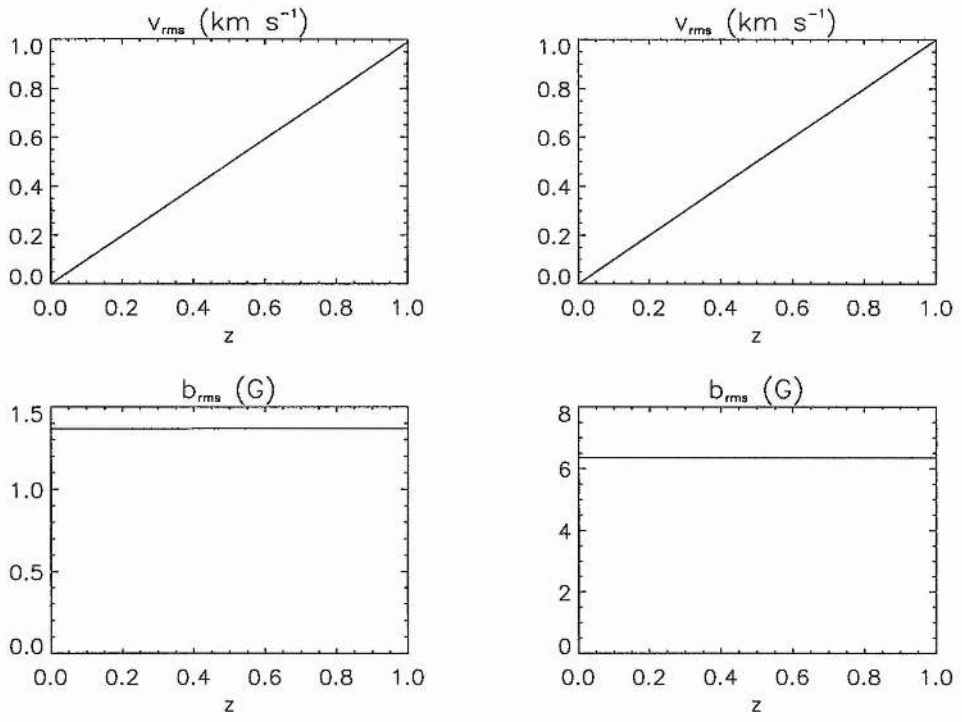

Figure 4.3: Root-mean-square velocity and magnetic field perturbations arising from photospheric shearing. The loop has 10^4 km half-length and inverse aspect ratio 0.1, with density 2×10^{10} cm^{-3} and r.m.s. photospheric velocity of 1 km s^{-1}. The left column corresponds to a background field of 10G and the right 100G.

ratios and large magnetic fields. The former result indicates that thin flux tubes are expected to be locations of lower energy release, while the latter supports the observation that the regions with stronger fields (such as active regions) have greater heating. The actual levels of heating obtained with fields of a few hundred gauss can easily reach values of 10^3–10^4 Wm^{-2} (10^6–10^7 erg cm^{-2}s^{-1}), which is a little higher than the observed levels of heating. However, it should be noted that the line-of-sight magnetic field component along a coronal arcade cannot be easily determined observationally, particularly because the displacement of line spectra through the Zeeman effect can be less than the widths of the lines themselves. These results show that it is possible to attain observed levels of heating for a range of values of coronal density, loop aspect ratio and magnetic field strength.

4.8 Velocity and magnetic fields

Now that the calculations for the turbulent viscosity and magnetic diffusivity have been performed it is possible to say something about the magnitudes of the velocity and magnetic fields

induced by the shearing, Eqs. (4.2), (4.25) and (4.26). Since only the spectrum of kinetic energy is known at the photosphere and not the individual components, $\hat{V}_n$, of the photospheric driving flow it is not possible to calculate the velocity and magnetic field perturbations at a particular position. However, the property that the average in the x-direction may be expressed as

$$\langle v^2(x,z)\rangle = \sum_{n=1}^{\infty} |\hat{v}_n(z)|^2, \tag{4.63}$$

can be used, where $\hat{V}_0$ has been taken to be zero to avoid problems when the Kolmogorov spectrum, Eq. (4.9), is applied. A similar expression is obtained for the magnetic field, and taking the square root of each gives a root-mean-square value for the perturbation at height z. These have been plotted in Fig. 4.3 for the usual 10^4 km half-length, 0.1 inverse aspect ratio loop, with density 2×10^{10} cm^{-3} and r.m.s. photospheric velocity of 1 km s^{-1}. The two cases 10G and 100G background magnetic field have been examined. The apparently linear nature of the r.m.s. velocity and constant r.m.s. magnetic field perturbation may be explained by the following argument. $\hat{\nu}_1$ and $\hat{\eta}_1$ are expected to be small since they represent inverse viscous and resistive Lundquist numbers, respectively. Combining these leads to $H_1 = \sqrt{\hat{\eta}_1\hat{\nu}_1}$ being small. In the limit $H_1 \to 0$: $H_n \to 0, \lambda_n \to 0, \sigma_- \to 0$ and $\sigma_+ \to 1$. Taking the Taylor expansion, $\sigma_-/H_n \simeq H_n(n\pi/q)^2 + O(H_n^3)$, also gives $\sigma_-/H_n \to 0$ while $\sigma_+/H_n \to \infty$. Equation (4.25) can also be written as

$$\hat{v}_n(z) = \frac{\hat{V}_n}{\sqrt{1+4\lambda_n^2}}\left(\sigma_+\frac{\sinh\alpha z}{\sinh\alpha} + \sigma_-\frac{\sinh\beta z}{\sinh\beta}\right), \tag{4.64}$$

since $\sigma_+\sigma_- = \lambda_n^2$ and where $\alpha = \sigma_-/H_n$ and $\beta = \sigma_+/H_n$. Making use of the limits

$$\lim_{\alpha\to0}\frac{\sinh\alpha z}{\sinh\alpha} = z, \tag{4.65}$$

$$\lim_{\beta\to\infty}\frac{\sinh\beta z}{\sinh\beta} = \begin{cases} -1 & z=-1, \\ 0 & -1<z<1, \\ 1 & z=1, \end{cases} \tag{4.66}$$

leads to

$$\lim_{H_1\to0}\hat{v}_n(z) = \hat{V}_n z, \tag{4.67}$$

$$\lim_{H_1\to0} v_{\rm rms}(z) = \overline{v}\,|z|. \tag{4.68}$$

Next, turning to the magnetic field

$$\hat{b}_n(z) = \sqrt{\frac{7}{5}}\frac{\hat{V}_n}{\sqrt{1+4\lambda_n^2}}\left(\sigma_+\frac{\cosh\alpha z}{\sinh\alpha} - \sigma_-\frac{\cosh\beta z}{\sinh\beta}\right), \tag{4.69}$$

since $\hat{\nu}_n/H_n = \sqrt{\hat{\nu}_n/\hat{\eta}_n} = \sqrt{7/5}$. Now

$$\lim_{\alpha\to0+}\frac{\cosh\alpha z}{\sinh\alpha} = \infty, \tag{4.70}$$

$$\lim_{\beta\to\infty}\frac{\cosh\beta z}{\sinh\beta} = \begin{cases} 0 & -1<z<1 \\ 1 & z=\pm1 \end{cases}, \tag{4.71}$$

so that the second term in the bracket of Eq. (4.69) vanishes, but the first term becomes infinite. A useful approximation can be made, however, by Taylor expanding this term in αz and noticing that for $|z| \leq 1$ terms beyond zeroth order are negligible for small α. Thus,

$$\hat{b}_n(z) \simeq \sqrt{\frac{7}{5}}\,\hat{V}_n \left[\sinh\left(\frac{H_1\pi^2\sqrt{n}}{q^2}\right)\right]^{-1}, \tag{4.72}$$

which gives an r.m.s. magnetic field perturbation independent of z to zeroth order.

4.9 Self-consistency of the model

The consistency of the solutions for the large-scale velocity and magnetic field perturbations, Eqs. (3.21) and (3.22), for the scale-dependent solutions, Eqs. (4.25) and (4.26) (note that Eqs. (4.1) and (4.2) apply here), with the prescribed Kraichnan spectrum, Eq. (3.66), can now be re-examined. The dimensionless Kraichnan spectrum is first re-expressed with a weighting factor similar to the Kolmogorov spectrum, Eq. (4.9), as

$$\hat{E}_n = C\iota\sqrt{\frac{Fq}{2\pi}}n^{-3/2}, \tag{4.73}$$

where $\iota = 2/\zeta(3/2) \simeq 0.766$ has been given in terms of the Riemann zeta function. The comparison in Fig. 4.4 shows a greatly improved match between the imposed Kraichnan spectrum and the spectra resulting from the introduction of scale-dependent nonlinear effects. Whereas there was greater variation of the calculated spectra between photosphere and corona in the scale-independent case because the expansion parameter $\alpha = \sigma_-/H \propto Hn^2$, in the scale-dependent case $\alpha \propto H_1 n^{1/2}$ so that for large n the expansions and limits, Eqs. (4.65)–(4.69), are more accurate since α is then much smaller: the improvement over Fig. 3.4 is apparent. The kinetic energy spectrum, however, is four orders of magnitude lower than the imposed Kraichnan spectrum which is to be expected since the Kraichnan spectrum really only becomes applicable at scales at which equipartition of kinetic and magnetic energy is apparent. At large scales the magnetic energy dominates the kinetic energy in the corona, and so the extrapolation of the kinetic energy spectrum inertial range, in particular, must be regarded as an approximation whose effect cannot be determined a priori. For the magnetic energy spectrum at large scales there should strictly be a maximum in the spectrum and then a fall-off to zero towards larger scales: this is reflected in the calculated magnetic energy spectrum having a slightly different power law exponent to that of Kraichnan, namely -2.67. A simple dimensional argument leads to the conclusion that this will have little effect on heating magnitudes. Write the turbulent magnetic diffusivity as

$$\eta(k) = \int_k^\infty \frac{\sqrt{kE(k)}}{k^2}\mathrm{d}k, \tag{4.74}$$

and let $E(k) = Ak^{-\gamma}$, where $\gamma > 1$. If the total energy per unit mass is required to be some characteristic speed squared, i.e. $\int_{k_{\min}}^\infty E(k)\mathrm{d}k = \overline{v}^2$, then $A = \overline{v}^2(\gamma-1)k_{\min}^{\gamma-1}$. The original expression

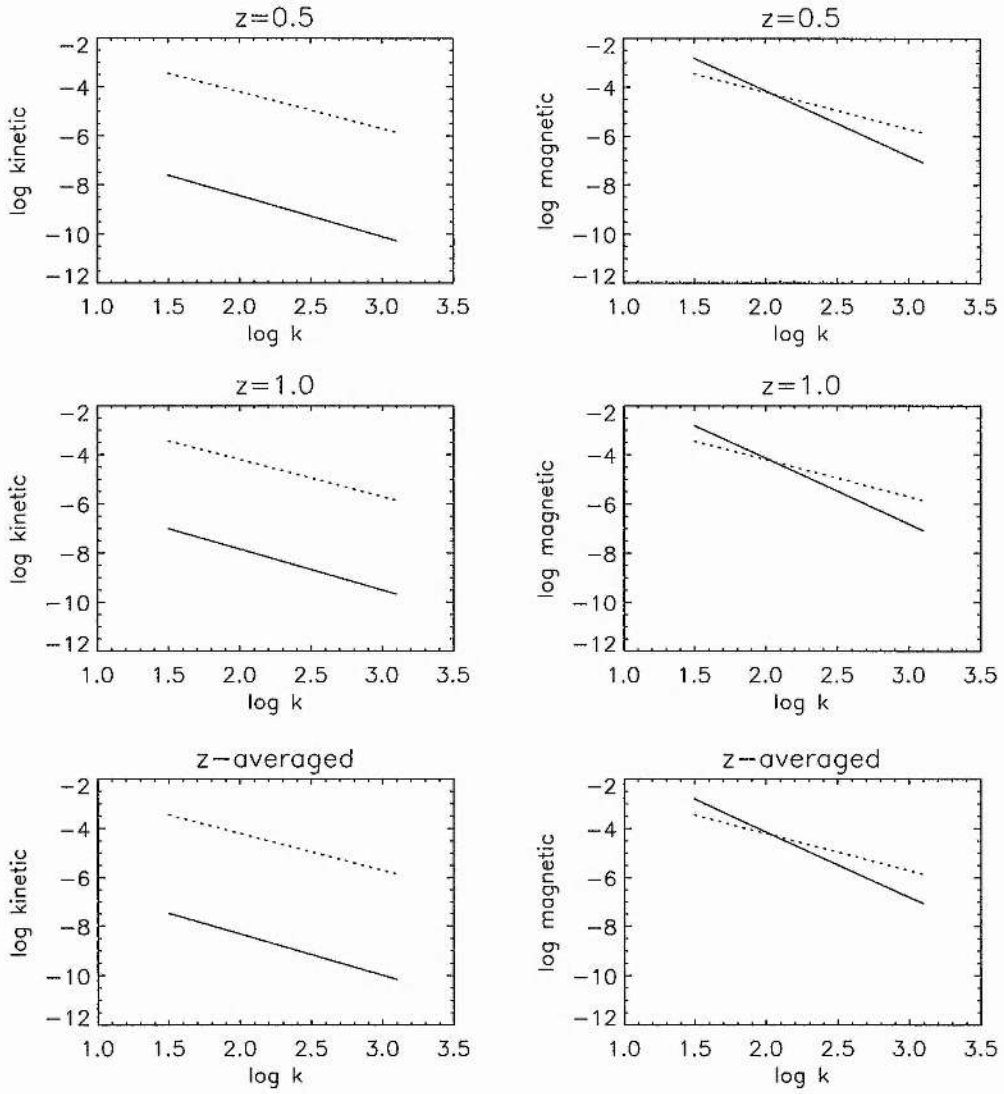

Figure 4.4: Comparison of $|\hat{v}_n(z)|^2/2$ and $|\hat{b}_n(z)|^2/2$ (solid lines) for the scale-dependent turbulent viscosity and magnetic diffusivity using the weighted spectrum, Eq. (4.9) and the local eddy-damping rate averaged over z with the imposed Kraichnan spectrum, Eq. (4.73), for large scales (dotted lines). $z = 0.5$ represents a region of the corona while $z = 1.0$ gives the results at the photosphere; $k = n\pi/q$ is the dimensionless wavenumber. As in Fig. 3.4 the calculated kinetic energy spectrum at the photosphere (solid line) is a $k^{-5/3}$ Kolmogorov spectrum.

for the turbulent magnetic diffusivity, Eq. (4.74), may now be evaluated as

$$\eta(k) = \frac{2\sqrt{\gamma-1}}{\gamma+1}\,\overline{v}\,k_{\rm min}^{(\gamma-1)/2}k^{-(\gamma+1)/2}, \tag{4.75}$$

which, when evaluated at the largest scale, gives

$$\eta(k_{\rm min}) = \frac{2\sqrt{\gamma-1}}{\gamma+1}\frac{\overline{v}}{k_{\rm min}}. \tag{4.76}$$

Once the characteristic speed and maximum scale have been determined it is unlikely that there will be more than an order of magnitude difference in the turbulent magnetic diffusivity, and hence heating, if γ varies by much. This is further strengthened by the fact that there is little difference between the heating obtained with scale-independent and scale-dependent coefficients (Fig. 4.1) despite greatly differing spectral behaviour (Figs. 3.4 and 4.4).

Chapter 5

Twisted Flux Tube

5.1 Calculation of the global steady state

Consider a flux tube being twisted by vortical motions at the photosphere (Fig. 5.1) and modelled as a straight cylinder (Fig. 5.2) defined in the region $-l \leq z \leq l,\ 0 \leq \theta < 2\pi,\ 0 \leq r \leq h$ in cylindrical polar coordinates. The dimensionless MHD equations, Eqs. (3.15)–(3.20), are used once again but this time with a pressure tensor, p, in the momentum equation:

$$\frac{\partial \boldsymbol{v}}{\partial \tau} + (\boldsymbol{v} \cdot \nabla)\boldsymbol{v} = -\nabla \cdot \mathsf{p} + \boldsymbol{j} \times \boldsymbol{b} + \nu \nabla^2 \boldsymbol{v}. \tag{5.1}$$

The pressure tensor has $p_{rr} = p_{\theta\theta} = p_\perp$, $p_{zz} = p_\parallel$ and the other components zero. In dimensionless coordinates, non-dimensionalised with respect to l again, the coronal flux tube is located in the region $-1 \leq z \leq 1,\ 0 \leq \theta < 2\pi,\ 0 \leq r \leq q$, where $q = h/l$ is the inverse aspect ratio of the flux tube. Time-independent solutions for the velocity and magnetic fields are sought, of the form

$$\boldsymbol{v} = v(r,z)\,\hat{\boldsymbol{\theta}}, \tag{5.2}$$

$$\boldsymbol{b} = \hat{\boldsymbol{z}} + b(r,z)\,\hat{\boldsymbol{\theta}}. \tag{5.3}$$

A boundary flow $V(r)\,\hat{\boldsymbol{\theta}}$ is imposed at the photosphere, with $V(r)$ being considered as a stochastic function. To model the twisting nature of this flow, the velocity component $v(r,z)$ is chosen to be an odd function of z to ensure rotation in opposite directions at the top and bottom of the straightened cylinder, corresponding to rotation in the same sense at the photosphere (Figs. 5.1 and 5.2); the magnetic field component $b(r,z)$ is assumed to be even in z to give a simple helical field. The velocity and perturbed magnetic field are assumed to be zero at the edge of the flux tube, $r = q$, for simplicity. A footpoint boundary condition is again obtained from the requirement that the electric field, $\mathbf{e} = -\boldsymbol{v} \times \boldsymbol{b} + \eta \boldsymbol{j}$, have its tangential component continuous across the photospheric boundary. With flux freezing implying $\eta = 0$ in the photosphere, the photospheric and coronal

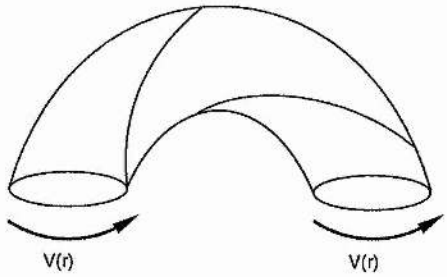

Figure 5.1: A flux tube twisted up by the vortical motions of convection cells at the photosphere.

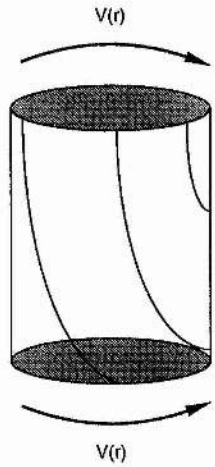

Figure 5.2: Straight cylindrical model of the twisted flux tube.

electric fields at $z = 1$ are

$$\boldsymbol{e}_{\rm phot} = -V(r)\,\hat{\mathbf{r}}, \tag{5.4}$$

$$\boldsymbol{e}_{\rm corona} = -\left(V(r) + \eta\frac{\partial b}{\partial z}\right)\hat{\mathbf{r}} + \frac{\eta}{r}\frac{\partial}{\partial r}(rb)\hat{\mathbf{z}}. \tag{5.5}$$

Comparison of the r-components of Eqs. (5.4) and (5.5) shows that $\partial b/\partial z = 0$ at $z = \pm 1$ is required to ensure this continuity. The boundary conditions are thus :

$$v(r,z) = -v(r,-z), \tag{5.6}$$

$$b(r,z) = b(r,-z), \tag{5.7}$$

$$v(r,1) = V(r), \tag{5.8}$$

$$\frac{\partial b}{\partial z} = 0 \text{ at } z = \pm 1, \tag{5.9}$$

$$v(q,z) = 0, \tag{5.10}$$

$$b(q,z) = 0. \tag{5.11}$$

The θ-components of Eqs. (5.1) and (3.16) are

$$\frac{\partial b}{\partial z} + \nu\nabla^2 v = \nu\frac{v}{r^2}, \tag{5.12}$$

$$\frac{\partial v}{\partial z} + \eta\nabla^2 b = \eta\frac{b}{r^2}, \tag{5.13}$$

while the r- and z-components of Eq. (3.16) vanish identically and the r- and z-components of Eq. (5.1) reduce to

$$\frac{\partial}{\partial r}\left(p_\perp + \frac{b^2}{2}\right) = \frac{v^2 - b^2}{r}, \tag{5.14}$$

$$\frac{\partial}{\partial z}\left(p_\parallel + \frac{b^2}{2}\right) = 0, \tag{5.15}$$

which determine the gas pressure once the velocity and magnetic field have been calculated. A simple scalar pressure is inadequate, since if $p_\perp = p_\parallel$ then the requirement that the z-derivative of Eq. (5.14) equal the r-derivative of Eq. (5.15) implies that $v^2 - b^2$ must be independent of z. However, the choice of $v(r,z)$ as an odd function of z and $b(r,z)$ as an even function of z precludes the possibility that $v \equiv b$, so that both v and b must individually be independent of z. Equation (5.12) simplifies to $\mathrm{d}^2v/\mathrm{d}r^2 + 1/r\,\mathrm{d}v/\mathrm{d}r - v/r^2 = 0$, with general solution $v = Ar + B/r$: the only solution satisfying Eq. (5.10) which is not singular at $r = 0$ is then $v \equiv 0$; and likewise for b. A pressure tensor is thus required in order to retain z-dependence and enable the coronal v and b to be sustained by the photospheric flow against dissipation. Kulsrud (1984) uses a pressure tensor of the form used here when formulating a fluid theory for collisionless plasmas. This is probably more appropriate for fusion problems than is MHD but is harder to justify in the present context. However, it does provide a means to find a simple exact solution to the momentum and induction equations and so is hereafter retained.

Expressing the Laplacian in cylindrical geometry, Eqs. (5.12) and (5.13) become

$$\frac{\partial^2 v}{\partial r^2} + \frac{\partial^2 v}{\partial z^2} + \frac{1}{r}\frac{\partial v}{\partial r} - \frac{v}{r^2} + \frac{1}{\nu}\frac{\partial b}{\partial z} = 0, \tag{5.16}$$

$$\frac{\partial^2 b}{\partial r^2} + \frac{\partial^2 b}{\partial z^2} + \frac{1}{r}\frac{\partial b}{\partial r} - \frac{b}{r^2} + \frac{1}{\eta}\frac{\partial v}{\partial z} = 0. \tag{5.17}$$

Solutions for v and b are sought in the form of Fourier-Bessel expansions (Watson, 1958, Chap. 18)

$$v(r,z) = \sum_{n=1}^{\infty} \hat{v}_n(z)\, J_1\left(\frac{\gamma_n r}{q}\right), \tag{5.18}$$

$$b(r,z) = \sum_{n=1}^{\infty} \hat{b}_n(z)\, J_1\left(\frac{\gamma_n r}{q}\right), \tag{5.19}$$

where γ_n is the nth root of the first-order Bessel function of the first kind, J_1. The photospheric velocity, $V(r)$, may also be written in this form as

$$V(r) = \sum_{n=1}^{\infty} \hat{V}_n\, J_1\left(\frac{\gamma_n r}{q}\right). \tag{5.20}$$

In all these expansions the hatted quantities are now Fourier-Bessel transforms given by

$$\mathcal{FB}(f(r)) = \hat{f}_{n,p} = \frac{2}{q^2}\left[\mathrm{J}_{p+1}(\gamma_n)\right]^{-2} \int_0^q r \mathrm{J}_p\left(\frac{\gamma_n r}{q}\right) f(r)\mathrm{d}r, \tag{5.21}$$

and where the orthogonality condition is

$$\int_0^q r \mathrm{J}_p\left(\frac{\gamma_n r}{q}\right) \mathrm{J}_p\left(\frac{\gamma_m r}{q}\right) \mathrm{d}r = \frac{q^2}{2}\mathrm{J}^2_{p+1}(\gamma_n)\delta_{nm}. \tag{5.22}$$

Throughout this chapter the case $p = 1$ is taken — $\hat{f}_n$ will be used to denote this case without explicitly including the subscript 1.

Equations (5.16) and (5.17), with the use of Eqs. (5.18) and (5.19), then simplify to

$$\frac{\mathrm{d}\hat{b}_n}{\mathrm{d}z} + \nu\left(\frac{\mathrm{d}^2\hat{v}_n}{\mathrm{d}z^2} - \frac{\gamma_n^2}{q^2}\hat{v}_n\right) = 0, \tag{5.23}$$

$$\frac{\mathrm{d}\hat{v}_n}{\mathrm{d}z} + \eta\left(\frac{\mathrm{d}^2\hat{b}_n}{\mathrm{d}z^2} - \frac{\gamma_n^2}{q^2}\hat{b}_n\right) = 0, \tag{5.24}$$

with transformed boundary conditions

$$\hat{v}_n(z) = -\hat{v}_n(-z), \tag{5.25}$$

$$\hat{b}_n(z) = \hat{b}_n(-z), \tag{5.26}$$

$$\hat{v}_n(1) = \hat{V}_n, \tag{5.27}$$

$$\frac{\mathrm{d}\hat{b}_n}{\mathrm{d}z} = 0 \text{ at } z = 1. \tag{5.28}$$

The approach of Sect. 4.5 is followed once more, with the consequence that ν and η in Eqs. (5.23) and (5.24) become $\hat{\nu}_n$ and $\hat{\eta}_n$. These are approximated as $\hat{\eta}_n \simeq \eta(k)$ and $\hat{\nu}_n \simeq \nu(k)$ with $\eta(k)$ and

$\nu(k)$ again given by Eqs. (4.48) and (4.49). Thus

$$\hat{\eta}_n = \left(\frac{\gamma_n}{\gamma_1}\right)^{-3/2} \hat{\eta}_1, \tag{5.29}$$

$$\hat{\nu}_n = \left(\frac{\gamma_n}{\gamma_1}\right)^{-3/2} \hat{\nu}_1, \tag{5.30}$$

where $\hat{\nu}_1$ and $\hat{\eta}_1$ are given by Eqs. (4.54) and (4.56).

A solution to Eqs. (5.23) and (5.24) of the form $\exp(\sigma z)$ is again sought and the boundary conditions are applied to obtain

$$\hat{v}_n(z) = \frac{\lambda_n^2 \hat{V}_n}{\sqrt{1+4\lambda_n^2}} \left(\frac{\sinh \frac{\sigma_- z}{H_n}}{\sigma_- \sinh \frac{\sigma_-}{H_n}} + \frac{\sinh \frac{\sigma_+ z}{H_n}}{\sigma_+ \sinh \frac{\sigma_+}{H_n}} \right), \tag{5.31}$$

$$\hat{b}_n(z) = \frac{\hat{\nu}_n}{H_n} \frac{\lambda_n^2 \hat{V}_n}{\sqrt{1+4\lambda_n^2}} \left(\frac{\cosh \frac{\sigma_- z}{H_n}}{\sigma_- \sinh \frac{\sigma_-}{H_n}} - \frac{\cosh \frac{\sigma_+ z}{H_n}}{\sigma_+ \sinh \frac{\sigma_+}{H_n}} \right), \tag{5.32}$$

where

$$\lambda_n = \sqrt{\hat{\eta}_n \hat{\nu}_n} \frac{\gamma_n}{q}, \tag{5.33}$$

$$H_n = \sqrt{\hat{\eta}_n \hat{\nu}_n}, \tag{5.34}$$

$$\sigma_\pm = \frac{1}{2}(\sqrt{1+4\lambda_n^2} \pm 1), \tag{5.35}$$

which differs from Eqs. (4.25) and (4.26) in the parameter λ_n and the form of $\hat{V}_n$ yet to be derived.

Using the photospheric electric field, Eq. (5.4), the Poynting flux out of the cylinder (i.e. from corona to photosphere) is

$$\begin{aligned} \phi_{\text{zPoynt}} &= \hat{\boldsymbol{z}} \cdot (\mathbf{e} \times \boldsymbol{b}) \\ &= -V(r)\, b(r,1). \end{aligned} \tag{5.36}$$

Similarly, the viscous flux is

$$\begin{aligned} \phi_{\text{zvisc}} &= \hat{\boldsymbol{z}} \cdot (-\boldsymbol{v} \cdot \Pi) \\ &= -v\, \Pi_{\theta z}, \end{aligned} \tag{5.37}$$

where Π is the dimensionless viscous stress tensor, whose divergence gives the viscous force. Its form is not known in physical space, following the adoption of the form for the viscous force in Fourier-Bessel space with scale-dependent turbulent viscosity and magnetic diffusivity. Taking the form for the velocity to be that of Eq. (5.2), the conventional viscous stress tensor with constant viscosity reduces to $\Pi_{r\theta} = \nu(\partial v/\partial r - v/r)$ and $\Pi_{\theta z} = \nu \partial v/\partial z$, with all other components being zero. The stress tensor is chosen which has

$$\Pi_{r\theta} = \sum_{n=1}^{\infty} \hat{V}_n \left[-\frac{2}{r} \mathrm{J}_1\left(\frac{\gamma_n r}{q}\right) + \frac{\gamma_n}{q} \mathrm{J}_0\left(\frac{\gamma_n r}{q}\right) \right], \tag{5.38}$$

$$\Pi_{\theta z} = \sum_{n=1}^{\infty} \hat{\nu}_n \frac{\mathrm{d}\hat{v}_n}{\mathrm{d}z} \mathrm{J}_1\left(\frac{\gamma_n r}{q}\right), \tag{5.39}$$

all other components being zero, which then satisfies the assumed form for the viscous force in Fourier-Bessel space: $\mathcal{FB}(\nabla \cdot \Pi) = \hat{\nu}_n(\mathrm{d}^2\hat{v}_n/\mathrm{d}z^2 - (\gamma_n^2/q^2)\hat{v}_n)$, leading to

$$\hat{\Pi}_n^{\theta z} = \hat{\nu}_n \frac{\mathrm{d}\hat{v}_n}{\mathrm{d}z}. \tag{5.40}$$

The Poynting and viscous fluxes are averaged over a circle of radius q, with the average being defined as

$$\langle f \rangle = \frac{1}{\pi q^2} \int_0^q 2\pi r f(r) \mathrm{d}r. \tag{5.41}$$

Unlike the Fourier transform, neither the transform of the product of two functions nor that of the average of a function leads to a concise expression in Fourier-Bessel space. However, the transform of the average of the product of two functions can be expressed as

$$\langle f(r)\, g(r) \rangle = \sum_{n=1}^{\infty} \hat{f}_{n,p}\, \hat{g}_{n,p}\, \mathrm{J}_{p+1}^2(\gamma_n), \tag{5.42}$$

by means of the orthogonality condition, Eq. (5.22). Applying Eq. (5.42) to Eqs. (5.36) and (5.37), the average absolute Poynting and viscous flux densities become

$$|\langle \phi_{\mathrm{zPoynt}} \rangle| = \sum_{n=1}^{\infty} \frac{\hat{V}_n^2 \mathrm{J}_2^2(\gamma_n)}{\hat{\eta}_n} \frac{\frac{H_n}{\sqrt{1+4\lambda_n^2}} \sinh \frac{\sqrt{1+4\lambda_n^2}}{H_n} + H_n \sinh \frac{1}{H_n}}{\cosh \frac{\sqrt{1+4\lambda_n^2}}{H_n} - \cosh \frac{1}{H_n}}, \tag{5.43}$$

$$|\langle \phi_{\mathrm{zvisc}} \rangle| = \sum_{n=1}^{\infty} \frac{\hat{V}_n^2 \mathrm{J}_2^2(\gamma_n)}{\hat{\eta}_n} \frac{2\lambda_n^2 \frac{H_n}{\sqrt{1+4\lambda_n^2}} \sinh \frac{\sqrt{1+4\lambda_n^2}}{H_n}}{\cosh \frac{\sqrt{1+4\lambda_n^2}}{H_n} - \cosh \frac{1}{H_n}}, \tag{5.44}$$

respectively. The average total flux density directed into the corona and summed over both boundaries is $F = 2\,|\langle \phi_{\mathrm{zvisc}} \rangle| + 2\,|\langle \phi_{\mathrm{zPoynt}} \rangle|$. Re-writing this in the form of hyperbolic cotangents gives

$$\begin{aligned} F &= 2\sum_{n=1}^{N_c} \sqrt{\frac{\hat{\nu}_n}{\hat{\eta}_n}} \frac{\hat{V}_n^2 J_2^2(\gamma_n)}{\sqrt{1+4\lambda_n^2}} \left[\sigma_+^2 \coth \frac{\sigma_-}{H_n} + \sigma_-^2 \coth \frac{\sigma_+}{H_n} \right] \\ &\quad + 2\sum_{n=N_c+1}^{\infty} \sqrt{\frac{\hat{\nu}_n}{\hat{\eta}_n}} \frac{\hat{V}_n^2 J_2^2(\gamma_n)}{\sqrt{1+4\lambda_n^2}} (1+2\lambda_n^2), \end{aligned} \tag{5.45}$$

which differs from Eq. (4.46) in that $|\hat{V}_n|^2$ is replaced by $\hat{V}_n^2 J_2^2(\gamma_n)$, the former hatted quantity being a Fourier transform and the latter a Fourier-Bessel transform. The wavenumber cutoff condition also changes: starting from $\sigma_\pm/H_n > 20$, the equation corresponding to Eq. (4.44) is

$$\gamma_n^2 > 20q^2 \left(20 \mp Y \left(\frac{\gamma_n}{\gamma_1} \right)^{3/2} \right). \tag{5.46}$$

Since Y is large and $n > 1$ the positive case has the Y term dominant so that

$$\gamma_n > \frac{400 q^4 Y^2}{\gamma_1^3}. \tag{5.47}$$

Finally, approximating $\gamma_n \simeq n\pi$ gives Eq. (4.45) as a starting estimate for n which can then be adjusted until Eq. (5.46) is satisfied.

The analysis used to obtain the form of $\hat{V}_n^2$ in Heyvaerts and Priest (1992) must also be repeated, this time using the cylindrical average, Eq. (5.41). Starting from Eq. (3.49) and the relation

$$c_{a0}^2 \sum_{n=1}^{\infty} V_n^2 \mathrm{J}_2^2(\gamma_n) = \int_{k_{\min}}^{\infty} \overline{V}^2(k)\mathrm{d}k = \overline{v}^2, \tag{5.48}$$

the appropriate weighted spectrum which satisfies this relation is

$$\hat{V}_n^2 = \frac{2}{3}\delta \left(\frac{\overline{v}}{c_{a0}}\right)^2 \mathrm{J}_2^{-2}(\gamma_n) n^{-5/3}, \tag{5.49}$$

with $\delta = 3/(2\zeta(5/3)) \simeq 0.706$ again.

The two expressions for F, Eqs. (4.55) and (5.45), may now be equated to give

$$\begin{aligned} 1 \;=\; & \frac{224C^2}{3645}\sqrt{\frac{7}{5}}\delta \left(\frac{\overline{v}}{c_{a0}}\right)^2 \left(\frac{\gamma_1}{q}\right)^{-3} Y^2 \left\{ \sum_{n=1}^{N_c} \frac{n^{-5/3}}{\sqrt{1+4\lambda_n^2}} \left[\sigma_+^2 \coth\frac{\sigma_-}{H_n} + \sigma_-^2 \coth\frac{\sigma_+}{H_n}\right] \right. \\ & \left. + \sum_{n=N_c+1}^{\infty} \frac{n^{-5/3}}{\sqrt{1+4\lambda_n^2}}(1+2\lambda_n^2) \right\}, \end{aligned} \tag{5.50}$$

which superficially differs from Eq. (4.57) in that π/q is replaced by γ_1/q, but also with

$$\lambda_n \;=\; \frac{\gamma_1^{3/2}}{q\,Y\gamma_n^{1/2}}, \tag{5.51}$$

$$H_n \;=\; \left(\frac{\gamma_1}{\gamma_n}\right)^{3/2} \frac{1}{Y}, \tag{5.52}$$

and again $Y = 1/H_1 = \sqrt{7/5}/\hat{\nu}_1$. Once this has been solved for Y the dimensionless turbulent viscosity and magnetic diffusivity may be obtained using

$$\hat{\nu}_n \;=\; \sqrt{\frac{7}{5}} Y^{-1} \left(\frac{\gamma_1}{\gamma_n}\right)^{3/2}, \tag{5.53}$$

$$\hat{\eta}_n \;=\; \sqrt{\frac{5}{7}} Y^{-1} \left(\frac{\gamma_1}{\gamma_n}\right)^{3/2}. \tag{5.54}$$

Finally the heating flux is calculated from Eq. (4.55).

5.2 Results

Figure 5.3 displays the results obtained with this model for a flux tube of half-length 10^4 km, plasma density 2×10^{16} m^{-3} (2×10^{10} cm^{-3}), r.m.s. photospheric velocity 1 km s^{-1}, and with the background magnetic field strength varying from 1 to 500 G and inverse aspect ratio varying from 0.1 to 1.0. The levels of heating obtained are of the same order of magnitude as those for a sheared arcade of similar proportions (Chap. 4), showing that the twisting process is equally viable

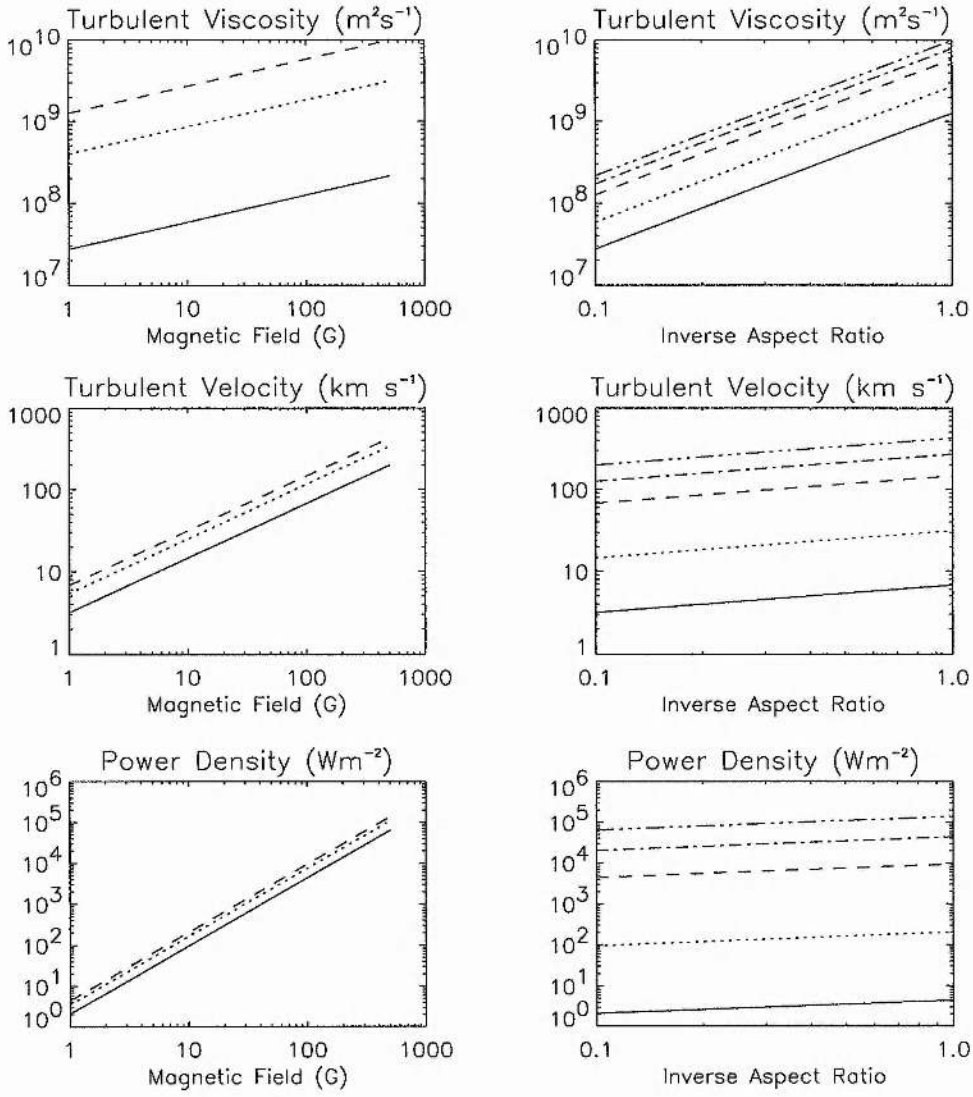

Figure 5.3: Variation of turbulent variables with magnetic field in gauss and with inverse aspect ratio. On the left different curves represent flux tubes with inverse aspect ratios of 0.1 (solid), 0.5 (dotted) and 1.0 (dashed) while on the right the curves represent mean magnetic fields, B_0, of 1G, 10G, 100G, 250G and 500G in ascending order. The density is 2×10^{16} m^{-3} (2×10^{10} cm^{-3}), r.m.s. photospheric velocity is 1 km s^{-1} and the half-loop length is 10^4 km.

for the purposes of coronal heating. This similarity arises because the equations for Y in each model differ only in the λ_n term, which is $\pi/(qY\sqrt{n})$ in the sheared arcade model and $\gamma_1^{3/2}/(qY\gamma_n^{1/2})$ in the twisted flux tube, and also in the coefficient of the transcendental equation, $(\pi/q)^{-3}$ rather than $(\gamma_1/q)^{-3}$. Since for large n, $\gamma_{n+1}-\gamma_n \simeq \pi$ there should be little difference in the heating. Figure 5.3, furthermore, shows that the observed levels of coronal heating of 10 Wm^{-2} (10^4 erg $\mathrm{cm}^{-2}\mathrm{s}^{-1}$) for the quiet Sun to 10^4 Wm^{-2} (10^7 erg $\mathrm{cm}^{-2}\mathrm{s}^{-1}$) for an active region are attainable with an appropriate choice of parameters in this model.

5.3 Velocity and magnetic fields

As with the sheared arcade it is not possible to evaluate the velocity and magnetic fields at large scales since Eqs. (5.31) and (5.32) both depend on the transform of the stochastic photospheric velocity, $\hat{V}_n$, whose behaviour is unknown — only that of $\hat{V}_n^2$ has been estimated. However, the property that

$$\langle v^2(z)\rangle = \sum_{n=1}^{\infty} \hat{v}_n^2(z)\mathrm{J}_2^2(\gamma_n), \tag{5.55}$$

with a similar expression for $b(z)$, may be used to find the r.m.s. velocity and magnetic field using Eqs. (5.31) and (5.49), namely

$$v_{\mathrm{rms}} = \sqrt{\langle v^2(z)\rangle}. \tag{5.56}$$

For a density of 2×10^{16} m^{-3} (2×10^{10} cm^{-3}), half-length 10^4 km, inverse aspect ratio 0.1 and r.m.s. photospheric velocity 1 km s^{-1}, it is found that the coronal r.m.s. velocity varies linearly from 0 km s^{-1} at the loop summit ($z=0$) to 1 km s^{-1} at the photosphere ($z=1$) for B_0 both 10 and 100 G, while the r.m.s. magnetic field perpendicular to the background field is virtually constant with height, differences only appearing in the fourth or fifth significant digit. For a background field of 10 G, the transverse field component is $B_\perp = 1.35$ G and for $B_0 = 100$G, $B_\perp = 6.3$ G.

These results vary little from those of the sheared arcade (Fig. 4.3) where the linear and constant behaviour was accounted for by taking appropriate limits of the expressions for $\hat{v}_n$ and $\hat{b}_n$, except that here $B_\perp$ refers to an azimuthal field component.

5.4 Influence of helicity

In deriving their model Heyvaerts and Priest assume that there is no helicity injected into the coronal plasma by the shearing process. In reality, though, shearing and twisting motions do introduce helicity, which measures the linkage of vortex and flux tubes (Moffatt, 1978; Berger and Field, 1984) and which may affect the energy dissipation process and equilibrium of the structure (Dahlburg et al., 1988; Vekstein et al., 1993; Vekstein et al., 1994; Wolfson et al., 1994) — see also Sect. 1.3.5. Indeed, Pouquet et al. (1976) showed that the injection of kinetic helicity drives

an inverse cascade of magnetic helicity to large scales, although the total energy still cascades to small scales, which has the effect of creating large coherent structures with some associated energy, thus reducing the amount cascading to heat the medium, a process also related to the alpha effect (Keinigs, 1983; Matthaeus et al., 1986; Seehafer, 1994). These structures will exist for long periods of time but eventually succumb to the effects of molecular viscous and resistive forces which, although small at large scales, will take effect in due course. An excellent summary of the effects of both kinetic and magnetic helicity on turbulent flows may be found in Moffatt (1978, Chap. 11), who also further discusses the results of Pouquet et al. (1976).

For the purposes of heating calculations it was desirable to use scale-dependent turbulent viscosity and magnetic diffusivity in order to link the large and small-scale effects; with a Cartesian geometry and the Fourier transforms used in the sheared arcade model of Chap. 4 expressions for the transforms of products, and vector derivatives are readily available, but such quantities are not so easily expressed in terms of the Fourier-Bessel transforms of the present model. The work of this chapter has so far relied on the fact that the transforms of the Laplacian of a vector function and of the average of a product of two functions of radius can be written easily, but when calculating helicities and their rates of injection products and curls are present, making expression in terms of Fourier-Bessel transforms difficult if the viscosity and magnetic diffusivity are r-dependent. The inverse cascade of magnetic helicity to the large scales of a turbulent system, where molecular viscous and resistive forces are negligible, permits reversion to the use of a constant, scale-independent turbulent viscosity and magnetic diffusivity without greatly affecting the conclusions but considerably simplifying the mathematics. This is further backed up by Schoenberg et al. (1984) who use theoretical and empirical arguments based on the reversed field pinch to show that, for the purposes of helicity decay, an effective resistivity is close to the molecular value, whereas for energy decay their effective resistivity greatly exceeds molecular values indicating that turbulence enhances the decay of energy to a much greater extent than it does magnetic helicity. In the following, previously derived expressions will be referred to but in each of these $\hat{\eta}_n = \eta$, $\hat{\nu}_n = \nu$ and $H_n = \sqrt{\eta\nu}$.

The cross helicity $H_c = 1/2\langle \boldsymbol{v} \cdot \boldsymbol{b} \rangle$ at large scales can be shown to be zero from Eqs. (5.2) and (5.3) by noting that $v(x, z)$ is an odd function of z while $b(x, z)$ is even. This is encouraging because the derivation of Pouquet et al.'s energy and helicity spectral evolution equations assumes zero cross-helicity. The kinetic helicity[1], $H_v = 1/2\langle \boldsymbol{v} \cdot \nabla \times \boldsymbol{v} \rangle$, also vanishes at large scales, but the large-scale magnetic helicity $H_m = 1/2\langle \boldsymbol{a} \cdot \boldsymbol{b} \rangle$ is not zero as is now shown. The magnetic vector potential $\boldsymbol{a}$ is defined as $\boldsymbol{b} = \nabla \times \boldsymbol{a}$ which, when taken component-wise along with Eq. (5.3), is

$$\frac{\partial a_\theta}{\partial z} = 0, \tag{5.57}$$

$$\frac{\partial a_r}{\partial z} - \frac{\partial a_z}{\partial r} = b, \tag{5.58}$$

[1] See Moffatt (1978, Sect. 10.5) for details of how kinetic helicity may be injected by sub-photospheric convective motions.

$$\frac{1}{r}\frac{\partial}{\partial r}(ra_\theta) = 1. \tag{5.59}$$

Equations (5.57) and (5.59) together require that $a_\theta = r/2$, the arbitrary constant of integration having been chosen to be zero to avoid a singular vector potential at $r = 0$. The value of a_z is then determined from Eq. (5.58) and, in general, depends on the choice of gauge for $\boldsymbol{a}$. The magnetic helicity will always have a contribution arising from the θ-components of the vector potential and magnetic field which, from the above value for a_θ and Eqs. (5.3), (5.19) and (5.32), leads to

$$H_m = \frac{1}{2\eta}\sum_{n=1}^{\infty}\left(\frac{\gamma_n}{q}\right)^{-3}\hat{V}_n \mathrm{J}_2(\gamma_n), \tag{5.60}$$

where γ_n are the zeros of the first-order Bessel function of the first kind, J_1. This expression is appropriate for the axisymmetric gauge with $a_z = 0$ since the magnetic helicity is then independent of a_r for this simple model. Other gauges would change this value but the key point is that it is non-zero in general. The global magnetic helicity evolution equation is (c.f. Vekstein (1987a))

$$\frac{\partial H_m}{\partial t} = \frac{1}{2}\int(\boldsymbol{a}\cdot\boldsymbol{v})(\boldsymbol{b}\cdot\mathrm{d}\boldsymbol{S}) - \frac{1}{2}\int(\boldsymbol{a}\cdot\boldsymbol{b})(\boldsymbol{v}\cdot\mathrm{d}\boldsymbol{S}) - \frac{1}{2}\int(\eta\boldsymbol{j}\times\boldsymbol{a})\cdot\mathrm{d}\boldsymbol{S} - \frac{1}{2}\int\phi\boldsymbol{b}\cdot\mathrm{d}\boldsymbol{S} - \int\eta\boldsymbol{j}\cdot\boldsymbol{b}\,\mathrm{d}V, \tag{5.61}$$

but with the factor of $1/2$ in the definition of global helicity, all quantities dimensionless and with the electrostatic potential, ϕ, given by

$$\boldsymbol{e} = -\nabla\phi - \frac{\partial\boldsymbol{a}}{\partial t}. \tag{5.62}$$

In a steady state the rate of injection of helicity is given by the four surface terms on the right side of Eq. (5.61), while the rate of decay of helicity within the flux tube is given by the volume term. In order to calculate the rate of injection an expression for the electrostatic potential is required, which can be obtained from the steady state electric field equation obtained from Eqs. (3.18) and (5.62):

$$-\nabla\phi = \eta\boldsymbol{j} - \boldsymbol{v}\times\boldsymbol{b}. \tag{5.63}$$

Using the forms for the velocity and magnetic fields, Eqs. (5.2) and (5.3), this simplifies to

$$\frac{\partial\phi}{\partial r} = \eta\frac{\partial b}{\partial z} + v, \tag{5.64}$$

$$\frac{\partial\phi}{\partial z} = -\frac{\eta}{r}\frac{\partial}{\partial r}(rb), \tag{5.65}$$

with solution

$$\phi = \sum_{n=1}^{\infty}\frac{H\lambda_n^3\hat{V}_n}{\sqrt{1+4\lambda_n^2}}\left[\frac{\sinh\left(\frac{\sigma_+ z}{H}\right)}{\sigma_+^2\sinh\left(\frac{\sigma_+}{H}\right)} - \frac{\sinh\left(\frac{\sigma_- z}{H}\right)}{\sigma_-^2\sinh\left(\frac{\sigma_-}{H}\right)}\right]\mathrm{J}_0\left(\frac{\gamma_n r}{q}\right) + \phi_0, \tag{5.66}$$

where ϕ_0 is an arbitrary constant.

Substitution of Eqs. (5.2), (5.3), (5.18), (5.19), (5.31) and (5.32), and the associated current density and electrostatic potential, Eq. (5.66), into Eq. (5.61) shows that

$$\int(\boldsymbol{a}\cdot\boldsymbol{b})(\boldsymbol{v}\cdot\mathrm{d}\boldsymbol{S}) = 0, \tag{5.67}$$

$$\int \phi \boldsymbol{b} \cdot \mathrm{d}\boldsymbol{S} = 0, \tag{5.68}$$

$$\int \eta \boldsymbol{j} \cdot \boldsymbol{b} \mathrm{d}V = 0, \tag{5.69}$$

$$\frac{1}{2}\int (\boldsymbol{a}\cdot\boldsymbol{v})(\boldsymbol{b}\cdot\mathrm{d}\boldsymbol{S}) = -\pi q^2 \sum_{n=1}^{\infty} \hat{V}_n J_0(\gamma_n)\frac{q}{\gamma_n}, \tag{5.70}$$

$$-\frac{1}{2}\int (\eta \boldsymbol{j}\times\boldsymbol{a})\cdot\mathrm{d}\boldsymbol{S} = \pi q^2 \sum_{n=1}^{\infty} \hat{V}_n J_0(\gamma_n)\frac{q}{\gamma_n}. \tag{5.71}$$

Thus the helicity injected through both photospheric boundaries, Eq. (5.70), by the twisting motions is extracted at the same rate into the surrounding corona through the curved surface of the flux tube, Eq. (5.71). (Note that $J_0(\gamma_1) < 0$ so that the largest contribution to the sum in the injection term is indeed positive.) Thus, there is no net injection or dissipation of helicity within the flux tube, a result which is independent of any gauge of the vector potential, gauge-dependence only being introduced if the vector potential changes with time. This can be seen by posing the helicity evolution equation in the form given by Jensen and Chu (1984):

$$\frac{\partial H_m}{\partial t} = -\int \left(\phi \boldsymbol{b} + \frac{1}{2}\boldsymbol{a}\times\frac{\partial \boldsymbol{a}}{\partial t}\right)\cdot\mathrm{d}\boldsymbol{S} - \int \eta \boldsymbol{j}\cdot\boldsymbol{b}\,\mathrm{d}V. \tag{5.72}$$

The rate of injection simplifies to $-\int \phi \boldsymbol{b}\cdot\mathrm{d}\boldsymbol{S}$ in the steady state which, since the vector potential does not appear in the expression defining ϕ, Eq. (5.63), is sufficient to show gauge-invariance. Thus the use of the non-invariant magnetic helicity suffices in the steady-state context with no need to resort to gauge-invariant relative helicity (Berger and Field, 1984).

The fact that there is a continual flow of magnetic helicity, at the same rate as it is injected from the photosphere, from the single flux tube under consideration to its surroundings indicates that the flux tube is not entirely isolated so that some consideration should be given to the ultimate destiny of this helicity. Parker has considered the scenario of flux tubes emerging from the photosphere into the corona which then interact as a result of the convective motions of the footpoints (Parker, 1982, 1983a, 1983b, 1983c). His main conclusion is that a state of equilibrium is not possible and that magnetic discontinuities in the form of current sheets inevitably arise at the point of contact between tubes of like twist. Reconnection then occurs to relax the system to that of a lower magnetic energy, heating the corona in the process. Bogdan (1984) also considers this process from a kinematic standpoint and concludes that a system of many tubes with roughly equal numbers of tubes of each sense of twist would relax in this manner until eventually only two large tubes of opposite twist remain. From a turbulence point of view this represents an inverse cascade of magnetic helicity, with the twist initially present at medium scales being converted to twist at the largest scales of the system represented by the final two large flux tubes.

Heyvaerts and Priest (1984) produce a more detailed model by calculating the amount of free energy which is released if the stressed arcade relaxes to a state in which the global magnetic helicity is conserved following the application of this notion in fusion physics (Taylor, 1974).

Browning and Priest (1986) provide further mathematical backing for this paper by showing that, as long as the gauge for the magnetic vector potential is used consistently, the evolution of an ideal constant-α force-free field is gauge-invariant. Vekstein (1987a) considers the problem of coronal heating with the conservation of magnetic helicity constraint but for more general photospheric motions and perturbations to the magnetic field. This approach is also applied to the problem of closely packed flux tubes by Browning et al. (1986) starting from a nonlinear force-free field and relaxing to a linear force-free field with the same magnetic helicity — again coalescence of flux tubes occurs. For rigorous derivations of Woltjer's principle of minimum energy using relative helicity and coronal/photospheric boundary conditions three key papers are those of Aly (1993), Berger (1985) and Laurence and Avellaneda (1991). See also Browning (1988a, 1988b) and Hasegawa (1985).

These papers assume that the magnetic helicity is approximately conserved since it decays on a time-scale of hours to days in the corona (Berger, 1984). However, Choudhuri (1986) argues that there should be no such constraint because any helicity injected into the coronal flux tube by photospheric motions will be cancelled by subsequent motions in the opposite sense which he expects to occur in equal measure if the motions can be considered as random, thus returning to the model of Sturrock and Uchida (1981) in which no helicity constraint is imposed but rather the field is allowed to relax to a potential minimum magnetic energy state. Berger (1991) examines this model in greater detail.

Mathematically the global helicity can be written as the sum of a self-helicity, measuring the twist present in an individual flux tube, and a mutual helicity, measuring the braiding of flux tubes (Berger and Field, 1984; Song and Lysak, 1989; Wright and Berger, 1989, 1990, 1991). As the tubes merge, the reduction in the number of tubes present reduces the mutual-helicity contribution and so must increase the self-helicity if the total global magnetic helicity is considered to decay on a slow time-scale compared to that of coronal heating (Berger, 1984). From a still larger perspective tubes twisted too much can erupt with a resulting reconnection releasing a plasmoid and allowing the remaining flux to relax to a state of lower twist — in this way magnetic helicity can escape to the solar wind (House and Berger, 1987; Strauss and Otani, 1988; Sturrock, 1989, esp. pp. 391–392; Van Hoven, 1981; Low, 1994). Interestingly, in Aly's (1993) analysis of Taylor's relaxation in a semi-infinite corona he finds that if the imposed relative magnetic helicity exceeds a critical value a quasi-periodic regime of stressing, relaxing and ejection of energy and helicity at infinity results, while Vekstein et al. (1993), Vekstein et al. (1994) and Wolfson et al. (1994) reach a similar conclusion, this time with the residual field being potential. All of these processes are beyond the scope of the present work, which considers only the interaction of large and small-scale effects in a single flux tube, but go some way in accounting for the fate of the injected magnetic helicity. All that may be claimed is that helicity injection will not play a rôle in the cascade processes within this flux tube once a steady state has been established, but may contribute in some way on a larger scale as individual flux tubes interact generating current sheets and new possibilities for heating.

5.5 Two-dimensional turbulence

In the presence of a strong background magnetic field, such as occurs in arcades and flux tubes, it is natural to expect that the magnetofluid motions will not be isotropic but rather that they will have a preferred direction with the magnetic field acting as a guide line (Oughton et al., 1994). Montgomery and Turner (1981) use a perturbation approach to show that the turbulence can be decomposed into a 2D MHD spectrum perpendicular to the large-scale field and an isotropic spectrum of Alfvén waves, a conclusion given further support analytically by Zank and Matthaeus (1993), experimentally in magnetically confined fusion experiments (Liewer, 1985) and observationally with Voyager data (Matthaeus et al., 1990). Truly two-dimensional turbulence may be regarded as being composed of a stack of planes which completely confine the motion and with adjacent planes not interacting[2], clearly an idealisation since the Alfvén spectrum identified by Montgomery and Turner will inevitably lead to some interaction as Alfvén waves propagate along the background field. This situation is discussed by Kraichnan and Montgomery (1980) and investigated using the EDQNM closure by Pouquet (1978). Some of the properties of two-dimensional turbulence are known to differ from those of three-dimensional turbulence, especially the rugged invariants (Sect. 1.3.3); also the turbulent diffusivity is negative whenever the magnetic energy spectrum exceeds the kinetic energy spectrum, as is frequently the case in numerical simulations (Fyfe et al., 1977b; Orszag and Tang, 1978; Pouquet, 1978; Hossain et al., 1983; Ting et al., 1986; Biskamp and Welter, 1989; Politano et al., 1989). Given these differences and the fact that for a steady state there must be some interaction between planes in order to transport energy from the photosphere to the corona and balance the losses due to molecular viscosity and resistivity, it is more appropriate to use a turbulence model which admits such interactions in place of the purely two-dimensional case. Unfortunately to the author's knowledge no EDQNM expansion, like those of Pouquet et al. (1976) for 3D helical, isotropic MHD and Pouquet (1978) for 2D isotropic MHD, has been published for a $2\frac{1}{2}$D MHD model in which a uniform background field threads velocity and magnetic fields which are confined to a perpendicular plane and along which Alfvén waves are permitted to propagate (Strauss, 1976; Montgomery, 1982). However, the work of Pouquet (1978) will now be considered to see whether purely 2D MHD can reproduce coronal heating levels.

Pouquet (1978) has derived equations for the spectral energy evolution in two-dimensional turbulence with no cross helicity. As in Pouquet et al. (1976), they are obtained by applying the EDQNM approximation and expanding the resulting equations in terms of a small parameter to investigate non-local effects. Pouquet built a wavenumber cutoff denoted by k_m into her equations, such that $k \ll k_m < p$ or q, where k, p and q are the magnitudes of the wavenumbers comprising an interacting triad. Pouquet's equations, truncated by neglecting terms of order a^2 or above, are

$$\frac{\partial E_k^V}{\partial t} = -\left(\nu^{Vv} + \nu^{Vm}\right) k^2 E_k^V , \tag{5.73}$$

[2] In this case a uniform background magnetic field perpendicular to the $x-y$ plane does not change the 2D MHD equations since B_0 is constant and $\partial/\partial z \equiv 0$.

$$\frac{\partial E_k^M}{\partial t} = -\left(\nu^{Mv} + \nu^{Mm}\right) k^2 E_k^M, \tag{5.74}$$

where

$$\nu^{Vv} = \frac{\pi}{4} \int_{k_m}^{\infty} \theta_{kpp} \frac{\partial}{\partial p} \left(p E_p^V\right) \mathrm{d}p, \tag{5.75}$$

$$\nu^{Vm} = \frac{\pi}{4} \int_{k_m}^{\infty} \theta_{kpp} \left(3E_p^M - p\frac{\partial E_p^M}{\partial p}\right) \mathrm{d}p, \tag{5.76}$$

$$\nu^{Mv} = \pi \int_{k_m}^{\infty} \theta_{kpp} E_p^V \, \mathrm{d}p, \tag{5.77}$$

$$\nu^{Mm} = \pi \int_{k_m}^{\infty} \theta_{kpp} \left(-E_p^M\right) \mathrm{d}p, \tag{5.78}$$

and where the notation has the same meaning as in Sect. 1.3.2. One of the stages not explicitly stated is the expansion in terms of the small parameter, a, which bounds the ratio of the smallest to middle wavenumber in the interacting triad.

Pouquet (1978) finds that the turbulent viscosities ν^{Vv} (effect of small-scale kinetic energy on velocity fields) and ν^{Mm} (the effect of small-scale magnetic energy on magnetic fields) are negative, but that ν^{Mv} (effect of small-scale kinetic energy on magnetic fields) is positive. This results in a growth of magnetic energy whenever the magnetic spectrum exceeds the kinetic spectrum, for then $\nu^{Mv} + \nu^{Mm}$ is negative. The turbulent viscosity and magnetic diffusivity are identified, following Sect. 3.3 as

$$\frac{\eta_v}{\rho} = \frac{1}{2}\left(\nu^{Vv} + \nu^{Vm}\right), \tag{5.79}$$

$$\eta_m = \frac{1}{2}\left(\nu^{Mv} + \nu^{Mm}\right). \tag{5.80}$$

5.5.1 Equipartition

Although not explicitly mentioned so far, the diffusion term in the mean-field induction equation comprises the sum of both the turbulent and molecular magnetic diffusivities. In most cases the molecular value is neglected in favour of the dominant turbulent diffusivity, but now it must be reinstated because equipartition of kinetic and magnetic energy is postulated as a consequence of the Alfvén spectrum identified by Montgomery and Turner, with the result that $\eta_m = 0$ from Eqs. (5.77), (5.78) and (5.80)[3]. A steady state of magnetic energy would then be possible with molecular diffusion directly balancing energy injection at large scales and with no energy cascading to small scales. However, the magnetic energy is expected to be much larger than in the helical, isotropic case with only direct cascades because molecular diffusion is very small at these large scales.

[3] This assumption is inconsistent with the adoption of a purely two-dimensional turbulence model in calculating the turbulent diffusion since the effects of interacting planes have been neglected from the turbulence equations but used in justifying equipartition of kinetic and magnetic energy — the purpose of this section is to determine the validity of this simplifying assumption.

To calculate the turbulent viscosity Eq. (3.66) is used as the form for E_k^M and E_k^V in Eqs. (5.75), (5.76) and (5.79). For large time, t, and for $k \sim q$ the triad-relaxation time is once more

$$\theta_{kqq} \simeq \frac{1}{\mu_{kqq}} \sim \frac{1}{\sqrt{3}qc_{a0}}, \tag{5.81}$$

from Eqs. (1.110), (3.62) and (3.64). The turbulent viscosity is then

$$\frac{\eta_v}{\rho} = \frac{\pi C}{3\sqrt{3}}\sqrt{\frac{\varepsilon}{c_{a0}}}k^{-3/2}. \tag{5.82}$$

Since ε is the rate of transfer of total energy per unit mass, Eq. (3.71) still holds in two dimensions if the two-dimensional planes are considered to be stacked to form a three-dimensional volume. The expression now obtained in Fourier space may be regarded as an approximation to the desired Fourier-Bessel transform of the viscosity when $k = \gamma_n/h$. Applying Eq. (3.71) and non-dimensionalising Eq. (5.82) yields

$$\hat{\nu}_n = \frac{\pi C}{3\sqrt{3}}\left(\frac{F}{2}\right)^{1/2}\left(\frac{\gamma_n}{q}\right)^{-3/2}. \tag{5.83}$$

In particular, the case $n = 1$ may be inverted to give

$$F = \frac{54}{\pi^2 C^2}\left(\frac{\gamma_1}{q}\right)^3 \hat{\nu}_1^2. \tag{5.84}$$

The expression for the injected power density, Eq. (5.45), changes slightly because now the magnetic diffusivity is the molecular rather than the turbulent one, and so it will be constant. Writing η instead of $\hat{\eta}_n$ and noting that now $H_n = \sqrt{\eta\hat{\nu}_n}$, leads to

$$H_n = \left(\frac{\gamma_n}{\gamma_1}\right)^{-3/4} H, \tag{5.85}$$

$$\lambda_n = \gamma_1^{3/4}\gamma_n^{1/4}\frac{H}{q}, \tag{5.86}$$

where now $H = \sqrt{\eta\hat{\nu}_1}$. Equating Eq. (5.84) with the injected flux, Eq. (5.45), and invoking Eq. (5.49) yields a new transcendental equation for $Z = 1/H$:

$$1 = \frac{2}{81}\delta\pi^2 C^2 \gamma_1^{3/4}\left(\frac{\overline{v}}{c_{a0}}\right)^2\left(\frac{\gamma_1}{q}\right)^{-3}\eta Z^3\left\{\sum_{n=1}^{N_c}\frac{n^{-5/3}\gamma_n^{-3/4}}{\sqrt{1+4\lambda_n^2}}\left[\sigma_+^2\coth\frac{\sigma_-}{H_n}+\sigma_-^2\coth\frac{\sigma_+}{H_n}\right]\right.$$
$$\left.+\sum_{n=N_c+1}^{N_A}\frac{n^{-5/3}\gamma_n^{-3/4}}{\sqrt{1+4\lambda_n^2}}(1+2\lambda_n^2)\right\}, \tag{5.87}$$

where now the wavenumber cutoff, N_c, is determined by the inequality

$$\gamma_n < 20^{4/5}q^{8/5}\gamma_1^{-3/5}Z^{4/5}. \tag{5.88}$$

Noting that $\gamma_n \lesssim n\pi$, the cutoff may be chosen as

$$N_C = \left[\frac{20^{4/5}q^{8/5}Z^{4/5}}{\pi\gamma_1^{3/5}}\right]. \tag{5.89}$$

The Spitzer molecular magnetic diffusivity is used, $\eta_m = 5.2 \times 10^7 \ln\Lambda\, T^{-3/2}$ m^{2}s^{-1}. With a temperature $T = 10^6$ K and density $\rho = 10^{16}$ m^{-3}, the Coulomb logarithm, $\ln\Lambda$, is approximately 18.2 (interpolated from values in Priest (1982)) leading to $\eta_m = 0.9447$ m^{2}s^{-1}, which may then be non-dimensionalised and inserted into Eq. (5.87). Finally,

$$\hat{\nu}_n = \left(\frac{\gamma_n}{\gamma_1}\right)^{-3/2} \frac{1}{\eta Z^2}, \tag{5.90}$$

and the power density can be obtained from Eq. (5.84).

Results

Equation (5.87) is solved numerically for a flux tube of half-length 10^4 km, density 2×10^{16} m^{-3} (2×10^{10} cm^{-3}) and a photospheric velocity of 1 km s^{-1}, as before, with the results being presented in Fig. 5.4. The levels of heating are much higher than those observed in sites of the highest energy release in the corona. A simple explanation for this can be found by examining Eq. (5.45). Depending on the magnitudes of λ_n and H_n various approximations for F are possible. The condition $\lambda_n < 1/2$ is equivalent to

$$n < \frac{\gamma_n}{\pi} < \frac{(qZ)^4}{16\pi\gamma_1^3}, \tag{5.91}$$

the value of the right side of which lies between 7×10^{13} and 9×10^{23} for q varying from 0.1 to 1.0 and B_0 from 1 to 500 G. Since the largest n used is always less than N_A which, for these parameter ranges along with $\overline{v} = 1$ km s^{-1} and density $= 2 \times 10^{16}$ m^{-3}, is at most 1.9×10^6, now that the series is truncated once convergence to a specified accuracy has been achieved, $\lambda_n \ll 1/2$ and so $\sqrt{1+4\lambda_n^2} \simeq 1 + 2\lambda_n^2 - 2\lambda_n^4 + O(\lambda_n^6)$, whence $\sigma_+ \simeq 1 + \lambda_n^2 + O(\lambda_n^4)$, $\sigma_- \simeq \lambda_n^2 - \lambda_n^4 + O(\lambda_n^6)$. σ_+/H_n is then approximately $1/H_n = (\gamma_n/\gamma_1)^{3/4} Z$ which is much larger than unity when $n > 1, Z \gg 1$. Thus $\coth(\sigma_+/H_n) \simeq 1$. Similarly $\sigma_-/H_n \simeq \lambda_n^2/H_n$ and the value of its hyperbolic cotangent depends on the relative size of H_n. Re-arranging $H_n > \lambda_n^2$ gives

$$n < \frac{\gamma_n}{\pi} < \frac{(q^2 Z)^{4/5}}{\pi\gamma_1^{3/5}} = 20^{-4/5} N_c, \tag{5.92}$$

the value of the right side lying between 103 and 17135 so that $H_n > \lambda_n^2$ for low n, whence $\coth(\sigma_-/H_n) \simeq H_n/\lambda_n^2$. Noting that $\sqrt{\hat{\nu}_n/\eta} = (\gamma_n/\gamma_1)^{-3/4}/(\eta Z)$ the low-n contribution to the injected power density is

$$F_1 \simeq \frac{2q^2}{\eta} \sum_{n=1}^{[20^{-4/5}N_c]} \frac{\hat{V}_n^2 \mathrm{J}_2^2(\gamma_n)}{\gamma_n^2}. \tag{5.93}$$

In the range $[20^{-4/5}N_c] < n < N_c$,$H_n < \lambda_n^2$ with $\coth(\sigma_-/H_n) \simeq 1$ and a resulting contribution to the power density of

$$F_2 \simeq \frac{2\gamma_1^{3/4}}{\eta Z} \sum_{[20^{-4/5}N_c]+1}^{\infty} \frac{\hat{V}_n^2 \mathrm{J}_2^2(\gamma_n)}{\gamma_n^{3/4}}. \tag{5.94}$$

The additional factor $1/Z$ where Z is large and the continued decrease with n means that this

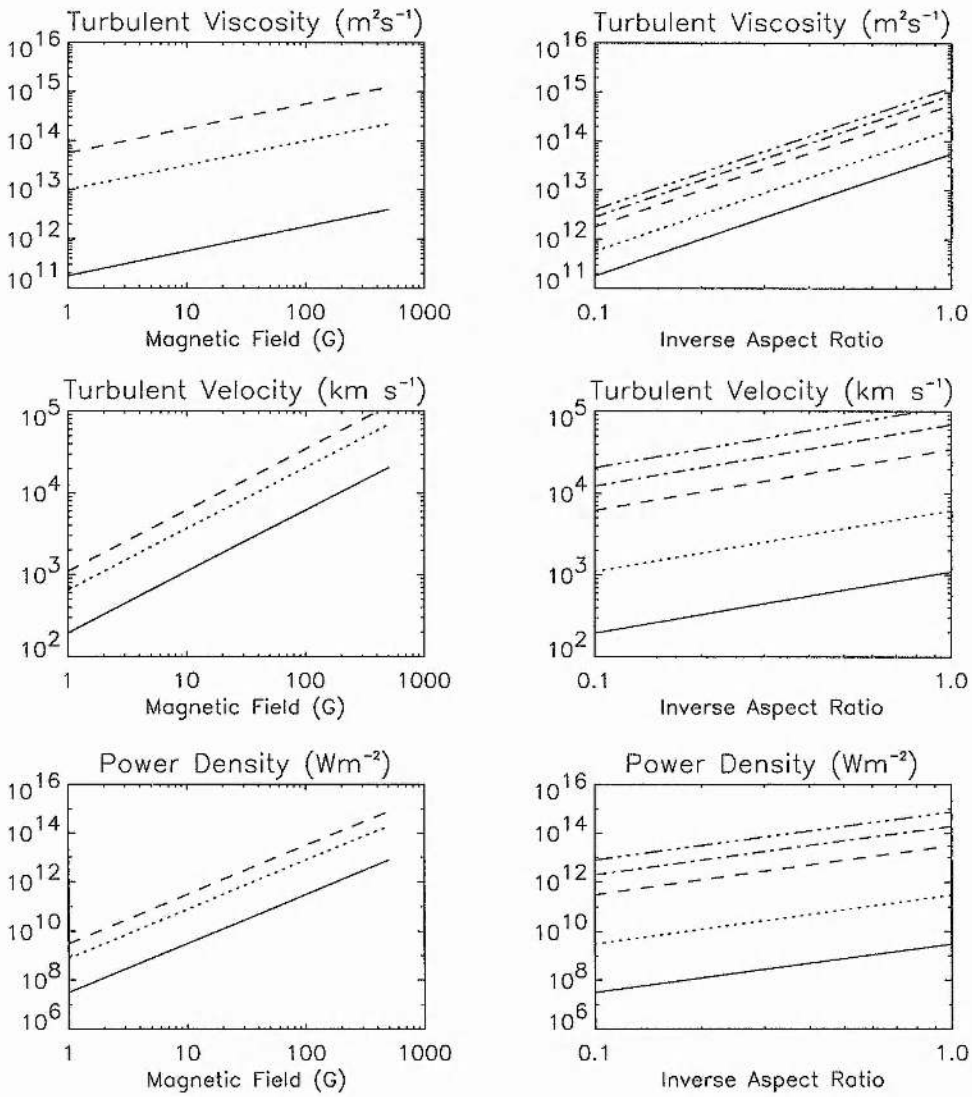

Figure 5.4: Two-dimensional turbulence model with equipartition of kinetic and magnetic energies in the inertial range. Parameters used are those of Fig. 5.3. On the left different curves represent flux tubes with inverse aspect ratios of 0.1 (solid), 0.5 (dotted) and 1.0 (dashed) while on the right the curves represent mean magnetic fields, B_0, of 1G, 10G, 100G, 250G and 500G in ascending order.

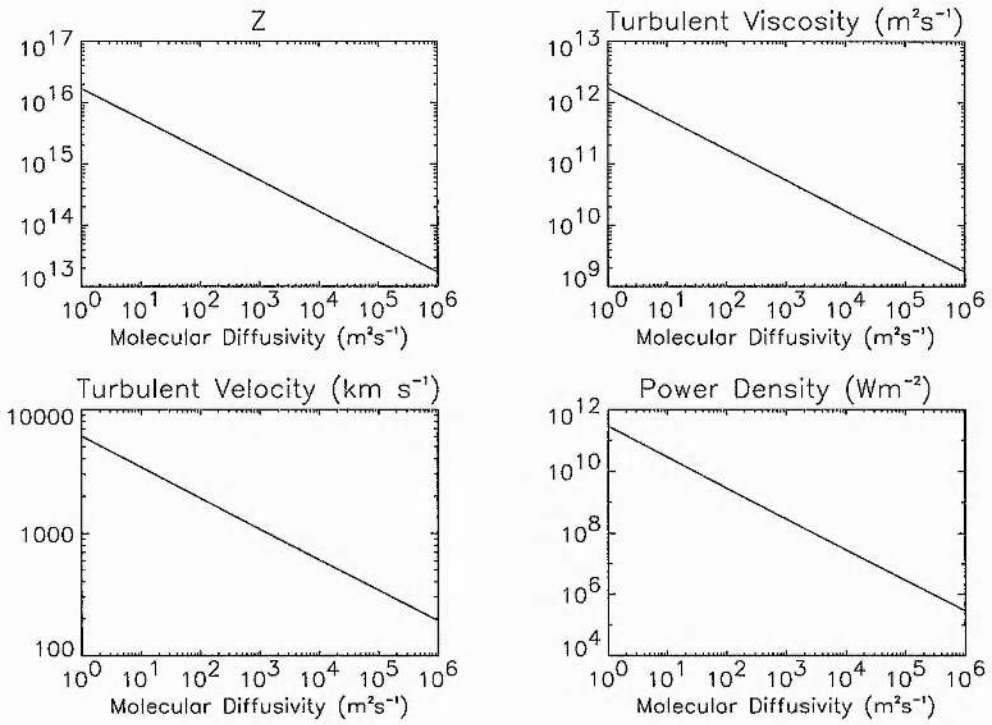

Figure 5.5: Variation of turbulent viscosity, velocity and power density with "molecular" magnetic diffusivity. The inverse aspect ratio is 0.1 and the magnetic field 100 G, while other parameters take the values given in Fig. 5.3. Z is a Hartmann number calculated at the largest scale.

second contribution is not likely to be important. The sum is taken to ∞ in theory because the above arguments equally well approximate the already approximated sum from $N_c + 1$ to ∞. Again the second sum converges since $\gamma_n^{-3/4}\hat{V}_n^2 \mathrm{J}_2^2(\gamma_n) \simeq n^{-29/12}$ so that even more so the flux can be regarded as being dominated by the first few terms of the first sum. Comparison with the small-scale dissipated flux, Eq. (5.84), noting that $\hat{\nu}_1 = 1/(\eta Z^2)$, then shows that (Fig. 5.5)

$$Z \propto \eta^{-1/4}, \tag{5.95}$$

$$\hat{\nu}_1 \propto \eta^{-1/2}, \tag{5.96}$$

$$F \propto \eta^{-1}. \tag{5.97}$$

Thus, in order to attain reasonable levels of heating, a much larger magnetic diffusivity is required, of turbulent proportions. This indicates that the assumption of equipartition in two-dimensional turbulence, which leads to the turbulent diffusivity being identically zero, is the primary cause of these unphysical results. This in turn arose because Alfvén waves were assumed to propagate along the background field perpendicular to the plane containing the turbulence when modelling the eddy relaxation, while a consequence of the idealised turbulence model used is that interaction between adjacent planes is mathematically prohibited — i.e. no Alfvén waves along the background field. The most appropriate alternative should use a turbulence model based on $2\frac{1}{2}$D MHD (sometimes called reduced MHD (Strauss, 1976; Montgomery, 1982)), in which the motions are essentially two-dimensional with a uniform background field along which Alfvén waves may propagate, thus allowing for interaction between planes. However, a simpler solution may lie in relaxing the imposition of exact equipartition, the consequences of which are now examined.

5.5.2 Non-equipartition

Numerical simulations of two-dimensional turbulence often find that at high wavenumbers equipartition is almost achieved, but with the magnetic energy spectrum exceeding the kinetic energy spectrum. For helical three-dimensional turbulence Pouquet et al. (1976) find that there has to be an order k^{-2} difference between the spectra ($E_k^M - E_k^V \propto k^{-2}$) in order to ensure a constant flux of total energy through a wavenumber in the inertial range. This has been confirmed for two-dimensional turbulence by Biskamp and Welter (1989), who find the spectral index to be about 2.5 for medium Reynolds numbers, approaching 2 as the Reynolds numbers increase. The turbulent magnetic diffusivity is then found to be negative from Eqs. (5.77), (5.78) and (5.80). The phenomenon of negative turbulent magnetic diffusivity has been discussed by Pouquet (1978); it leads to the inverse cascade of mean-square magnetic potential, which builds up at large scales. However, problems arise when trying to model the steady-state balance between energy injection and turbulent dissipation in the corona. Consider the energy equation for an incompressible plasma:

$$\frac{\partial}{\partial t}\int \left(\frac{v^2}{2} + \frac{b^2}{2}\right) \mathrm{d}V = -\int \left[\frac{v^2}{2}\boldsymbol{v} + \boldsymbol{v}\cdot\mathrm{p} + \nu\boldsymbol{\omega}\times\boldsymbol{v} - \boldsymbol{e}\times\boldsymbol{b}\right]\cdot\mathrm{d}\boldsymbol{S} - \int \left(\nu\omega^2 + \eta j^2\right)\mathrm{d}V, \tag{5.98}$$

obtained assuming that the pressure tensor is again of the form $p_{rr} = p_{\theta\theta} = p_\perp$, $p_{zz} = p_\parallel$, and that the component $\partial v_z/\partial z$ is zero. For the form of $\boldsymbol{v}$ used here, Eq. (5.2) with Eq. (5.10), the first two surface terms are zero. The third is the viscous flux calculated earlier which is expected to be much smaller than the Poynting flux, given by the fourth term, in the corona. The approach of Heyvaerts and Priest in neglecting the molecular magnetic diffusivity in favour of a turbulent diffusion term can no longer be followed because this would lead to the $\int \eta j^2 \mathrm{d}V$ term acting as an energy source at all scales. In order to maintain a steady state either all dissipation would have to be viscous in nature or the corona would have to supply energy to the photosphere or some combination of the two. These unappealing consequences can be changed by restoring the molecular magnetic diffusivity so that Eq. (5.74) has a term $2(\eta(k)+\eta)k^2E_k^M$ on the right where $\eta(k) \to 0$ as $k \to k_{\mathrm{diss}}$ but $\eta(k)+\eta < 0$ for $k \ll k_{\mathrm{diss}}$, enabling both the inverse cascade at inertial wavenumbers and resistive dissipation at high wavenumbers to be described. However this goes against the grain of the approach of Heyvaerts and Priest in attempting to model turbulent heating with a minimum of arbitrary parameters, requiring both the molecular magnetic diffusivity needed in Sect. 5.5.1 and an additional coefficient for the $O(k^{-2})$ difference between the kinetic and magnetic energy spectra, and so will not be pursued in this thesis.

Chapter 6

Alfvén Waves in Arcades

6.1 Ideal standing wave

It is worth examining the case of the ideal standing wave for comparison with the driven, damped standing wave. Following Heyvaerts and Priest (1992) an arcade solution is again sought, but now with time-dependence introduced:

$$\boldsymbol{v} = v(x,z,\tau)\,\hat{\boldsymbol{y}}, \tag{6.1}$$

$$\boldsymbol{b} = \hat{\boldsymbol{z}} + b(x,z,\tau)\,\hat{\boldsymbol{y}}. \tag{6.2}$$

The y-components of Eqs. (3.15) and (3.16) with $\eta = \nu = 0$ lead to

$$\frac{\partial v}{\partial \tau} = \frac{\partial b}{\partial z}, \tag{6.3}$$

$$\frac{\partial b}{\partial \tau} = \frac{\partial v}{\partial z}, \tag{6.4}$$

while the x- and z-components of Eq. (3.15) lead to the pressure balance condition, Eq. (3.25). In the ideal problem the tangential electric field component is now automatically continuous without requiring Eq. (3.27) to be true so only the prescribed velocity condition, Eq. (3.28), is required, leading to the solution

$$v(x,z,\tau) = \cos\omega\tau \frac{\sin\omega z}{\sin\omega} V(x), \tag{6.5}$$

$$b(x,z,\tau) = \sin\omega\tau \frac{\cos\omega z}{\sin\omega} V(x), \tag{6.6}$$

where the dispersion relation is

$$k_z = \pm\omega, \tag{6.7}$$

in dimensionless units and the odd and even natures of the velocity and magnetic field have been retained.

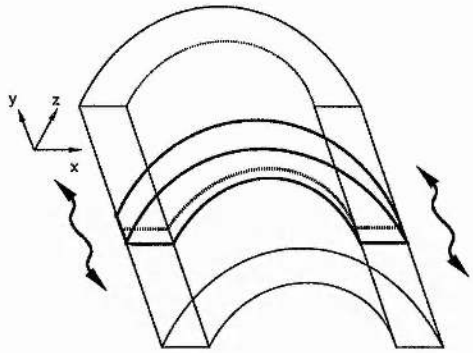

Figure 6.1: Arcade geometry: rapid photospheric motions drive Alfvén waves across arcade loops. The axes show the local Cartesian geometry being used.

6.2 Driven, damped standing wave

Including the viscosity and magnetic diffusivity and keeping the ansatz of Eqs. (6.1) and (6.2), the y-components of Eqs. (3.15) and (3.16) become, respectively,

$$\frac{\partial v}{\partial \tau} = \frac{\partial b}{\partial z} + \nu \nabla^2 v, \tag{6.8}$$

$$\frac{\partial b}{\partial \tau} = \frac{\partial v}{\partial z} + \eta \nabla^2 b, \tag{6.9}$$

and the pressure balance condition, Eq. (3.25), remains as before.

The boundary conditions are just those of the arcade investigated by Heyvaerts and Priest, namely that the tangential component of the electric field be continuous across the interface between the corona and photosphere, and that the velocity be prescribed at the photosphere. The velocity is again taken to be an odd function of z and the shear component of the magnetic field an even function of z. The boundary conditions are thus given by Eqs. (3.27), (3.28) and (4.28). Assuming periodic extension in the x-direction and invariance in the y-direction permits normal form solutions, $\exp(i\omega\tau + i\boldsymbol{k}\cdot\boldsymbol{r})$ to be sought, where $\boldsymbol{k} = k_x\hat{\boldsymbol{x}} + k_z\hat{\boldsymbol{z}}$ and $\boldsymbol{r} = x\hat{\boldsymbol{x}} + y\hat{\boldsymbol{y}} + z\hat{\boldsymbol{z}}$. This leads to the dispersion relation

$$-\omega^2 + i\omega k^2(\nu + \eta) + \eta\nu k^4 + k_z^2 = 0. \tag{6.10}$$

Photospheric boundary motions launch the wave into the coronal medium; the frequency is then purely real, as is the x-wavenumber ($k_x = n\pi/q$) which models structure across the width of the loop. The dispersion relation, Eq. (6.10), then determines the z-wavenumber in terms of these quantities as the solutions of

$$\eta\nu k_z^4 + k_z^2[1 + 2\eta\nu k_x^2 + i\omega(\nu + \eta)] + [\eta\nu k_x^4 - \omega^2 + i\omega k_x^2(\nu + \eta)] = 0, \tag{6.11}$$

which are

$$k_z = \pm\frac{1}{\sqrt{2\eta\nu}}\left\{-[1+2\eta\nu k_x^2+i\omega(\nu+\eta)] \pm [1+4\eta\nu k_x^2-\omega^2(\nu-\eta)^2+2i(\nu+\eta)\omega]^{1/2}\right\}^{1/2}, \quad (6.12)$$

with the $\pm$ signs being independent. This may be re-expressed as $\pm k_z^+$, $\pm k_z^-$, where

$$k_z^{\pm} = \frac{1}{2\sqrt{\eta\nu}}\left\{\left\{[\Delta_\pm^2+(\beta\pm\gamma_-)^2]^{1/2}-\Delta_\pm\right\}^{1/2} - i\left\{[\Delta_\pm^2+(\beta\pm\gamma_-)^2]^{1/2}+\Delta_\pm\right\}^{1/2}\right\}, \quad (6.13)$$

with $\pm$ now taking the same sign throughout. In these expressions new variables have been introduced as

$$\alpha = 1+4\eta\nu k_x^2-\omega^2(\nu-\eta)^2, \quad (6.14)$$

$$\beta = (\nu+\eta)\,\omega, \quad (6.15)$$

$$\gamma_\pm = \frac{1}{\sqrt{2}}\{\sqrt{\alpha^2+4\beta^2}\pm\alpha\}^{1/2}, \quad (6.16)$$

$$\Delta_\pm = 1+2\eta\nu k_x^2 \pm \gamma_+. \quad (6.17)$$

Application of the boundary conditions, Eqs. (3.27) and (3.33), leads to the solution

$$v = \mathrm{Re}\left[e^{i\omega\tau}\sum_{n=0}^{\infty} e^{i\frac{n\pi}{q}x}\hat{v}_n(z)\right], \quad (6.18)$$

$$b = \mathrm{Re}\left[e^{i\omega\tau}\sum_{n=0}^{\infty} e^{i\frac{n\pi}{q}x}\hat{b}_n(z)\right], \quad (6.19)$$

$$\hat{v}_n(z) = \frac{\hat{V}_n}{2}\left\{\frac{\sin k_z^+ z}{\sin k_z^+}+\frac{\sin k_z^- z}{\sin k_z^-}\right\} - \frac{\hat{V}_n}{2(\gamma_+ + i\gamma_-)}[1+i(\nu-\eta)\omega]\left\{\frac{\sin k_z^+ z}{\sin k_z^+}-\frac{\sin k_z^- z}{\sin k_z^-}\right\}, \quad (6.20)$$

$$\hat{b}_n(z) = \frac{\hat{V}_n}{\gamma_+ + i\gamma_-}(i\omega+\nu k_x^2)\left\{\frac{\cos k_z^+ z}{k_z^+\sin k_z^+}-\frac{\cos k_z^- z}{k_z^-\sin k_z^-}\right\}, \quad (6.21)$$

which is a spatially damped standing wave.

It can be seen that this solution reduces to that of the ideal standing wave, Eqs. (6.5), (6.6) and (6.7), since in the limit $\nu\to 0, \eta\to 0$, the new variables behave as follows: $\alpha\to 1, \beta\to 0, \gamma_+\to 1, \gamma_-\to 0, \Delta_+\to 2$ and $\Delta_-\to -2\omega^2\eta\nu$ (to leading order); furthermore $k_z^\pm\to -i\sqrt{\Delta_+/(2\eta\nu)}$ shows that $k_z^+\to -i\infty$ and $k_z^-\to\omega$. Also,

$$\lim_{k_i\to\pm\infty}\frac{\sin(k_r+ik_i)z}{\sin(k_r+ik_i)} = \begin{cases} 1 & z=1, \\ 0 & -1<z<1, \\ -1 & z=-1, \end{cases} \quad (6.22)$$

$$\lim_{k_i\to\pm\infty}\frac{\cos(k_r+ik_i)z}{\sin(k_r+ik_i)} = \begin{cases} \mp i & z=1, \\ 0 & -1<z<1, \\ \mp i & z=-1, \end{cases} \quad (6.23)$$

so that the perturbation transforms reduce to

$$\hat{v}_n(z) = \hat{V}_n\frac{\sin\omega z}{\sin\omega}, \quad (6.24)$$

$$\hat{b}_n(z) = -i\,\hat{V}_n\frac{\cos\omega z}{\sin\omega}, \quad (6.25)$$

which corresponds to the ideal solution of Eqs. (6.5) and (6.6) when combined with Eqs. (4.28), (6.18) and (6.19). In the limit $\omega \to 0$ but with non-zero ν and η, Eqs. (6.18) – (6.21) reduce to those of Eqs. (4.25) and (4.26) when $n \neq 0$. There is a difference, though, in the case of the zeroth order solution: when $\omega \neq 0$ the above solutions still satisfy the boundary conditions, whereas in the case $\omega = 0$ they do not. In this latter case the solution was $\hat{v}_0(z) = \hat{V}_0, \hat{b}_0 =$ arbitrary constant, the latter being chosen as zero (Sect. 4.5).

It is quadratic functions of the velocity and magnetic field which are of interest, namely the kinetic and magnetic energies and the Poynting and viscous fluxes. In general, these vary with position and time as the wave propagates, but they remain roughly constant on a global basis. It is thus necessary to define a means of calculating averages of quadratic quantities. Suppose

$$f = \mathrm{Re}\left(\mathrm{e}^{i\omega\tau}\phi\right), \tag{6.26}$$

$$g = \mathrm{Re}\left(\mathrm{e}^{i\omega\tau}\gamma\right), \tag{6.27}$$

$$\phi = \sum_n \mathrm{e}^{ik_n x}\hat{f}_n, \tag{6.28}$$

$$\gamma = \sum_n \mathrm{e}^{ik_n x}\hat{g}_n. \tag{6.29}$$

A time average is denoted with an overbar, and defined as the average over one cycle of the wave:

$$\overline{h} = \frac{\omega}{2\pi}\int_0^{2\pi/\omega} h(t)\,\mathrm{d}t. \tag{6.30}$$

The situation is more complicated when there is a spectrum of frequencies, as there is then no unique wave period over which to perform the above integration. Continuing with this notation, Eq. (6.30) leads to

$$\overline{fg} = \frac{1}{2}\mathrm{Re}(\phi^*\gamma), \tag{6.31}$$

where * denotes the complex conjugate. Spatial averaging is also performed over one cycle in the x-direction, which was periodically extended to permit Fourier analysis with a real k_x. The spatial average, denoted by angle brackets, is defined by Eq. (3.45) again, application of which leads to the result

$$\langle\phi^*\gamma\rangle = \mathrm{Re}\sum_n f_n^* g_n. \tag{6.32}$$

Combining Eqs. (6.31) and (6.32) leads to the desired result:

$$\langle\overline{fg}\rangle = \frac{1}{2}\sum_n \mathrm{Re}(f_n^* g_n). \tag{6.33}$$

Energy injection into the corona is again given by Eqs. (3.43) and (3.44). After some manipulation the total averaged Poynting and viscous fluxes injected into the corona at the boundaries $z = \pm 1$ can be shown to be

$$F = \frac{1}{2}\mathrm{Re}\sum_{n=1}^{\infty}|\hat{V}_n|^2(i\omega + \nu k_x^2)\left\{\frac{\cot k_z^+}{k_z^+}\left[\frac{1+i\omega(\nu-\eta)}{\gamma_+ + i\gamma_-} - 1\right] - \frac{\cot k_z^-}{k_z^-}\left[\frac{1+i\omega(\nu-\eta)}{\gamma_+ + i\gamma_-} + 1\right]\right\}. \tag{6.34}$$

In the corresponding expression of Heyvaerts and Priest, Eq. (3.48), and that of Chap. 4, Eq. (4.40), the η and ν always appear in the combination $\sqrt{\eta\nu}$ allowing a reduction in the number of unknowns. However, this is no longer the case and so η and ν must be treated as separate entities at this stage. Equation (6.34) in fact reduces to half the corresponding expression of Heyvaerts and Priest for time-independent shearing as $w \to 0$ due to the fact that the limit of a time-averaged quadratic quantity is half the time-independent quantity. But when deriving the form of $|\hat{V}_n|^2$ the time-average must also be taken into account — with a Kolmogorov spectrum for the photospheric velocity given dimensionally by Eq. (3.49) the new equality between continuous and discrete representations is given by

$$c_{a0}^2\langle\overline{V^2(x)}\rangle = \frac{c_{a0}^2}{2}\sum_{n=1}^{\infty}|\hat{V}_n|^2 = \int_{k_{\min}}^{\infty}\overline{V}^2(k)\mathrm{d}k = \overline{v}^2, \tag{6.35}$$

from Eqs. (3.49), (4.28) and (6.33) and by definition of the r.m.s. photospheric velocity. In particular, the choice

$$|\hat{V}_n|^2 = \frac{4}{3}\delta\left(\frac{\overline{v}}{c_{a0}}\right)^2 n^{-5/3}, \tag{6.36}$$

where $\delta = 3/(2\zeta(5/3))$ and $\zeta(x) = \sum_{n=1}^{\infty} n^{-x}$ is the Riemann Zeta function, satisfies Eq. (6.35). This is double the value obtained in Eq. (4.9) so that the overall effect of time-averaging the zero frequency limiting case just gives the flux obtained when the frequency is identically zero.

6.3 Wave inequalities

This section follows the method of Sect. 4.4 except that now Eq. (4.11) must be inserted in Eq. (6.35) to give the necessary condition for wave behaviour (photospheric time-scale less than Alfvén transit time) as

$$q < \frac{2\sqrt{3}}{\pi}\frac{\overline{v}}{c_{a0}}. \tag{6.37}$$

For typical coronal values of $q = 0.1$, r.m.s. photospheric velocity of 1 km s^{-1} and density 10^{15} m^{-3} (10^9 cm^{-3}) this inequality will only be satisfied if $c_{a0} < 11$ km s^{-1}, i.e. for a background field component less than 0.16 G. This being far too small for coronal loops indicates that the generation of waves by photospheric motions does not occur on a shearing time-scale. An alternative inequality may be derived by considering the driving frequency, ω, to be an independent parameter of the model imposed externally. The associated dimensional photospheric oscillation time-scale is $2\pi l/(\omega c_{a0})$; demanding that this be less than the Alfvénic time-scale $2l/c_{a0}$ leads to the inequality

$$\omega > \pi, \tag{6.38}$$

which simply says that for a wave description to be meaningful there is a minimum dimensionless frequency. Similarly, for a quasi-static arcade evolution the reverse case is true, $\omega < \pi$. This inequality is similar to that of Inverarity and Priest (1994) who had $\omega < 2\pi$; the factor 2 is here absent because the Alfvén time-scale is now based on the whole loop transit time.

6.4 Behaviour at small scales

Once again the nonlinear transfer is based on the work of Pouquet et al. (1976) for helical, isotropic, 3D MHD turbulence, the turbulent viscosity and magnetic diffusivity being given by Eqs. (4.50), (4.51), (4.54) and (4.56), while the power density at small scales is given by Eq. (4.55).

6.5 Steady state

A single nonlinear algebraic equation can now be formed using the expressions for the injected power density, Eq. (6.34), the dissipated power density, Eq. (4.55), and the relation between the turbulent viscosity and magnetic diffusivity, Eq. (4.54). It is rather cumbersome, however, and so is not presented explicitly.

6.6 Numerical Aspects

6.6.1 Wavenumber in the z-direction

It is first of all necessary to evaluate the z-wavenumber in terms of the frequency and x-wavenumber. Since ν and η effectively represent inverse viscous and resistive Lundquist numbers, respectively, they must certainly be less than one in a turbulent plasma and, in general, should be several orders of magnitude smaller. Thus $\beta = \omega(\nu + \eta)$ is expected to be small when compared with α, which is of order one. For calculating γ_+ this is not a problem, but for γ_- there is a loss of significance as $\sqrt{\alpha^2 + 4\beta^2}$ and α often differ after more than fifteen significant figures during the search for the value of $\hat{\nu}_1$, leading to γ_- being stored as zero in the computer's memory when in reality it is very small but non-zero. In this instance (and certain others) a Taylor expansion may be used. This difficulty is again repeated for the real parts of k_z^+ and k_z^-, where $|\beta \pm \gamma_-| \ll \Delta_\pm$, the right side of both inequalities again being of order one. In this case, though, the result is more severe because the small residual should then be amplified by dividing by $\sqrt{\eta\nu}$ to give an order one value; the computer, however, returns zero instead. Thus, the values of $k_z^\pm$ are not even of the correct order of magnitude when calculated numerically from Eq. (6.13). The particular intrinsic "black box" complex square root function used gives accurate values for k_z^+ from Eq. (6.12), but not for k_z^- where loss of significance is again apparent since $|\beta - \gamma_-|$ should be even smaller than $|\beta + \gamma_-|$. A satisfactory solution is obtained by returning to the quadratic equation, Eq. (6.11), and using the relation between the product of the roots. Thus,

$$k_z^- = -\frac{1}{k_z^+}\sqrt{\frac{\eta\nu k_x^4 - \omega^2 + i\omega k_x^2(\nu + \eta)}{\eta\nu}}. \tag{6.39}$$

The evaluation of the complex cotangent in the power density expression, Eq. (6.34), frequently leads to overflow whenever the imaginary part of $k_z^\pm$ is very large. In such cases it is useful

to express the cotangent of a complex number as

$$\cot(x+iy) = \frac{(1-\tanh^2 y)\tan x}{\tan^2 x + \tanh^2 y} - i\frac{(1+\tan^2 x)\tanh y}{\tan^2 x + \tanh^2 y}. \tag{6.40}$$

For $|y| > 19$, $\tanh y \simeq \pm 1$ to fifteen digit accuracy, substitution of which into Eq. (6.40) gives $\cot(x+iy) \simeq \pm i$ according to whether $y \lesseqgtr \mp 19$.

6.6.2 Convergence

The removal of the upper limit on n does not matter mathematically as the sum in Eq. (6.34) can be shown to be convergent. To prove this first of all write the dispersion relation, Eq. (6.10), including the behaviour of the various variables with n:

$$H^2 n^{-3} k_z^4 + k_z^2 \left[1 + \frac{2H^2\pi^2}{q^2} n^{-1} + i\omega(\hat{\nu}_1 + \hat{\eta}_1) n^{-3/2}\right] + \left[\frac{H^2\pi^4}{q^4} n - \omega^2 + i\frac{\omega\pi^2}{q^2}(\hat{\nu}_1 + \hat{\eta}_1) n^{1/2}\right] = 0, \tag{6.41}$$

where $H = \sqrt{\hat{\eta}_1 \hat{\nu}_1}$. A series solution can be sought for k_z of the form

$$k_z = \sum_{r=0}^{\infty} a_r n^{-r} + i \sum_{r=0}^{\infty} b_r n^{-r+3/2}, \tag{6.42}$$

with the first few terms giving the already-given exact solutions $\pm k_z^+$ and $\pm k_z^-$ as

$$k_z^+ = \left\{\frac{\omega}{2H}(\hat{\nu}_1 + \hat{\eta}_1) - \frac{\omega H \pi^2}{q^2}(\hat{\nu}_1 + \hat{\eta}_1) n^{-1} + \mathrm{O}(n^{-2})\right\} + i\left\{-\frac{n^{3/2}}{H} - \frac{H\pi^2}{q^2} n^{1/2} + \mathrm{O}(n^{-1/2})\right\}, \tag{6.43}$$

$$k_z^- = \left\{\frac{\omega}{2H}(\hat{\nu}_1 + \hat{\eta}_1) - \left[\frac{\omega^3 q^4}{16 H^5 \pi^4}(\hat{\nu}_1 + \hat{\eta}_1)(\hat{\nu}_1 - \hat{\eta}_1)^2 + \frac{\omega H \pi^2}{q^2}(\hat{\nu}_1 + \hat{\eta}_1)\right] n^{-1} + \mathrm{O}(n^{-2})\right\}$$
$$+ i\left\{-\frac{H\pi^2}{q^2} n^{1/2} - \left[\frac{w^2 q^2}{8H^3\pi^2}(\hat{\nu}_1 - \hat{\eta}_1)^2 - \frac{H^3\pi^4}{q^4}\right] n^{-1/2} + \mathrm{O}(n^{-3/2})\right\}. \tag{6.44}$$

The earlier approximation for $\cot(x+iy)$ can be proved to be formally true in the limit of large y:

$$\lim_{y \to \pm\infty} \cot(x+iy) = \mp i. \tag{6.45}$$

When taken together with the fact that $\lim_{n\to\infty} \mathrm{Re}\, k_z^{\pm} = \omega(\hat{\nu}_1 + \hat{\eta}_1)/(2H)$ and $\lim_{n\to\infty} \mathrm{Im}\, k_z^{\pm} = -\infty$, this means that both $\cot k_z^+$ and $\cot k_z^-$ tend to i as n tends to infinity. Writing $F = \sum_{n=1}^{\infty} F_n$, the general term of the flux series may then be expanded as

$$F_n = \frac{4}{3}\delta\left(\frac{\overline{v}}{c_{a0}}\right)^2 \sqrt{\frac{\hat{\nu}_1}{\hat{\eta}_1}}\, n^{-5/3} + o(n^{-5/3}), \tag{6.46}$$

where $f = o(n^s)$ means $\lim_{n\to\infty} f n^s = 0$. This expansion is true provided the conditions

$$n \gg \frac{q^4}{\pi^4 H^2}, \tag{6.47}$$

$$n \gg \frac{w^2 q^4}{2\pi^4}\left(\frac{1}{\hat{\nu}_1^2} + \frac{1}{\hat{\eta}_1^2}\right), \tag{6.48}$$

hold, which they certainly do in the limit of large n. Finally

$$\lim_{n\to\infty} n^{5/3} F_n = \frac{4}{3}\delta \left(\frac{\overline{v}}{c_{a0}}\right)^2 \sqrt{\frac{\hat{\nu}_1}{\hat{\eta}_1}}, \tag{6.49}$$

so that the limiting form of the comparison test shows that $\sum_{n=1}^{\infty} F_n$ is convergent. This, then, means that in the infinite sum being used it is legitimate to truncate the summation to obtain the value to a specified precision without worrying about the accumulation of higher terms. The actual truncation was carried out at the point at which the summation converged to a relative accuracy of 10^{-6} and a solution for $\hat{\nu}_1$ was sought to a relative accuracy of 10^{-5}. Despite this, the final solutions exhibit an accuracy of only 10^{-2} when compared with results obtained from a symbolic algebra code retaining 100 significant digits throughout which was better equipped to evaluate $k_z^{\pm}$ directly. Given the physical limitations of the model this is deemed acceptable.

6.7 Results

Two basic types of loop have been considered numerically: the first is the active region loop of previous chapters having half-length 10^4 km, background magnetic field 100 G and plasma density 2×10^{16} m^{-3} (2×10^{10} cm^{-3}) and the second being a longer loop found in the quiet corona with half-length 10^5 km, background magnetic field 10 G and plasma density 10^{15} m^{-3} (10^9 cm^{-3}). In each case an inverse aspect ratio of 0.1 is adopted, unless otherwise indicated, and the r.m.s. photospheric velocity is taken to be 1 km s^{-1}. The behaviour with a range of driven frequencies is displayed in Fig. 6.2 which also includes the results of steady-state shearing for comparison. In this figure peaks occur at dimensionless frequencies which are integer multiples of π, which is the frequency corresponding to the time for a wave to cross from one side of the loop to the other. These results are also presented in the form of envelope functions for a larger range of frequencies in Fig. 6.3. The dissipation lengths for each of the cases of Fig. 6.2 given as a multiple of the loop length ($|2 \operatorname{Im} k_z^{\pm}|^{-1}$ since k_z is non-dimensionalised with respect to the loop half-length but here it is multiples of the whole loop that are being counted) are plotted in Fig. 6.4. The k_z^- component, in particular, corresponds to damping in 32 loop lengths for the quiet coronal fundamental resonance.

Figure 6.3 displays the full range of frequencies available for loops of half-length 10^4 km (solid curve), 10^5 km (dotted curve) and 10^6 km (dashed curve) in the form of an envelope function which interpolates the maximum and minimum amplitudes of the curves in Fig. 6.2. For the resonant frequencies it is apparent that the greatest heating occurs for the fundamental, with the heating decreasing for the higher harmonics.

The curves indicate that each loop is capable of attaining the same levels of heating given the appropriate wave frequency; in particular, the fundamental resonance gives the same level of heating for each loop[1]. However, especially for the short active-region loops, the frequencies required

[1]Note that in the case of the turbulent viscosity this is weighted by the loop length, a fact erroneously neglected when plotting comparable diagrams in Inverarity and Priest (1994).

to do this are of order 1 s^{-1} which correspond to rapid footpoint motions; waves are thus likely to account for long-term heating of short loops only if frequencies much higher than those normally considered are present but they can account for the heating of longer loops without too much difficulty (Heyvaerts, 1990).

Comparison of the left and right graphs of Fig. 6.3 shows that the heating is higher for active region loops. However, when compared with the results of the steady state case calculated in Chap. 4 it can be seen that whenever a resonance occurs Alfvén waves contribute to the heating of a coronal loop to roughly the same extent as direct magnetic dissipation from photospheric shearing motions, otherwise the resulting heating is not high enough to account for the loss processes. The magnetic dissipation heating levels may be regarded as an upper bound for the wave heating.

The variation with magnetic field and inverse aspect ratio are given in Fig. 6.5 where the upper two lines represent the fundamental and first harmonic resonant frequencies, while the lower two are for 3/2 and 5/2 times the natural frequency (non-resonant). For the 10 G case the fundamental and first harmonic curves appear merged as well as the curves for the first two cases of anti-phase driving.

6.8 Velocity and magnetic fields

Having solved for the turbulent viscosity and magnetic diffusivity required to maintain a steady state, the r.m.s. velocity and magnetic field can be calculated from the relations

$$\overline{\langle v^2(x,z,\tau)\rangle} = \frac{1}{2}\sum_{n=1}^{\infty}|\hat{v}_n|^2, \tag{6.50}$$

$$\overline{\langle b^2(x,z,\tau)\rangle} = \frac{1}{2}\sum_{n=1}^{\infty}|\hat{b}_n|^2. \tag{6.51}$$

The square roots of these are values are plotted dimensionally in Fig. 6.6 for the active region and quiet coronal loops. One can average over the variation in z to give final r.m.s. values of 61 km s^{-1} and 4.0 G (corresponding to an Alfvén speed of 62 km s^{-1}) for the active-region loop, and 36 km s^{-1} and 0.52 G (corresponding to 36 km s^{-1}) for the quiet loop.

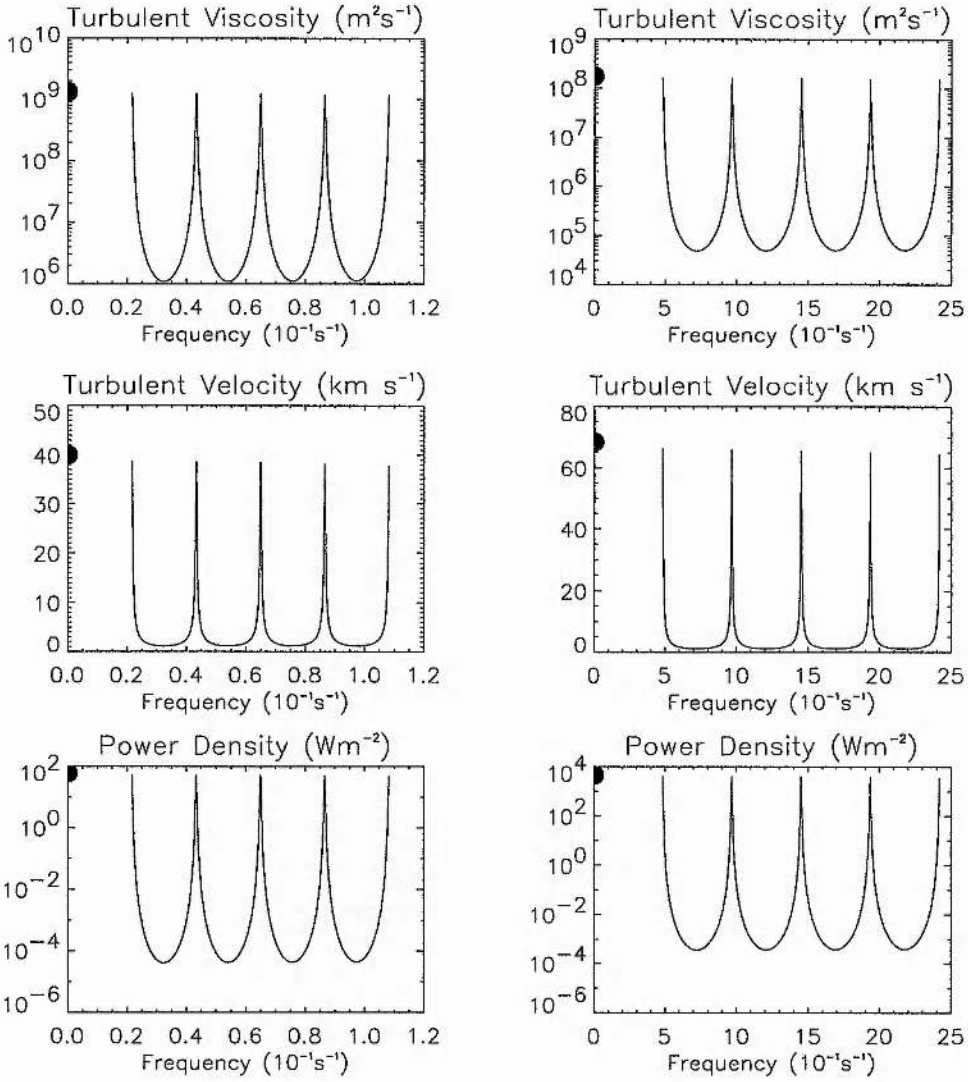

Figure 6.2: Results from matching injected power density and cascading power density for a quiet coronal loop of half-length 10^5 km, background magnetic field 10 G and density 10^{15} m^{-3} (10^9 cm^{-3}) on the left and an active region loop of half-length 10^4 km, background magnetic field 100 G and density 2×10^{16} m^{-3} (2×10^{10} cm^{-3}) on the right. The inverse aspect ratio is 0.1 and the r.m.s. photospheric velocity 1 km s^{-1} in each case. The large dot gives the corresponding result due to steady-state heating under similar conditions.

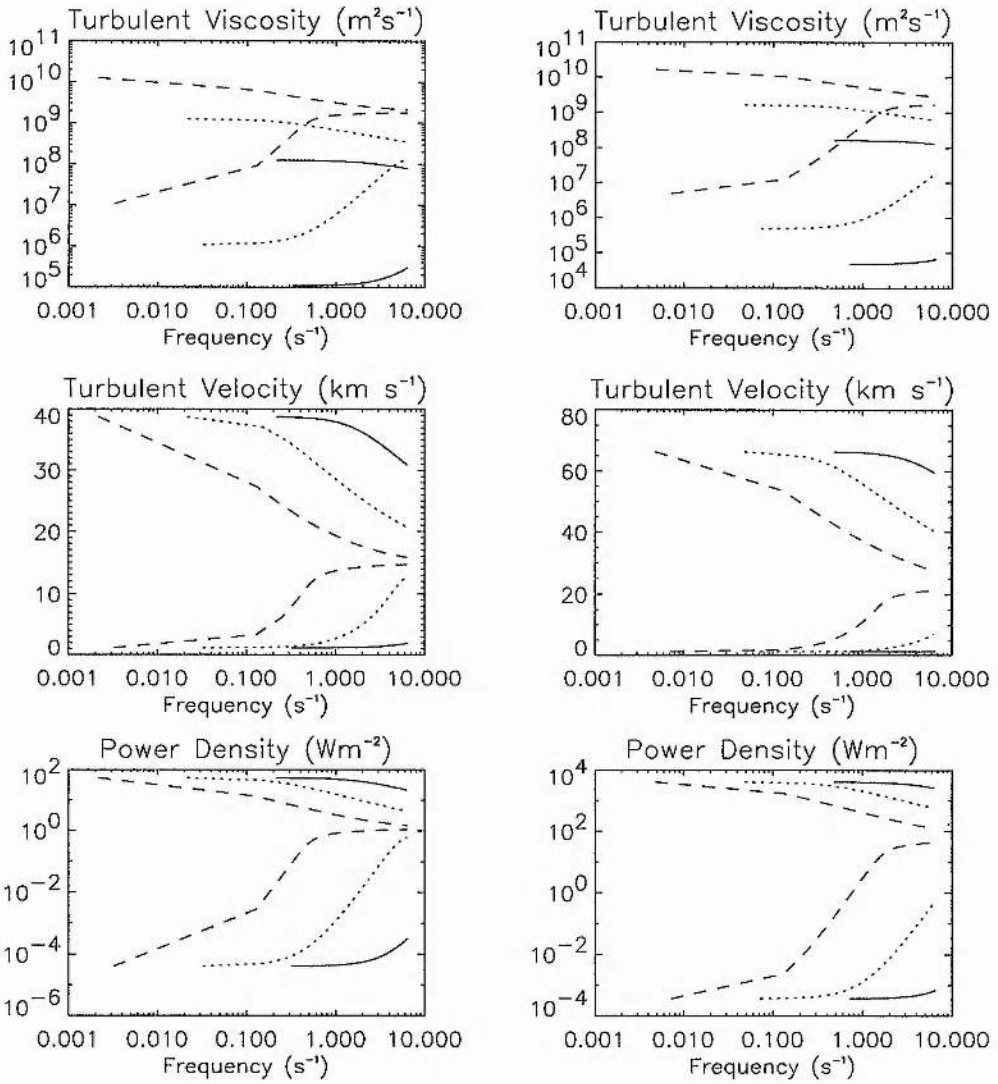

Figure 6.3: Envelope functions for the quiet coronal loop and active region loop of Fig. 6.2 on the left and right, respectively. The solid curves represent a loop of half-length 10^4 km, the dotted curves 10^5 km and the dashed curves 10^6 km. All other parameters take the same values as in the previous figure.

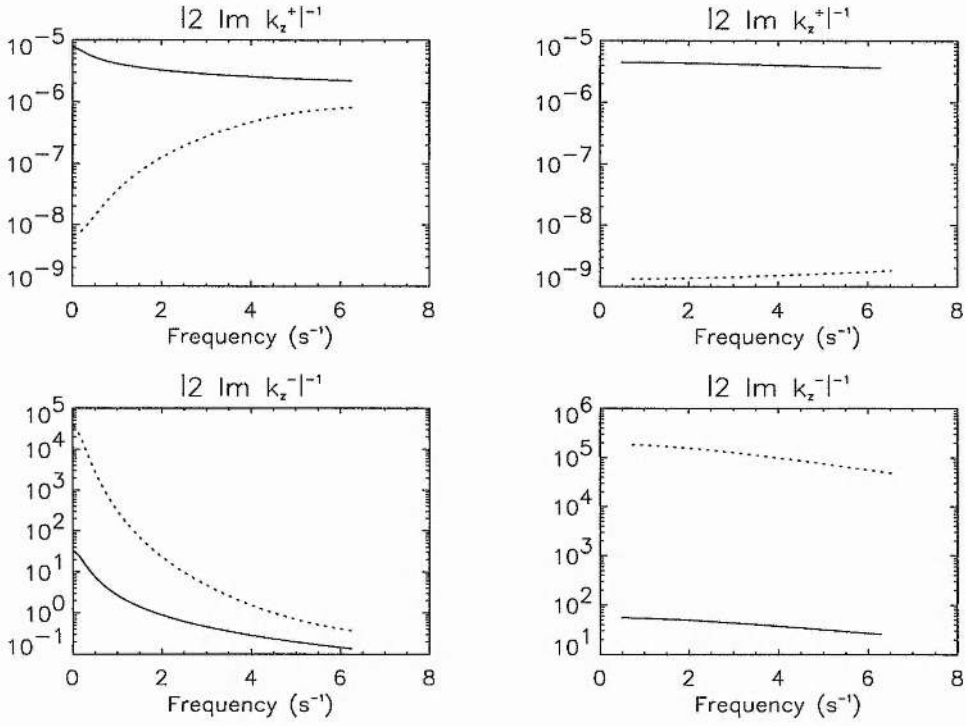

Figure 6.4: Dissipation lengths for the two scales ($|2 \text{ Im } k_z^{\pm}|^{-1}$) expressed as multiples of the loop length, plotted for the quiet and active coronal loops of Fig. 6.2 on the left and right, respectively. The solid line corresponds to the case of the driving frequency being in phase with the loop frequency, while for the dashed line the driving frequency is out of phase with the loop frequency.

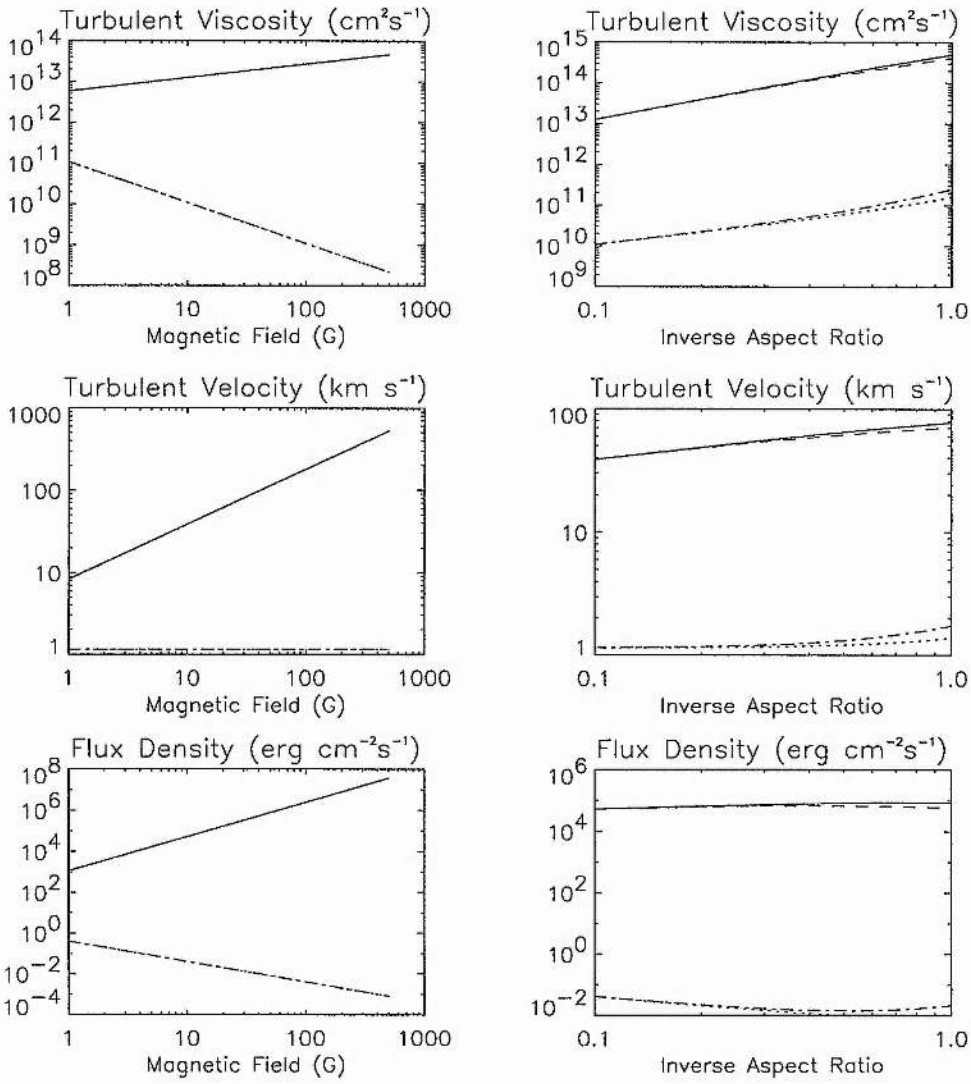

Figure 6.5: Variation of heating values with background magnetic field on the left and inverse aspect ratio on the right for a 2×10^5 km loop. The solid line represents the fundamental loop frequency, the dashed line the first harmonic (twice the fundamental) while the lower dotted and dot-dashed lines are for 3/2 and 5/2 times the loop frequency. For the magnetic field graphs the inverse aspect ratio has been fixed at 0.1, while for the inverse aspect ratio graphs the background magnetic field is 10 G. All other parameters are the same as in Fig. 6.2.

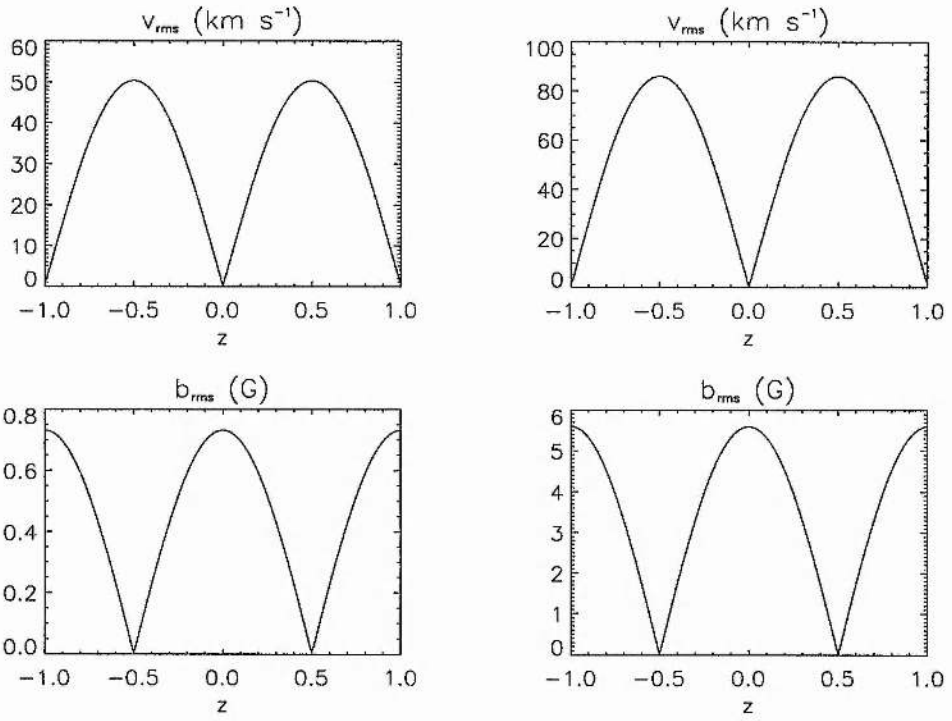

Figure 6.6: Root-mean-square velocity and magnetic field shear components for the quiet region (left) and active coronal loops (right) of Fig. 6.2.

Chapter 7

Laboratory Plasmas

7.1 Nuclear Fission

Modern society demands power. For most of the twentieth century the demand has been sated with fossil fuels, but with progressively increasing consumption and dwindling supplies we are facing up to the need for alternative sources. One of the most potent sources is locked into the very substance of matter by the strong nuclear force of the atom, which holds the protons and neutrons of the nucleus together against the mutual electrostatic repulsion the protons experience. Initially, naturally radioactive atoms were detected, notably by the Curies, in which unstable elements transmuted into others via the emission of nuclear particles and high energy electromagnetic radiation. Later it was found that elements could be artificially induced to become unstable by the addition of a neutron to the nucleus, but to the extent of breaking up into fragments with the release of substantially more energy than in the natural case. Furthermore, amongst the fragments are found neutrons which in turn destabilise other nuclei with the result that the reaction is self-sustaining once initiated. However, following the accidents at Three Mile Island and Chernobyl, and reports of leaks of cooling material, the public has become rightly suspicious of fission power. No matter how rigorous the safety procedures the process itself is inherently dangerous. Apart from safety there is the issue of the waste products, which are highly radioactive and long-lasting. Nirex, the U.K. nuclear waste disposal agency, designs bunkers to store the waste for millenia, while B.N.F.L. concentrates on re-processing waste. Recently it has been suggested that nuclear waste might be incinerated (Venneri et al., 1993), but fission as a whole remains an undesirable, yet essential component of daily life.

7.2 Nuclear Fusion

Fission relies on the fact that a large nucleus tends to be unstable and to disintegrate into slightly smaller components, either by progressive emission of radiation or via artificial means. In either case the rest mass of the atoms and particles following the reaction is less than at the start, the difference appearing as energy given by Einstein's relation $E = mc^2$. At the other end of the spectrum of scales, small atoms may be forced together into slightly larger atoms: again the initial rest mass exceeds the final, so that energy is released. However, in contrast to its larger relative, which is eager to disintegrate, the fusion reaction is opposed by the electrostatic repulsion of positively charged nuclei. If the nuclei can be made to approach sufficiently closely, however, the repulsion is surmounted by the close-range strong nuclear force which completes the process of forming a new nucleus. The overall energy released in the process exceeds the initial requirement and so makes fusion a viable energy source. In fact, per unit mass of fuel, fusion releases more energy than coal, oil, and even uranium; 2.5 million tons of coal release the energy equivalent of around 250 pounds of deuterium/tritium mixture (Eliezer and Eliezer, 1989, p67).

Further advantage arises from the availability of heavy water. Deuterium may be extracted from sea-water while short-lived tritium may be generated in sufficient quantities at the reactor. The process itself is less radioactive than fusion, in the sense that the fast neutrons are the only health hazard — the fusion products themselves are not radioactive. However, in order to contain the neutrons and utilise them to generate tritium, the reactor blanket, usually lithium, tends to transmute into radioactive elements. So in the short-term a society accepting fusion would have to continue to tolerate the problem of nuclear waste, but at least there is the potential in the future of finding a suitable means of shielding which will not generate radioactive elements.

Finally, the process is inherently safe — so safe in fact that it is extremely hard to sustain. A fission reactor can become critical unless action is taken to prevent this whereas, in the event of becoming unstable, a fusion reaction interacts with the container and drops in temperature until the thermal motions of the atoms are insufficient to initiate further reactions. The active effort must be employed in keeping the reaction going, while termination of the reaction requires no outside intervention.

7.3 Toroidal Fusion Devices

The historical development of the magnetically confined fusion reactor is worth examining as it gives some insight into the properties and problems of fusion power. It has already been said that, in order to initiate fusion reactions from the thermal motions of atoms, temperatures of the order of hundreds of millions of kelvins are required. This raises the problem that using any physical medium to confine the plasma causes the surface to vaporise, and the plasma to cool by conduction until the reaction can no longer be maintained. Magnetic fields can confine plasma since particles

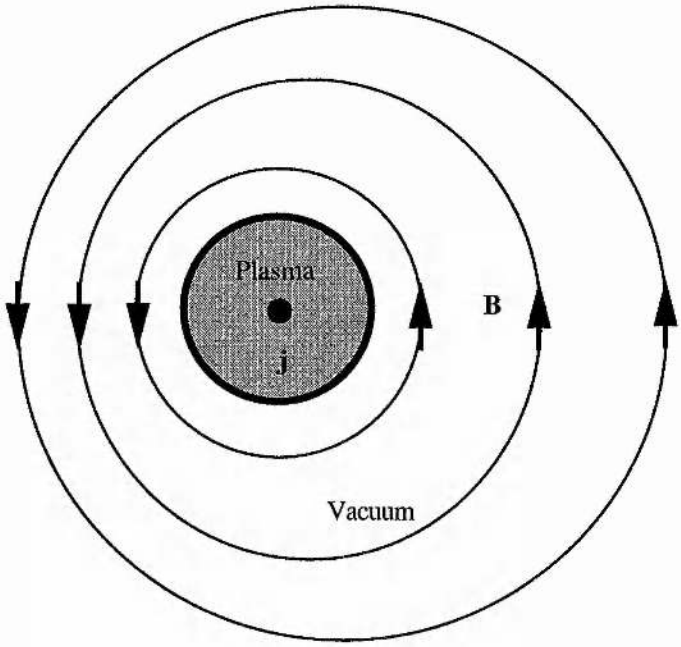

Figure 7.1: Purely poloidal magnetic field. In this and following poloidal cross-section diagrams the left represents the interior of the torus and the right the exterior.

tend to circulate around a field line — the stronger the field, the tighter the orbit — but without any opportunity for thermal loss. The original confinement device was the magnetic bottle. The field at the ends is stronger than that in the centre, so that as a particle approaches the end it rotates more. Since a magnetic force does no work on a particle the net result is that transverse momentum is converted into azimuthal rotation so that the particle remains within the bottle, bouncing back and forth. However, a particle which moves too quickly transversely will escape the bottle before it loses all its transverse momentum — the so-called loss cone for certain ratios of velocity perpendicular to the magnetic field to that parallel to the field. Rowlands (1981) discusses such mirror devices. The obvious way to stop this loss was to join the ends of the bottle to create a torus.

The first requirement of any field configuration is that the magnetic force balance the outward radial expansion of the plasma caused by the pressure forces, thus confining the plasma to a torus within the containment vessel torus — this is achieved equally well by both purely toroidal and purely poloidal fields. In each case, however, there are forces which tend to move the plasma outwards (Freidberg, 1987, Sect. 4.8). This happens for two reasons. First of all, although the plasma pressure is constant around any magnetic surface, Eq. (7.5), the area on the outside of the toroidal surface is greater than that on the inside, leading to a net pressure force directed outwards. Secondly, the magnetic field strength on the inside of the torus is stronger than that on the outside so that the net magnetic pressure force is directed outwards, even taking into account the larger

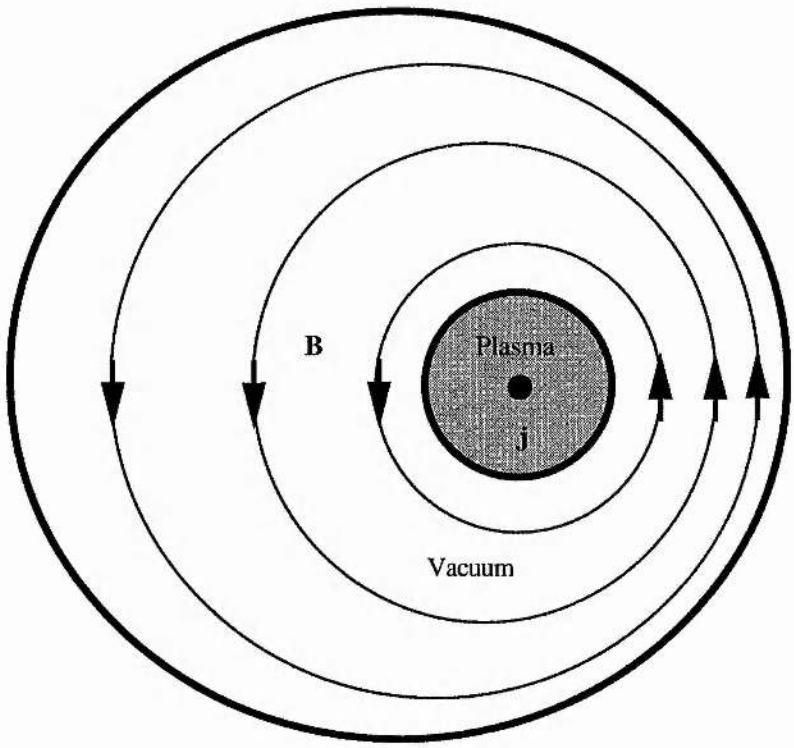

Figure 7.2: Purely poloidal magnetic field surrounded by a perfectly conducting shell.

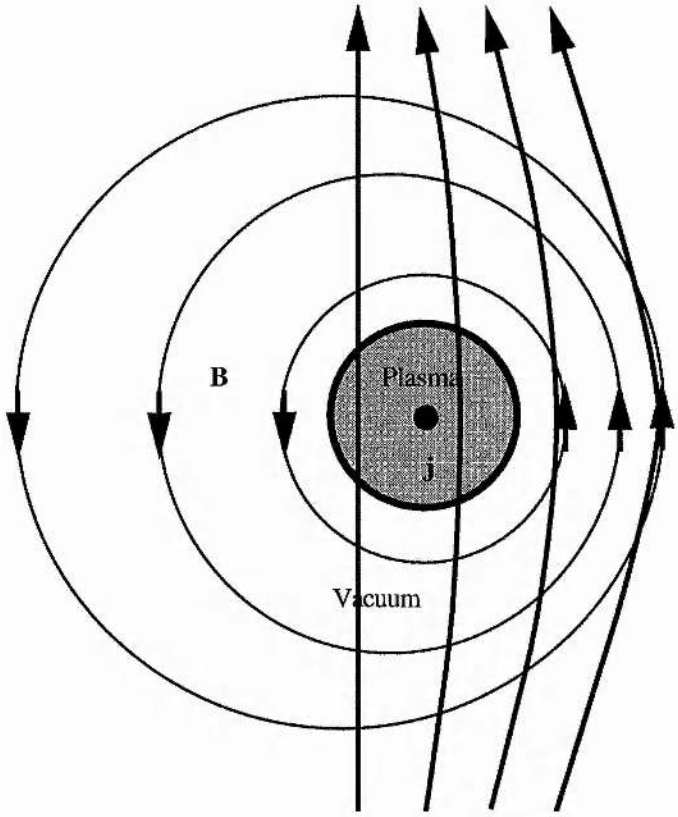

Figure 7.3: Purely poloidal magnetic field with vertical magnetic field superposed.

surface area on the outside of the torus (Fig. 7.1). There are two ways to counteract this problem, (Freidberg, 1982, p824). In the case of the purely poloidal magnetic field, a perfectly conducting shell placed around the plasma has the effect of causing a pile-up of field lines near the wall since the field cannot penetrate a perfect conductor (Fig. 7.2). An inward magnetic pressure force is then created to oppose the expansion. Alternatively, a set of field coils which generate a vertical magnetic field throughout the torus can introduce an inward component of magnetic force by reinforcing the magnetic field on the outside of the torus and reducing it on the inside (Fig. 7.3).

The purely poloidal field is subject to the sausage and kink instabilities. The sausage instability arises when a radial perturbation initiates an instability which causes a contraction to continue to pinch inwards and an expansion to continue outwards, making the magnetic surface resemble a string of sausages (Freidberg, 1987, Fig. 9.6). The kink instability, on the other hand, causes the entire plasma column to move outwards when an initial outward motion leads to a situation where the magnetic pressure on the inside of the torus exceeds that on the outside (Freidberg, 1987, Fig. 9.4).

A purely toroidal magnetic field, on the other hand, has an associated current which is purely poloidal. Once again the greater magnetic pressure force on the inside of the torus causes an outward force, although the demonstration of this is a little more complicated than in the case of the purely poloidal field. However, neither the introduction of a perfectly conducting shell nor of a

vertical field will counteract the expansion. In the former case, field lines are not trapped between the plasma core and conducting wall, while in the latter the vertical field remains unchanged, since there is no poloidal component to the original field.

Thus, the purely poloidal magnetic configuration is able to attain a state of radial and toroidal equilibrium, but is then subject to instabilities which change the shape and position of the confined plasma column while the purely toroidal field is not able to attain a state of toroidal equilibrium. It was discovered that neither a purely toroidal or poloidal field is adequate to confine the plasma. In the former case the field is susceptible to the so-called sausage and kink instabilities.

A helical field, consisting of both toroidal and poloidal field components has proved more successful in confining plasma. The toroidal field is generated by magnetic coils. The means of generating the poloidal field determines the reactor designation. The early stellarator (Sect. 7.7) used field coils again while the more recent tokamak (Sect. 7.6) relies on a toroidal current to generate the field. This has proved the most successful experiment so far and is the focus for the majority of magnetic confinement research.

The progress of fusion research is that of surmounting one particular problem only to find a new one, usually in the form of an instability of which there is a veritable zoo — kink and sausage instabilities have already been mentioned; others include the tearing, ballooning modes and also sawteeth and disruptions. Details of these may be found in Wesson (1987).

7.4 Coordinate systems

The natural coordinate system to use in describing a torus is the toroidal coordinate system (r, θ, ϕ) displayed in Fig. 7.4. In this diagram R is the major axis of the torus, r is the radial distance of the point on the torus from the centre of the poloidal cross-section, θ is the angle in the poloidal plane and ϕ is the angle around the torus when viewed in plan. The disadvantage of using this system is that the unit vectors $\hat{\boldsymbol{r}}, \hat{\boldsymbol{\theta}}$ and $\hat{\boldsymbol{\phi}}$ are not orthogonal. Toroidal coordinates are related to Cartesian coordinates by

$$x = (R + r\cos\theta)\cos\phi, \tag{7.1}$$

$$y = (R + r\cos\theta)\sin\phi, \tag{7.2}$$

$$z = r\sin\theta. \tag{7.3}$$

More common for large aspect ratio devices is to approximate the torus as a straightened cylinder: r and θ are retained while $z = R\phi$.

7.5 Fusion MHD

MHD must be regarded as simply a starting point in theoretical investigations of fusion which has achieved success in determining conditions for large-scale equilibrium of the plasma.

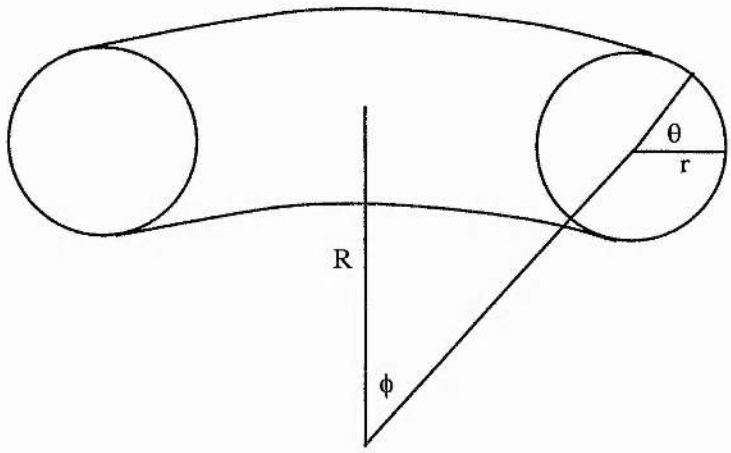

Figure 7.4: Toroidal coordinate system (r, θ, ϕ).

However, once MHD stability has been achieved there is still a host of kinetic instabilities, which MHD cannot describe, arising from charge separation effects and occurring on short time scales. The following examples of the use of MHD in determining stability criteria are taken from Wesson (1987) which contains many other aspects not discussed here.

The most basic equilibrium requirement comes by considering the magnetic force and the plasma pressure forces to dominate in the momentum equation, Eq. (3.15):

$$\boldsymbol{j} \times \boldsymbol{b} = \nabla p. \tag{7.4}$$

Taking the scalar product of Eq. (7.4) with $\boldsymbol{b}$ and $\boldsymbol{j}$ in turn shows that

$$\boldsymbol{b} \cdot \nabla p = \boldsymbol{j} \cdot \nabla p = 0, \tag{7.5}$$

implying that the plasma pressure is constant along magnetic field lines and current lines. Thus, both magnetic field lines and current lines lie along surfaces of constant pressure. In the straight cylinder approximation these surfaces can be taken to be nested cylinders and the axisymmetry of the problem is used to write the remaining magnetic field components as

$$b_r = -\frac{1}{r}\frac{\partial \psi}{\partial z}, \tag{7.6}$$

$$b_z = \frac{1}{r}\frac{\partial \psi}{\partial r}, \tag{7.7}$$

satisfying

$$\boldsymbol{b} \cdot \nabla \psi = \nabla \cdot \boldsymbol{b} = 0. \tag{7.8}$$

Thus, magnetic field lines in the $r - z$ plane can be drawn as contours of the function ψ, called a flux function. Equations (7.5) and (7.8) then make it clear that $p = p(\psi)$. Similarly, the current

density can be written as

$$j_r = -\frac{1}{r}\frac{\partial f}{\partial z}, \tag{7.9}$$

$$j_z = \frac{1}{r}\frac{\partial f}{\partial r}, \tag{7.10}$$

with $f = f(\psi)$. Equation (7.4) can now be written in terms of the flux functions f and ψ as

$$r\frac{\partial}{\partial r}\left(\frac{1}{r}\frac{\partial \psi}{\partial r}\right) + \frac{\partial^2 \psi}{\partial z^2} = -\mu_0 r^2 \frac{\mathrm{d}p}{\mathrm{d}\psi} - \mu_0^2 f(\psi)\frac{\mathrm{d}f}{\mathrm{d}\psi}, \tag{7.11}$$

which is known as the Grad-Shafranov equation. Specifying the functions p and f enables ψ to be found and hence two-dimensional cross-sections of flux surfaces to be plotted, such as Fig. 7.1. Freidberg (1982, Sect. IV(C)) applies the Grad-Shafranov equation to various types of fusion device. This approach is not necessarily consistent with the induction equation, Eq. (3.16), however.

The degree of twist of field lines is an important factor in determining stability of magnetic configurations. One measure of this is the safety factor, q, which is defined as the angle traversed in the toroidal direction so that the field line intersects a poloidal cross-section at the same place as when it started, divided by 2π. Given the equation for the field line

$$R\frac{\mathrm{d}\phi}{\mathrm{d}s} = \frac{B_\phi}{B_p}, \tag{7.12}$$

in which R is the magnitude of the position vector measured from the centre of the torus, s measures the distance travelled in the poloidal direction, B_ϕ is the toroidal magnetic field component and B_p the poloidal magnetic field component, the expression for the safety factor becomes

$$q = \frac{1}{2\pi}\oint \frac{B_\phi}{RB_p}\mathrm{d}s. \tag{7.13}$$

For a sufficiently large aspect ratio and circular cross-section the cylinder approximation is valid. Setting R as the major radius then gives $\mathrm{d}s = 2\pi \mathrm{d}r$, with r as the minor radius of the flux surface in question, giving

$$q = \frac{rB_\phi}{R_0 B_\theta}, \tag{7.14}$$

since the poloidal component is B_θ in cylindrical coordinates. See Wesson (1987, Sect. 3.4) for further properties.

Once a basic equilibrium has been determined its stability properties must be examined. Two approaches are commonly used. The first takes the MHD equation and superposes a perturbation onto the equilibrium. The new equations are next linearised in the perturbation quantities and solutions are sought of the form $\exp(i\boldsymbol{k}\cdot\boldsymbol{r} + i\omega t)$. The resulting equations can be combined into a single equation in terms of the perturbation displacement, $\boldsymbol{\xi}$, (Freidberg, 1987, Sect. 8.4):

$$-\omega^2 \rho \boldsymbol{\xi} = \boldsymbol{F}(\boldsymbol{\xi}), \tag{7.15}$$

where the function $\boldsymbol{F}$ is self-adjoint ($\int \boldsymbol{\eta}\cdot\boldsymbol{F}(\boldsymbol{\xi})\mathrm{d}\boldsymbol{r} = \int \boldsymbol{\xi}\cdot\boldsymbol{F}(\boldsymbol{\eta})\mathrm{d}\boldsymbol{r}$ with $\boldsymbol{\eta}$ another displacement vector). This, then, means that the eigenvalue, ω^2, of Eq. (7.15) is always positive. Since a perturbation is

stable whenever Im $\omega > 0$ and unstable when Im $\omega < 0$, and Im $\omega \neq 0$ only when Re $\omega = 0$ (since $\omega^2 > 0$), any transition from stability to instability must occur when $\omega \equiv 0$. From the complete set of eigenvalues of Eq. (7.15) a set of permissible frequencies can be found. If *any* of them has Im $\omega < 0$ then the perturbation is linearly unstable, while if *all* have Im $\omega > 0$ then the perturbation is linearly stable.

A second method considers the energy balance for the equilibrium and perturbation. If a perturbation acts to reduce the potential energy of the equilibrium, thus increasing the kinetic energy of the perturbation in the process, the perturbation will continue to grow and a state of instability exists. If, on the other hand, the potential energy is increased by the perturbation, this is at the expense of the perturbation kinetic energy and the perturbation is damped, indicating linear stability. The problem now becomes one of applying variational calculus to the energy equation formed by taking the scalar product of Eq. (7.15) with $\boldsymbol{\xi}^*$ and integrating over the volume:

$$\omega^2 K = \delta W, \tag{7.16}$$

where $K = 1/2 \int \rho |\boldsymbol{\xi}|^2 \mathrm{d}\boldsymbol{r}$ and $\delta W = -1/2 \int \boldsymbol{\xi}^* \cdot \boldsymbol{F}(\boldsymbol{\xi}) \mathrm{d}\boldsymbol{r}$. Freidberg (1987, Sect. 8.7) proves that any $\boldsymbol{\xi}$ which yields maximum or minimum values of ω^2 in Eq. (7.16) is an eigenfunction of Eq. (7.15). Thus an equilibrium is stable if and only if $\delta W \geq 0$. Other more complicated forms of the energy principle can be formed for boundary conditions more general than the perfectly conducting shell or vacuum boundary which apply in this simple case, but will not be pursued here. In general, the energy methods are used by applying trial functions, $\boldsymbol{\xi}$, to the equilibrium and trying to find any $\boldsymbol{\xi}$ such that $\delta W < 0$. In that sense the energy method is best suited for showing that an equilibrium is unstable.

Several conditions have been derived using the energy method. For the screw pinch, a cylinder of plasma confined by a helical field, a particular choice of trial function which is maximum near a resonant surface leads to a necessary condition for stability, known as the Suydam criterion (Wesson, 1981, Sect. 9.4.5):

$$\frac{rB_z^2}{8\mu_0}\left(\frac{q'}{q}\right)^2 + p' > 0, \tag{7.17}$$

where the prime denotes differentiation with respect to r. When this condition is satisfied the stabilising effects of the magnetic shear overcome the destabilising pressure gradient. Moving from a cylinder of plasma to the toroidal plasma of most fusion devices the introduction of additional curvature means that the previously stabilising magnetic shear still maintains its stabilising effect on the inside of the torus but has an opposite curvature, and hence destabilising effect, on the outside. This more complicated situation leads to another necessary condition for stability, the Mercier criterion (Freidberg, 1987, Sect. 10.5.4):

$$\frac{rB_\phi^2}{8\mu_0}\left(\frac{q'}{q}\right)^2 + p'(1-q^2) > 0. \tag{7.18}$$

When this condition fails an interchange mode starts, in which the outside edge of the plasma becomes unstable while the inside remains stable (Freidberg, 1987, Sect. 8.11.3).

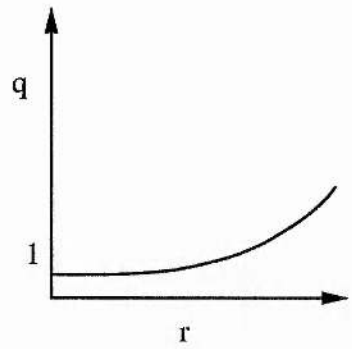

Figure 7.5: Safety factor profile for a tokamak.

Approximating the torus by a cylinder and requiring that all variables be periodic in θ and z, a perturbation may be written as $\boldsymbol{\xi} = \hat{\xi}(r) \exp(im\theta + inz/R)$, where R is the length of the major axis of the torus. Another class of instabilities exists which are unaffected by pressure and depend only on the shear, namely kink modes. A sufficient condition for stability is then (Freidberg, 1987, Sect. 9.6.4)

$$\frac{1}{q_a} < \frac{n}{m}, \tag{7.19}$$

where now q_a is the safety factor at the wall. The $m = 1$ mode is stabilised by

$$q_a > 1, \tag{7.20}$$

which is known as the Kruskal-Shafranov condition and which implies an upper limit on the toroidal current. Further limitations must also be placed on the pressure, described in terms of the plasma β (Wesson, 1987, Sect. 6.12); experiments have produced values of 0.05–0.1.

In practice the existence of instabilities is not necessarily a prohibition on stable operation. An instability may be comparatively benign, growing for a short time and then saturating as nonlinear effects become more important. However, when the safety factor is such that $q = m/n$ at some surface $r = r_{\rm res}$ the effects of the instability become greatly pronounced. Keeping the range of the safety factor as small as possible then limits the possible number of modes which may become resonant. If the Kruskal-Shafranov condition, Eq. (7.20), holds then all instabilities with $m = 1$, in particular the kink mode, are benign (Wesson, 1987, Fig. 6.1.2). In practice only a few combinations of m and n will be a potential problem.

The applications of these concepts are now described for three fusion devices: the tokamak, stellarator and reversed field pinch. Others are also discussed by Robinson (1981) and Freidberg (1982).

7.6 Tokamak

The name tokamak is an anglicisation of a Russian acronym "toroidalnaya kamera magnitnaya" which describes a particular type of toroidal magnetic confinement device. The tokamak, like the reversed field pinch (Sect. 7.8), uses a plasma current to generate the poloidal field component, rather than coils. At present the tokamak configuration is the focal point of magnetic confinement fusion research. Devices now generally have a toroidal field, generated by external coils, of a few tesla while the poloidal field, which is generated by the MA current, is smaller than the toroidal component by the order of the device inverse aspect ratio ($\simeq 0.4$ for JET, the Joint European Torus). The radial safety factor profile increases from a central value of about 0.7 monotonically towards the edge and a value of 3–4 (Fig. 7.5). Thus the Kruskal-Shafranov condition, Eq. (7.20), holds and kink modes are suppressed. In practice the situation is more complicated, however, and an $m = 1$ mode may occur. These have been associated with the sawtooth phenomenon.

Jensen and Chu (1984) and Wesson (1987, Sect. 3.11) discuss the current drive mechanism; for the purposes of this introduction, however, the tokamak is assumed to have reached the state where the magnetic field configuration is of the form desired for confining the plasma.

Some stability properties have been mentioned in the preceding section. However, MHD is only the starting point for a stability analysis. Once the global ideal MHD instabilities, such as the kink instability, have been overcome there remain the resistive MHD instabilities, such as the tearing mode, and even after those there are kinetic instabilities, such as the $\boldsymbol{E} \times \boldsymbol{B}$ drift, which cannot be described by MHD as they involve charge separation effects. Wesson (1987, Chaps. 6 & 7) and Callen et al. (1992) give details of other instabilities. In the tokamak the toroidal expansion of the plasma is opposed by the addition of a vertical magnetic field (Sect. 7.3), but there are homogeneity difficulties associated with such an addition (O'Brien and Robinson, 1993, Sect. 8.2).

The desired temperatures for fusion reactions to occur through collisions are beyond the reach of resistive heating effects of the current flowing through the plasma. As the temperature rises, the plasma resistance falls off as $T_e^{-3/2}$, where T_e is the electron temperature. Beyond 10^7 K other forms of heating, such as the injection of neutral particles or resonance effects of injected radio-frequency waves, are required (Wesson, 1987, Chap. 5)[1]. The relevance of MHD in heating studies is therefore open to question[2].

Operational parameters having been achieved, however, the behaviour of most tokamak experiments is far from stable. Oscillatory behaviour in the fields and temperatures superposed on a "sawtooth" crash are often observed (O'Brien and Robinson, 1993, Sect. 8.3) after which there is a disruption of the containment and the experiment ends. There has been a considerable improvement in the confinement time of the experiments from the milliseconds of the 1950's to about a second in the 1990's, but reactions are only approaching the point where the energy released by nuclear fusion

[1] MHD theories of Alfvén resonance heating are given by Kappraff and Tataronis (1977) and Poedts et al. (1989)

[2] The studies of Chaps. 8 and 9 sidestep this problem by only considering the steady state and by only being concerned with the loss of kinetic and magnetic energies which are then assumed to be converted into heat.

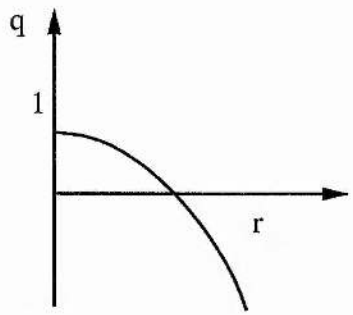

Figure 7.6: Safety factor profile for a reversed field pinch.

balances the energy required to maintain the reaction. Further difficulties remain, such as the need to remove reaction products and re-supply the vessel while the reaction proceeds and the means to avoid reaction disruption. See also Kadomtsev (1988) for a history of the tokamak, Todd (1993) for a discussion of the engineering issues involved and Green (1981), who discusses the then nascent JET experiment.

7.7 Stellarator

The stellarator is another toroidal device which uses helical magnetic fields, the poloidal field component of which is generated with helical conductors. The outward expansion of the toroidal plasma can be compensated for by adjusting the helical conductors since there is a stronger vacuum field than in the tokamak. While being more complicated from an engineering point of view, the stellarator is physically simpler since large currents are no longer required, thus reducing the severity of many instabilities and the likelihood of turbulence. The little current present is required to cancel the effects of the kinetic $\boldsymbol{E} \times \boldsymbol{B}$ drift. However, there is also the side-effect that Ohmic heating will be less effective in heating the plasma so that additional heating sources are required. Experiments are able to operate without disruptions and a safety factor of $q \simeq 1$ is possible, thus reducing the impact of ideal MHD instabilities (Sect. 7.5). See Lees (1981) for further experimental details and Freidberg (1987, Sects. 7.5 & 7.6) for an analysis of stellarator equilibria.

7.8 Reversed Field Pinch

The reversed field pinch (RFP) appears similar to the tokamak — plasma contained within a torus, toroidal magnetic field generated by external coils and with a current driven by an externally generated electric field. In fact there are considerable differences in behaviour, the major one being that the toroidal and poloidal field components are of the same order, unlike the tokamak where the toroidal component is several times the poloidal. This leads to the safety factor being less than

unity whereby the second term of the Mercier criterion, Eq. (7.18), is negative when $\mathrm{d}p/\mathrm{d}r < 0$, which is the case because the densest plasma is nearest the centre of the toroidal channel. Thus it is necessary that $\mathrm{d}q/\mathrm{d}r \neq 0$ (Fig. 7.6). In practice the shear is large enough that the toroidal field component reverses direction between the centre and minor radius, leading to the name of the device.

A second difference between the RFP and tokamak lies in the toroidal stability of the devices. The RFP can operate with larger plasma pressures of order $\beta = 0.1$ compared with experimental values of order 0.05 for the tokamak. This leads to a greater tendency for the plasma column to drift outwards making either a vertical field or a conducting shell around the plasma even more important. The latter option is most commonly chosen. This additional engineering requirement absent in the tokamak is offset by the theoretical possibility that ignition might be achieved as a result of unaided Ohmic heating within the dense plasma.

Finally, the behaviour of the RFP is better suited to a magnetohydrodynamic description than the tokamak. The cylinder approximation works well as the toroidal field is not dominant as with the tokamak, so that the slight bending required to "straighten" the torus is less noticeable against the comparatively strong poloidal field effects. Furthermore, higher pressure and greater turbulence results in a sufficiently collisional plasma for the MHD assumptions to hold approximately. From this starting point Taylor (1974) made an important advance in modelling the RFP using an energy argument. He noted that the global twist of the field, expressed in terms of the magnetic helicity, $H_\mathrm{m} = 1/2 \int \boldsymbol{A} \cdot \boldsymbol{B} \mathrm{d}V$, where $\boldsymbol{B} = \nabla \times \boldsymbol{A}$, would be expected to be conserved on relaxation time-scales. From this constraint it has been proved that the minimum energy configuration is that of a constant-α force-free field,

$$\nabla \times \boldsymbol{B} = \alpha \boldsymbol{B}, \tag{7.21}$$

and α constant everywhere (Chandrasekhar and Woltjer, 1958; Reiman, 1981; Faber et al., 1982; Riyopoulos et al., 1982; Taylor, 1986; Laurence and Avellaneda, 1991). Thus, given the likely growth of an instability, the plasma cannot relax any further than this state. Furthermore,

$$\alpha = \frac{2\Theta}{a}, \tag{7.22}$$

where the pinch parameter, Θ, is given by

$$\Theta = \frac{B_\theta(a)}{\overline{B_\phi}}. \tag{7.23}$$

A simple solution (Lundquist, 1951) is

$$B_\phi = B_0 J_0(\alpha r), \tag{7.24}$$

$$B_\theta = B_0 J_1(\alpha r), \tag{7.25}$$

which is stable to ideal and resistive modes for $\alpha r \leq 3.176, 3.104$, respectively. In addition the field reverses for $\alpha r > 2.405$ (Bodin and Newton, 1980). Although this solution is not in perfect

agreement with experiments, especially at the wall, it is adequate for simple investigations. Other formulations have been found which include the effects of the non-negligible plasma pressure.

Self-reversal of the field has been found in devices such as ZETA and its successors, lasting up to 3 ms, during which the plasma behaved in a stable, quiescent manner if the current exceeded 0.3 MA. Loss of stability can arise when the reversed field diffuses and the Mercier criterion is no longer satisfied.

Further details of RFP theory and experiment can be found in Bodin and Newton (1980) and Bodin (1987).

7.9 Boundary Conditions

An important difference between astrophysical and laboratory plasmas is that the former are unbounded whilst the latter reside within a metallic confinement vessel. Despite the fact that magnetic fields are used to keep the plasma away from the walls, the effects of the vessel are important. Before discussing the different possibilities pertaining to fusion, the general jump conditions on the electric flux density, $\boldsymbol{D}$, the electric field, $\boldsymbol{E}$, the magnetic flux density, $\boldsymbol{B}$, and the magnetic field, $\boldsymbol{H}$, are now given (Lorrain et al., 1988, pp. 197, 207 & 371):

$$(\boldsymbol{D}_1 - \boldsymbol{D}_2) \cdot \hat{\boldsymbol{n}} = \sigma_{\text{free}}, \tag{7.26}$$

$$(\boldsymbol{E}_1 - \boldsymbol{E}_2) \times \hat{\boldsymbol{n}} = 0, \tag{7.27}$$

$$(\boldsymbol{J}_1 - \boldsymbol{J}_2) \times \hat{\boldsymbol{n}} = \frac{\mathrm{d}\sigma}{\mathrm{d}t}, \tag{7.28}$$

$$(\boldsymbol{B}_1 - \boldsymbol{B}_2) \cdot \hat{\boldsymbol{n}} = 0, \tag{7.29}$$

$$(\boldsymbol{H}_1 - \boldsymbol{H}_2) \times \hat{\boldsymbol{n}} = 0. \tag{7.30}$$

In the above relations the subscripts 1 and 2 refer to the two sides of the interface, $\hat{\boldsymbol{n}}$ is the normal to the interface and σ is the surface charge density which consists of both bound and free charges. The electric flux density is related to the electric field by $\boldsymbol{D} = \epsilon_0 \boldsymbol{E} + \boldsymbol{P}$, where $\boldsymbol{P}$ is the polarisation which arises from an anisotropic charge distribution within a medium. Similarly the magnetic flux density and magnetic field are related by $\boldsymbol{B} = \mu_0(\boldsymbol{H} + \boldsymbol{M})$, where $\boldsymbol{M}$ is the magnetisation vector, or magnetic moment per unit volume, which arises in inherently magnetic materials. For a rigid boundary an additional restriction on the velocity is that the normal component of the velocity is zero at the boundary or, more realistically, full no-slip conditions give the requirement that $\boldsymbol{v} = \boldsymbol{0}$ at the boundary.

7.9.1 Perfect conductor

The containing vessel may be regarded as being a perfect conductor (cf. Sect. 7.3) with the consequence that the electric field is identically zero within. Furthermore, there can be no charge

build-up within the conductor so the polarisation is also zero. Charge is free to build up on the surface, however, so that Eq. (7.26) shows that the normal component of the electric field, which is now proportional to the electric flux density, may be discontinuous across the boundary. Equation (7.27), however, leads to the restriction

$$\boldsymbol{E} \times \hat{\boldsymbol{n}} = \boldsymbol{0}, \tag{7.31}$$

at the boundary. With an infinite conductivity and zero electric field it is possible to have a finite current density within the conductor, so Eq. (7.28) just determines this quantity without imposing any restrictions on the current density on the other side of the boundary.

For the helical fields in fusion devices it is desirable to prevent the magnetic field lines from intersecting the wall, otherwise gyro-motions of ions and electrons lead to hot plasma coming into contact with cold metal causing damage and loss of confinement. The condition

$$\boldsymbol{B} \cdot \hat{\boldsymbol{n}} = 0, \tag{7.32}$$

is thus imposed at the wall. Finally, Eq. (7.30) just gives the tangential magnetic field within the conductor.

7.9.2 Insulator

Unlike reversed field pinches, tokamaks do not require a highly conducting shell to surround the plasma, so another set of boundary conditions to model is that of an insulating boundary, which may consist of a dielectric material coating a metal wall. Again surface charges may be present so no conditions are imposed on the normal electric field. However, the medium may now have an electric field within since charge separation and polarisation are now permitted. Thus, Eq. (7.27) no longer imposes a constraint on the tangential electric field in the medium in contact with the insulator, but rather gives the electric field within the insulator. For the magnetic conditions Eq. (7.32) is again imposed, there being no constraint on the tangential magnetic field again. A new property of the insulator, though, is that current cannot flow into or through the medium. Thus, at the wall

$$\boldsymbol{J} \cdot \hat{\boldsymbol{n}} = 0. \tag{7.33}$$

7.9.3 Vacuum

A further approach is to imagine the plasma to be separated from the wall by a vacuum. This concept leads to difficulties, however, which are illustrated in Fig. 7.7 in which a field-free plasma with gas pressure is confined by a circular magnetic field permeating a vacuum. Pressure balance requires a discontinuity in the magnetic field which is incompatible with Eq. (7.30) since the magnetisation is zero in each medium. The resolution of the problem arises from the fact that

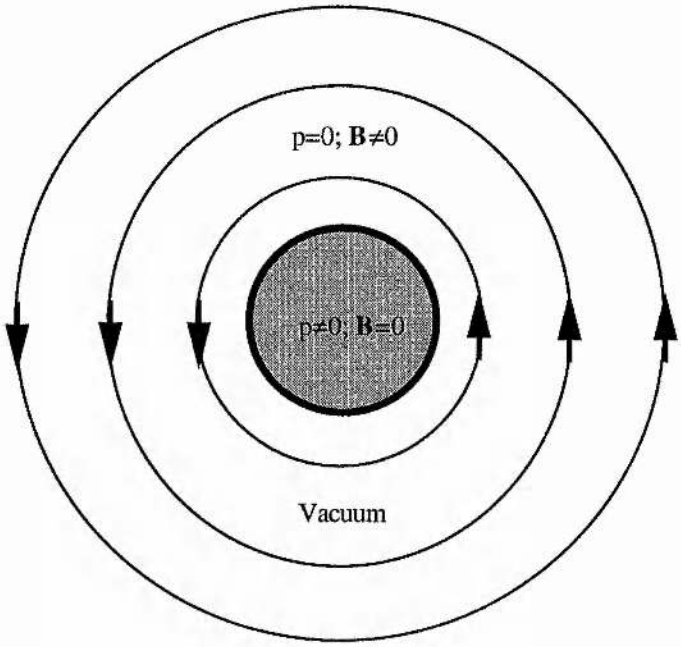

Figure 7.7: Field-free plasma confined by a circular magnetic field in a vacuum.

it is not possible to have a sharp boundary between a plasma and a vacuum. Rather, a change in properties occurs over a finite distance making application of any boundary conditions a dangerous process. An alternative solution is to consider the interface to be a sharp boundary and replace Eq. (7.30) with

$$(\boldsymbol{B}_1 - \boldsymbol{B}_2) \times \hat{\boldsymbol{n}} = \boldsymbol{K}, \tag{7.34}$$

where $\boldsymbol{K}$ is the surface current density on the interface.

Chapter 8

Solar-type solutions

8.1 Existence of solutions

Having found an equilibrium configuration for the straight cylinder in Chap. 5 the obvious question to ask is whether a similar type of solution may be found in the fusion context. As before, fields will be sought in the form of Eqs. (5.2) and (5.3) but now with different constraints on $v(r,z)$ and $b(r,z)$. For a start the cylinder is now obtained by breaking and straightening a torus so that any solutions for physically measurable quantities should be periodic in z. However, the solutions obtained in the corona, Eqs. (5.31) and (5.32), are exponential in z and so are not appropriate here. The boundary conditions discussed in Sect. 7.9 are applied to Eqs. (5.12) and (5.13) to determine whether solutions to the new boundary-value problem exist. The method of analysis depends on constructing an energy equation by multiplying Eq. (5.12) by v and Eq. (5.13) by b to give

$$\nu v\nabla^2 v + \eta b\nabla^2 b - \frac{\nu v^2 + \eta b^2}{r^2} + \frac{\partial}{\partial z}(vb) = 0. \tag{8.1}$$

The identity $v\nabla^2 v = \nabla\cdot(v\nabla v) - |\nabla v|^2$ is used, the resulting expression is integrated over the volume of the cylinder, and the divergence theorem is applied to obtain

$$\int_S (\nu v\nabla v + \eta b\nabla b)\cdot \mathrm{d}\boldsymbol{S} - \int_V \left(\nu\,|\nabla v|^2 + \eta\,|\nabla b|^2 + \frac{\nu v^2 + \eta b^2}{r^2}\right)\mathrm{d}V + \int_V \frac{\partial}{\partial z}(vb)\mathrm{d}V = 0, \tag{8.2}$$

where S represents the surface and V the volume of the cylinder, respectively. In the final term of the left side the part of the volume integral relating to the variation in z is performed to give the expression $[vb]_{-1}^{1}$ which vanishes because v and b are both periodic in z with period 2. The electric field associated with this ansatz is

$$e = -\left(v + \eta\frac{\partial b}{\partial z}\right)\hat{\mathbf{r}} + \frac{\eta}{r}\frac{\partial}{\partial r}(rb)\hat{z}. \tag{8.3}$$

8.1.1 Plasma in direct contact with a conducting wall

Equation (7.32) is automatically satisfied by Eq. (5.3), while Eqs. (7.31) and (8.3) together require that $\nabla b \cdot \hat{\boldsymbol{n}} = -b$ at the wall. The no-slip boundary condition gives $v = 0$ at the wall. With these conditions Eq. (8.2) becomes

$$\int_V \left[\nu \left| \nabla v \right|^2 + \eta \left| \nabla b \right|^2 + \frac{\nu v^2 + \eta b^2}{r^2} \right] \mathrm{d}V + \int_S \eta b^2 \mathrm{d}S = 0, \tag{8.4}$$

the integrands of which are positive definite — the only possible solution to the above equation in a visco-resistive medium requires $\nabla v = \nabla b = \mathbf{0}, v = b = 0$. Hence only trivial fields will satisfy the ansatz of Eqs. (5.2) and (5.3) when conducting boundary conditions are applied in the case of the plasma being in direct contact with the containment vessel wall. Relaxing the no-slip condition could possibly give a non-zero v and b if and only if $\int \nu v \nabla v \cdot \mathrm{d}\boldsymbol{S} > 0$.

8.1.2 Plasma in direct contact with an insulating wall

The only difference with the preceding section is that no longer does $\nabla b \cdot \hat{\boldsymbol{n}} = -b$ at the wall, but instead Eq. (7.33) implies that $\partial b / \partial z = 0$ at the wall. From Eq. (8.2) it can be seen that solutions for v and b are not ruled out.

8.2 Solutions

Following the analysis of Chap. 5 the problem reduces to solving the coupled Eqs. (5.16) and (5.17). The toroidal nature of a tokamak forces the velocity and magnetic fields to be periodic in z in a cylindrical model, enabling the functions v and b to be Fourier analysed along the length of the cylinder in the form:

$$v(r,z) = v_0(r) + \sum_{n=1}^{\infty} v_n(r) e^{in\pi z}, \tag{8.5}$$

$$b(r,z) = b_0(r) + \sum_{n=1}^{\infty} b_n(r) e^{in\pi z}, \tag{8.6}$$

Equations (5.16) and (5.17) now reduce to

$$\frac{\mathrm{d}^2 v_0}{\mathrm{d}r^2} + \frac{1}{r}\frac{\mathrm{d}v_0}{\mathrm{d}r} - \frac{v_0}{r^2} = 0, \tag{8.7}$$

$$\frac{\mathrm{d}^2 b_0}{\mathrm{d}r^2} + \frac{1}{r}\frac{\mathrm{d}b_0}{\mathrm{d}r} - \frac{b_0}{r^2} = 0, \tag{8.8}$$

$$\frac{\mathrm{d}^2 v_n}{\mathrm{d}r^2} + \frac{1}{r}\frac{\mathrm{d}v_n}{\mathrm{d}r} - \left(n^2\pi^2 + \frac{1}{r^2} \right) v_n + \frac{in\pi}{\nu} b_n = 0, \tag{8.9}$$

$$\frac{\mathrm{d}^2 b_n}{\mathrm{d}r^2} + \frac{1}{r}\frac{\mathrm{d}b_n}{\mathrm{d}r} - \left(n^2\pi^2 + \frac{1}{r^2} \right) b_n + \frac{in\pi}{\eta} v_n = 0. \tag{8.10}$$

Equations (8.7) and (8.8) may be solved directly to give

$$v_0(r) = A_0 r + \frac{B_0}{r}, \tag{8.11}$$

$$b_0(r) = C_0 r + \frac{D_0}{r}, \tag{8.12}$$

where A_0, B_0, C_0, and D_0 are constants. The need for non-singular solutions at $r = 0$ requires that $B_0 = D_0 = 0$, so that

$$v_0 = A_0 r, \tag{8.13}$$

$$b_0 = C_0 r. \tag{8.14}$$

Eliminating v_n from Eqs. (8.9) and (8.10) leads to the equation

$$b_n^{\mathrm{IV}} + \frac{2}{r} b_n''' - b_n'' \left(2n^2\pi^2 + \frac{3}{r^3}\right) + b_n' \left(\frac{3}{r^3} - \frac{2n^2\pi^2}{r}\right) + b_n \left[n^2\pi^2 \left(n^2\pi^2 + \frac{1}{\eta\nu}\right) - \frac{3}{r^4} + \frac{2n^2\pi^2}{r^2}\right] = 0. \tag{8.15}$$

Series solutions are now sought and it is found that the two independent solutions which do not have logarithmic singularities at $r = 0$ are

$$\sum_{m=0}^{\infty} \frac{c_{2m}}{(m+2)!(m+1)!} r^{2m+3}, \tag{8.16}$$

and

$$\sum_{m=0}^{\infty} \frac{c_{2m}}{(m+1)!m!} r^{2m+1}, \tag{8.17}$$

where c_{2m} may be expressed in the following ways :

$$c_{2m} = i\sqrt{\eta\nu}\,(n\pi)^m 2^{-2m-1} \left[\left(n\pi - \frac{i}{\sqrt{\eta\nu}}\right)^{m+1} - \left(n\pi + \frac{i}{\sqrt{\eta\nu}}\right)^{m+1}\right] \tag{8.18}$$

$$= 2^{-2m} \sum_{k=0}^{[m/2]} \binom{m+1}{2k+1} (n\pi)^{2m-2k} (-\eta\nu)^{-k}, \tag{8.19}$$

and $[n/2]$ denotes the integer part of $n/2$. Alternatively, for computational purposes a recurrence relation may be used:

$$c_0 = 1, \tag{8.20}$$

$$c_2 = \frac{n^2\pi^2}{2}, \tag{8.21}$$

$$c_{2m+4} = \frac{n^2\pi^2}{2} c_{2m+2} - \frac{n^2\pi^2}{16} \left(n^2\pi^2 + \frac{1}{\eta\nu}\right) c_{2m}. \tag{8.22}$$

Both series are convergent for all r. A more concise notation which includes both Eqs. (8.16) and (8.17) as special cases is

$$B_k^j(r) = \sum_{m=0}^{\infty} \frac{c_{2m}}{(m+j+k)!(m+j)!} r^{2m+2j+1}. \tag{8.23}$$

The general forms of v_n and b_n are then

$$v_n(r) = A_n B_1^0(r) + B_n B_1^1(r), \tag{8.24}$$

$$b_n(r) = C_n B_1^0(r) + D_n B_1^1(r). \tag{8.25}$$

8.2.1 Plasma in direct contact with a conducting wall

The tangential electric field boundary condition, Eq. (7.27), is applied first and leads to the condition

$$\frac{\mathrm{d}}{\mathrm{d}r}(rb_n) = 0 \text{ at } r = a, \tag{8.26}$$

for all n. Applying this gives,

$$b_0(r) = 0, \tag{8.27}$$

$$b_n(r) = \frac{C_n}{B_0^1(a)}\left[B_1^0(r)B_0^1(a) - B_1^1(r)B_0^0(a)\right], \tag{8.28}$$

where the property

$$\frac{\mathrm{d}}{\mathrm{d}r}(rB_1^j(r)) = 2B_0^j(r), \tag{8.29}$$

has been used. $v_0(r)$ is meanwhile unchanged, but

$$v_n(r) = \frac{i\eta C_n}{n\pi B_0^1(a)}\left[4B_0^1(a)B_1^{-1}(r) - (n^2\pi^2 B_0^1(a) + 4B_0^0(a))B_1^0(r) + n^2\pi^2 B_0^0(a)B_1^1(r)\right], \tag{8.30}$$

from Eq. (8.10) and the properties

$$\frac{\mathrm{d}^2 B_1^1}{\mathrm{d}r^2} - \frac{B_1^1}{r^2} + \frac{1}{r}\frac{\mathrm{d}B_1^1}{\mathrm{d}r} = 4B_1^0, \tag{8.31}$$

$$\frac{\mathrm{d}^2 B_1^0}{\mathrm{d}r^2} - \frac{B_1^0}{r^2} + \frac{1}{r}\frac{\mathrm{d}B_1^0}{\mathrm{d}r} = 4B_1^{-1}. \tag{8.32}$$

The conclusion of Sect. 8.1.1 that only a trivial solution is possible for a conducting boundary with no-slip boundary conditions is verified since then $C_n = 0$ for all n, whence $v = b = 0$. Even leaving C_n undetermined by not imposing the no-slip condition still leaves an undesirable solution, however. The toroidal current can be written as

$$I_z = \oint ba\,\mathrm{d}\theta = 2\pi a\, b(a, z), \tag{8.33}$$

by Ampère's law. With $b_0(r) = 0$ from the tangential electric field continuity condition it can be seen that there is no net toroidal current, only a current oscillating along the cylinder. Conservation of current then requires that there must be current flowing from the plasma to the conducting wall and vice-versa along the cylinder. This is not a satisfactory solution, especially for a tokamak.

8.2.2 Plasma in direct contact with insulating wall

The condition that no current flow into the wall, Eq. (7.33), leads to the requirement that $\partial b/\partial z = 0$ at the wall. In terms of Eq. (8.6) this translates into the requirement

$$b_n = 0 \text{ at } r = a, \tag{8.34}$$

for $n \neq 0$, whence

$$b_n = \frac{C_n}{B_1^1(a)}\left[B_1^0(r)B_1^1(a) - B_1^1(r)B_1^0(a)\right], \tag{8.35}$$

with the velocity components being obtained from Eq. (8.10) as

$$v_n(r) = \frac{i\eta C_n}{n\pi B_1^1(a)}\left[4B_1^1(a)B_1^{-1}(r) - (n^2\pi^2 B_1^1(a) + 4B_1^0(a))B_1^0(r) + n^2\pi^2 B_1^0(a)B_1^1(r)\right], \tag{8.36}$$

when $n \neq 0$. Since the wall is an insulator all the current flows in the toroidal direction, not changing with z. Equation (8.33) then gives

$$b_0(r) = \frac{I_z r}{2\pi a^2}. \tag{8.37}$$

Finally, if a no-slip condition is imposed it can be seen that $C_n = 0$ when $n \neq 0$, and $A_0 = 0$ so that

$$v(r,z) = 0, \tag{8.38}$$

$$b(r,z) = \frac{I_z r}{2\pi a^2}. \tag{8.39}$$

This is just the copper bar solution to be discussed in Sect. 9.1. The main point about this equilibrium is that there is no flow at all so that it is not turbulent (wave-driven and electrostatic turbulence not being amenable to steady-state MHD analysis).

But what happens if the no-slip condition is relaxed? Without trying to determine the unknown C_n Fourier coefficients it is still possible to answer this question by examining the energy injected into the plasma, again in the form of the Poynting and viscous fluxes. In Chap. 5 these fluxes were injected through the flat ends of the cylinder, corresponding to the photosphere. In the fusion situation, however, the flux contribution corresponds to the curved surface of the tube, an element of which has magnitude $a\mathrm{d}\theta\mathrm{d}z$. Thus the Poynting flux and viscous flux contributions are given by

$$\text{Poynting contribution} = \int_{\theta=0}^{2\pi}\int_{z=-1}^{1}(\boldsymbol{e}\times\boldsymbol{b})\cdot\hat{\mathbf{r}}\,a\,\mathrm{d}\theta\,\mathrm{d}z = 2\pi a\int_{z=-1}^{1}\frac{\eta b}{r}\frac{\partial}{\partial r}(rb)\mathrm{d}z, \tag{8.40}$$

$$\text{Viscous contribution} = \int_{\theta=0}^{2\pi}\int_{z=-1}^{1}(-\nu\boldsymbol{\omega}\times\boldsymbol{v})\cdot\hat{\mathbf{r}}\,a\,\mathrm{d}\theta\,\mathrm{d}z = 2\pi a\int_{z=-1}^{1}\frac{\nu v}{r}\frac{\partial}{\partial r}(rv)\mathrm{d}z. \tag{8.41}$$

The Poynting flux averaged over the curved surface area is then

$$P = \frac{\eta I_z^2}{2\pi^2 a^3}, \tag{8.42}$$

which corresponds to an energy injection per unit volume of $\eta\overline{j}^2/2$, where $\overline{j} = I_z/(\pi a^2)$ is an averaged toroidal current density.

The viscous flux heating the plasma should be zero physically since the driving mechanism in a fusion device is electromagnetic in nature. However by relaxing the no-slip condition this is no longer automatically true. For the ansatz under consideration, Eq. (5.2), the vorticity is not parallel to the velocity so the only way to keep the viscous heating zero is to adopt the boundary condition $(\boldsymbol{\omega} \times \boldsymbol{v}) \cdot \hat{\mathbf{r}} = 0$ at the wall. This in turn forces ω_z to be zero at the wall whence

$$\frac{\partial}{\partial r}(rv) = 0 \text{ at } r = a. \tag{8.43}$$

However, from Eqs. (8.13), (8.29) and (8.36) it can be seen that $A_0 = C_n = 0$. Thus relaxing the no-slip condition makes no difference — a copper bar equilibrium with no flow once more results.

8.3 Plasma bounded by a vacuum

In a vacuum there can be no current flow and, in the absence of an applied voltage, the electric field is zero. In Sect. 7.9.3 the problems of considering the plasma/vacuum interface to be a sharp boundary were discussed, principally that not all "boundary conditions" are applicable. The two conditions which still apply are that the magnetic flux is conserved across the interface, Eq. (7.29), and that $\oint \boldsymbol{E} \cdot \mathrm{d}\boldsymbol{l}$ is conserved in a steady state, Eq. (7.27). In the latter case this just recovers Eq. (7.31) applied at the plasma/vacuum boundary, while Eq. (7.32) is automatically satisfied by the choice of the plasma magnetic field, Eq. (5.3). Furthermore, if the velocity field is taken to be continuous across the interface a "no-slip" boundary condition is obtained and the situation of Sect. 8.1.1 is recovered, whereby the only possible solution is $\boldsymbol{v} = \mathbf{0}$ and $\boldsymbol{b} = \hat{\boldsymbol{z}}$. Otherwise, if a discontinuous velocity is permitted then the resulting solution possesses no net toroidal current (Sect. 8.2.1). This situation can be contrasted with that of Poedts et al. (1989) in which the radial component of the magnetic field is non-zero across the plasma/vacuum boundary.

8.4 Summary

For the solar-type ansatz of Eqs. (5.2) and (5.3) in a cylinder and with periodicity in z required, the only steady-state solutions possess no flow and will not be turbulent. Plasma in direct contact with a conducting boundary, or separated from either a conducting or insulating wall by a vacuum, has only $\boldsymbol{b} = \hat{\boldsymbol{z}}$ as a solution. Plasma in direct contact with an insulating boundary can maintain the helical copper bar equilibrium $\boldsymbol{b} = \hat{\boldsymbol{z}} + I_z r/(2\pi a^2)\hat{\boldsymbol{\theta}}$. Only these simplistic solutions can be obtained because of the restriction imposed by the adoption of Eqs. (5.2) and (5.3) for the velocity and magnetic fields. The many boundary conditions required in the fusion context and the limited degree of freedom conspire to severely limit the possible steady-state solutions to only those without flow.

Chapter 9

Single-mode global solution

9.1 Copper bar equilibrium

The incompressible, visco-resistive MHD equations, Eqs. (3.15)–(3.20), admit the equilibrium solution:

$$\boldsymbol{v}^{(0)} = 0, \tag{9.1}$$

$$\boldsymbol{b}^{(0)} = b_0\hat{\boldsymbol{z}} + \frac{rj_0}{2}\hat{\boldsymbol{\phi}}, \tag{9.2}$$

$$\boldsymbol{j}^{(0)} = j_0\hat{\boldsymbol{z}}, \tag{9.3}$$

$$\boldsymbol{e}^{(0)} = \eta j_0\hat{\boldsymbol{z}}, \tag{9.4}$$

$$p^{(0)} = \frac{j_0^2a^2}{4}\left(1-\frac{r^2}{a^2}\right), \tag{9.5}$$

where the cylindrical coordinates now used are (r,ϕ,z) with the plasma column being defined by $0 \le r \le a$, $0 \le \phi < 2\pi$, $-1 \le z \le 1$ once more (cf. Chap. 5), the boundary condition being that $p^{(0)} = 0$ at $r = a$ and with j_0 and b_0 constant. This solution is in fact the only time-independent, axisymmetric, zero-flow equilibrium solution which is driven by a constant applied electric field.

9.2 Perturbed flow

Storer (1983) solved the linearised, resistive, incompressible MHD equations in the absence of viscosity about the copper bar equilibrium, Eqs. (9.1)–(9.5), using the ansatz that the perturbed magnetic field is constant-α force-free ($\nabla\times\boldsymbol{b}^{(1)} = \alpha\boldsymbol{b}^{(1)}$ with α constant) while the perturbed velocity is a Beltrami flow ($\nabla\times\boldsymbol{v}^{(1)} = \alpha\boldsymbol{v}^{(1)}$). The resulting dispersion relation was then shown numerically to have no steady-state solution for the perturbations. The details of this paper are omitted as they are just a particular form of those of Montgomery et al. (1989) and Agim and Montgomery (1991) who repeated the analysis including the viscosity. They calculated the velocity and magnetic fields

up to second order in the small expansion parameter ε, which represents the ratio of first order perturbation to the base field. The solutions to first order, again adopting the ansatz of a linear force-free field and Beltrami flow, are

$$\boldsymbol{v}^{(1)} = \zeta \boldsymbol{A}_{nmq} \exp(-i\omega\tau), \tag{9.6}$$

$$\boldsymbol{b}^{(1)} = \varepsilon \boldsymbol{A}_{nmq} \exp(-i\omega\tau), \tag{9.7}$$

$$p^{(1)} = \varepsilon \left\{ \left[(j_0 - \lambda_{nmq} b_0)\lambda_{nmq} - k_n \left(\frac{m j_0}{2} - k_n b_0 \right) - \frac{k_n^2 j_0}{\lambda_{nmq}} \right] \rho_{nmq} + \frac{\lambda_{nmq} j_0 r}{2} \frac{\partial \rho_{nmq}}{\partial r} \right\} \times \exp(-i\omega\tau) + \text{const.}, \tag{9.8}$$

where the general solution for the linear force-free field ($\nabla \times \boldsymbol{A}_{nmq} = \lambda_{nmq} \boldsymbol{A}_{nmq}$) in cylindrical coordinates has been used (Chandrasekhar and Kendall, 1957):

$$\boldsymbol{A}_{nmq} = \lambda_{nmq} \nabla \times (\rho_{nmq} \hat{\boldsymbol{z}}) + \nabla \times (\nabla \times (\rho_{nmq} \hat{\boldsymbol{z}})), \tag{9.9}$$

$$\rho_{nmq} = J_m(\gamma_{nmq} r) \exp(im\phi - ik_n z), \tag{9.10}$$

$$\gamma_{nmq}^2 = \lambda_{nmq}^2 - k_n^2, \tag{9.11}$$

where J_m is the m-th order Bessel function of the first kind and γ_{nmq} is the q-th zero of the Bessel function for fixed m and n. In the dimensionless scheme of this thesis q is a positive integer, m is an integer and $k_n = n\pi$ — from now on the indices n, m and q are not included explicitly. Furthermore $b_0 = 1$ strictly, but the parameter b_0 has been explicitly retained to parallel the results of Agim and Montgomery (1991) as closely as possible while not necessarily following the same non-dimensionalisation procedure. The amplitudes of the first-order velocity and magnetic fields are related by

$$\zeta = -\left(\frac{\omega + i\eta\lambda^2}{m j_0/2 - k_n b_0} \right) \varepsilon, \tag{9.12}$$

and the dispersion relation is

$$(\omega + i\eta\lambda^2)(\omega + i\nu\lambda^2) = \left(\frac{m j_0}{2} - k_n b_0 \right) \left(\frac{m j_0}{2} - k_n b_0 + \frac{k_n j_0}{\lambda} \right). \tag{9.13}$$

The values of γ and λ are determined from the boundary condition that $v_r = b_r = 0$ at $r = a$ (cf. Sect. 7.9)

$$\frac{m\lambda}{a} \mathrm{J}_m(\gamma a) - k_n \left. \frac{\mathrm{d}\mathrm{J}_m(\gamma r)}{\mathrm{d}r} \right|_{r=a} = 0, \tag{9.14}$$

where λ takes one of the values $\pm\sqrt{\gamma^2 + k_n^2}$ according to the size of the desired safety factor in comparison with the mode number ratio m/n, Eq. (9.31).

The purpose of the investigators of these solutions was to examine the stability of the uniform current copper bar equilibrium (Montgomery et al., 1989; Agim and Montgomery, 1991; Montgomery, 1992; Bevir et al., 1993). Denoting the right side of the dispersion relation by f, the frequency is found to be

$$\omega = -\frac{i(\nu + \eta)\lambda^2}{2} \left[1 \pm \sqrt{1 - \frac{4(f + \nu\eta\lambda^4)}{(\nu + \eta)^2 \lambda^4}} \right], \tag{9.15}$$

from which it can be seen that the frequency has a positive imaginary part whenever $f + \eta\nu\lambda^4 \leq 0$. In fact the only way that the frequency can be purely real is when $f + \eta\nu\lambda^4 = 0$ at which time $\omega = 0$ — one of the roots thus changes from being purely real to having an imaginary component at this threshold while the other is purely imaginary with a negative imaginary part, corresponding to a purely decaying mode. What this is saying is that for a fixed b_0 and with k_n, λ and γ depending on the geometry and boundary conditions, as j_0 is increased there comes a point when the copper bar equilibrium becomes unstable for some m, n and q with the instability always being marginal when $\omega = 0$.

The point of marginal stability having been established Agim and Montgomery (1991) proceeded to calculate the MHD variables to second order in the small parameter ε at $\omega = 0$:

$$\boldsymbol{v} = \frac{\eta\lambda^2\varepsilon}{mj_0/2 - k_n b_0}(A\cos\psi\,\hat{\mathbf{r}} + B\sin\psi\,\hat{\boldsymbol{\phi}} + C\sin\psi\,\hat{\boldsymbol{z}}), \tag{9.16}$$

$$\begin{aligned}\boldsymbol{b} &= b_0\hat{\boldsymbol{z}} + \frac{rj_0}{2}\hat{\boldsymbol{\phi}} + \varepsilon(-A\sin\psi\hat{\mathbf{r}} + B\cos\psi\hat{\boldsymbol{\phi}} + C\cos\psi\hat{\boldsymbol{z}}) \\ &\quad + \frac{\varepsilon^2\lambda^2}{mj_0/2 - k_n b_0}\left[\frac{1}{r}\int_0^r r'A(r')B(r')\mathrm{d}r'\hat{\boldsymbol{\phi}} + \left(\int_0^r A(r')C(r')\mathrm{d}r' + b_c\right)\hat{\boldsymbol{z}}\right],\end{aligned} \tag{9.17}$$

$$\boldsymbol{j} = j_0\hat{\boldsymbol{z}} + \varepsilon\lambda(-A\sin\psi\hat{\mathbf{r}} + B\cos\psi\hat{\boldsymbol{\phi}} + C\cos\psi\hat{\boldsymbol{z}}) + \frac{\varepsilon^2\lambda^2}{mj_0/2 - k_n b_0}(-AC\hat{\boldsymbol{\phi}} + AB\hat{\boldsymbol{z}}), \tag{9.18}$$

$$\begin{aligned}\boldsymbol{e} &= \eta j_0\hat{\boldsymbol{z}} + \varepsilon\eta\lambda\left\{-\sin\psi\left[A + \frac{\lambda}{mj_0/2 - k_n b_0}\left(Bb_0 - C\frac{rj_0}{2}\right)\right]\hat{\mathbf{r}}\right. \\ &\quad \left. + \cos\psi\left(B + \frac{\lambda}{mj_0/2 - k_n b_0}Ab_0\right)\hat{\boldsymbol{\phi}} + \cos\psi\left(C - \frac{\lambda}{mj_0/2 - k_n b_0}A\frac{rj_0}{2}\right)\hat{\boldsymbol{z}}\right\},\end{aligned} \tag{9.19}$$

$$\begin{aligned}p &= \text{const.} + \frac{j_0^2a^2}{4}\left(1 - \frac{r^2}{a^2}\right) + \varepsilon\left\{\left[(j_0 - \lambda b_0)\lambda - k_n\left(mj_0/2 - k_n b_0\right) - \frac{k_n^2 j_0}{\lambda}\right]\rho + \frac{\lambda j_0 r}{2}\frac{\partial\rho}{\partial r}\right\} \\ &\quad - \frac{\varepsilon^2\lambda^2}{mj_0/2 - k_n b_0}\left[b_0\int_0^r A(r')C(r')\mathrm{d}r' + \frac{j_0}{2}\int_0^r r'A(r')B(r')\mathrm{d}r'\right. \\ &\quad \left. + j_0\int_0^r \frac{1}{r'}\int_0^{r'} r''A(r'')B(r'')\mathrm{d}r''\mathrm{d}r'\right] - \frac{\eta^2\lambda^4\varepsilon^2}{2(mj_0/2 - k_n b_0)^2}\left[A^2\cos^2\psi + B^2\sin^2\psi + C^2\sin^2\psi\right],\end{aligned} \tag{9.20}$$

where b_c is a constant chosen so that $\int_0^a b_z^{(2)}\mathrm{d}r = 0$, and

$$\psi = m\phi - k_n z, \tag{9.21}$$

$$\rho = \mathrm{J}_m(\gamma r)\exp i\psi, \tag{9.22}$$

$$A = \frac{\lambda m}{r}\mathrm{J}_m(\gamma r) - k_n\frac{\mathrm{dJ}_m(\gamma r)}{\mathrm{d}r}, \tag{9.23}$$

$$B = -\lambda\frac{\mathrm{dJ}_m(\gamma r)}{\mathrm{d}r} + \frac{mk_n}{r}\mathrm{J}_m(\gamma r), \tag{9.24}$$

$$C = \gamma^2\mathrm{J}_m(\gamma r), \tag{9.25}$$

$$\lambda^2 = \gamma^2 + k_n^2. \tag{9.26}$$

In a steady state the dispersion relation, Eq. (9.13), simplifies to

$$-\eta\nu\lambda^4 = \left(\frac{mj_0}{2} - k_n b_0\right)\left(\frac{mj_0}{2} - k_n b_0 + \frac{k_n j_0}{\lambda}\right). \tag{9.27}$$

The safety factor, q_s, may be used to simplify this equation. Defining $q_s = rb_z/(R_0 b_\phi)$ (Wesson, 1987, Sect. 3.4) with $b_\phi = rj_0/2$, $b_z = b_0$, the major radius written as $R_0 = 2/(2\pi) = n/k_n$ for a dimensionless circumference of 2 and $k_n = n\pi$, leads to

$$q_s = \frac{2k_n b_0}{nj_0}, \tag{9.28}$$

whence

$$-\eta\nu\lambda^4 = \frac{j_0^2}{4}(m - q_s n)(m - q_s n + 2k_n/\lambda), \tag{9.29}$$

which gives

$$m - q_s n = \frac{-k_n j_0 \pm \sqrt{k_n^2 j_0^2 - 4\eta\nu\lambda^6}}{\lambda j_0}. \tag{9.30}$$

Letting $\alpha = -k_n j_0$ and $\beta = \sqrt{k_n^2 j_0^2 - 4\eta\nu\lambda^6}$ it can be seen that $\beta^2 - \alpha^2 < 0$, whence $-k_n j_0 < \sqrt{k_n^2 j_0^2 - 4\eta\nu\lambda^6} < k_n j_0$ and, after choosing $k_n > 0$,

$$q_s \lesseqgtr \frac{m}{n} \iff \lambda \lesseqgtr 0. \tag{9.31}$$

By a similar argument

$$m - nq_s + \frac{2k_n}{\lambda} \lesseqgtr 0 \iff \lambda \lesseqgtr 0. \tag{9.32}$$

Returning to Eq. (9.13), the critical current at which marginal stability is attained can be calculated to be

$$j_0 = \frac{2}{m(m\lambda + 2k_n)}\left[k_n b_0(m\lambda + k_n) \pm \sqrt{k_n^4 b_0^2 - m\eta\nu\lambda^5(m\lambda + 2k_n)}\right]. \tag{9.33}$$

After some analysis it can be proved that when $\lambda > 0$ there are two real critical currents, when $-2k_n/m < \lambda < 0$ only the root corresponding to the plus sign is real, and when $\lambda < -2k_n/m$ both critical currents are again real. Since it is envisaged that the fusion device under consideration will have the toroidal current increased from zero, in the cases where there are two critical currents the lower positive value is chosen. In each case a necessary condition is that $k_n^4 b_0^2 > m\eta\nu\lambda^5(m\lambda + 2k_n)$. When $-2k_n/m < \lambda < 0$ this is clearly satisfied; when $\lambda > 0$ or $\lambda < -2k_n/m$, however, this translates into a necessary bound on $\eta\nu$:

$$\eta\nu < \frac{k_n^4 b_0^2}{m\lambda^5(m\lambda + 2k_n)}, \tag{9.34}$$

the right side of which is always positive.

A calculation procedure can now be outlined. First of all the values of η and ν are determined from physical considerations. Next the mode of interest is chosen by selecting positive values for m, n and q. The size of the helical component of the perturbed flow, ε, is then chosen and it is decided whether the as yet unknown safety factor, q_s, should be less than or greater than m/n; the sign of λ is determined from Eq. (9.31). Equation (9.14) is now solved for γ with the $\pm$ sign having been chosen according to the sign of λ. The value of λ is found from $\lambda = \pm\sqrt{\gamma^2 + k_n^2}$, where $k_n = n\pi$. Equation (9.34) is next checked if $\lambda > 0$ or $\lambda < -2k_n/m$ and, if satisfied, the critical current, Eq. (9.33), is calculated.

It is the energy injection rate of the above solution which is of interest in the context of turbulence. The energy equation for an incompressible magneto-fluid is once more used, but this time with Ω denoting the dimensionless vorticity to avoid confusion with the instability frequency:

$$\frac{\partial}{\partial t}\left(\frac{v^2+b^2}{2}\right) = -\nabla\cdot\left[-\boldsymbol{e}\times\boldsymbol{b}+\nu\boldsymbol{\Omega}\times\boldsymbol{v}+\left(p+\frac{v^2}{2}\right)\boldsymbol{v}\right]-\eta j^2-\nu\Omega^2. \tag{9.35}$$

The Agim and Montgomery solution uses the boundary condition $v_r = 0$ at $r = a$, and this particular solution also has $\Omega \parallel \boldsymbol{v}$ at $r = a$ following the adoption of a first-order Beltrami flow. Thus, there is no viscous energy injection at the wall and so the only source term is the Poynting flux through the curved surface, averaged over z and ϕ, of

$$P = \frac{\eta a j_0^2}{2} + \frac{\varepsilon^2\lambda^2\eta j_0}{a(mj_0/2-k_nb_0)}\int_0^a rA(r)B(r)\mathrm{d}r. \tag{9.36}$$

It is useful to re-write this as

$$P = \frac{\eta a j_0^2}{2} + \frac{\varepsilon^2\lambda\eta k_n}{a(m-nq_s)}\int_0^a r(A^2(r)+B^2(r)+C^2(r))\mathrm{d}r, \tag{9.37}$$

where the relation $\int_0^a r(A^2(r)+B^2(r)+C^2(r))\mathrm{d}r = 2\lambda/k_n\int_0^a rA(r)B(r)\mathrm{d}r$ has been used. Application of Eq. (9.31) now shows that the second-order contribution of the Poynting flux is negative. With the energy injection being reduced and the fact that this pertains to a steady state, the energy dissipation is lower once the helical instability has started. Montgomery et al. (1989) consider this to be the principal result of their paper; they argue that lower rate of dissipation means that this new perturbed flow will be preferred over the original equilibrium (Montgomery and Phillips, 1988, 1989; Montgomery, 1990). However, although the Poynting flux has been reduced it should still be positive and this requirement provides a bound on the amplitude of the helical perturbation. Starting from Eq. (9.36) the inequality

$$\varepsilon^2 < -\frac{a^2j_0(mj_0-2k_nb_0)}{4\lambda^2\int_0^a rA(r)B(r)\mathrm{d}r}, \tag{9.38}$$

is obtained. The initial choice of ε can now be verified as being physically viable and altered if necessary.

In a steady state this energy injection is balanced by dissipation. P is re-dimensionalised using the mass density, now written as ρ_0 to avoid confusion with the Chandrasekhar-Kendall function ρ, the Alfvén speed based on the uniform z-component of the equilibrium magnetic field, $c_{a0} = b_0/\sqrt{\mu_0\rho_0}$, and the half-length of the cylinder, l, giving

$$P(\rho_0c_{a0}^3)2\pi h2l = \varepsilon_T\rho_0\pi h^2 2l, \tag{9.39}$$

where ε_T is the heating power per unit mass. Thus,

$$\varepsilon_T = \frac{2c_{a0}^3}{h}P. \tag{9.40}$$

The analysis of Heyvaerts and Priest (1992) may be followed to calculate the effective viscosity and magnetic diffusivity due to the turbulent plasma. Equation (4.48) is once again used, this time written as,

$$\eta(k) = \frac{4\,C}{9\sqrt{3}}\sqrt{\frac{2P}{a}}k^{-3/2}, \tag{9.41}$$

where Eq. (9.40) has been used in place of Eq. (3.71). Once again Eq. (4.49) holds. Unlike the solar situation where many scales were present in the model, the present model considers only a single mode so there is no trouble in defining the scale at which the turbulent magnetic diffusivity and viscosity should be evaluated: $k = |\lambda| = \sqrt{\gamma^2 + k_n^2}$. Equation (9.41) can be rearranged as

$$P = \frac{243a}{32C^2}k^3\eta^2, \tag{9.42}$$

which, when balanced with the previous expression for P, Eq. (9.37), gives

$$\eta = \frac{16C^2}{243a^2k^3}\frac{j_0}{(mj_0 - 2k_nb_0)}\left[a^2j_0(mj_0 - 2k_nb_0) + 4\varepsilon^2\lambda^2 I\right], \tag{9.43}$$

where $I = \int_0^a rA(r)B(r)\mathrm{d}r > 0$. The steady-state dispersion relation, Eq. (9.27), with $\nu = (7/5)\eta$ (Chaps. 3 and 4) gives

$$\eta^2 = -\frac{5}{28\lambda^4}(mj_0 - 2k_nb_0)(mj_0 - 2k_nb_0 + \frac{2k_nj_0}{\lambda}). \tag{9.44}$$

Equating Eqs. (9.43) and (9.44) yields a sixth-order polynomial[1] in j_0:

$$\begin{aligned}
0 \;=\;& 7168C^4\lambda^5a^4m^2j_0^6 - 28672C^4\lambda^5a^4mk_nb_0j_0^5 \\
&+a^2\left[28672C^4\lambda^5(a^2k_n^2b_0^2 + 2\varepsilon^2\lambda^2mI) + 295245a^2k^6m^3(m\lambda + 2k_n)\right]j_0^4 \\
&-4a^2k_nb_0\left[28672C^4\lambda^7\varepsilon^2I + 295245a^2k^6m^2(2m\lambda + 3k_n)\right]j_0^3 \\
&+8\left[14336C^4\lambda^9\varepsilon^4I^2 + 885735a^4k^6mk_n^2b_0^2(m\lambda + k_n)\right]j_0^2 \\
&-4723920a^4k^6k_n^3b_0^3(2m\lambda + k_n)j_0 + 4723920a^4k^6\lambda k_n^4b_0^4.
\end{aligned} \tag{9.45}$$

The integral I is evaluated using the recurrence relations of Agim and Montgomery (1991):

$$\begin{aligned}
\int_0^a rA(r)B(r)\mathrm{d}r \;&=\; k_n\lambda\left[\gamma aJ_m(\gamma a)J_{m-1}(\gamma a) + \gamma^2\int_0^a rJ_m^2(\gamma r)\mathrm{d}r\right] \\
&\quad -\frac{m(\lambda + k_n)^2}{2}J_m^2(\gamma a),
\end{aligned} \tag{9.46}$$

$$\gamma^2\int_0^a rJ_m^2(\gamma r)\mathrm{d}r \;=\; \gamma^2\int_0^a rJ_{m-2}^2(\gamma r)\mathrm{d}r - 2(m-1)J_{m-1}^2(\gamma a), \tag{9.47}$$

$$\int_0^a rJ_1^2(\gamma r)\mathrm{d}r \;=\; \int_0^a rJ_0^2(\gamma r)\mathrm{d}r - \frac{a}{\gamma}J_0(\gamma a)J_1(\gamma a), \tag{9.48}$$

$$\int_0^a rJ_0^2(\gamma r)\mathrm{d}r \;=\; \frac{a^2}{2}\left[J_0^2(\gamma a) + J_1^2(\gamma a)\right]. \tag{9.49}$$

[1]Now that η is a function of j_0 there are more than two possible values for j_0.

Major radius	3 m
Minor radius	1.2 m
Toroidal field	2.0 T
Proton density	10^{20} m^{-3}
Perturbed field / toroidal field	10^{-5}

Table 9.1: Typical parameters for the JET tokamak.

The advantage of having an algebraic equation instead of the transcendental equations encountered until now is that all six complex roots can be found very accurately using a library routine without having to be concerned with missing roots, which is always a danger with iterative methods. Once found, the purely real roots can be identified and the smallest positive root be taken as the solution relevant to this problem. Even then, however, it may not be a solution to the problem of balancing the injected and dissipated fluxes: the value of η corresponding to this root, obtained from Eq. (9.43), may be negative. Having found j_0 it is thus necessary to find the corresponding η and check that Eqs. (9.36) and (9.42) do balance.

9.3 Results and discussion

The model parameters are chosen to approximate those of the JET experimental tokamak and are listed in Table 9.1. From this $l = 6\pi, a = 1/(5\pi), b_0 = 1$ and $c_{a0} = 4.36 \times 10^6$ ms^{-1}. The ratio of the helical perturbation field strength to the toroidal field strength is chosen as $\varepsilon = 10^{-5}$. Values of m, n and q are next cycled round and the two possibilities of $\lambda \gtrless 0$ taken in turn; the corresponding values for γ, η, the current corresponding to j_0 and the heating power are then calculated and presented in the following pages. Although the values of m, n and q were looped from 1–10, 1–10 and 1–4, respectively, not all appear in the program output since some combinations did not admit any real solutions to Eq. (9.45). The values expected for the JET tokamak would give a current of the order of 1 MA, a heating power of order 1 MW and a safety factor, q_s, greater than 1. The classical electron collision diffusivity can also be calculated from Spitzer's formula. Wesson (1987, Sects. 2.10, 12.5 & 12.10) indicate that an appropriate value for the Coulomb logarithm in a hydrogen plasma is $\ln\Lambda = 17$. Taking a temperature of 1 keV ($\simeq 10^7$ K) gives a parallel resistivity of $2.8 \times 10^{-8}\Omega$m leading to a parallel diffusivity of 2.2×10^{-2} m^{2}s^{-1}, the perpendicular component being approximately double this value.

With the exception of the (5,3,1) and (6,5,1) modes, it can be seen in Table 9.2 that these solutions result in heating much higher than is expected. Furthermore, it is not possible to predict which mode will become unstable first as each of these solutions occurs for different values of the turbulent magnetic diffusivity, η. The incorrect nature of these results is probably due to the fact that the steady-state solutions used are marginally stable. Fluctuations in the driving current near

m	n	q	Current (MA)	Safety factor	Power (MW)	η (m^2s^{-1})
1	1	1	4.0	1.2	1.4×10^5	1.7×10^3
1	1	3	4.5	1.1	1.0×10^2	11
2	1	1	2.6	1.8	1.4×10^4	4.1×10^2
2	1	1	2.2	2.1	5.2×10^3	2.2×10^2
2	1	2	2.5	1.9	1.1×10^2	17
2	2	1	4.2	1.1	6.8×10^4	7.6×10^2
2	2	2	4.4	1.1	8.7×10^3	1.4×10^2
3	1	1	1.7	2.9	4.2×10^2	51
3	1	1	1.5	3.1	1.1×10^2	25
3	2	1	3.5	1.4	2.2×10^4	3.7×10^2
3	2	1	3.0	1.6	6.9×10^3	1.9×10^2
3	2	2	3.4	1.4	53	9.5
3	3	1	4.3	1.1	3.5×10^4	4.0×10^2
3	3	2	4.5	1.1	1.0×10^3	38
4	2	1	2.5	1.9	1.4×10^3	71
4	2	1	2.3	2.1	2.5×10^2	28
4	3	1	3.9	1.2	1.6×10^4	2.4×10^2
4	3	1	3.3	1.4	4.4×10^3	1.1×10^2
4	4	1	4.4	1.1	1.7×10^4	2.2×10^2
5	3	1	3.0	1.6	9.4×10^2	47
5	3	1	2.7	1.8	8.2	4.0
5	4	1	4.1	1.2	8.9×10^3	1.4×10^2
5	4	1	3.6	1.3	1.4×10^3	53
5	5	1	4.4	1.1	6.5×10^3	1.1×10^2
6	4	1	3.4	1.4	86	12
6	5	1	4.3	1.1	3.0×10^3	69
6	5	1	3.8	1.3	7.0	3.0
6	6	1	4.5	1.1	1.0×10^3	35
7	6	1	4.4	1.1	1.1×10^2	11

Table 9.2: Selection of steady-state modes from Appendix A which have critical currents less than 5 MA.

the critical current will then lead to the mode either growing or decaying in time. The accompanying loss of time-independence then makes this method inapplicable. It would be better to examine the nonlinear saturation of a growing perturbation and use this as the basic equilibrium. However, the flow is still unlikely to be turbulent when only one mode is present. When Shan et al. (1991) expressed their perturbation fields as superpositions of Chandrasekhar-Kendall functions, which have since been shown to form a complete orthogonal set under boundary conditions appropriate to this problem (Yoshida, 1992a), they found that as the driving electric field was increased so that the current passed its first threshold the single-mode saturated instability itself became unstable with a new multi-mode state forming. Further increase led to a state which was considered to be turbulent. From a theoretical viewpoint, however, even the calculation of the saturation amplitude becomes a formidable task (Stuart, 1958; Landau and Lifschitz, 1987, Chap. 3).

The formalism of the Heyvaerts and Priest closure to find the turbulent magnetic diffusivity and heating power met with little success in achieving realistic levels of power output. This is probably because the single-mode expansion of Montgomery et al. (1989) and Agim and Montgomery (1991) is not expected to last for any great length of time as it is only marginally stable. Once the steady state is lost, either due to a mode decaying in time or becoming unstable, the Heyvaerts and Priest method ceases to apply and other, more complicated methods must be used which consider both injection, inertial transfer and dissipation of energy separately.

Chapter 10

Conclusions

10.1 The trouble with turbulence theory

10.1.1 Fourier space

Throughout this thesis Fourier analysis has been employed to describe the velocity and magnetic fields. However, Fourier analysis is the language of periodic functions, or those which tend to zero at infinity. Neither of these conditions is necessarily satisfied in a turbulent medium (mathematically neither the velocity nor magnetic fields are absolutely- or square-integrable) so that any usage of Fourier analysis necessitates the imposition of additional constraints. Most commonly the medium is divided into periodic boxes requiring the assumption of homogeneity to justify this physically. The alternative of considering an infinite medium in which the velocity and magnetic fields are zero at infinity prevents the turbulence from being sustained by boundary motions or fields injecting energy, a problem shared in the periodic case where energy injected at one side is extracted at the opposite face at the same rate. A second necessary assumption is that artificial forcing must be imposed everywhere within the medium to sustain turbulence against dissipation and yet have homogeneous behaviour. Finally, Fourier analysis requires the presence of infinitely many scales, physically since the fluid and MHD equations are nonlinear and hence couple all the Fourier amplitudes together, and mathematically since only an *infinite* set of sinusoids constitutes a complete orthogonal basis. Energy present at any scale is thus transferred to all others given sufficient time. Physical considerations show that having an infinite number of scales is not reasonable since energy cannot be transferred to sub-molecular scales and any turbulent medium is finite in reality. A truncation of Fourier space to a finite set of scales is thus required — but the resulting equations can then be shown no longer to conserve certain inviscid and ideal invariants of the original equations expressed in configuration space. In other words, the system we are forced to use as a result of the incompatibility of Fourier space with actual properties of turbulence is *mathematically different from the original fluid and MHD equations.* Fortunately, certain rugged invariants do survive the

truncation to a finite number of Fourier scales otherwise there would be no value at all in analysing the Fourier representation of turbulence. However, the exact set of rugged invariants varies with the dimensionality of the problem. For example, the mean-square potential is a rugged invariant of 2D MHD in which the magnetic helicity has no meaning, while for 3D MHD it is instead the magnetic helicity which is a rugged invariant. Adding a uniform background field then leads to the magnetic helicity ceasing to be a rugged invariant — rather a total magnetic helicity must be introduced which depends on the background field and vector potential gauge (Sect. 1.3.3).

Persisting with the truncated Fourier space it is found that the original equations transform to an infinite set of equations for the Fourier amplitudes with an infinite number of unknowns. Further closure assumptions are then required to find approximate solutions to the approximated system of equations, which are extremely complicated for even the most restrictive assumptions of the properties of the turbulence — homogeneity, isotropy, reflection invariance etc.

It can be seen, then, that Fourier space is not the most promising domain for turbulence theory. Since the 1960s fluid turbulence research has tentatively moved into the realms of renormalisation group theory and other constructs of functional analysis. MHD turbulence must also seek an alternative formalism if long-term significant progress is to be made.

10.1.2 Turbulent viscosity and magnetic diffusivity

The eddy viscosity approach is a convenience employed in fluid turbulence investigations in order to remove the explicit small-scale fluctuation terms from the equation for the mean flow while still including their implicit effects. The concept of an enhanced viscosity and resistivity is motivated by numerical simulations which can only be run for limited times after which scales are generated which cannot be resolved by the computer. Having a larger viscosity and magnetic diffusivity causes the large gradients to be dissipated sufficiently quickly to prevent the appearance of features at unresolvable scales. In the context of theory, however, the idea of enhancing these parameters in the presence of turbulent flow is dangerously misleading — it is better to think of the problem as one of nonlinear effects in the presence of *molecular* viscosity and magnetic diffusivity. In particular, in incompressible MHD the flow of energy is between small and large scales and between kinetic and magnetic energies so that the situation is much more complicated (Sect. 1.3.1).

10.2 Solar turbulence

The model of Heyvaerts and Priest (1992) has here been considered in detail and improved mathematically. Some aspects of the model still give cause for concern and do not appear to be easily resolvable; at the root of the problem is the lack of a turbulence model which is appropriate for the solar corona. Until a model is produced which takes into account the effects of the strong background magnetic fields present in active regions the best available models seem to be those of Heyvaerts and

Priest (1992), which suffers from the drawbacks described in the following paragraphs, and Gómez and Ferro Fontán (1992), which treats the turbulence in a less physical and more phenomenological manner but which permits energy spectra to be calculated within the model.

Adoption of a constant turbulent viscosity and magnetic diffusivity in the solar models led to the imposed Kraichnan spectrum being over 15 orders of magnitude different from the spectrum calculated from the model velocity and magnetic field Fourier components. When a scale-dependent turbulent viscosity and magnetic diffusivity are incorporated instead, inferred from the isotropic, helical, eddy-damped quasi-normal Markovian approximation of 3D MHD turbulence, the situation improves until the imposed and calculated spectra are within an order of magnitude of each other. This is because the scale-dependent parameters used are based on analytical considerations rather than being completely ad hoc as were the constant parameters.

The intention of Heyvaerts and Priest (1992) was to create a model of coronal turbulence which did not include arbitrary parameters, such as eddy-relaxation times. The way this was done was by imposing a Kraichnan inertial spectrum at all scales of the model. This has two drawbacks, namely that at the large scales of the model the inertial range axioms simply do not apply and that the arbitrary parameters of other models have just been replaced by an arbitrary spectrum.

The presence of the strong background magnetic field has not been dealt with in a sufficiently consistent manner. When considering the small-scale turbulence, Alfvén waves propagating along this background field have been considered the dominant cause of eddy relaxation. However, the turbulence model used to calculate the relation between the dissipated power and the turbulent magnetic diffusivity and viscosity assumes that all velocity and magnetic field fluctuations are isotropic in three dimensions, even for magnetic fields of the order of a hundred Gauss! A 2D MHD model used to account for the strong field effects by considering all fluctuations to be confined to planes perpendicular to the background magnetic field has the problem, though, that there is no means for energy to be transmitted from the photosphere to the corona to re-supply the kinetic and magnetic energy losses there.

It has proved possible to obtain "sensible" levels of coronal heating for vastly different and even incorrect physical models. For example, the procedure of Sect. 5.5.2 was actually implemented, although the results have not been presented in this thesis, and it was found that appropriate heating power densities could be obtained by a judicious choice of the coefficient to the order k^{-2} correction to the Kraichnan spectrum, despite the fact that the physics involved is not really appropriate for coronal heating.

10.3 Laboratory turbulence

Attempts to apply the approach of Heyvaerts and Priest (1992) to laboratory situations failed because a steady-state equilibrium with many scales present could not be found. The simple ansatzes of the solar section of this thesis are inappropriate due to the more stringent boundary

conditions of fusion plasmas: only solutions with no flow were found and these are not expected to be turbulent. The single mode solution with flow of Montgomery et al. (1989) and Agim and Montgomery (1991) is in a state of marginal stability and so is not an appropriate representation of a steady state.

10.4 Further work

In both the solar and laboratory contexts the details of small-scale effects are not well known. For the Sun, dissipation occurs at scales of a few hundred metres while the best observations so far available have a resolution of about 700 km. The laboratory situation, meanwhile, suffers from the problem that, at the high temperatures used, probes will either be damaged by the plasma or else will change the local properties so that the measurements obtained are questionable. Until better solar observations and diagnostic techniques are developed which do not affect laboratory plasmas the real behaviour of turbulence in each can only be speculated upon. In any case there is little point in pursuing models which neglect important physical effects, especially with regard to the effects of the strong magnetic field and dimensionality of models on the rugged invariants. Work is presently in progress in examining the model of Gómez and Ferro Fontán (1992) in which the power spectra are calculated as part of the model rather than being imposed arbitrarily. Beyond that, it is envisaged that a basic model for coronal turbulence will be developed which is based on reduced MHD, in which the fluctuating velocity and magnetic fields are confined to a plane perpendicular to the background field. This model would still be incompressible and so could permit an evaluation of the severity of neglecting the important effects of the background field. In the long term, however, the effects of compressibility and intermittency must be included. This would necessitate a jettisoning of Fourier space, and its associated mathematics, and so represents a long-term goal.

Appendix A

Single-mode solution program output

The following pages give the output from a program implementing the algorithm given in Chap. 9. m, n and q are the poloidal, toroidal and radial mode-numbers, respectively, while q_s is the safety factor. eta is the turbulent magnetic diffusivity and the current is the critical value at which the copper bar equilibrium becomes marginally stable.

```
B0 = 2.0 epsilon =  0.10000E-04

m =  1 n =  1 q =  1 gamma =  53.8998 lambda =  -54.2648
eta =  0.72083E+04 m^2/s  current =    6.196 MA  q_s =  0.77472E+00
power =  0.14463E+07 MW

m =  1 n =  1 q =  1 gamma =  65.9057 lambda =   66.2045
eta =  0.16731E+04 m^2/s  current =    4.041 MA  q_s =  0.11877E+01
power =  0.14149E+06 MW

m =  1 n =  1 q =  2 gamma = 104.0611 lambda = -104.2506
eta =  0.73827E+03 m^2/s  current =    5.444 MA  q_s =  0.88168E+00
power =  0.10757E+06 MW

m =  1 n =  1 q =  2 gamma = 116.0304 lambda =  116.2003
eta =  0.30093E+03 m^2/s  current =    4.335 MA  q_s =  0.11072E+01
power =  0.24751E+05 MW
```

```
m =  1 n =  1 q =  3 gamma = 153.7172 lambda = -153.8456
eta =  0.12147E+03 m^2/s  current =    5.224 MA  q_s =  0.91877E+00
power =  0.93587E+04 MW

m =  1 n =  1 q =  3 gamma = 165.6784 lambda =  165.7975
eta =  0.11325E+02 m^2/s  current =    4.462 MA  q_s =  0.10758E+01
power =  0.10182E+03 MW

m =  1 n =  2 q =  1 gamma =  48.6788 lambda =  -50.2747
eta =  0.77532E+05 m^2/s  current =   18.106 MA  q_s =  0.26511E+00
power =  0.13306E+09 MW
eta =  0.21475E+05 m^2/s  current =    9.675 MA  q_s =  0.49614E+00
power =  0.10208E+08 MW
eta =  0.41755E+04 m^2/s  current =    9.603 MA  q_s =  0.49985E+00
power =  0.38591E+06 MW

m =  1 n =  2 q =  1 gamma =  70.0762 lambda =   71.1940
eta =  0.41913E+04 m^2/s  current =    7.111 MA  q_s =  0.67497E+00
power =  0.11042E+07 MW

m =  1 n =  2 q =  2 gamma =  99.1333 lambda =  -99.9266
eta =  0.48189E+04 m^2/s  current =   12.705 MA  q_s =  0.37779E+00
power =  0.40361E+07 MW

m =  1 n =  2 q =  2 gamma = 120.3905 lambda =  121.0445
eta =  0.10108E+04 m^2/s  current =    7.963 MA  q_s =  0.60280E+00
power =  0.31565E+06 MW

m =  1 n =  2 q =  3 gamma = 148.8896 lambda = -149.4190
eta =  0.10918E+04 m^2/s  current =   11.496 MA  q_s =  0.41755E+00
power =  0.69269E+06 MW

m =  1 n =  2 q =  3 gamma = 170.1156 lambda =  170.5791
eta =  0.29728E+03 m^2/s  current =    8.374 MA  q_s =  0.57323E+00
power =  0.76411E+05 MW
```

```
m =  1 n =  2 q =  4 gamma = 198.4507 lambda = -198.8482
eta =  0.28665E+03 m^2/s  current =   10.976 MA  q_s =  0.43732E+00
power =  0.11254E+06 MW

m =  1 n =  3 q =  1 gamma =  45.1172 lambda =  -48.8965
eta =  0.43871E+06 m^2/s  current =   41.307 MA  q_s =  0.11620E+00
power =  0.39193E+10 MW
eta =  0.54111E+05 m^2/s  current =   14.583 MA  q_s =  0.32915E+00
power =  0.59625E+08 MW
eta =  0.58957E+04 m^2/s  current =   14.402 MA  q_s =  0.33328E+00
power =  0.70785E+06 MW

m =  1 n =  3 q =  1 gamma =  72.8684 lambda =  75.2669
eta =  0.59940E+04 m^2/s  current =   14.381 MA  q_s =  0.33378E+00
power =  0.26686E+07 MW
eta =  0.12510E+05 m^2/s  current =   14.314 MA  q_s =  0.33533E+00
power =  0.11624E+08 MW
eta =  0.64968E+04 m^2/s  current =    9.617 MA  q_s =  0.49910E+00
power =  0.31350E+07 MW

m =  1 n =  3 q =  2 gamma =  95.7430 lambda =  -97.5808
eta =  0.16871E+05 m^2/s  current =   22.865 MA  q_s =  0.20992E+00
power =  0.46070E+08 MW

m =  1 n =  3 q =  2 gamma = 123.3400 lambda =  124.7720
eta =  0.18330E+04 m^2/s  current =   11.081 MA  q_s =  0.43316E+00
power =  0.11369E+07 MW

m =  1 n =  3 q =  3 gamma = 145.5701 lambda = -146.7854
eta =  0.34057E+04 m^2/s  current =   19.194 MA  q_s =  0.25008E+00
power =  0.63898E+07 MW

m =  1 n =  3 q =  3 gamma = 173.1285 lambda =  174.1516
eta =  0.66719E+03 m^2/s  current =   11.853 MA  q_s =  0.40494E+00
power =  0.40956E+06 MW
```

```
m =  1 n =  3 q =  4 gamma = 195.1687 lambda = -196.0768
eta =  0.10859E+04 m^2/s  current =   17.750 MA  q_s =  0.27043E+00
power =  0.15485E+07 MW

m =  1 n =  3 q =  4 gamma = 222.7121 lambda =  223.5083
eta =  0.19096E+03 m^2/s  current =   12.326 MA  q_s =  0.38941E+00
power =  0.70922E+05 MW

m =  1 n =  4 q =  1 gamma =  42.8603 lambda =  -49.6856
eta =  0.11612E+07 m^2/s  current =   68.835 MA  q_s =  0.69732E-01
power =  0.28807E+11 MW
eta =  0.92904E+05 m^2/s  current =   19.527 MA  q_s =  0.24581E+00
power =  0.18441E+09 MW
eta =  0.74532E+04 m^2/s  current =   19.202 MA  q_s =  0.24997E+00
power =  0.11869E+07 MW

m =  1 n =  4 q =  1 gamma =  74.7382 lambda =   78.8508
eta =  0.71668E+04 m^2/s  current =   19.180 MA  q_s =  0.25026E+00
power =  0.43864E+07 MW
eta =  0.20368E+05 m^2/s  current =   19.038 MA  q_s =  0.25212E+00
power =  0.35426E+08 MW
eta =  0.84439E+04 m^2/s  current =   11.753 MA  q_s =  0.40842E+00
power =  0.60889E+07 MW

m =  1 n =  4 q =  2 gamma =  93.4866 lambda =  -96.8060
eta =  0.46164E+05 m^2/s  current =   37.344 MA  q_s =  0.12853E+00
power =  0.33679E+09 MW

m =  1 n =  4 q =  2 gamma = 125.3289 lambda =  127.8241
eta =  0.26756E+04 m^2/s  current =   13.812 MA  q_s =  0.34753E+00
power =  0.26045E+07 MW

m =  1 n =  4 q =  3 gamma = 143.3423 lambda = -145.5290
eta =  0.79836E+04 m^2/s  current =   28.780 MA  q_s =  0.16678E+00
power =  0.34220E+08 MW
```

```
m =  1 n =  4 q =  3 gamma = 175.1641 lambda =  176.9579
eta =  0.10809E+04 m^2/s  current =   14.978 MA  q_s =  0.32047E+00
power =  0.11277E+07 MW

m =  1 n =  4 q =  4 gamma = 192.9595 lambda = -194.5894
eta =  0.25173E+04 m^2/s  current =   25.658 MA  q_s =  0.18708E+00
power =  0.81334E+07 MW

m =  1 n =  4 q =  4 gamma = 224.7722 lambda =  226.1730
eta =  0.41910E+03 m^2/s  current =   15.722 MA  q_s =  0.30531E+00
power =  0.35399E+06 MW

m =  1 n =  5 q =  1 gamma =  41.4306 lambda =  -51.9947
eta =  0.18343E+07 m^2/s  current =   92.617 MA  q_s =  0.51826E-01
power =  0.82384E+11 MW
eta =  0.12776E+06 m^2/s  current =   24.495 MA  q_s =  0.19596E+00
power =  0.39969E+09 MW
eta =  0.87042E+04 m^2/s  current =   24.002 MA  q_s =  0.19998E+00
power =  0.18551E+07 MW

m =  1 n =  5 q =  1 gamma =  76.0283 lambda =  82.2634
eta =  0.83562E+04 m^2/s  current =   23.979 MA  q_s =  0.20018E+00
power =  0.67713E+07 MW
eta =  0.28570E+05 m^2/s  current =   23.747 MA  q_s =  0.20213E+00
power =  0.79155E+08 MW
eta =  0.10016E+05 m^2/s  current =   13.637 MA  q_s =  0.35197E+00
power =  0.97274E+07 MW

m =  1 n =  5 q =  2 gamma =  91.9536 lambda =  -97.1721
eta =  0.10759E+06 m^2/s  current =   57.321 MA  q_s =  0.83739E-01
power =  0.18503E+10 MW
eta =  0.15557E+05 m^2/s  current =   24.169 MA  q_s =  0.19860E+00
power =  0.38683E+08 MW
eta =  0.96095E+04 m^2/s  current =   24.064 MA  q_s =  0.19947E+00
power =  0.14759E+08 MW
```

```
m =  1 n =  5 q =  2 gamma = 126.7129 lambda =  130.5493
eta =  0.34907E+04 m^2/s  current =   16.239 MA  q_s =  0.29558E+00
power =  0.47227E+07 MW

m =  1 n =  5 q =  3 gamma = 141.8085 lambda = -145.2467
eta =  0.16243E+05 m^2/s  current =   40.810 MA  q_s =  0.11762E+00
power =  0.14082E+09 MW

m =  1 n =  5 q =  3 gamma = 176.5835 lambda =  179.3563
eta =  0.15132E+04 m^2/s  current =   17.808 MA  q_s =  0.26954E+00
power =  0.23013E+07 MW

m =  1 n =  5 q =  4 gamma = 191.4311 lambda = -193.9918
eta =  0.48619E+04 m^2/s  current =   34.951 MA  q_s =  0.13734E+00
power =  0.30061E+08 MW

m =  1 n =  5 q =  4 gamma = 226.2099 lambda =  228.3810
eta =  0.66922E+03 m^2/s  current =   18.844 MA  q_s =  0.25472E+00
power =  0.92930E+06 MW

m =  1 n =  6 q =  1 gamma =  40.4986 lambda =  -55.3296
eta =  0.22891E+07 m^2/s  current =  113.575 MA  q_s =  0.42263E-01
power =  0.15460E+12 MW
eta =  0.15362E+06 m^2/s  current =   29.477 MA  q_s =  0.16284E+00
power =  0.69633E+09 MW
eta =  0.97166E+04 m^2/s  current =   28.803 MA  q_s =  0.16665E+00
power =  0.27857E+07 MW

m =  1 n =  6 q =  1 gamma =  76.9494 lambda =  85.6880
eta =  0.94839E+04 m^2/s  current =   28.777 MA  q_s =  0.16680E+00
power =  0.98575E+07 MW
eta =  0.36719E+05 m^2/s  current =   28.444 MA  q_s =  0.16875E+00
power =  0.14777E+09 MW
eta =  0.11233E+05 m^2/s  current =   15.352 MA  q_s =  0.31266E+00
power =  0.13828E+08 MW
```

```
m =  1 n =  6 q =  2 gamma =  90.8759 lambda =  -98.3852
eta =  0.21278E+06 m^2/s  current =   82.115 MA  q_s =  0.58454E-01
power =  0.75108E+10 MW
eta =  0.23734E+05 m^2/s  current =   29.090 MA  q_s =  0.16501E+00
power =  0.93447E+08 MW
eta =  0.10172E+05 m^2/s  current =   28.853 MA  q_s =  0.16636E+00
power =  0.17166E+08 MW

m =  1 n =  6 q =  2 gamma = 127.7119 lambda =  133.1598
eta =  0.42505E+04 m^2/s  current =   18.430 MA  q_s =  0.26044E+00
power =  0.74306E+07 MW

m =  1 n =  6 q =  3 gamma = 140.7129 lambda = -145.6755
eta =  0.30269E+05 m^2/s  current =   55.883 MA  q_s =  0.85894E-01
power =  0.49338E+09 MW

m =  1 n =  6 q =  3 gamma = 177.6113 lambda =  181.5682
eta =  0.19467E+04 m^2/s  current =   20.391 MA  q_s =  0.23539E+00
power =  0.39515E+07 MW

m =  1 n =  6 q =  4 gamma = 190.3331 lambda = -194.0307
eta =  0.85085E+04 m^2/s  current =   45.920 MA  q_s =  0.10453E+00
power =  0.92120E+08 MW

m =  1 n =  6 q =  4 gamma = 227.2523 lambda =  230.3580
eta =  0.93117E+03 m^2/s  current =   21.729 MA  q_s =  0.22090E+00
power =  0.18463E+07 MW

m =  1 n =  7 q =  1 gamma =  39.8690 lambda =  -59.3631
eta =  0.25458E+07 m^2/s  current =  133.107 MA  q_s =  0.36061E-01
power =  0.23617E+12 MW
eta =  0.17007E+06 m^2/s  current =   34.465 MA  q_s =  0.13927E+00
power =  0.10540E+10 MW
eta =  0.10517E+05 m^2/s  current =   33.603 MA  q_s =  0.14284E+00
power =  0.40302E+07 MW
```

```
m =  1 n =  7 q =  1 gamma =  77.6278 lambda =   89.2217
eta =  0.10531E+05 m^2/s  current =   33.574 MA  q_s =  0.14297E+00
power =  0.13721E+08 MW
eta =  0.44447E+05 m^2/s  current =   33.130 MA  q_s =  0.14488E+00
power =  0.24442E+09 MW
eta =  0.12135E+05 m^2/s  current =   16.953 MA  q_s =  0.28313E+00
power =  0.18218E+08 MW

m =  1 n =  7 q =  2 gamma =  90.0927 lambda = -100.2553
eta =  0.35335E+06 m^2/s  current =  108.846 MA  q_s =  0.44099E-01
power =  0.21917E+11 MW
eta =  0.31721E+05 m^2/s  current =   34.017 MA  q_s =  0.14110E+00
power =  0.17662E+09 MW
eta =  0.11085E+05 m^2/s  current =   33.651 MA  q_s =  0.14264E+00
power =  0.21570E+08 MW

m =  1 n =  7 q =  2 gamma = 128.4575 lambda =  135.7784
eta =  0.49395E+04 m^2/s  current =   20.436 MA  q_s =  0.23488E+00
power =  0.10639E+08 MW

m =  1 n =  7 q =  3 gamma = 139.9027 lambda = -146.6534
eta =  0.52732E+05 m^2/s  current =   74.455 MA  q_s =  0.64469E-01
power =  0.15277E+10 MW

m =  1 n =  7 q =  3 gamma = 178.3817 lambda =  183.7239
eta =  0.23694E+04 m^2/s  current =   22.770 MA  q_s =  0.21081E+00
power =  0.60647E+07 MW

m =  1 n =  7 q =  4 gamma = 189.5158 lambda = -194.5525
eta =  0.13984E+05 m^2/s  current =   58.885 MA  q_s =  0.81514E-01
power =  0.25085E+09 MW

m =  1 n =  7 q =  4 gamma = 228.0348 lambda =  232.2376
eta =  0.11973E+04 m^2/s  current =   24.409 MA  q_s =  0.19665E+00
power =  0.31276E+07 MW
```

```
m =  1 n =  8 q =  1 gamma =  39.4284 lambda =  -63.8844
eta =  0.26614E+07 m^2/s  current =  151.937 MA  q_s =  0.31592E-01
power =  0.32168E+12 MW
eta =  0.17882E+06 m^2/s  current =   39.455 MA  q_s =  0.12166E+00
power =  0.14523E+10 MW
eta =  0.11143E+05 m^2/s  current =   38.404 MA  q_s =  0.12499E+00
power =  0.56394E+07 MW

m =  1 n =  8 q =  1 gamma =  78.1410 lambda =   92.9119
eta =  0.11493E+05 m^2/s  current =   38.371 MA  q_s =  0.12509E+00
power =  0.18455E+08 MW
eta =  0.51485E+05 m^2/s  current =   37.808 MA  q_s =  0.12696E+00
power =  0.37035E+09 MW
eta =  0.12767E+05 m^2/s  current =   18.479 MA  q_s =  0.25975E+00
power =  0.22773E+08 MW

m =  1 n =  8 q =  2 gamma =  89.5068 lambda = -102.6551
eta =  0.50626E+06 m^2/s  current =  134.989 MA  q_s =  0.35558E-01
power =  0.48297E+11 MW
eta =  0.39425E+05 m^2/s  current =   38.955 MA  q_s =  0.12322E+00
power =  0.29290E+09 MW
eta =  0.12029E+05 m^2/s  current =   38.452 MA  q_s =  0.12483E+00
power =  0.27267E+08 MW

m =  1 n =  8 q =  2 gamma = 129.0300 lambda =  138.4751
eta =  0.55507E+04 m^2/s  current =   22.297 MA  q_s =  0.21527E+00
power =  0.14251E+08 MW

m =  1 n =  8 q =  3 gamma = 139.2854 lambda = -148.0778
eta =  0.86109E+05 m^2/s  current =   96.501 MA  q_s =  0.49740E-01
power =  0.41937E+10 MW

m =  1 n =  8 q =  3 gamma = 178.9763 lambda =  185.9008
eta =  0.27730E+04 m^2/s  current =   24.976 MA  q_s =  0.19218E+00
power =  0.86055E+07 MW
```

```
m =  1 n =  8 q =  4 gamma = 188.8887 lambda = -195.4624
eta =  0.21968E+05 m^2/s  current =   74.165 MA  q_s =  0.64721E-01
power =  0.62776E+09 MW

m =  1 n =  8 q =  4 gamma = 228.6401 lambda =  234.1002
eta =  0.14618E+04 m^2/s  current =   26.911 MA  q_s =  0.17837E+00
power =  0.47754E+07 MW

m =  1 n =  9 q =  1 gamma =  39.1101 lambda =  -68.7558
eta =  0.26856E+07 m^2/s  current =  170.414 MA  q_s =  0.28167E-01
power =  0.40837E+12 MW
eta =  0.18199E+06 m^2/s  current =   44.445 MA  q_s =  0.10800E+00
power =  0.18752E+10 MW
eta =  0.11642E+05 m^2/s  current =   43.205 MA  q_s =  0.11110E+00
power =  0.76743E+07 MW

m =  1 n =  9 q =  1 gamma =  78.5379 lambda =   96.7778
eta =  0.12371E+05 m^2/s  current =   43.168 MA  q_s =  0.11119E+00
power =  0.24164E+08 MW
eta =  0.57669E+05 m^2/s  current =   42.479 MA  q_s =  0.11300E+00
power =  0.52510E+09 MW
eta =  0.13176E+05 m^2/s  current =   19.957 MA  q_s =  0.24052E+00
power =  0.27411E+08 MW

m =  1 n =  9 q =  2 gamma =  89.0576 lambda = -105.4941
eta =  0.65239E+06 m^2/s  current =  159.637 MA  q_s =  0.30068E-01
power =  0.87043E+11 MW
eta =  0.46606E+05 m^2/s  current =   43.901 MA  q_s =  0.10934E+00
power =  0.44423E+09 MW
eta =  0.12939E+05 m^2/s  current =   43.254 MA  q_s =  0.11097E+00
power =  0.34236E+08 MW

m =  1 n =  9 q =  2 gamma = 129.4800 lambda =  141.2899
eta =  0.60825E+04 m^2/s  current =   24.045 MA  q_s =  0.19962E+00
power =  0.18177E+08 MW
```

```
m =  1 n =  9 q =  3 gamma = 138.8032 lambda = -149.8802
eta =  0.13117E+06 m^2/s  current =  121.263 MA  q_s =  0.39583E-01
power =  0.10091E+11 MW

m =  1 n =  9 q =  3 gamma = 179.4464 lambda =  188.1456
eta =  0.31521E+04 m^2/s  current =  27.039 MA  q_s =  0.17752E+00
power =  0.11527E+08 MW

m =  1 n =  9 q =  4 gamma = 188.3952 lambda = -196.6990
eta =  0.33253E+05 m^2/s  current =  91.998 MA  q_s =  0.52175E-01
power =  0.14659E+10 MW

m =  1 n =  9 q =  4 gamma = 229.1200 lambda =  235.9952
eta =  0.17204E+04 m^2/s  current =  29.258 MA  q_s =  0.16406E+00
power =  0.67765E+07 MW

m =  1 n = 10 q =  1 gamma =  38.8738 lambda =  -73.8852
eta =  0.26540E+07 m^2/s  current =  188.714 MA  q_s =  0.25435E-01
power =  0.49488E+12 MW
eta =  0.18138E+06 m^2/s  current =  49.433 MA  q_s =  0.97100E-01
power =  0.23114E+10 MW
eta =  0.12044E+05 m^2/s  current =  48.006 MA  q_s =  0.99987E-01
power =  0.10192E+08 MW

m =  1 n = 10 q =  1 gamma =  78.8508 lambda =  100.8231
eta =  0.13169E+05 m^2/s  current =  47.964 MA  q_s =  0.10008E+00
power =  0.30962E+08 MW
eta =  0.62924E+05 m^2/s  current =  47.146 MA  q_s =  0.10181E+00
power =  0.70688E+09 MW
eta =  0.13405E+05 m^2/s  current =  21.405 MA  q_s =  0.22424E+00
power =  0.32080E+08 MW
```

```
m =  1 n = 10 q =  2 gamma =  88.7060 lambda = -108.7042
eta =  0.78189E+06 m^2/s  current =  182.800 MA  q_s =  0.26258E-01
power =  0.13679E+12 MW
eta =  0.53084E+05 m^2/s  current =   48.855 MA  q_s =  0.98250E-01
power =  0.63051E+09 MW
eta =  0.13793E+05 m^2/s  current =   48.058 MA  q_s =  0.99880E-01
power =  0.42566E+08 MW

m =  1 n = 10 q =  2 gamma = 129.8409 lambda =  144.2446
eta =  0.65370E+04 m^2/s  current =   25.706 MA  q_s =  0.18673E+00
power =  0.22341E+08 MW

m =  1 n = 10 q =  3 gamma = 138.4186 lambda = -152.0116
eta =  0.18600E+06 m^2/s  current =  147.474 MA  q_s =  0.32548E-01
power =  0.21168E+11 MW

m =  1 n = 10 q =  3 gamma = 179.8258 lambda =  190.4866
eta =  0.35033E+04 m^2/s  current =   28.983 MA  q_s =  0.16562E+00
power =  0.14777E+08 MW

m =  1 n = 10 q =  4 gamma = 187.9986 lambda = -198.2203
eta =  0.48615E+05 m^2/s  current =  112.442 MA  q_s =  0.42689E-01
power =  0.32065E+10 MW

m =  1 n = 10 q =  4 gamma = 229.5084 lambda =  237.9537
eta =  0.19700E+04 m^2/s  current =   31.471 MA  q_s =  0.15252E+00
power =  0.91084E+07 MW

m =  2 n =  1 q =  1 gamma =  77.5110 lambda =  -77.7652
eta =  0.41071E+03 m^2/s  current =    2.610 MA  q_s =  0.18391E+01
power =  0.13818E+05 MW

m =  2 n =  1 q =  1 gamma =  83.7121 lambda =   83.9475
eta =  0.22468E+03 m^2/s  current =    2.233 MA  q_s =  0.21493E+01
power =  0.52020E+04 MW
```

```
m =  2 n =  1 q =  2 gamma = 129.0813 lambda = -129.2341
eta =  0.17389E+02 m^2/s  current =    2.523 MA  q_s =  0.19028E+01
power =  0.11369E+03 MW

m =  2 n =  2 q =  1 gamma =  74.4884 lambda =  -75.5410
eta =  0.22835E+04 m^2/s  current =    5.751 MA  q_s =  0.83459E+00
power =  0.39154E+06 MW

m =  2 n =  2 q =  1 gamma =  86.4353 lambda =   87.3440
eta =  0.76406E+03 m^2/s  current =    4.198 MA  q_s =  0.11435E+01
power =  0.67762E+05 MW

m =  2 n =  2 q =  2 gamma = 126.1139 lambda = -126.7384
eta =  0.35045E+03 m^2/s  current =    5.326 MA  q_s =  0.90119E+00
power =  0.43553E+05 MW

m =  2 n =  2 q =  2 gamma = 138.0654 lambda =  138.6361
eta =  0.13678E+03 m^2/s  current =    4.402 MA  q_s =  0.10905E+01
power =  0.86837E+04 MW

m =  2 n =  2 q =  3 gamma = 176.4547 lambda = -176.9016
eta =  0.10022E+02 m^2/s  current =    5.167 MA  q_s =  0.92897E+00
power =  0.96863E+02 MW

m =  2 n =  3 q =  1 gamma =  71.8098 lambda =  -74.2426
eta =  0.67853E+04 m^2/s  current =    9.627 MA  q_s =  0.49861E+00
power =  0.32819E+07 MW

m =  2 n =  3 q =  1 gamma =  88.7463 lambda =   90.7260
eta =  0.13990E+04 m^2/s  current =    5.964 MA  q_s =  0.80481E+00
power =  0.25459E+06 MW

m =  2 n =  3 q =  2 gamma = 123.4919 lambda = -124.9222
eta =  0.10406E+04 m^2/s  current =    8.472 MA  q_s =  0.56657E+00
power =  0.36772E+06 MW
```

```
m =  2 n =  3 q =  2 gamma = 140.4554 lambda =  141.7146
eta =  0.34169E+03 m^2/s  current =    6.356 MA  q_s =  0.75516E+00
power =  0.57882E+05 MW

m =  2 n =  3 q =  3 gamma = 173.8610 lambda = -174.8798
eta =  0.23416E+03 m^2/s  current =    8.068 MA  q_s =  0.59496E+00
power =  0.51085E+05 MW

m =  2 n =  3 q =  3 gamma = 190.8314 lambda =  191.7601
eta =  0.25080E+02 m^2/s  current =    6.556 MA  q_s =  0.73219E+00
power =  0.77261E+03 MW

m =  2 n =  4 q =  1 gamma =  69.5733 lambda =  -73.9736
eta =  0.15531E+05 m^2/s  current =   14.472 MA  q_s =  0.33167E+00
power =  0.17009E+08 MW

m =  2 n =  4 q =  1 gamma =  90.6450 lambda =   94.0647
eta =  0.20402E+04 m^2/s  current =    7.580 MA  q_s =  0.63327E+00
power =  0.60350E+06 MW

m =  2 n =  4 q =  2 gamma = 121.2849 lambda = -123.8616
eta =  0.22232E+04 m^2/s  current =   12.026 MA  q_s =  0.39915E+00
power =  0.16360E+07 MW

m =  2 n =  4 q =  2 gamma = 142.4387 lambda =  144.6390
eta =  0.57701E+03 m^2/s  current =    8.181 MA  q_s =  0.58669E+00
power =  0.17549E+06 MW

m =  2 n =  4 q =  3 gamma = 171.6758 lambda = -173.5058
eta =  0.59520E+03 m^2/s  current =   11.219 MA  q_s =  0.42784E+00
power =  0.32233E+06 MW

m =  2 n =  4 q =  3 gamma = 192.8509 lambda =  194.4817
eta =  0.13330E+03 m^2/s  current =    8.502 MA  q_s =  0.56457E+00
power =  0.22770E+05 MW
```

```
m =  2 n =  4 q =  4 gamma = 221.6167 lambda = -223.0373
eta =  0.10221E+03 m^2/s  current =   10.818 MA  q_s =  0.44369E+00
power =  0.20192E+05 MW

m =  2 n =  5 q =  1 gamma =  67.7772 lambda =  -74.7041
eta =  0.30377E+05 m^2/s  current =   20.533 MA  q_s =  0.23377E+00
power =  0.67014E+08 MW

m =  2 n =  5 q =  1 gamma =  92.1809 lambda =   97.3872
eta =  0.26456E+04 m^2/s  current =    9.078 MA  q_s =  0.52875E+00
power =  0.11261E+07 MW

m =  2 n =  5 q =  2 gamma = 119.4789 lambda = -123.5401
eta =  0.40455E+04 m^2/s  current =   16.054 MA  q_s =  0.29899E+00
power =  0.53752E+07 MW

m =  2 n =  5 q =  2 gamma = 144.0577 lambda =  147.4435
eta =  0.82781E+03 m^2/s  current =    9.896 MA  q_s =  0.48504E+00
power =  0.38262E+06 MW

m =  2 n =  5 q =  3 gamma = 169.8801 lambda = -172.7606
eta =  0.11240E+04 m^2/s  current =   14.652 MA  q_s =  0.32761E+00
power =  0.11348E+07 MW

m =  2 n =  5 q =  3 gamma = 194.5051 lambda =  197.0259
eta =  0.25551E+03 m^2/s  current =   10.351 MA  q_s =  0.46371E+00
power =  0.86979E+05 MW

m =  2 n =  5 q =  4 gamma = 219.8300 lambda = -222.0635
eta =  0.32346E+03 m^2/s  current =   13.973 MA  q_s =  0.34352E+00
power =  0.19957E+06 MW

m =  2 n =  6 q =  1 gamma =  66.3644 lambda =  -76.3247
eta =  0.53115E+05 m^2/s  current =   28.035 MA  q_s =  0.17121E+00
power =  0.21850E+09 MW
```

```
m =  2 n =  6 q =  1 gamma =  93.4182 lambda =  100.7382
eta =  0.31941E+04 m^2/s  current =   10.485 MA  q_s =  0.45782E+00
power =  0.18168E+07 MW

m =  2 n =  6 q =  2 gamma = 118.0191 lambda = -123.8941
eta =  0.66609E+04 m^2/s  current =   20.625 MA  q_s =  0.23272E+00
power =  0.14698E+08 MW

m =  2 n =  6 q =  2 gamma = 145.3739 lambda =  150.1825
eta =  0.10837E+04 m^2/s  current =   11.516 MA  q_s =  0.41683E+00
power =  0.69302E+06 MW

m =  2 n =  6 q =  3 gamma = 168.4186 lambda = -172.5864
eta =  0.18523E+04 m^2/s  current =   18.395 MA  q_s =  0.26094E+00
power =  0.30725E+07 MW

m =  2 n =  6 q =  3 gamma = 195.8543 lambda =  199.4496
eta =  0.38715E+03 m^2/s  current =   12.113 MA  q_s =  0.39625E+00
power =  0.20716E+06 MW

m =  2 n =  6 q =  4 gamma = 218.3719 lambda = -221.6022
eta =  0.61968E+03 m^2/s  current =   17.340 MA  q_s =  0.27681E+00
power =  0.72792E+06 MW

m =  2 n =  6 q =  4 gamma = 245.8411 lambda =  248.7148
eta =  0.40020E+02 m^2/s  current =   12.505 MA  q_s =  0.38386E+00
power =  0.42923E+04 MW

m =  2 n =  7 q =  1 gamma =  65.2615 lambda =  -78.6988
eta =  0.85085E+05 m^2/s  current =   37.149 MA  q_s =  0.12921E+00
power =  0.61468E+09 MW

m =  2 n =  7 q =  1 gamma =  94.4174 lambda =  104.1590
eta =  0.36760E+04 m^2/s  current =   11.819 MA  q_s =  0.40613E+00
power =  0.26600E+07 MW
```

```
m =  2 n =  7 q =  2 gamma = 116.8419 lambda = -124.8458
eta =  0.10224E+05 m^2/s  current =   25.806 MA  q_s =  0.18600E+00
power =  0.35434E+08 MW

m =  2 n =  7 q =  2 gamma = 146.4470 lambda =  152.9090
eta =  0.13372E+04 m^2/s  current =   13.053 MA  q_s =  0.36772E+00
power =  0.11137E+07 MW

m =  2 n =  7 q =  3 gamma = 167.2294 lambda = -172.9165
eta =  0.28124E+04 m^2/s  current =   22.480 MA  q_s =  0.21352E+00
power =  0.71235E+07 MW

m =  2 n =  7 q =  3 gamma = 196.9582 lambda =  201.8092
eta =  0.52455E+03 m^2/s  current =   13.798 MA  q_s =  0.34789E+00
power =  0.39394E+06 MW

m =  2 n =  7 q =  4 gamma = 217.1810 lambda = -221.5898
eta =  0.10012E+04 m^2/s  current =   20.938 MA  q_s =  0.22924E+00
power =  0.19000E+07 MW

m =  2 n =  7 q =  4 gamma = 246.9614 lambda =  250.8473
eta =  0.12014E+03 m^2/s  current =   14.294 MA  q_s =  0.33580E+00
power =  0.39686E+05 MW

m =  2 n =  8 q =  1 gamma =  64.3995 lambda =  -81.6940
eta =  0.12675E+06 m^2/s  current =   47.953 MA  q_s =  0.10010E+00
power =  0.15259E+10 MW

m =  2 n =  8 q =  1 gamma =  95.2293 lambda =  107.6812
eta =  0.40884E+04 m^2/s  current =   13.097 MA  q_s =  0.36649E+00
power =  0.36355E+07 MW

m =  2 n =  8 q =  2 gamma = 115.8891 lambda = -126.3206
eta =  0.14886E+05 m^2/s  current =   31.662 MA  q_s =  0.15160E+00
power =  0.77810E+08 MW
```

```
m =  2 n =  8 q =  2 gamma = 147.3277 lambda =  155.6666
eta =  0.15827E+04 m^2/s  current =   14.521 MA  q_s =  0.33056E+00
power =  0.16459E+07 MW

m =  2 n =  8 q =  3 gamma = 166.2567 lambda = -173.6891
eta =  0.40370E+04 m^2/s  current =   26.938 MA  q_s =  0.17819E+00
power =  0.14876E+08 MW

m =  2 n =  8 q =  3 gamma = 197.8677 lambda =  204.1525
eta =  0.66465E+03 m^2/s  current =   15.412 MA  q_s =  0.31145E+00
power =  0.65476E+06 MW

m =  2 n =  8 q =  4 gamma = 216.2027 lambda = -221.9690
eta =  0.14786E+04 m^2/s  current =   24.784 MA  q_s =  0.19368E+00
power =  0.41652E+07 MW

m =  2 n =  8 q =  4 gamma = 247.8861 lambda =  252.9311
eta =  0.20442E+03 m^2/s  current =   16.018 MA  q_s =  0.29966E+00
power =  0.11779E+06 MW

m =  2 n =  9 q =  1 gamma =  63.7218 lambda =  -85.1952
eta =  0.17733E+06 m^2/s  current =   60.403 MA  q_s =  0.79466E-01
power =  0.33872E+10 MW

m =  2 n =  9 q =  1 gamma =  95.8940 lambda =  111.3257
eta =  0.44324E+04 m^2/s  current =   14.332 MA  q_s =  0.33491E+00
power =  0.47217E+07 MW

m =  2 n =  9 q =  2 gamma = 115.1127 lambda = -128.2524
eta =  0.20788E+05 m^2/s  current =   38.255 MA  q_s =  0.12547E+00
power =  0.15881E+09 MW

m =  2 n =  9 q =  2 gamma = 148.0568 lambda =  158.4884
eta =  0.18159E+04 m^2/s  current =   15.928 MA  q_s =  0.30136E+00
power =  0.22866E+07 MW
```

```
m =  2 n =  9 q =  3 gamma = 165.4549 lambda = -174.8516
eta =  0.55594E+04 m^2/s  current =   31.798 MA  q_s =  0.15095E+00
power =  0.28780E+08 MW

m =  2 n =  9 q =  3 gamma = 198.6236 lambda =  206.5165
eta =  0.80493E+03 m^2/s  current =   16.963 MA  q_s =  0.28297E+00
power =  0.99406E+06 MW

m =  2 n =  9 q =  4 gamma = 215.3923 lambda = -222.6917
eta =  0.20627E+04 m^2/s  current =   28.894 MA  q_s =  0.16613E+00
power =  0.81846E+07 MW

m =  2 n =  9 q =  4 gamma = 248.6562 lambda =  255.0052
eta =  0.29142E+03 m^2/s  current =   17.682 MA  q_s =  0.27147E+00
power =  0.24532E+06 MW

m =  2 n = 10 q =  1 gamma =  63.1843 lambda =  -89.1072
eta =  0.23466E+06 m^2/s  current =   74.324 MA  q_s =  0.64582E-01
power =  0.67865E+10 MW

m =  2 n = 10 q =  1 gamma =  96.4427 lambda =  115.1045
eta =  0.47119E+04 m^2/s  current =   15.534 MA  q_s =  0.30899E+00
power =  0.58979E+07 MW

m =  2 n = 10 q =  2 gamma = 114.4750 lambda = -130.5847
eta =  0.28054E+05 m^2/s  current =   45.641 MA  q_s =  0.10517E+00
power =  0.30529E+09 MW

m =  2 n = 10 q =  2 gamma = 148.6655 lambda =  161.3978
eta =  0.20340E+04 m^2/s  current =   17.284 MA  q_s =  0.27771E+00
power =  0.30298E+07 MW

m =  2 n = 10 q =  3 gamma = 164.7884 lambda = -176.3606
eta =  0.74124E+04 m^2/s  current =   37.092 MA  q_s =  0.12941E+00
power =  0.52500E+08 MW
```

```
m =  2 n = 10 q =  3 gamma = 199.2576 lambda =  208.9292
eta =  0.94330E+03 m^2/s  current =   18.458 MA  q_s =  0.26005E+00
power =  0.14136E+07 MW

m =  2 n = 10 q =  4 gamma = 214.7149 lambda = -223.7193
eta =  0.27642E+04 m^2/s  current =   33.286 MA  q_s =  0.14420E+00
power =  0.14903E+08 MW

m =  2 n = 10 q =  4 gamma = 249.3036 lambda =  257.0994
eta =  0.37988E+03 m^2/s  current =   19.290 MA  q_s =  0.24884E+00
power =  0.42719E+06 MW

m =  3 n =  1 q =  1 gamma =  98.1166 lambda =  -98.3175
eta =  0.50592E+02 m^2/s  current =    1.671 MA  q_s =  0.28723E+01
power =  0.42373E+03 MW

m =  3 n =  1 q =  1 gamma = 102.2793 lambda =  102.4721
eta =  0.25025E+02 m^2/s  current =    1.537 MA  q_s =  0.31226E+01
power =  0.11738E+03 MW

m =  3 n =  2 q =  1 gamma =  96.0513 lambda =  -96.8698
eta =  0.36920E+03 m^2/s  current =    3.502 MA  q_s =  0.13705E+01
power =  0.21583E+05 MW

m =  3 n =  2 q =  1 gamma = 104.2259 lambda =  104.9808
eta =  0.18541E+03 m^2/s  current =    2.964 MA  q_s =  0.16196E+01
power =  0.69283E+04 MW

m =  3 n =  2 q =  2 gamma = 149.1818 lambda = -149.7101
eta =  0.95296E+01 m^2/s  current =    3.390 MA  q_s =  0.14161E+01
power =  0.53080E+02 MW

m =  3 n =  3 q =  1 gamma =  94.0982 lambda =  -95.9676
eta =  0.10014E+04 m^2/s  current =    5.521 MA  q_s =  0.86934E+00
power =  0.15440E+06 MW
```

```
m =  3 n =  3 q =  1 gamma = 106.0100 lambda =  107.6728
eta =  0.40040E+03 m^2/s  current =    4.299 MA  q_s =  0.11166E+01
power =  0.34861E+05 MW

m =  3 n =  3 q =  2 gamma = 147.2481 lambda = -148.4497
eta =  0.16116E+03 m^2/s  current =    5.243 MA  q_s =  0.91542E+00
power =  0.14800E+05 MW

m =  3 n =  3 q =  2 gamma = 159.1841 lambda =  160.2963
eta =  0.37925E+02 m^2/s  current =    4.451 MA  q_s =  0.10784E+01
power =  0.10319E+04 MW

m =  3 n =  4 q =  1 gamma =  92.3134 lambda =  -95.6735
eta =  0.20294E+04 m^2/s  current =    7.755 MA  q_s =  0.61898E+00
power =  0.62829E+06 MW

m =  3 n =  4 q =  1 gamma = 107.6063 lambda =  110.5023
eta =  0.64181E+03 m^2/s  current =    5.558 MA  q_s =  0.86359E+00
power =  0.96820E+05 MW

m =  3 n =  4 q =  2 gamma = 145.4762 lambda = -147.6312
eta =  0.39680E+03 m^2/s  current =    7.218 MA  q_s =  0.66501E+00
power =  0.88248E+05 MW

m =  3 n =  4 q =  2 gamma = 160.8264 lambda =  162.7784
eta =  0.12527E+03 m^2/s  current =    5.803 MA  q_s =  0.82717E+00
power =  0.11791E+05 MW

m =  3 n =  4 q =  3 gamma = 196.6258 lambda = -198.2256
eta =  0.22182E+02 m^2/s  current =    6.991 MA  q_s =  0.68661E+00
power =  0.66757E+03 MW

m =  3 n =  5 q =  1 gamma =  90.7275 lambda =  -96.0127
eta =  0.35157E+04 m^2/s  current =   10.224 MA  q_s =  0.46949E+00
power =  0.19057E+07 MW
```

```
m =  3 n =  5 q =  1 gamma = 109.0099 lambda =  113.4466
eta =  0.89105E+03 m^2/s  current =    6.754 MA  q_s =  0.71064E+00
power =  0.20193E+06 MW

m =  3 n =  5 q =  2 gamma = 143.8904 lambda = -147.2800
eta =  0.72911E+03 m^2/s  current =    9.323 MA  q_s =  0.51484E+00
power =  0.29584E+06 MW

m =  3 n =  5 q =  2 gamma = 162.2822 lambda =  165.2951
eta =  0.22353E+03 m^2/s  current =    7.101 MA  q_s =  0.67598E+00
power =  0.39309E+05 MW

m =  3 n =  5 q =  3 gamma = 195.0464 lambda = -197.5603
eta =  0.14754E+03 m^2/s  current =    8.948 MA  q_s =  0.53642E+00
power =  0.29238E+05 MW

m =  3 n =  6 q =  1 gamma =  89.3485 lambda =  -96.9762
eta =  0.54881E+04 m^2/s  current =   12.944 MA  q_s =  0.37083E+00
power =  0.47848E+07 MW

m =  3 n =  6 q =  1 gamma = 110.2302 lambda =  116.4985
eta =  0.11359E+04 m^2/s  current =    7.898 MA  q_s =  0.60775E+00
power =  0.35538E+06 MW

m =  3 n =  6 q =  2 gamma = 142.4951 lambda = -147.3977
eta =  0.11681E+04 m^2/s  current =   11.568 MA  q_s =  0.41494E+00
power =  0.76114E+06 MW

m =  3 n =  6 q =  2 gamma = 163.5578 lambda =  167.8463
eta =  0.32864E+03 m^2/s  current =    8.351 MA  q_s =  0.57481E+00
power =  0.88965E+05 MW

m =  3 n =  6 q =  3 gamma = 193.6522 lambda = -197.2876
eta =  0.31037E+03 m^2/s  current =   11.000 MA  q_s =  0.43637E+00
power =  0.12886E+06 MW
```

```
m =  3 n =  6 q =  3 gamma = 214.7740 lambda =  218.0575
eta =  0.15023E+02 m^2/s  current =    8.608 MA  q_s =  0.55763E+00
power =  0.40762E+03 MW

m =  3 n =  7 q =  1 gamma =  88.1673 lambda =  -98.5287
eta =  0.79316E+04 m^2/s  current =   15.921 MA  q_s =  0.30149E+00
power =  0.10482E+08 MW

m =  3 n =  7 q =  1 gamma = 111.2839 lambda =  119.6601
eta =  0.13686E+04 m^2/s  current =    8.998 MA  q_s =  0.53348E+00
power =  0.55900E+06 MW

m =  3 n =  7 q =  2 gamma = 141.2811 lambda = -147.9689
eta =  0.17203E+04 m^2/s  current =   13.959 MA  q_s =  0.34386E+00
power =  0.16702E+07 MW

m =  3 n =  7 q =  2 gamma = 164.6683 lambda =  170.4408
eta =  0.43739E+03 m^2/s  current =    9.557 MA  q_s =  0.50224E+00
power =  0.16501E+06 MW

m =  3 n =  7 q =  3 gamma = 192.4333 lambda = -197.3956
eta =  0.51346E+03 m^2/s  current =   13.151 MA  q_s =  0.36500E+00
power =  0.35323E+06 MW

m =  3 n =  7 q =  3 gamma = 215.9096 lambda =  220.3438
eta =  0.71643E+02 m^2/s  current =    9.885 MA  q_s =  0.48560E+00
power =  0.95649E+04 MW

m =  3 n =  7 q =  4 gamma = 242.8589 lambda = -246.8094
eta =  0.64590E+02 m^2/s  current =   12.710 MA  q_s =  0.37766E+00
power =  0.10926E+05 MW

m =  3 n =  8 q =  1 gamma =  87.1649 lambda = -100.6198
eta =  0.10790E+05 m^2/s  current =   19.154 MA  q_s =  0.25060E+00
power =  0.20661E+08 MW
```

```
m =  3 n =  8 q =  1 gamma = 112.1909 lambda =  122.9367
eta =  0.15840E+04 m^2/s  current =   10.060 MA  q_s =  0.47711E+00
power =  0.81202E+06 MW

m =  3 n =  8 q =  2 gamma = 140.2318 lambda = -148.9684
eta =  0.23884E+04 m^2/s  current =   16.502 MA  q_s =  0.29088E+00
power =  0.32850E+07 MW

m =  3 n =  8 q =  2 gamma = 165.6320 lambda =  173.0913
eta =  0.54720E+03 m^2/s  current =   10.725 MA  q_s =  0.44754E+00
power =  0.27049E+06 MW

m =  3 n =  8 q =  3 gamma = 191.3734 lambda = -197.8646
eta =  0.75881E+03 m^2/s  current =   15.404 MA  q_s =  0.31160E+00
power =  0.77697E+06 MW

m =  3 n =  8 q =  3 gamma = 216.8986 lambda =  222.6468
eta =  0.13122E+03 m^2/s  current =   11.126 MA  q_s =  0.43143E+00
power =  0.33103E+05 MW

m =  3 n =  8 q =  4 gamma = 241.7964 lambda = -246.9658
eta =  0.18011E+03 m^2/s  current =   14.809 MA  q_s =  0.32414E+00
power =  0.85114E+05 MW

m =  3 n =  9 q =  1 gamma =  86.3186 lambda = -103.1923
eta =  0.13976E+05 m^2/s  current =   22.632 MA  q_s =  0.21209E+00
power =  0.37388E+08 MW

m =  3 n =  9 q =  1 gamma = 112.9713 lambda =  126.3340
eta =  0.17792E+04 m^2/s  current =   11.093 MA  q_s =  0.43270E+00
power =  0.11119E+07 MW

m =  3 n =  9 q =  2 gamma = 139.3275 lambda = -150.3659
eta =  0.31711E+04 m^2/s  current =   19.199 MA  q_s =  0.25001E+00
power =  0.59551E+07 MW
```

```
m =  3 n =  9 q =  2 gamma = 166.4682 lambda =  175.8108
eta =  0.65597E+03 m^2/s  current =   11.859 MA  q_s =  0.40475E+00
power =  0.40732E+06 MW

m =  3 n =  9 q =  3 gamma = 190.4536 lambda = -198.6714
eta =  0.10477E+04 m^2/s  current =   17.764 MA  q_s =  0.27021E+00
power =  0.14994E+07 MW

m =  3 n =  9 q =  3 gamma = 217.7597 lambda =  224.9823
eta =  0.19270E+03 m^2/s  current =   12.334 MA  q_s =  0.38917E+00
power =  0.73663E+05 MW

m =  3 n =  9 q =  4 gamma = 240.8713 lambda = -247.4202
eta =  0.31552E+03 m^2/s  current =   16.986 MA  q_s =  0.28258E+00
power =  0.26265E+06 MW

m =  3 n = 10 q =  1 gamma =  85.6052 lambda = -106.1890
eta =  0.17381E+05 m^2/s  current =   26.341 MA  q_s =  0.18223E+00
power =  0.63013E+08 MW

m =  3 n = 10 q =  1 gamma = 113.6434 lambda =  129.8564
eta =  0.19529E+04 m^2/s  current =   12.100 MA  q_s =  0.39668E+00
power =  0.14547E+07 MW

m =  3 n = 10 q =  2 gamma = 138.5486 lambda = -152.1300
eta =  0.40632E+04 m^2/s  current =   22.052 MA  q_s =  0.21766E+00
power =  0.10126E+08 MW

m =  3 n = 10 q =  2 gamma = 167.1948 lambda =  178.6111
eta =  0.76203E+03 m^2/s  current =   12.963 MA  q_s =  0.37030E+00
power =  0.57637E+06 MW

m =  3 n = 10 q =  3 gamma = 189.6551 lambda = -199.7921
eta =  0.13806E+04 m^2/s  current =   20.232 MA  q_s =  0.23725E+00
power =  0.26480E+07 MW
```

```
m =  3 n = 10 q =  3 gamma = 218.5106 lambda =  227.3648
eta =  0.25517E+03 m^2/s  current =   13.512 MA  q_s =  0.35525E+00
power =  0.13331E+06 MW

m =  3 n = 10 q =  4 gamma = 240.0653 lambda = -248.1516
eta =  0.47145E+03 m^2/s  current =   19.245 MA  q_s =  0.24941E+00
power =  0.59164E+06 MW

m =  4 n =  2 q =  1 gamma = 116.0616 lambda = -116.7399
eta =  0.70537E+02 m^2/s  current =    2.536 MA  q_s =  0.18924E+01
power =  0.13789E+04 MW

m =  4 n =  2 q =  1 gamma = 122.2543 lambda =  122.8985
eta =  0.27871E+02 m^2/s  current =    2.283 MA  q_s =  0.21022E+01
power =  0.25117E+03 MW

m =  4 n =  3 q =  1 gamma = 114.5499 lambda = -116.0904
eta =  0.24481E+03 m^2/s  current =    3.918 MA  q_s =  0.12252E+01
power =  0.16333E+05 MW

m =  4 n =  3 q =  1 gamma = 123.6776 lambda =  125.1058
eta =  0.11384E+03 m^2/s  current =    3.348 MA  q_s =  0.14337E+01
power =  0.44201E+04 MW

m =  4 n =  4 q =  1 gamma = 113.1163 lambda = -115.8747
eta =  0.51049E+03 m^2/s  current =    5.383 MA  q_s =  0.89167E+00
power =  0.70627E+05 MW

m =  4 n =  4 q =  1 gamma = 125.0037 lambda =  127.5052
eta =  0.21692E+03 m^2/s  current =    4.370 MA  q_s =  0.10985E+01
power =  0.16991E+05 MW

m =  4 n =  4 q =  2 gamma = 167.7466 lambda = -169.6189
eta =  0.48952E+02 m^2/s  current =    5.184 MA  q_s =  0.92592E+00
power =  0.20370E+04 MW
```

```
m =  4 n =  5 q =  1 gamma = 111.7823 lambda = -116.1131
eta =  0.87518E+03 m^2/s  current =    6.937 MA  q_s =  0.69190E+00
power =  0.20887E+06 MW

m =  4 n =  5 q =  1 gamma = 126.2224 lambda =  130.0732
eta =  0.32981E+03 m^2/s  current =    5.354 MA  q_s =  0.89656E+00
power =  0.41698E+05 MW

m =  4 n =  5 q =  2 gamma = 166.4128 lambda = -169.3522
eta =  0.15515E+03 m^2/s  current =    6.613 MA  q_s =  0.72583E+00
power =  0.20367E+05 MW

m =  4 n =  5 q =  2 gamma = 180.9193 lambda =  183.6266
eta =  0.12306E+02 m^2/s  current =    5.527 MA  q_s =  0.86843E+00
power =  0.16333E+03 MW

m =  4 n =  6 q =  1 gamma = 110.5613 lambda = -116.8119
eta =  0.13406E+04 m^2/s  current =    8.583 MA  q_s =  0.55923E+00
power =  0.49902E+06 MW

m =  4 n =  6 q =  1 gamma = 127.3301 lambda =  132.7937
eta =  0.44688E+03 m^2/s  current =    6.305 MA  q_s =  0.76124E+00
power =  0.81460E+05 MW

m =  4 n =  6 q =  2 gamma = 165.1842 lambda = -169.4315
eta =  0.29080E+03 m^2/s  current =    8.101 MA  q_s =  0.59255E+00
power =  0.71647E+05 MW

m =  4 n =  6 q =  2 gamma = 182.0629 lambda =  185.9251
eta =  0.61343E+02 m^2/s  current =    6.537 MA  q_s =  0.73425E+00
power =  0.42129E+04 MW

m =  4 n =  7 q =  1 gamma = 109.4586 lambda = -117.9645
eta =  0.19020E+04 m^2/s  current =   10.321 MA  q_s =  0.46505E+00
power =  0.10344E+07 MW
```

```
m =  4 n =  7 q =  1 gamma = 128.3288 lambda =  135.6566
eta =  0.56391E+03 m^2/s  current =    7.229 MA  q_s =  0.66401E+00
power =  0.13828E+06 MW

m =  4 n =  7 q =  2 gamma = 164.0650 lambda = -169.8581
eta =  0.45666E+03 m^2/s  current =    9.648 MA  q_s =  0.49751E+00
power =  0.17803E+06 MW

m =  4 n =  7 q =  2 gamma = 183.1009 lambda =  188.3093
eta =  0.11363E+03 m^2/s  current =    7.522 MA  q_s =  0.63815E+00
power =  0.15018E+05 MW

m =  4 n =  7 q =  3 gamma = 216.0409 lambda = -220.4724
eta =  0.43411E+02 m^2/s  current =    9.331 MA  q_s =  0.51443E+00
power =  0.35179E+04 MW

m =  4 n =  8 q =  1 gamma = 108.4731 lambda = -119.5535
eta =  0.25479E+04 m^2/s  current =   12.150 MA  q_s =  0.39505E+00
power =  0.19324E+07 MW

m =  4 n =  8 q =  1 gamma = 129.2240 lambda =  138.6559
eta =  0.67776E+03 m^2/s  current =    8.128 MA  q_s =  0.59058E+00
power =  0.21330E+06 MW

m =  4 n =  8 q =  2 gamma = 163.0540 lambda = -170.6260
eta =  0.65258E+03 m^2/s  current =   11.256 MA  q_s =  0.42642E+00
power =  0.36850E+06 MW

m =  4 n =  8 q =  2 gamma = 184.0377 lambda =  190.7787
eta =  0.16793E+03 m^2/s  current =    8.483 MA  q_s =  0.56585E+00
power =  0.34109E+05 MW

m =  4 n =  8 q =  3 gamma = 215.0238 lambda = -220.8209
eta =  0.12739E+03 m^2/s  current =   10.833 MA  q_s =  0.44310E+00
power =  0.30438E+05 MW
```

```
m =  4 n =  9 q =  1 gamma = 107.5991 lambda = -121.5537
eta =  0.32622E+04 m^2/s  current =   14.067 MA  q_s =  0.34123E+00
power =  0.33293E+07 MW

m =  4 n =  9 q =  1 gamma = 130.0234 lambda =  141.7880
eta =  0.78618E+03 m^2/s  current =    9.005 MA  q_s =  0.53302E+00
power =  0.30690E+06 MW

m =  4 n =  9 q =  2 gamma = 162.1462 lambda = -171.7241
eta =  0.87746E+03 m^2/s  current =   12.926 MA  q_s =  0.37135E+00
power =  0.67917E+06 MW

m =  4 n =  9 q =  2 gamma = 184.8800 lambda =  193.3349
eta =  0.22319E+03 m^2/s  current =    9.422 MA  q_s =  0.50942E+00
power =  0.62709E+05 MW

m =  4 n =  9 q =  3 gamma = 214.1064 lambda = -221.4482
eta =  0.22427E+03 m^2/s  current =   12.380 MA  q_s =  0.38772E+00
power =  0.95144E+05 MW

m =  4 n = 10 q =  1 gamma = 106.8280 lambda = -123.9357
eta =  0.40251E+04 m^2/s  current =   16.065 MA  q_s =  0.29878E+00
power =  0.53724E+07 MW

m =  4 n = 10 q =  1 gamma = 130.7355 lambda =  145.0504
eta =  0.88760E+03 m^2/s  current =    9.865 MA  q_s =  0.48658E+00
power =  0.41882E+06 MW

m =  4 n = 10 q =  2 gamma = 161.3344 lambda = -173.1376
eta =  0.11293E+04 m^2/s  current =   14.656 MA  q_s =  0.32751E+00
power =  0.11531E+07 MW

m =  4 n = 10 q =  2 gamma = 185.6358 lambda =  195.9808
eta =  0.27853E+03 m^2/s  current =   10.343 MA  q_s =  0.46410E+00
power =  0.10172E+06 MW
```

```
m =  4 n = 10 q =  3 gamma = 213.2817 lambda = -222.3442
eta =  0.33388E+03 m^2/s  current =   13.973 MA  q_s =  0.34351E+00
power =  0.21344E+06 MW

m =  5 n =  3 q =  1 gamma = 134.0439 lambda = -135.3627
eta =  0.46687E+02 m^2/s  current =    3.050 MA  q_s =  0.15738E+01
power =  0.94173E+03 MW

m =  5 n =  3 q =  1 gamma = 141.4245 lambda =  142.6752
eta =  0.40313E+01 m^2/s  current =    2.735 MA  q_s =  0.17547E+01
power =  0.82216E+01 MW

m =  5 n =  4 q =  1 gamma = 132.8589 lambda = -135.2152
eta =  0.14384E+03 m^2/s  current =    4.148 MA  q_s =  0.11571E+01
power =  0.89094E+04 MW

m =  5 n =  4 q =  1 gamma = 142.5439 lambda =  144.7426
eta =  0.52756E+02 m^2/s  current =    3.591 MA  q_s =  0.13368E+01
power =  0.14701E+04 MW

m =  5 n =  5 q =  1 gamma = 131.7297 lambda = -135.4240
eta =  0.27381E+03 m^2/s  current =    5.291 MA  q_s =  0.90725E+00
power =  0.32436E+05 MW

m =  5 n =  5 q =  1 gamma = 143.5988 lambda =  146.9952
eta =  0.10831E+03 m^2/s  current =    4.422 MA  q_s =  0.10855E+01
power =  0.64911E+04 MW

m =  5 n =  6 q =  1 gamma = 130.6665 lambda = -135.9961
eta =  0.43675E+03 m^2/s  current =    6.478 MA  q_s =  0.74099E+00
power =  0.83575E+05 MW

m =  5 n =  6 q =  1 gamma = 144.5840 lambda =  149.4181
eta =  0.16817E+03 m^2/s  current =    5.232 MA  q_s =  0.91741E+00
power =  0.16433E+05 MW
```

```
m =  5 n =  6 q =  2 gamma = 186.7056 lambda = -190.4736
eta =  0.27317E+02 m^2/s  current =    6.255 MA  q_s =  0.76736E+00
power =  0.89824E+03 MW

m =  5 n =  7 q =  1 gamma = 129.6761 lambda = -136.9319
eta =  0.63120E+03 m^2/s  current =    7.710 MA  q_s =  0.62258E+00
power =  0.17819E+06 MW

m =  5 n =  7 q =  1 gamma = 145.4972 lambda =  151.9996
eta =  0.23020E+03 m^2/s  current =    6.023 MA  q_s =  0.79694E+00
power =  0.32418E+05 MW

m =  5 n =  7 q =  2 gamma = 185.7058 lambda = -190.8431
eta =  0.94544E+02 m^2/s  current =    7.402 MA  q_s =  0.64845E+00
power =  0.10823E+05 MW

m =  5 n =  8 q =  1 gamma = 128.7620 lambda = -138.2255
eta =  0.85418E+03 m^2/s  current =    8.986 MA  q_s =  0.53416E+00
power =  0.33566E+06 MW

m =  5 n =  8 q =  1 gamma = 146.3386 lambda =  154.7307
eta =  0.29271E+03 m^2/s  current =    6.797 MA  q_s =  0.70619E+00
power =  0.55288E+05 MW

m =  5 n =  8 q =  2 gamma = 184.7767 lambda = -191.4916
eta =  0.17297E+03 m^2/s  current =    8.581 MA  q_s =  0.55939E+00
power =  0.36595E+05 MW

m =  5 n =  9 q =  1 gamma = 127.9246 lambda = -139.8659
eta =  0.11014E+04 m^2/s  current =   10.305 MA  q_s =  0.46578E+00
power =  0.57816E+06 MW

m =  5 n =  9 q =  1 gamma = 147.1101 lambda =  157.6044
eta =  0.35431E+03 m^2/s  current =    7.556 MA  q_s =  0.63526E+00
power =  0.85604E+05 MW
```

```
m =  5 n =  9 q =  2 gamma = 183.9186 lambda = -192.4157
eta =  0.26216E+03 m^2/s  current =    9.791 MA  q_s =  0.49027E+00
power =  0.85289E+05 MW

m =  5 n =  9 q =  2 gamma = 203.3066 lambda =  211.0244
eta =  0.22727E+02 m^2/s  current =    7.804 MA  q_s =  0.61510E+00
power =  0.84548E+03 MW

m =  5 n = 10 q =  1 gamma = 127.1620 lambda = -141.8380
eta =  0.13676E+04 m^2/s  current =   11.665 MA  q_s =  0.41148E+00
power =  0.92962E+06 MW

m =  5 n = 10 q =  1 gamma = 147.8151 lambda =  160.6149
eta =  0.41394E+03 m^2/s  current =    8.301 MA  q_s =  0.57821E+00
power =  0.12367E+06 MW

m =  5 n = 10 q =  2 gamma = 183.1300 lambda = -193.6090
eta =  0.36142E+03 m^2/s  current =   11.031 MA  q_s =  0.43512E+00
power =  0.16514E+06 MW

m =  5 n = 10 q =  2 gamma = 204.0448 lambda =  213.4997
eta =  0.53212E+02 m^2/s  current =    8.589 MA  q_s =  0.55886E+00
power =  0.48001E+04 MW

m =  6 n =  4 q =  1 gamma = 151.9467 lambda = -154.0112
eta =  0.11604E+02 m^2/s  current =    3.384 MA  q_s =  0.14184E+01
power =  0.85681E+02 MW

m =  6 n =  5 q =  1 gamma = 150.9754 lambda = -154.2093
eta =  0.68734E+02 m^2/s  current =    4.291 MA  q_s =  0.11185E+01
power =  0.30179E+04 MW

m =  6 n =  5 q =  1 gamma = 161.0244 lambda =  164.0604
eta =  0.30250E+01 m^2/s  current =    3.760 MA  q_s =  0.12766E+01
power =  0.70389E+01 MW
```

```
m =  6 n =  6 q =  1 gamma = 150.0453 lambda = -154.7088
eta =  0.13956E+03 m^2/s  current =    5.224 MA  q_s =  0.91879E+00
power =  0.12563E+05 MW

m =  6 n =  6 q =  1 gamma = 161.9000 lambda =  166.2313
eta =  0.35399E+02 m^2/s  current =    4.463 MA  q_s =  0.10756E+01
power =  0.10027E+04 MW

m =  6 n =  7 q =  1 gamma = 149.1623 lambda = -155.5116
eta =  0.22356E+03 m^2/s  current =    6.183 MA  q_s =  0.77636E+00
power =  0.32743E+05 MW

m =  6 n =  7 q =  1 gamma = 162.7267 lambda =  168.5657
eta =  0.69866E+02 m^2/s  current =    5.152 MA  q_s =  0.93169E+00
power =  0.40727E+04 MW

m =  6 n =  8 q =  1 gamma = 148.3303 lambda = -156.6157
eta =  0.31974E+03 m^2/s  current =    7.166 MA  q_s =  0.66979E+00
power =  0.68414E+05 MW

m =  6 n =  8 q =  1 gamma = 163.5028 lambda =  171.0549
eta =  0.10551E+03 m^2/s  current =    5.829 MA  q_s =  0.82346E+00
power =  0.97054E+04 MW

m =  6 n =  9 q =  1 gamma = 147.5514 lambda = -158.0163
eta =  0.42667E+03 m^2/s  current =    8.175 MA  q_s =  0.58717E+00
power =  0.12512E+06 MW

m =  6 n =  9 q =  1 gamma = 164.2281 lambda =  173.6912
eta =  0.14154E+03 m^2/s  current =    6.495 MA  q_s =  0.73901E+00
power =  0.18287E+05 MW

m =  6 n =  9 q =  2 gamma = 204.9095 lambda = -212.5692
eta =  0.23531E+02 m^2/s  current =    7.901 MA  q_s =  0.60755E+00
power =  0.92642E+03 MW
```

```
m =  6 n = 10 q =  1 gamma = 146.8263 lambda = -159.7054
eta =  0.54255E+03 m^2/s  current =    9.207 MA  q_s =  0.52135E+00
power =  0.20887E+06 MW

m =  6 n = 10 q =  1 gamma = 164.9034 lambda =  176.4681
eta =  0.17731E+03 m^2/s  current =    7.151 MA  q_s =  0.67120E+00
power =  0.30095E+05 MW

m =  6 n = 10 q =  2 gamma = 204.1673 lambda = -213.6168
eta =  0.70523E+02 m^2/s  current =    8.870 MA  q_s =  0.54118E+00
power =  0.84451E+04 MW

m =  7 n =  6 q =  1 gamma = 168.9206 lambda = -173.0762
eta =  0.11158E+02 m^2/s  current =    4.387 MA  q_s =  0.10941E+01
power =  0.11244E+03 MW

m =  7 n =  7 q =  1 gamma = 168.1308 lambda = -173.7884
eta =  0.52915E+02 m^2/s  current =    5.174 MA  q_s =  0.92769E+00
power =  0.25600E+04 MW

m =  7 n =  8 q =  1 gamma = 167.3762 lambda = -174.7610
eta =  0.10064E+03 m^2/s  current =    5.977 MA  q_s =  0.80310E+00
power =  0.94178E+04 MW

m =  7 n =  8 q =  1 gamma = 180.6855 lambda =  187.5470
eta =  0.20640E+01 m^2/s  current =    5.096 MA  q_s =  0.94200E+00
power =  0.48954E+01 MW

m =  7 n =  9 q =  1 gamma = 166.6592 lambda = -175.9916
eta =  0.15378E+03 m^2/s  current =    6.795 MA  q_s =  0.70638E+00
power =  0.22456E+05 MW

m =  7 n =  9 q =  1 gamma = 181.3600 lambda =  189.9716
eta =  0.23693E+02 m^2/s  current =    5.688 MA  q_s =  0.84393E+00
power =  0.67041E+03 MW
```

```
m =  7 n = 10 q =  1 gamma = 165.9815 lambda = -177.4759
eta =  0.21162E+03 m^2/s  current =    7.629 MA  q_s =  0.62921E+00
power =  0.43607E+05 MW

m =  7 n = 10 q =  1 gamma = 181.9967 lambda =  192.5374
eta =  0.45580E+02 m^2/s  current =    6.272 MA  q_s =  0.76527E+00
power =  0.25831E+04 MW

m =  8 n =  9 q =  1 gamma = 185.3732 lambda = -193.8065
eta =  0.19702E+02 m^2/s  current =    5.825 MA  q_s =  0.82405E+00
power =  0.49220E+03 MW

m =  8 n = 10 q =  1 gamma = 184.7437 lambda = -195.1360
eta =  0.51404E+02 m^2/s  current =    6.525 MA  q_s =  0.73560E+00
power =  0.34202E+04 MW
```

Bibliography

Agim, Y. Z. and Montgomery, D. (1991). Nonideal, helical, vortical magnetohydrodynamic steady states, *Plasma Phys. Contr. Fusion* **33**(8): 881–902.

Aly, J. J. (1993). A model for magnetic energy storage and Taylor's relaxation in the solar corona. I: Helicity-constrained minimum energy state in a half-cylinder, *Phys. Fluids B* **5**(1): 151–163.

André, J. C. and Lesieur, M. (1977). Influence of helicity on the evolution of isotropic turbulence at high Reynolds number, *J. Fluid Mech.* **81**(1): 187–207.

Antiochos, S. K. (1994). The physics of coronal closed-field structures, *Adv. Space Res.* **14**(4): 139–148.

Athay, R. G. and White, O. R. (1978). Chromospheric and coronal heating by sound waves, *Ap. J.* **226**: 1135–1139.

Athay, R. G. and White, O. R. (1979a). Chromospheric oscillations observed with OSO8 II. Average power spectra for Si II, *Ap. J. Supp.* **39**: 333–346.

Athay, R. G. and White, O. R. (1979b). Chromospheric oscillations observed with OSO8 IV. Power and phase spectra for C IV, *Ap. J.* **229**: 1147–1162.

Axford, W. I. (1984). Magnetic field reconnection, *in* E. W. Hones, Jr. (ed.), *Magnetic Reconnection in Space and Laboratory Plasmas*, Vol. 30 of *Geophysical Monograph Series*, American Geophysical Union, Washington, pp. 1–8.

Bahcall, J. N. and Cribier, M. (1990). The standard solar model, *in* G. Berthomieu and M. Cribier (eds), *Inside the Sun*, Kluwer Academic Publishers, Dordrecht, pp. 21–41.

Basdevant, C., Lesieur, M. and Sadourny, R. (1978). Subgrid-scale modelling of enstrophy transfer in two-dimensional turbulence, *J. Atmos. Sci.* **35**: 1028–1042.

Batchelor, G. K. (1953). *The Theory of Homogeneous Turbulence*, Cambridge University Press.

Batchelor, G. K. (1967). *An Introduction to Fluid Dynamics*, Cambridge University Press.

Batchelor, G. K. (1969). Computation of the energy spectrum in homogeneous two-dimensional turbulence, *Phys. Fluids Suppl. II* pp. 233–239.

Berger, M. A. (1984). Rigorous new limits on magnetic helicity dissipation in the solar corona, *Geophys. Astrophys. Fluid Dyn.* **30**: 79–104.

Berger, M. A. (1985). Structure and stability of constant-α force-free fields, *Ap. J. Supp.* **59**: 433–444.

Berger, M. A. (1991). Generation of coronal magnetic fields by random surface motions I. Mean square twist and current density, *Astron. Astrophys.* **252**: 369–376.

Berger, M. A. and Field, G. B. (1984). The topological properties of magnetic helicity, *J. Fluid Mech.* **147**: 133–148.

Bevir, M. K., Caloutsis, A. and Gimblett, C. G. (1993). A note on minimum dissipation plasma states, *Plasma Phys. Contr. Fusion* **35**(2): 133–149.

Biskamp, D. (1993). *Nonlinear Magnetohydrodynamics*, Vol. 1 of *Cambridge Monographs on Plasma Physics*, Cambridge University Press.

Biskamp, D. and Welter, H. (1989). Dynamics of decaying two-dimensional magnetohydrodynamic turbulence, *Phys. Fluids B* **1**(10): 1964–1979.

Bodin, H. A. B. (1987). Reversed field pinch: status and trends, *Plasma Phys. Contr. Fusion* **29**(10A): 1297–1307.

Bodin, H. A. B. and Newton, A. A. (1980). Reversed-field-pinch research, *Nucl. Fus.* **20**(10): 1255–1324.

Bodo, G., Massaglia, S., Rosner, R. and Ferrari, A. (1991). The finite-amplitude behaviour of the Joule mode under astrophysical conditions, *Ap. J.* **370**: 398–406.

Bogdan, T. J. (1984). The turbulent twisted magnetic flux tube gas, *Phys. Fluids* **27**(4): 994–1004.

Braginskii, S. I. (1965). Transport processes in a plasma, *in* M. A. Leontovich (ed.), *Reviews of Plasma Physics*, Vol. 1, Consultants Bureau, New York, pp. 205–311.

Browning, P. K. (1988a). Magnetic relaxation in solar and laboratory plasmas, *Plasma Phys. Contr. Fusion* **30**(1): 1–10.

Browning, P. K. (1988b). Helicity injection and relaxation in a solar-coronal magnetic loop with a free surface, *J. Plasma Phys.* **40**(2): 263–280.

Browning, P. K. (1991). Mechanisms of solar coronal heating, *Plasma Phys. Contr. Fusion* **33**(6): 539–571.

Browning, P. K. and Priest, E. R. (1986). Heating of coronal arcades by magnetic tearing turbulence, using the Taylor-Heyvaerts hypothesis, *Astron. Astrophys.* **159**: 129–141.

Browning, P. K., Sakurai, T. and Priest, E. R. (1986). Coronal heating in closely-packed flux tubes: a Taylor-Heyvaerts relaxation theory, *Astron. Astrophys.* **158**: 217–227.

Bruner, Jr., E. C. (1978). Dynamics of the solar transition zone, *Ap. J.* **226**: 1140–1146.

Bruner, Jr., E. C. (1981). OSO8 observational limits to the acoustic coronal heating mechanism, *Ap. J.* **247**: 317–324.

Callen, J. D., Carreras, B. A. and Stambaugh, R. D. (1992). Stability and transport processes in tokamak plasmas, *Phys. Today* **45**(1): 34–42.

Cally, P. S. (1991). Phase-mixing and surface-waves — a new interpretation, *J. Plasma Phys.* **45**: 453–479.

Cargill, P. J. (1994). The experimental signatures of coronal heating mechanisms, *in* J. L. Burch and J. H. Waite, Jr. (eds), *Solar System Plasmas in Space and Time*, Vol. 84 of *Geophysical Monographs*, American Geophysical Union.

Cattaneo, F. and Vainshtein, S. I. (1991). Suppression of turbulent transport by a weak magnetic field, *Ap. J.* **376**: L21–L24.

Chandrasekhar, S. and Kendall, P. C. (1957). On force-free magnetic fields, *Ap. J.* **126**: 457–460.

Chandrasekhar, S. and Woltjer, L. (1958). On force-free magnetic fields, *Proc. Nat. Acad. Sci.* **44**(4): 285–289.

Chekhlov, A., Orszag, S. A., Sukoriansky, S., Galperin, B. and Staroselsky, I. (1994). Direct numerical simulation tests of eddy viscosity in two dimensions, *Phys. Fluids* **6**(7): 2548–2550.

Chiuderi, C. and Van Hoven, G. (1979). The dynamics of filament formation: the thermal instability in a sheared magnetic field, *Ap. J.* **232**: L69–L73.

Chiueh, T. and Zweibel, E. G. (1987). The structure and dissipation of forced current sheets in the solar atmosphere, *Ap. J.* **317**: 900–917.

Chollet, J. and Lesieur, M. (1981). Parameterization of small scales of three-dimensional isotropic turbulence utilizing spectral closures, *J. Atmos. Sci.* **38**: 2747–2757.

Choudhuri, A. R. (1986). Magnetic helicity as a constraint on coronal dissipation, *in* A. I. Poland (ed.), *Coronal and Prominence Plasmas*, Vol. CP-2442 of *NASA Conference Publications*, pp. 451–456.

Clark, Jr., A. (1964). Production and dissipation of magnetic energy by differential fluid motions, *Phys. Fluids* **7**(8): 1299–1305.

Cowling, T. G. (1976). *Magnetohydrodynamics*, Monographs on Astronomical Subjects, Adam Hilger, Bristol.

Curle, N. and Davies, H. J. (1968). *Modern Fluid Dynamics*, Vol. 1, Van Nostrand, London.

Dahlburg, R. B., Dahlburg, J. P. and Mariska, J. T. (1988). Helical magnetohydrodynamic turbulence and the coronal heating problem, *Astron. Astrophys.* **198**: 300–310.

Davis, R. and Cox, A. N. (1991). Solar neutrino experiments, *in* A. N. Cox, W. C. Livingston and M. S. Matthews (eds), *Solar Interior and Atmosphere*, The University of Arizona Press, Tucson, pp. 51–85.

Davis, R., Lande, K., Lee, C. K., Cleveland, B. T. and Ullman, J. (1990). Report on the Homestake chlorine solar neutrino experiment, *in* G. Berthomieu and M. Cribier (eds), *Inside the Sun*, Kluwer Academic Publishers, Dordrecht, pp. 171–177.

Deubner, F.-L. (1975). Observations of low wavenumber nonradial eigenmodes of the sun, *Astron. Astrophys.* **44**: 371–375.

Dixon, A. M., Berger, M. A., Browning, P. K. and Priest, E. R. (1989). A generalisation of the Woltjer minimum-energy principle, *Astron. Astrophys.* **225**: 156–166.

Domaradzki, J. A., Metcalfe, R. W., Rogallo, R. S. and Riley, J. J. (1987). Analysis of subgrid-scale eddy viscosity with use of results from direct numerical simulations, *Phys. Rev. Lett.* **58**(6): 547–550.

Duvall, Jr., T. L., Harvey, J. W., Libbrecht, K. G., Popp, B. D. and Pomerantz, M. A. (1988). Frequencies of solar p-mode oscillations, *Ap. J.* **324**: 1158–1171.

Dziembowski, W. A. and Goode, P. R. (1990). The internal rotation and magnetism of the sun from its oscillations, *in* A. N. Cox, W. C. Livingston and M. S. Matthews (eds), *Solar Interior and Atmosphere*, The University of Arizona Press, Tucson, pp. 501–518.

Eddington, A. S. (1920). The internal constitution of stars, *Nature* **106**: 14–20.

Eliezer, Y. and Eliezer, S. (1989). *The Fourth State of Matter: An Introduction to the Physics of Plasma*, Adam Hilger, Bristol.

Faber, V., White, A. B. and Wing, G. M. (1982). An analysis of Taylor's theory of toroidal plasma relaxation, *J. Math. Phys.* **23**(8): 1524–1537.

Frazier, E. N. (1968). A spatio-temporal analysis of velocity fields in the solar photosphere, *Z. Astrophys.* **68**(5): 345–346.

Freidberg, J. P. (1982). Ideal magnetohydrodynamic theory of magnetic fusion systems, *Rev. Mod. Phys.* **54**(3): 801–902.

Freidberg, J. P. (1987). *Ideal Magnetohydrodynamics*, Modern Perspectives in Energy, Plenum Press, New York.

Frisch, U., Pouquet, A., Léorat, J. and Mazure, A. (1975). Possibility of an inverse cascade of magnetic helicity in magnetohydrodynamic turbulence, *J. Fluid Mech.* **68**(4): 769–778.

Fyfe, D. and Montgomery, D. (1976). High-beta turbulence in two-dimensional magnetohydrodynamics, *J. Plasma Phys.* **16**(2): 181–191.

Fyfe, D., Joyce, G. and Montgomery, D. (1977a). Magnetic dynamo action in two-dimensional turbulent magneto-hydrodynamics, *J. Plasma Phys.* **17**(2): 317–335.

Fyfe, D., Montgomery, D. and Joyce, G. (1977b). Dissipative, forced turbulence in two-dimensional magnetohydrodynamics, *J. Plasma Phys.* **17**(3): 369–398.

Galeev, A. A., Rosner, R., Serio, S. and Vaiana, G. S. (1981). Dynamics of coronal structures: magnetic field-related heating and loop energy balance, *Ap. J.* **243**: 301–308.

Ghosh, S., Matthaeus, W. H. and Montgomery, D. (1988). The evolution of cross-helicity in driven/dissipative two-dimensional magnetohydrodynamics, *Phys. Fluids* **31**(8): 2171–2184.

Golub, L., Herant, M., Kalata, K., Lovas, I., Nystrom, G., Pardo, F., Spiller, E. and Wilczynski, J. (1990). Sub-arcsecond observations of the solar X-ray corona, *Nature* **344**: 842–844.

Golub, L., Maxson, C., Rosner, R., Serio, S. and Vaiana, G. S. (1980). Magnetic fields and coronal heating, *Ap. J.* **238**: 343–348.

Golub, L., Zirin, H. and Wang, H. (1994). The roots of coronal structure in the sun's surface, *Solar Phys.* **153**: 179–198.

Gómez, D. O. (1990). Heating of the solar corona, *Fund. Cosm. Phys.* **14**(2–3): 131–233.

Gómez, D. O. and Ferro Fontán, C. (1992). Development of magnetohydrodynamic turbulence in coronal loops, *Ap. J.* **394**: 662–669.

Gómez, D. O., Martens, P. C. H. and Golub, L. (1993a). Normal incidence X-ray telescope power spectra of X-ray emission from solar active regions I. Observations, *Ap. J.* **405**(2): 767.

Gómez, D. O., Martens, P. C. H. and Golub, L. (1993b). NIXT power spectra of X-ray emission from solar active regions II. Theory, *Ap. J.* **405**(2): 773–781.

Goossens, M. (1991). MHD waves and wave heating in nonuniform plasmas, *in* E. R. Priest and A. W. Hood (eds), *Advances in Solar System Magnetohydrodynamics*, Cambridge University Press, pp. 137–172.

Gosling, J. T. (1992). Coronal mass ejections: the link between solar and geomagnetic activity, *Phys. Fluids B* **5**(7 Part 2): 2638–2645.

Gosling, J. T. (1993). The solar flare myth, *J. Geophys. Res.* **98**(A11): 18937–18949.

Grappin, R., Frisch, U., Léorat, J. and Pouquet, A. (1982). Alfvénic fluctuations as asymptotic states of MHD turbulence, *Astron. Astrophys.* **105**: 6–14.

Grappin, R., Pouquet, A. and Léorat, J. (1983). Dependence of MHD turbulence spectra on the velocity field—magnetic field correlation, *Astron. Astrophys.* **126**: 51–58.

Green, B. J. (1981). The next generation tokamaks, *in* R. D. Gill (ed.), *Plasma Physics and Nuclear Fusion Research*, Academic Press, London, chapter 18, pp. 416–431.

Hara, H., Tsuneta, S., Lemen, J. R., Acton, L. W. and McTiernan, J. M. (1992). High-temperature plasmas in active regions observed with the soft X-ray telescope aboard Yohkoh, *Publ. Ast. Soc. Japan* **44**(5): L135–L140.

Hasegawa, A. (1985). Self-organization processes in continuous media, *Adv. Phys.* **34**(1): 1–42.

Heyvaerts, J. (1990). Coronal heating by D.C. currents, *in* E. R. Priest and V. Krishan (eds), *Basic Plasma Processes on the Sun*, Vol. 142 of *I.A.U. Symposium*, International Astronomical Union, Kluwer, Dordrecht, pp. 207–214.

Heyvaerts, J. and Priest, E. R. (1983). Coronal heating by phase-mixed shear Alfvén waves, *Astron. Astrophys.* **117**(2): 220–234.

Heyvaerts, J. and Priest, E. R. (1984). Coronal heating by reconnection in DC current systems. A theory based on Taylor's hypothesis, *Astron. Astrophys.* **137**(1): 63–78.

Heyvaerts, J. and Priest, E. R. (1992). A self-consistent turbulent model for solar coronal heating, *Ap. J.* **390**(1): 297–308.

Heyvaerts, J., Priest, E. R. and Rust, D. M. (1977). An emerging flux model for the solar flare phenomenon, *Ap. J.* **216**: 123–137.

Hollweg, J. V. (1978). Fast wave evanescence in the solar corona, *Geophys. Res. Lett.* **5**(8): 731–734.

Hollweg, J. V. (1983). Coronal heating by waves, *in* M. Neugebauer (ed.), *Solar Wind Five*, Vol. 2280 of *NASA Conference Publications*, pp. 5–21.

Hollweg, J. V. (1984a). Alfvénic resonant cavities in the solar atmosphere: Simple aspects, *Solar Phys.* **91**(2): 269–288.

Hollweg, J. V. (1984b). Resonances of coronal loops, *Ap. J.* **277**: 392–403.

Hollweg, J. V. (1987). Resonance absorption of magnetohydrodynamic surface waves: Physical discussion, *Ap. J.* **312**: 880–885.

Hollweg, J. V. (1990). Heating of the solar corona, *Comp. Phys. Rep.* **12**(4): 205–232.

Hollweg, J. V. and Yang, G. (1988). Resonance absorption of compressible magnetohydrodynamic waves at thin "surfaces", *J. Geophys. Res.* **93**(A6): 5423–5436.

Holzer, T. E. (1979). The solar wind and related astrophysical phenomena, *in* C. F. Kennel, L. J. Lanzerotti and E. N. Parker (eds), *Solar System Plasma Physics*, North Holland, pp. 101–176.

Hones, Jr., E. W. (ed.) (1984). *Magnetic Reconnection in Space and Laboratory Plasmas*, Vol. 30 of *Geophysical Monograph Series*, American Geophysical Union, Washington.

Hossain, M., Matthaeus, W. H. and Montgomery, D. (1983). Long-time states of inverse cascades in the presence of a maximum length scale, *J. Plasma Phys.* **30**(3): 479–493.

Hossain, M., Vahala, G. and Montgomery, D. (1985). Forced magnetohydrodynamic turbulence in a uniform external magnetic field, *Phys. Fluids* **28**(10): 3074–3081.

House, L. L. and Berger, M. A. (1987). The ejection of helical field structures through the outer corona, *Ap. J.* **323**: 406–413.

Inverarity, G. W. and Priest, E. R. (1993a). Turbulent coronal heating in a twisted flux tube, *in* P. Hennequin and M. A. Dubois (eds), *Magnetic Turbulence and Transport*, Proceedings of Cargèse Workshop July 1992, Editions de Physique, pp. 229–234.

Inverarity, G. W. and Priest, E. R. (1993b). Self-consistent turbulent coronal heating, *in* M. F. Heyn, W. Kernbichler and K. Biernat (eds), *Current Topics in Astrophysical and Fusion Plasma Research*, Proceedings of International Workshop on Plasma Physics February 1993, dbv-Verlag Graz, pp. 210–215.

Inverarity, G. W. and Priest, E. R. (1994). Turbulent coronal heating by Alfvén waves, *in* M. F. Heyn, W. Kernbichler and K. Biernat (eds), *Current Topics in Astrophysical and Fusion Plasma Research*, Proceedings of International Workshop on Plasma Physics February 1994, dbv-Verlag Graz, pp. 109–114.

Inverarity, G. W. and Priest, E. R. (1995a). Turbulent coronal heating II. Twisted flux tube, *Astron. Astrophys.* **296**(2): 395–404.

Inverarity, G. W. and Priest, E. R. (1995b). Turbulent coronal heating III. Wave heating in coronal loops, *Astron. Astrophys.* In press.

Inverarity, G. W., Priest, E. R. and Heyvaerts, J. (1995). Turbulent coronal heating I. Sheared arcade, *Astron. Astrophys.* **293**(3): 913–926.

Ionson, J. A. (1978). Resonant absorption of Alfvénic surface waves and the heating of solar coronal loops, *Ap. J.* **226**: 650–673.

Iroshnikov, P. S. (1964). Turbulence of a conducting fluid in a strong magnetic field, *Sov. Astron.—AJ* **7**(4): 566–571.

Jeffreys, H. (1931). *Cartesian Tensors*, Cambridge University Press.

Jensen, T. H. and Chu, M. S. (1984). Current drive and helicity injection, *Phys. Fluids* **27**(12): 2881–2885.

Kadomtsev, B. B. (1988). Evolution of the tokamak, *Plasma Phys. Contr. Fusion* **30**(14): 2031–2049.

Kappraff, J. M. and Tataronis, J. A. (1977). Resistive effects on Alfvén wave heating, *J. Plasma Phys.* **18**(2): 209–226.

Keinigs, R. K. (1983). A new interpretation of the alpha effect, *Phys. Fluids* **26**(9): 2558–2560.

Kippenhahn, R. (1994). *Discovering the Secrets of the Sun*, Wiley, Chichester.

Kolmogorov, A. N. (1941). The local structure of turbulence in incompressible viscous fluid for very large Reynolds number, *Dokl. Akad. Nauk. SSSR* **30**: 301–305.

Kraichnan, R. H. (1965). Inertial-range spectrum of hydromagnetic turbulence, *Phys. Fluids* **8**(7): 1385–1387.

Kraichnan, R. H. (1967). Inertial ranges in two-dimensional turbulence, *Phys. Fluids* **10**(7): 1417–1423.

Kraichnan, R. H. (1971). Inertial-range transfer in two- and three-dimensional turbulence, *J. Fluid Mech.* **47**(3): 525–535.

Kraichnan, R. H. (1973). Helical turbulence and absolute equilibrium, *J. Fluid Mech.* **59**(4): 745–752.

Kraichnan, R. H. (1976). Eddy viscosity in two and three dimensions, *J. Atmos. Sci.* **33**: 1521–1536.

Kraichnan, R. H. and Montgomery, D. (1980). Two-dimensional turbulence, *Rep. Prog. Phys.* **43**: 547–619.

Kulsrud, R. M. (1984). MHD description of a plasma, *in* A. A. Galeev and R. N. Sudan (eds), *Basic Plasma Physics — I: Handbook of Plasma Physics*, Vol. 1, North-Holland, Amsterdam.

Kuperus, M., Ionson, J. A. and Spicer, D. S. (1981). On the theory of coronal heating mechanisms, *Ann. Rev. Astron. Astrophys.* **19**: 7–40.

Landau, L. D. and Lifschitz, E. M. (1987). *Fluid Mechanics*, Vol. 6 of *Course of Theoretical Physics*, 2nd edn, Pergamon Press, Oxford.

Laurence, P. and Avellaneda, M. (1991). On Woltjer's variational principle for force-free fields, *J. Math. Phys.* **32**(5): 1240–1253.

Lees, D. J. (1981). Stellarator confinement devices, *in* R. D. Gill (ed.), *Plasma Physics and Nuclear Fusion Research*, Academic Press, London, chapter 16, pp. 386–399.

Leibacher, J. and Stein, R. F. (1971). A new description of the solar five-minute oscillation, *Astrophys. Lett.* **7**(3): 191–192.

Leighton, R. B., Noyes, R. W. and Simon, G. W. (1962). Velocity fields in the solar atmosphere I. Preliminary report, *Ap. J.* **135**: 474–499.

Leith, C. E. (1971). Atmospheric predictability and two-dimensional turbulence, *J. Atmos. Sci* **28**: 145–161.

Léorat, J., Pouquet, A. and Frisch, U. (1981). Fully developed MHD turbulence near critical magnetic Reynolds number, *J. Fluid Mech.* **104**: 419–443.

Lesieur, M. (1990). *Turbulence in Fluids*, Vol. 1 of *Fluid Mechanics and its Applications*, 2nd edn, Kluwer, Dordrecht.

Leslie, D. C. (1973). *Developments in the Theory of Turbulence*, Oxford University Press.

Libbrecht, K. G. and Woodard, M. F. (1990). Solar-cycle effects on solar oscillation frequencies, *Nature* **345**: 779–782.

Liewer, P. C. (1985). Measurements of microturbulence in tokamaks and comparisons with theories of turbulence and anomalous transport, *Nucl. Fus.* **25**(5): 543–621.

Lighthill, M. J. (1958). *Introduction to Fourier analysis and generalised functions*, Cambridge monographs on mechanics and applied mathematics, Cambridge University Press.

Lin, R. P., Schwartz, R. A., Kane, S. R., Pelling, R. M. and Hurley, K. C. (1984). Solar hard X-ray microflares, *Ap. J.* **283**: 421–425.

Longcope, D. W. and Sudan, R. N. (1992). Quasi-static evolution of coronal magnetic fields, *Ap. J.* **384**: 305–318.

Lorrain, P., Corson, D. R. and Lorrain, F. (1988). *Electromagnetic fields and waves*, 3rd edn, Freeman.

Low, B. C. (1994). Magnetohydrodynamic processes in the solar corona: Flares, coronal mass ejections and magnetic helicity, *Phys. Plasmas* **1**(5): 1684–1690.

Low, B. C. and Wolfson, R. (1988). Spontaneous formation of electric current sheets and the origin of solar flares, *Ap. J.* **324**(1): 574–581.

Lundquist, S. (1951). On the stability of magneto-hydrostatic fields, *Phys. Rev.* **83**(2): 307–311.

Marsch, E. (1994). Theoretical models for the solar wind, *Adv. Space Res.* **14**(4): 103–121.

Martens, P. C. and Gómez, D. O. (1992). Spatial power-spectra from Yokhoh soft X-ray images, *Publ. Ast. Soc. Jap.* **44**(5): 187–191.

Matthaeus, W. H. and Goldstein, M. L. (1982). Measurement of the rugged invariants of magneto-hydrodynamic turbulence in the solar wind, *J. Geophys. Res.* **87**(A8): 6011–6028.

Matthaeus, W. H. and Montgomery, D. (1980). Selective decay hypothesis at high mechanical and magnetic Reynolds numbers, *Ann. N.Y. Acad. Sci.* pp. 203–222.

Matthaeus, W. H. and Zhou, Y. (1989). Extended inertial range phenomenology of magnetohydrodynamic turbulence, *Phys. Fluids B* **1**(9): 1929–1931.

Matthaeus, W. H., Goldstein, M. L. and Lantz, S. R. (1986). The alpha dynamo parameter and measurability of helicities in magnetohydrodynamic turbulence, *Phys. Fluids* **29**(5): 1504–1508.

Matthaeus, W. H., Goldstein, M. L. and Roberts, D. A. (1990). Evidence for the presence of quasi-two-dimensional nearly incompressible fluctuations in the solar wind, *J. Geophys. Res.* **95**(A12): 20673–20683.

McComb, W. D. (1990). *The Physics of Fluid Turbulence*, Oxford Engineering Science Series, Oxford University Press.

Mein, P. (1966). The macroscopic velocity field in the solar atmosphere, resulted from the measurements of the displacements of Fraunhofer lines, *Ann. Astrophys. (France)* **29**(3): 153–191.

Mihalas, D., Däppen, W. and Hummer, D. G. (1988). The equation of state for stellar envelopes II. Algorithm and selected results, *Ap. J.* **331**: 815–825.

Mikić, Z., Schnack, D. D. and Van Hoven, G. (1989). Creation of current filaments in the solar corona, *Ap. J.* **338**: 1148–1157.

Millionshtchikov, M. (1941). On the theory of homogeneous isotropic turbulence, *C. R. Acad. Sci. URSS* **32**: 615–618.

Moffatt, H. K. (1978). *Magnetic Field Generation in Electrically Conducting Fluids*, Cambridge Monographs on Mechanics and Applied Mathematics, Cambridge University Press.

Montgomery, D. (1977). Implications of Navier-Stokes turbulence theory for plasma turbulence, *Proc. Indian Acad. Sci.* **86A**(2): 87–110.

Montgomery, D. (1982). Major disruptions, inverse cascades, and the Strauss equations, *Physica Scripta* **T2/1**: 83–88.

Montgomery, D. (1990). Relaxed states of MHD turbulence: Minimum dissipation or minimum energy?, *in* E. R. Priest and V. Krishan (eds), *Basic Plasma Processes on the Sun*, Vol. 142 of *I.A.U. Symposium*, International Astronomical Union, Kluwer, Dordrecht, pp. 207–214.

Montgomery, D. (1992). Magnetohydrodynamic stability thresholds as a function of Hartmann number and pinch ratio, *Plasma Phys. Contr. Fusion* **34**(6): 1157–1162.

Montgomery, D. (1993). Hartmann, Lundquist, and Reynolds: The role of dimensionless numbers in nonlinear magnetofluid behavior, *Plasma Phys. Contr. Fusion* **35**: B105–B113.

Montgomery, D. and Phillips, L. (1988). Minimum dissipation rates in magnetohydrodynamics, *Phys. Rev. A* **38**(6): 2953–2964.

Montgomery, D. and Phillips, L. (1989). MHD turbulence: relaxation processes and variational principles, *Physica D* **37**: 215–226.

Montgomery, D. and Turner, L. (1981). Anisotropic magnetohydrodynamic turbulence in a strong external magnetic field, *Phys. Fluids* **24**(5): 825–831.

Montgomery, D. and Turner, L. (1982). Two-and-a-half-dimensional magnetohydrodynamic turbulence, *Phys. Fluids* **25**(2): 345–349.

Montgomery, D., Phillips, L. and Theobald, M. L. (1989). Helical, dissipative, magnetohydrodynamic states with flow, *Phys. Rev. A* **40**(3): 1515–1523.

Montgomery, D., Turner, L. and Vahala, G. (1978). Three-dimensional magnetohydrodynamic turbulence in cylindrical geometry, *Phys. Fluids* **21**(5): 757–764.

Nakahata, M. and the Kamiokande II Collaboration (1990). The Kamiokande solar neutrino experiment, *in* G. Berthomieu and M. Cribier (eds), *Inside the Sun*, Kluwer Academic Publishers, Dordrecht, pp. 179–186.

Oboukhov, A. M. (1941). On the distribution of energy in the spectrum of turbulent flow, *C.R. Acad. Sci. URSS* **32**: 19.

O'Brien, M. R. and Robinson, D. C. (1993). Tokamak experiments, *in* R. Dendy (ed.), *Plasma Physics: An Introductory Course*, Culham Laboratory, Cambridge University Press, pp. 189–208.

Ogawara, Y., Acton, L. W., Bentley, R. D., Bruner, M. E., Culhane, J. L., Hiei, E., Hirayama, T., Hudson, H. S., Kosugi, T., Lemen, J. R., Strong, K. R., Tsuneta, S., Uchida, Y., Watanabe, T. and Yoshimori, M. (1992). The status of Yohkoh in orbit: An introduction to the initial scientific results, *Publ. Ast. Soc. Jap.* **44**(5): L41–L44.

Ogura, Y. (1963). A consequence of the zero-fourth-cumulant approximation in the decay of isotropic turbulence, *J. Fluid Mech.* **16**(1): 33–40.

Orszag, S. A. (1970). Analytical theories of turbulence, *J. Fluid Mech.* **41**(2): 363–386.

Orszag, S. A. (1977). Lectures on the statistical theory of turbulence, *in* R. Balian and J. L. Peube (eds), *Fluid Dynamics*, Les Houches Summer School of Theoretical Physics, Gordon and Breach, pp. 235–374.

Orszag, S. A. and Kruskal, M. D. (1968). Formulation of the theory of turbulence, *Phys. Fluids* **11**(1): 43–60.

Orszag, S. A. and Tang, C.-M. (1978). Small-scale structure of two-dimensional magnetohydrodynamic turbulence, *J. Fluid Mech.* **90**: 129–143.

Oughton, S., Priest, E. R. and Matthaeus, W. H. (1994). The influence of a mean magnetic field on 3-dimensional magnetohydrodynamic turbulence, *J. Fluid Mech.* **280**: 95–117.

Parker, E. N. (1958). Dynamics of the interplanetary gas and magnetic fields, *Ap. J.* **128**: 664–676.

Parker, E. N. (1972). Topological dissipation and the small-scale fields in turbulent gases, *Ap. J.* **174**: 499–510.

Parker, E. N. (1982). The rapid dissipation of magnetic fields in highly conducting fluids, *Geophys. Astrophys. Fluid Dyn.* **22**: 195–218.

Parker, E. N. (1983a). Magnetic neutral sheets in evolving fields I. General theory, *Ap. J.* **264**: 635–641.

Parker, E. N. (1983b). Magnetic neutral sheets in evolving fields II. Formation of the solar corona, *Ap. J.* **264**: 642–647.

Parker, E. N. (1983c). The hydrodynamics of magnetic nonequilibrium, *Geophys. Astrophys. Fluid Dyn.* **24**: 79–108.

Parker, E. N. (1987a). Stimulated dissipation of magnetic discontinuities and the origin of solar flares, *Solar Phys.* **111**(2): 297–308.

Parker, E. N. (1987b). Why do stars emit X-rays?, *Physics Today* **40**(7): 36–42.

Parker, E. N. (1988). Nanoflares and the solar X-ray corona, *Ap. J.* **330**: 474–479.

Parker, E. N. (1993). Resistive dissipation and magnetic field topology in the stellar corona, *Ap. J.* **407**: 342–346.

Phan, T. D. and Sonnerup, B. U. O. (1990). MHD stagnation-point flows at a current sheet including viscous and resistive effects: general two-dimensional solutions, *J. Plasma Phys.* **44**(3): 525–546.

Poedts, S., Kerner, W. and Goossens, M. (1989). Alfvén wave heating in resistive MHD, *J. Plasma Phys.* **42**(1): 27–58.

Politano, H., Pouquet, A. and Sulem, P. L. (1989). Inertial ranges and resistive instabilities in two-dimensional magnetohydrodynamic turbulence, *Phys. Fluids B* **1**(12): 2330–2339.

Pouquet, A. (1978). On two-dimensional magnetohydrodynamic turbulence, *J. Fluid Mech.* **88**(1): 1–16.

Pouquet, A. and Patterson, G. S. (1978). Numerical simulation of helical magnetohydrodynamic turbulence, *J. Fluid Mech.* **85**(2): 305–323.

Pouquet, A., Frisch, U. and Léorat, J. (1976). Strong MHD helical turbulence and the nonlinear dynamo effect, *J. Fluid Mech.* **77**(2): 321–354.

Pouquet, A., Meneguzzi, M. and Frisch, U. (1986). Growth of correlations in magnetohydrodynamic turbulence, *Phys. Rev. A* **33**(6): 4266–4276.

Priest, E. R. (1978). The structure of coronal loops, *Solar Phys.* **58**: 57–87.

Priest, E. R. (1982). *Solar Magnetohydrodynamics*, Vol. 21 of *Geophysical and Astrophysical Monographs*, Reidel, Dordrecht.

Priest, E. R. (1984). Magnetic reconnection in the sun, *in* E. W. Hones, Jr. (ed.), *Magnetic Reconnection in Space and Laboratory Plasmas*, Vol. 30 of *Geophysical Monograph Series*, American Geophysical Union, Washington, pp. 63–78.

Priest, E. R. (1985). The magnetohydrodynamics of current sheets, *Rep. Prog. Phys* **48**: 955–1090.

Priest, E. R. (1991). The formation of current sheets and coronal heating, *in* P. Ulmschneider, E. Priest and R. Rosner (eds), *Mechanisms of Chromospheric and Coronal Heating*, Springer-Verlag, Berlin.

Priest, E. R. (1992a). *Proceedings 26th ESLAB Symposium ESA SP-346*, p. 13.

Priest, E. R. (1992b). Basic magnetic configuration and energy supply processes for an interacting flux model of eruptive solar flares, *in* Z. Švestka, B. V. Jackson and M. E. Machado (eds), *Eruptive Solar Flares*, Vol. 399 of *Lecture Notes in Physics*, Springer-Verlag, Berlin, pp. 15–32.

Priest, E. R. (1993). Coronal heating mechanisms, *in* J. F. Linsky and S. Serio (eds), *Physics of Solar and Stellar Coronae*, Vol. 184 of *Astrophysics and Space Science Library*, Kluwer, Dordrecht, pp. 515–532.

Priest, E. R. and Hood, A. W. (eds) (1991). *Advances in Solar System Magnetohydrodynamics*, Cambridge University Press.

Priest, E. R. (ed.) (1981). *Solar Flare Magnetohydrodynamics*, Vol. 1 of *The Fluid Mechanics of Astrophysics and Geophysics*, Gordon and Breach, New York.

Priest, E. R., Hood, A. W. and Anzer, U. (1989). A twisted flux-tube model for solar prominences I. General properties, *Ap. J.* **344**: 1010–1025.

Proctor, R. A. (1899). *The Orbs Around Us*, Longmans, Green & Co., London.

Proudman, I. and Reid, W. H. (1954). On the decay of a normally distributed and homogeneous turbulent velocity field, *Phil. Trans. Roy. Soc.* **A247**: 163–189.

Reiman, A. (1981). Taylor relaxation in a torus of arbitrary aspect ratio and cross section, *Phys. Fluids* **24**(5): 956–963.

Riyopoulos, S., Bondeson, A. and Montgomery, D. (1982). Relaxation toward states of minimum energy in a compact torus, *Phys. Fluids* **25**(1): 107–115.

Roberts, P. H. (1967). *An Introduction to Magnetohydrodynamics*, Longmans, London.

Robertson, H. P. (1940). The invariant theory of isotropic turbulence, *Proc. Cam. Phil. Soc.* **36**: 209–223.

Robinson, D. (1981). Pinch and tokamak confinement devices, *in* R. D. Gill (ed.), *Plasma Physics and Nuclear Fusion Research*, Academic Press, London, chapter 15, pp. 358–383.

Rogallo, R. S. and Moin, P. (1984). Numerical simulations of turbulent flows, *Ann. Rev. Fluid Mech.* **16**: 99–137.

Rose, H. A. and Sulem, P. L. (1978). Fully developed turbulence and statistical mechanics, *J. de Phys.* **39**(5): 441–484.

Rosner, R., Golub, L., Coppi, B. and Vaiana, G. S. (1978). Heating of coronal plasma by anomalous current dissipation, *Ap. J.* **222**: 317–332.

Rosner, R., Tucker, W. H. and Vaiana, G. S. (1978). Dynamics of the quiescent solar corona, *Ap. J.* **220**: 643–665.

Roudier, T. and Muller, R. (1986). Structure of the solar granulation, *Solar Phys.* **107**: 11–26.

Rowlands, G. (1981). Mirror devices, *in* R. D. Gill (ed.), *Plasma Physics and Nuclear Fusion Research*, Academic Press, London, chapter 17, pp. 401–413.

Roxburgh, I. W. (1985). Present problems of the solar interior, *Solar Phys.* **100**: 21–51.

Saba, J. L. R. and Strong, K. T. (1991). Coronal dynamics of a quiescent active region, *Ap. J.* **375**: 789–799.

Sakurai, T. and Levine, R. H. (1981). Generation of coronal electric currents due to convective motions on the photosphere, *Ap. J.* **248**: 817–829.

Schoenberg, K. F., Moses, R. W. J. and Hagenson, R. L. (1984). Plasma resistivity in the presence of a reversed-field pinch dynamo, *Phys. Fluids* **27**(7): 1671–1676.

Schwarz, S. J. and Leroy, B. (1982). Propagation of waves in an atmosphere in the presence of a magnetic field, *Astron. Astrophys.* **112**: 93–103.

Seehafer, N. (1994). Alpha effect in the solar atmosphere, *Astron. Astrophys.* **284**: 593–598.

Shan, X., Montgomery, D. and Chen, H. (1991). Nonlinear magnetohydrodynamics by Galerkin-method computation, *Phys. Rev. A* **44**(10): 6800–6818.

Shebalin, J. V., Matthaeus, W. H. and Montgomery, D. (1983). Anisotropy in MHD turbulence due to a mean magnetic field, *J. Plasma Phys.* **29**(3): 525–547.

Shercliff, J. A. (1965). *A Textbook of Magnetohydrodynamics*, Pergamon Press, Oxford.

Song, Y. S. and Lysak, R. L. (1989). Evaluation of twist helicity of flux transfer event flux tubes, *J. Geophys. Res.* **94**(A5): 5273–5281.

Stanišić, M. M. (1988). *The Mathematical Theory of Turbulence*, 2nd edn, Springer-Verlag, New York.

Stephani, H. (1989). *Differential Equations: Their solution using symmetries*, Cambridge University Press.

Storer, R. G. (1983). Spectrum of an exactly soluble resistive magnetohydrodynamic model, *Plasma Phys.* **25**(11): 1279–1282.

Strauss, H. R. (1976). Nonlinear, three-dimensional magnetohydrodynamics of noncircular tokamaks, *Phys. Fluids* **19**(1): 134–140.

Strauss, H. R. and Otani, N. F. (1988). Current sheets in the solar corona, *Ap. J.* **326**: 418–424.

Stribling, T. and Matthaeus, W. H. (1990). Statistical properties of ideal three-dimensional magnetohydrodynamics, *Phys. Fluids B* **2**(9): 1979–1988.

Stribling, T. and Matthaeus, W. H. (1991). Relaxation processes in a low-order three-dimensional magnetohydrodynamic model, *Phys. Fluids B* **3**(8): 1848–1864.

Stribling, T., Matthaeus, W. H. and Ghosh, S. (1994). Nonlinear decay of magnetic helicity in magnetohydrodynamic turbulence with a mean magnetic field, *J. Geophys. Res.* **99**(A2): 2567–2576.

Stuart, J. T. (1958). On the non-linear mechanics of hydrodynamic stability, *J. Fluid Mech.* **4**: 1–21.

Sturrock, P. A. (1989). The role of eruption in solar flares, *Solar Phys.* **121**(1/2): 387–397.

Sturrock, P. A. and Uchida, Y. (1981). Coronal heating by stochastic magnetic pumping, *Ap. J.* **246**: 331–336.

Sturrock, P. A., Kaufman, P., Moore, R. L. and Smith, D. E. (1984). Energy release in solar flares, *Solar Phys.* **94**: 341–357.

Tatsumi, T. and Yanase, S. (1981). The modified cumulant expansion for two-dimensional isotropic turbulence, *J. Fluid Mech.* **110**: 475–496.

Taylor, J. B. (1974). Relaxation of toroidal plasma and generation of reverse magnetic fields, *Phys. Rev. Lett.* **33**(19): 1139–1141.

Taylor, J. B. (1986). Relaxation and magnetic reconnection in plasmas, *Rev. Mod. Phys.* **58**(3): 741–763.

Temple, G. F. J. (1960). *Cartesian Tensors: An Introduction*, Monographs on physical subjects, Methuen, London.

Tennekes, H. and Lumley, J. L. (1972). *A First Course in Turbulence*, The MIT Press, Cambridge, Massachusetts.

Ting, A. C., Matthaeus, W. H. and Montgomery, D. (1986). Turbulent relaxation processes in magnetohydrodynamics, *Phys. Fluids* **29**(10): 3261–3274.

Todd, T. N. (1993). How to build a tokamak, *in* R. Dendy (ed.), *Plasma Physics: An Introductory Course*, Culham Laboratory, Cambridge University Press, pp. 443–473.

Tucker, W. H. (1973). Heating of the solar active regions by magnetic energy dissipation: the steady state case, *Ap. J.* **186**: 285–289.

Ulmschneider, P., Priest, E. R. and Rosner, R. (eds) (1991). *Mechanisms of Chromospheric and Coronal Heating*, Springer-Verlag, Berlin.

Ulrich, R. K. (1970). The five minute oscillations of the solar surface, *Ap. J.* **162**: 993–1002.

Ulrich, R. K. and Cox, A. N. (1991). The computation of standard solar models, *in* A. N. Cox, W. C. Livingston and M. S. Matthews (eds), *Solar Interior and Atmosphere*, The University of Arizona Press, Tucson, pp. 162–191.

Vaiana, G. S. and Rosner, R. (1978). Recent advances in coronal physics, *Ann. Rev. Astron. Astrophys.* **16**: 393–428.

Vaiana, G. S., Krieger, A. S. and Timothy, A. F. (1973). Identification and analysis of structures in the corona from X-ray photography, *Solar Phys.* **32**(1): 81–116.

van Ballegooijen, A. A. (1985). Electric currents in the solar corona and the existence of magnetostatic equilibrium, *Ap. J.* **298**: 421–430.

van Ballegooijen, A. A. (1986). Cascade of magnetic energy as a mechanism of coronal heating, *Ap. J.* **311**: 1001–1014.

van Ballegooijen, A. A. (1988). Force free field and coronal heating. I. The formation of current sheets, *Geophys. Astrophys. Fluid Dyn.* **41**(3–4): 181–211.

Van Hoven, G. (1981). Simple-loop flares: magnetic instabilities, *in* E. R. Priest (ed.), *Solar Flare Magnetohydrodynamics*, Vol. 1 of *The Fluid Mechanics of Astrophysics and Geophysics*, Gordon and Breach, New York, pp. 217–275.

Van Hoven, G. (1993). The generation of solar magnetic activity: photospheric flows and coronal fields, *Adv. Space Res.* **13**(9): 15–22.

Vekstein, G. E. (1987a). The theory of magnetic coronal heating, *Astron. Astrophys.* **182**(2): 324–328.

Vekstein, G. E. (1987b). *Sov. J. Plasma Phys.* **13**: 263.

Vekstein, G. E. and Priest, E. R. (1992). Magnetohydrodynamic equilibria and cusp formation at an X-type neutral line by footpoint shearing, *Ap. J.* **384**(1): 333–340.

Vekstein, G. E., Priest, E. R. and Steele, C. D. C. (1993). On the problem of magnetic coronal heating by turbulent relaxation, *Ap. J.* **417**: 781–789.

Vekstein, G. E., Priest, E. R. and Wolfson, R. (1994). Coronal magnetic field evolution under reconnective relaxation, *Space Science Rev.* **70**: 303–307.

Vekstein, G., Priest, E. R. and Amari, T. (1991). Formation of current sheets in force-free magnetic fields, *Astron. Astrophys.* **243**: 492–500.

Venneri, F., Bowman, C. and Jameson, R. (1993). Accelerators address nuclear waste problems, *Physics World* **6**(8): 40–45.

Walijeski, K., Dere, K. P. and Moses, D. (1992). Observational tests of coronal heating models, Vol. ESA SP-348. Proceedings of the First SOHO Workshop, Annapolis, Maryland, USA.

Watson, G. N. (1958). *A Treatise on the Theory of Bessel Functions*, 2nd edn, Cambridge University Press.

Wentzel, D. G. (1979). Hydromagnetic surface waves on cylindrical fluxtubes, *Astron. Astrophys.* **76**: 20–23.

Wesson, J. (1987). *Tokamaks*, Vol. 20 of *The Oxford Engineering Science Series*, Oxford University Press.

Wesson, J. A. (1981). MHD stability theory, *in* R. D. Gill (ed.), *Plasma Physics and Nuclear Fusion Research*, Academic Press, London, chapter 9, pp. 191–233.

White, O. R. and Athay, R. G. (1979a). Chromospheric oscillations observed with OSO8 I. Measurements and analytic methods, *Ap. J. Supp.* **39**: 317–331.

White, O. R. and Athay, R. G. (1979b). Chromospheric oscillations observed with OSO8 III. Average phase spectra for Si II, *Ap. J. Supp.* **39**: 347–358.

Withbroe, G. L. and Kalkofen, W. (1993). Solar variability and its terrestrial effects, *Preprint Series 3767*, Harvard-Smithsonian Center for Astrophysics, Cambridge, MA.

Withbroe, G. L. and Noyes, R. W. (1977). Mass and energy flow in the solar chromosphere and corona, *Ann. Rev. Astron. Astrophys.* **15**: 363–387.

Wolfson, R., Vekstein, G. E. and Priest, E. R. (1994). Nonlinear evolution of the coronal magnetic field under reconnective relaxation, *Ap. J.* **428**: 345–353.

Woltjer, L. (1958). A theorem on force-free magnetic fields, *Proc. Nat. Acad. Sci.* **44**(6): 489–491.

Wright, A. N. and Berger, M. A. (1989). The effect of reconnection upon the linkage and interior structure of magnetic flux tubes, *J. Geophys. Res.* **94**(A2): 1295–1302.

Wright, A. N. and Berger, M. A. (1990). The interior structure of reconnected flux tubes in a sheared plasma flow, *J. Geophys. Res.* **95**(A6): 8029–8036.

Wright, A. N. and Berger, M. A. (1991). A physical description of magnetic helicity evolution in the presence of reconnection lines, *J. Plasma Phys.* **46**(1): 179–199.

Yoshida, Z. (1992a). Eigenfunction expansions associated with the curl derivatives in cylindrical geometries: completeness of Chandrasekhar-Kendall eigenfunctions, *J. Math. Phys.* **33**(4): 1252–1256.

Zank, G. P. and Matthaeus, W. H. (1992). The equations of reduced magnetohydrodynamics, *J. Plasma Phys.* **48**(1): 85–100.

Zank, G. P. and Matthaeus, W. H. (1993). Nearly incompressible fluids. II: Magnetohydrodynamics, turbulence, and waves, *Phys. Fluids A* **5**(1): 257–273.

Zirker, J. B. (1993). Coronal heating, *Solar Phys.* **148**(1): 43–60.

Index